Characterisation and Application of Radiation Hard Sensors for LHC and ILC

Von der Fakultät für Mathematik, Naturwissenschaften und Informatik
der Brandenburgischen Technischen Universität Cottbus

zur Erlangung des akademischen Grades

Doktor der Naturwissenschaften
(Dr. rer. nat.)

genehmigte Dissertation

vorgelegt von

Dipl. Physikerin

Olga Novgorodova

geboren am 2. Februar 1984 in Moskau

Gutachter: Prof. Dr. Wolfgang Lohmann

Gutachter: Prof. Dr. Jürgen Reif

Gutachter: Prof. Dr. Hermann Kolanoski

Tag der mündlichen Prüfung: 25.06.2013

Erklärung über frühere Promotionsanträge

Hiermit versichere ich, dass ich bisher noch keinen Antrag für ein Promotionsverfahren eingereicht habe.

Cottbus, den 28.03.2013

Olga Novgorodova

Selbständigkeitserklärung

Hiermit versichere ich, dass ich die vorliegende Arbeit selbständig und nur unter Verwendung der angegeb enen Quellen und Hilfsmittel angefertigt habe.

Cottbus, den 28.03.2013

Olga Novgorodova

Erklärung zu Schutzrechten

Hiermit versichere ich, dass die Veröffentlichung der Dissertation keine bestehenden Schutzrechte verletzt.

Cottbus, den 28.03.2013

Olga Novgorodova

Abstract

The Large Hadron Collider (LHC) currently in operation intends to explore particle physics on the TeV scale. The International Linear Collider (ILC) and the Compact Linear Collider (CLIC) are being designed to measure the properties of particles possibly discovered at the LHC with high precision. Very forward detector systems at these machines are needed for the precise measurement of the luminosity and to approach full polar angle coverage. In the current detector concepts for linear collider detectors two electromagnetic calorimeters, Beam Calorimeter (BeamCal) and Luminosity Calorimeter (LumiCal), are foreseen. Both calorimeters are designed as sandwich calorimeters with tungsten absorber layers instrumented with finely segmented sensors. Due to a large amount of beamstrahlung remnants hitting BeamCal at the innermost radii, the sensors must withstand up to 1 MGy radiation dose per year. In this thesis two types of sensor materials were investigated: single crystal chemical vapour deposition diamonds (scCVDD) and gallium arsenide doped by chromium (GaAs:Cr).

The very forward calorimeters ensure coverage for high energy electrons, positrons and photons down to very low polar angles. Within this thesis, simulation studies are presented for different beam parameters of the ILC. A new sensor segmentation was proposed to achieve better reconstruction efficiency of single high-energy electrons, positrons and photons on top of the beamstrahlung background.

Only for a few years ago polycrystalline diamond sensors have been used for beam diagnostics in high-energy physics experiments. The Compact Muon Solenoid experiment, CMS, at the LHC is instrumented with several detectors for the Beam Conditions and Radiation Monitoring. The Fast Beam Conditions Monitor (BCM1F) is part of these systems. Here for the first time single crystal diamond sensors have been used. Eight detectors, comprising each a single crystal sensor and front-end electronics, are positioned around the beam pipe on both sides of the interaction region. They monitor the beam halo to protect the inner CMS detectors from adverse beam conditions and ensure high quality data for CMS. In this thesis, BCM1F data is evaluated for intrinsic time resolution and performance under harsh radiation conditions. Furthermore, it is investigated if it can be used for a bunch by bunch on-line luminosity measurement.

The second type of sensor, made of GaAs:Cr, was produced in Tomsk State University and tested as a candidate for the BeamCal for future ILC and CLIC detectors. Several GaAs:Cr sensors were characterized in the laboratory for leakage current and capacitances and used for test beam investigations. Two sensors were assembled with a fan-out, front-end and ADC ASICs to build a fully functional prototype of a sensor plane. Several test beam campaigns were done to measure the performance of the system.

Kurzfassung

Der International Linear Collider (ILC) und der Compact Linear Collider (CLIC) werden entwickelt, um die Forschung am momentan operierenden Large Hadron Collider (LHC), die Erforschung der Teilchenphysik bei TeV-Energien, fortzuführen. Das Vorwärtsdetektorsystem an Maschinen mit solch hohen Energien benötigt strahlenharte Detektoren nahe an der Strahlachse. Das Beam Calorimeter (BeamCal) ist als Samplingkalorimeter mit 30 Wolframabsorberlagen und fein segmentierten Sensoren ausgelegt. Wegen der hohen Belastung durch Beamstrahlung, die das Kalorimeter im Bereich des inneren Radius trifft, müssen die Sensoren eine Strahlendosis von bis zu 1 MGy pro Jahr aushalten. In dieser Arbeit werden zwei Arten von Sensormaterialien untersucht: Einkristalldiamanten-Sensoren (scCVD) und Galliumarsenid-Sensoren mit Chrom-Dotierung (GaAs:Cr).

Diamantsensoren sind in der Strahldiagnostik an Hochenergiephysik-Experimenten weit verbreitet. Das Compact Muon Solenoid (CMS) Experiment am LHC ist mit mehreren Detektoren zur Überwachung der Strahlqualität ausgestattet (Beam Conditions and Radiation Monitoring – BRM). Ein Detektor dieses Systems ist der Fast Beam Conditions Monitor (BCM1F), in welchen zum ersten Mal monokristalline Sensoren verwendet werden. BCM1F überwacht den Strahl, um die inneren CMS-Subdetektoren zu schützen und um eine möglichst hohe Datenqualität sicherzustellen. In dieser Arbeit werden die spezifische Zeitauflösung und der Grad der Strahlenschädigung von BCM1F bestimmt. Außerdem wird untersucht, ob sich BCM1F zur paketweisen Echtzeitmessung der Luminosität eignet.

Der zweite untersuchte Sensortyp, hergestellt aus GaAs:Cr, wurde als Kandidat für das BeamCal an einem zukünftigen ILC- oder CLIC-Detektors von der Universität Tomsk entwickelt. Im Rahmen dieser Arbeit wurden mehrere GaAs:Cr-Wafer im Labor charakterisiert. Dabei wurden die Leckströme und Kapazitäten bestimmt, um Sensoren für weitergehende Untersuhungen im Teststrahl auszuwählen. Die Sensoren wurden mit “fan-out”, Frontend-Elektronik und Analog-Digital-Wandlern bestückt, um eine voll funktionsfähige Sensorebene zu erhalten. Mehrere Teststrahl-Kampagnen wurden durchgeführt, um die Sensorebene zu charakterisieren.

Das BeamCal eines Linear Collider Detectors dient dazu, hochenergetische Elektronen, Positronen und Photonen bei sehr kleinen Polarwinkeln zu erkennen. Im Rahmen dieser Arbeit wurden Simulationsstudien für verschiedene ILC-Strahlparameter durchgeführt. Anhand dieser Simulationen wird eine alternative Segmentierung des Sensors vorgeschlagen, um eine höhere Rekonstruktionseffizienz für einzelne hochenergetische Elektronen, Positronen oder Photonen bei gleichzeitigem Beamstrahlungsuntergrund zu erreichen.

Contents

Abbreviations

ADC	Analog-to-Digital Converter
ALICE	A Large Ion Collider Experiment
ASIC	an Application-Specific Integrated Circuit
ATLAS	A Toroidal LHC Apparatus
BCM1F	Beam Condition Monitor 1 Fast
BCM1L	Beam Condition Monitor 1 Leakage
BeamCal	Beam Calorimeter
BHC	Beam Halo Counter
BPM	Beam Position Monitor
BSC	Beam Scintillation Counter
BX	Bunch Crossing
CCD	Charge Collection Distance
CCE	Charge Collection Effciency
CERN	Conseil Européen pour la Recherche Nucléaire – European Organization for Nuclear Research.
CMOS	Complementary metal-oxide semiconductor
CDF	The Collider Detector at Fermilab
cms	Center-of-Mass System
CMS	Compact Muon Solenoid
CVD	Chemical Vapor Deposition
DCal	Detector Calibration Mode
DALINAC	Darmstadt Linear Accelerator
DC	Direct current
DESY	Deutsches Elektronen-Synchrotron
DUT	Detector Under Test
ECAL	Electromagnetic Calorimeter
ENC	Equivalent noise charge
FE	Front end
Fermilab	Fermi National Accelerator Laboratory
FPGA	Field-programmable gate array
GEANT	Geometry and Tracking software package
HCAL	Hadronic Calorimeter
HERA	Hadron-Elektron-Ring-Anlage
HF	Forward Hadronic Calorimeter
HB	Hadronic calorimeter, barrel
HE	Hadronic calorimeter, endcap
HEP	High-energy physics

ILC	International Linear Collider
ILD	International Large Detector
IP	Interaction Point
LC	Linear Collider
LEP	Large Electron Positron Collider
LHC	Large Hadron Collider
LHCb	Large Hadron Collider beauty experiment
LINAC	Linear accelerator
LLD	Linear laser driver
LSB	Least Signifiacnt Bit
LumiCal	Luminosity Calorimeter
LUT	Look-up table
MC	Monte-Carlo
MIP	Minimum Ionizing Particle
MPV	Most Probable Value
NIM	Nuclear instrumentation module standard
pcCVDD	Polycrystalline CVD Diamond
PCB	Printed Circuit Board
PS	Proton Synchrotron
RadFET	Radiation-sensitive field-effect transistor
RADMON	RADiation MONitor
RDR	Reference Design Report
R&D	Research and Development
scCVDD	single-crystal CVD Diamond
SB2009	Standard Baseline ILC Beam Parametrers for 2009
SID	Silicon Detector
SLAC	Stanford Linear Accelerator Center
SNR	Signal-to-Noise Ratio
SDT	Standard Data Taking Mode
SPS	Super Proton Synchrotron
SRAM	Static Random-Access Memory
TDC	Time to Digital Converter
VME	VERSA Module Eurocard bus standard

Introduction

After more than 20 years of planning and preparation the Large Hadron Collider, LHC, started operation in September 2008. It aims to allow physicists to test predictions of different theories of particle physics. From the experiments answers are expected to the still unsolved questions of fundamental physics. It also can come up with unexpected results no one ever thought.

In the last few decades, physicists end up with the Standard Model of particle physics. The Standard Model is able to describe all measurements of the interaction of fundamental particles of the Universe at an energy up to about a TeV. There are still unanswered questions like: What is the origin of mass? Why do fundamental particles weigh the amount they do? Why do some particles have no mass at all? What is 96% of the universe made of? Why does Nature appear to have this bias for matter over antimatter? Do extra dimensions of space really exist?

To answer these questions experimental data are required, and the experiments to achieve this are at the LHC. The LHC machine is the most complex accelerator and storage ring ever built. It has allowed already to discover a particle that is a strong candidate for a Higgs boson similar to that predicted by the Standard Model to explain the generation of mass for fundamental particles. The mass of this particle is measured to be about 125 GeV.

Currently a project for a new kind of accelerator and collider is in the phase of preparation. The International Linear Collider, ILC, will be a next-generation electron-positron collider for making precision measurements of the LHC discoveries. Both machines are complementary in their physics potential.

To study new physics processes very high energy is needed. High energies allow to create heavy particles. To discover exceedingly rare particles high luminosity is required. The LHC is accelerating 2808 bunches of protons and each bunch contains 115 billions of protons. It was designed to collide bunches every 25 ns, but in 2009-2012 it was operated with 50 ns between bunch collisions. The collision products are then tracked in the detector volumes of ATLAS, CMS, ALICE, LHCb, TOTEM and LHCf. Two of them, the ATLAS and the CMS experiments, are large, general purpose particle detectors. The ALICE and LHCb experiments have more specific goals and the last two, TOTEM and LHCf, are much smaller and are for very specialized research.

Each beam stores the enormous energy of 350 MJ. This energy is enough to damage the detectors in case of the loss of the beam. A system monitoring the beam conditions and providing signal in case of dangerous situation is necessary. The systems for the beam monitoring are installed in CMS and other experiments as well as around the LHC accelerator.

The protection systems of CMS are independent from the CMS data acquisition and power supply. Some of the systems are located near the beam pipe, as beam condition monitors in CMS, where radiation hard sensors are needed. They provide fast and slow measurements of beam conditions and beam losses.

One of the systems is the Fast Beam Conditions Monitor, BCM1F. Single crystal chemical vapor deposition diamonds were used for the first time in this detector. BCM1F counts particles with a nanosecond time resolution. Its description and validation are a part of this thesis and can be found in chapter 4.

From the data collected in the experiments cross sections of investigated processes are needed to perform comparison with the theory. For the measurement of cross section the luminosity, characterizing the probability of a proton-proton collision, is needed. A precise luminosity measurement is required both for LHC and ILC. In the CMS experiment the luminosity is monitored by measuring the flux of collision products. In van der Meer scans the visible cross section is determind and the measured flux is calibrated to the luminosity. Through the 2011-2012 run CMS relied on the forward hadronic calorimeter, HF, for both the on-line and offline measurement of the luminosity. In addition, the luminosity was measured by the inner pixel detector. Due to slow pixel detector operation, it cannot provide on-line measurements. During 2012 operation BCM1F was an independent on-line luminosity measurement tool. In this thesis, the ability of BCM1F to measure the luminosity in real time is demonstrated and the bunch-by-bunch luminosity measurement is discussed in chapter 5.

The ILC detector requires an even more precise luminosity measurement and in addition an excellent hermeticity. There are two electromagnetic calorimeters foreseen in the very forward region, located on both sides of interaction point, IP. The Luminosity Calorimeter, LumiCal, will be used to measure the small-angle Bhabha scattering, being the gauge process for the luminosity measurement.The Beam Calorimeter, BeamCal, will be located as near as possible to the beam-pipe and covers the lowest possible polar angle in the ILC detector. The forward region is described in chapter 6. BeamCal will measure high-energy electrons, positrons or photons at low polar angle. Their detection will be a challenge due to background coming from e^+ e^- pairs of beamstrahlung photon conversions. The deposition of these pairs will also provide the ILC with a fast luminosity measurement and beam diagnostics. Two different sensor segmentations are compared for the single high energy electron shower reconstruction efficiency on top of the large beamstrahlung background. Chapter 7 summarizes the results obtained from the simulation studies.

As the high radiation environment due to beamstrahlung pairs sets a requirement on the sensors used for the BeamCal, a new material, GaAs:Cr, was proved before to be a good candidate. Several sets of sensors with two types of segmentation were characterized in the laboratory. The measurements and results are presented in chapter 2. A prototype of the BeamCal sensor plane based on the GaAs:Cr sensor was prepared and investigated in the laboratory and in several test-beam campaigns in the electron beam with energies between 2-4.5 GeV. The preparation of the test beams is described in the chapter 8 and the data analysis in the chapter 9.

Chapter 1

Solid State Detectors for Radiation

Introduction

Over a long time in high energy and nuclear physics a lot of different types of detectors have been developed. Charged particles deposit energy in the detector's medium by ionisation or excitation and photons by the photoelectric effect, Compton scattering and pair production. Neutral hadrons have to interact with nuclei of the detector material to create charged particles which will be detected. Finally, these depositions are transformed, for example, in electronic signals recorded and analysed by computers.

Detectors can be classified into gaseous, liquid and solid state detectors. In gaseous detectors, ions and electrons drift in the electric field and the current is measured. In solid state detectors, free electrons and "holes", called charge carriers, are created, and drift in an applied electric field.

In this thesis only solid state detectors will be considered. Widely used are semiconductor detectors, in particular silicon. Using silicon detectors for high fluences, cooling is required to reduce the leakage current. For detectors operated at room temperatures other materials are considered. The main focus of this thesis is the radiation tolerance of the detectors at room temperature. In this respect GaAs (semiconductor) and diamond (insulator) are considered. There is also a lot of effort ongoing to make silicon sensors more radiation hard, but this topic will not be discussed here. This chapter is describing solid state detectors made of GaAs and diamond sensors.

1.1 Solid State Detectors

Most solid state detectors are produced of semiconductor materials and some from insulators. A semiconductor material differs from insulators by its relatively larger electrical conductivity. Insulators and semiconductors change the electrical resistivity with temperature. The behavior of semiconductors can be manipulated by adding impurities (doping). The semiconductor conductivity is explained by "free" electrons and holes, which are called *charge carriers*. The doping is made by adding into the material, a small amount of impurities. Impurity atoms act as either donors or acceptors to the intrinsic semiconductor. They are also called semiconductor materials of *n-type* for donors and *p-type* for acceptor

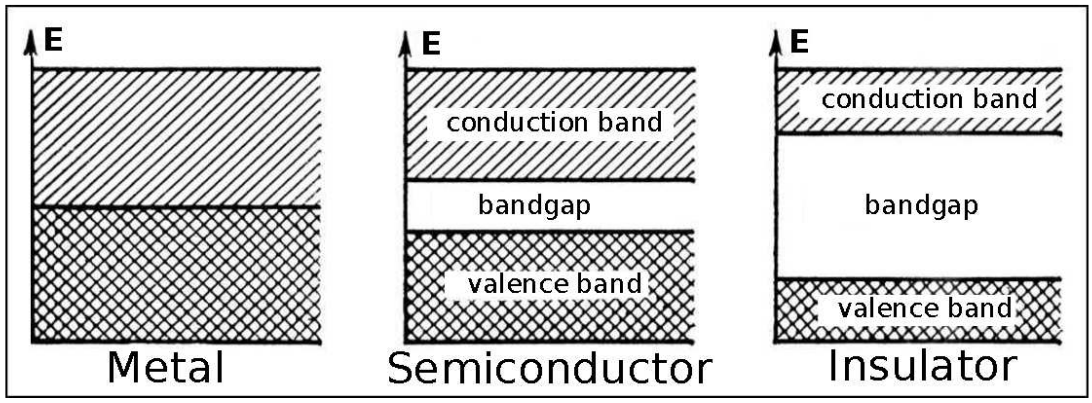

Figure 1.1: Simplified band structure of metal, semiconductor and insulator. E is the energy of electron states.

impurities. The impurities change the electron and hole concentrations of the semiconductor.

A pure semiconductor is called an *intrinsic* semiconductor. The doping procedure is often made by adding impurities during the manufacturing process. After adding impurities in intrinsic semiconductor is called "extrinsic".

Pure elements in Group IV of the periodic system are mostly semiconductors. The most commonly used materials are silicon and germanium. Another possibilities to get semiconductors is to combine neighbor groups of elements (III and V, II and VI, IV and VI). There is a large amount of semiconductors in use e.g. gallium arsenide.

Semiconductors are crystalline materials in which outer shell energy levels follow the band structure [1]. Figure 1.1 shows the band structure of a metal, a semiconductor and an insulator. The band structure of metals, semiconductors and insulators is described by a *valence band*, a *forbidden* energy *band gap* and a *conduction band*.

The energy bands contain many electron energy levels, which are shown as the energy areas. The energy band gap, E_g, is without any energy level. The energy levels in the valence band are filled. In the higher energy conduction band, E_c, electrons are detached from the parent atom and can freely move around the full crystal.

The semiconductor energy band gap height depends on the lattice spacing between the atoms. The lattice spacing depends on the temperature and pressure.

In an insulator at room temperature, electrons are located in the valence band. Due to the low energy of thermal photons the probability to excite electrons to the conduction band is extremely small. With an applied external field only a very low current flow through the insulators.

An important parameter of solids is the *Fermi level*. It describes the top of the electron energy levels at zero K temperature. As electrons are fermions they follow the Pauli principle and cannot exist in identical quantum states. Then at zero K electrons will stay at the lowest available energy states, called *Fermi sea*. The *Fermi level* is the surface of the *Fermi sea*. In this state there are no electrons which will have enough energy to rise above the surface.

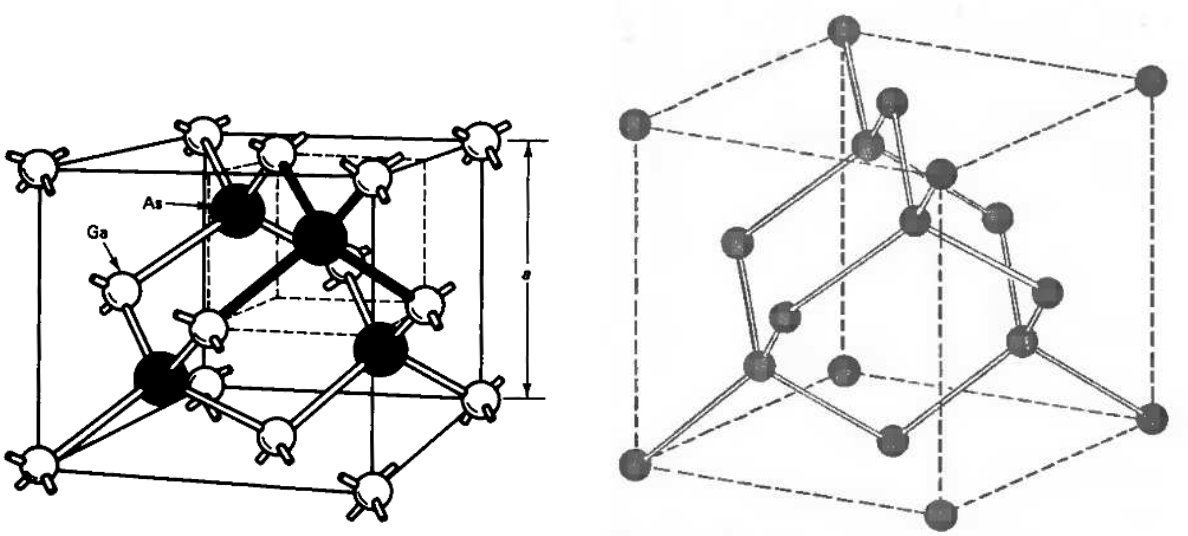

(a) (b)

Figure 1.2: (a) Crystal structure of GaAs and (b) of diamond [2].

Carbon, silicon, germanium and tin are elements in ascending order of atomic number in Group IV A of the periodic table. Atoms of these elements are characterized by having four valence electrons in their outermost shell. Further four are required to make up the full complement of the shell. All solidify by forming elemental, covalently bonded crystals where the four valence electrons of one atom are shared between its four nearest neighbors so that every atom effectively gains eight electrons in its valence shell.

GaAs is a compound semiconductor with a wider band gap than silicon. Figure 1.2(a) shows the GaAs crystal lattice, called *zincblende*. The two atom types form two interpenetrating face-centered cubic lattices. The zincblende structure has tetrahedral shape. Each atom's nearest neighbors consist of four atoms of the opposite type. They are positioned like the four vertices of a regular tetrahedron. The arrangement of atoms in the zincblende structure is the same as in the cubic structure of diamond, as shown in Figure 1.2(b) but with alternating types of atoms.

1.1.1 Charge Carriers

Charge carriers are called charged particles which are free to move. Examples are electrons, ions and holes. In semiconductors, charge carriers are electrons and holes. Holes are in fact the traveling vacancies in the valence-band,E_v. They act as mobile positive charges both in GaAs:Cr and diamond. Charge carriers are characterized by their lifetime, mobility and concentration in the detector bulk. In an electric field charge carriers move with a drift velocity being a function of the field strength.

The mean kinetic energy of charge carriers is $\frac{3}{2}kT$, where k is the Boltzmann constant and T the temperature. At room temperature, the mean velocity is around 10^7 cm/s, the mean free path is about 10^{-5} cm and the mean lifetime is $\tau \approx 10^{-12}$ s. But without an external electric field the charge carriers will not be displaced in average. After applying an electric field, they are accelerated in the direction to the electrode of opposite charge.

In addition, they will have random collisions with the lattice. The averaged drift velocity of charge carriers in semiconductors at low applied electric field is:

$$\nu_{\mathrm{n}} = -\frac{q \cdot \tau_{\mathrm{c}}^{n}}{m_{\mathrm{n}}} E = -\mu_{\mathrm{n}} E,$$

$$\nu_{\mathrm{p}} = \frac{q \cdot \tau_{\mathrm{c}}^{p}}{m_{\mathrm{p}}} E = \mu_{\mathrm{p}} E,$$

where $\mu_{\mathrm{n,p}}$ are electron (n type) and hole (p type) mobilities, $\tau_{\mathrm{c}^{n,p}}$ the charge carriers mean collision time, $m_{\mathrm{n,p}}$ are electron and hole mass and ε the electrical field [3].

1.1.2 Schottky Contact

A metal-semiconductor contact is forming a so called Schottky contact. It is a potential barrier between the metal and semiconductor band structures. Not all metal-semiconductor junctions form Schottky barriers. A metal-semiconductor junction that does not rectify current is called an ohmic contact.

Figure 1.3 shows the band diagrams before and after the Schottky contact between metal and n-type semiconductor is formed. If there is no externally applied voltage, the Fermi level,E_F, of the metal and the semiconductor must be equal. In metals the Fermi level is the top of the electron sea. For semiconductors the Fermi level is located higher and is determined by the doping levels, as showing in Figure 1.3a. Then the work function of the semiconductor, $\mathrm{F_s}$, is smaller than that of the metal, $\mathrm{F_m}$. Where the work function is the minimum thermodynamic work necessary to put an electron from a solid to a point in the vacuum, E_{vac}. Hence, electrons will flow from the semiconductor into the metal. This generates a potential barrier along the interface region, as shown in Figure 1.3b.

The potential gradient will force electrons in the semiconductor to move away from the metal-semiconductor interface. Positive donor ions are left, forming a depleted region.

1.2 Energy Loss and Signal Formation

Charged relativistic particles passing through matter deposit energy, mainly due to electromagnetic interaction with electrons and nuclei. In addition, these particles will be deflected in the coulomb field of nuclei leading to multiple scattering.

The mean energy loss due to ionisation (or stopping power) for particles other than electrons is given by the Bethe-Bloch formula [5]:

$$-\langle\frac{dE}{dx}\rangle = Kz^2\frac{Z}{A}\frac{1}{\beta^2}\left(\frac{1}{2}\ln(\frac{2m_e c^2\beta^2\gamma^2 T_{max}}{I^2}) - \beta^2 - \frac{\delta(\beta\gamma)}{2}\right),$$

where m_e is the electron mass,

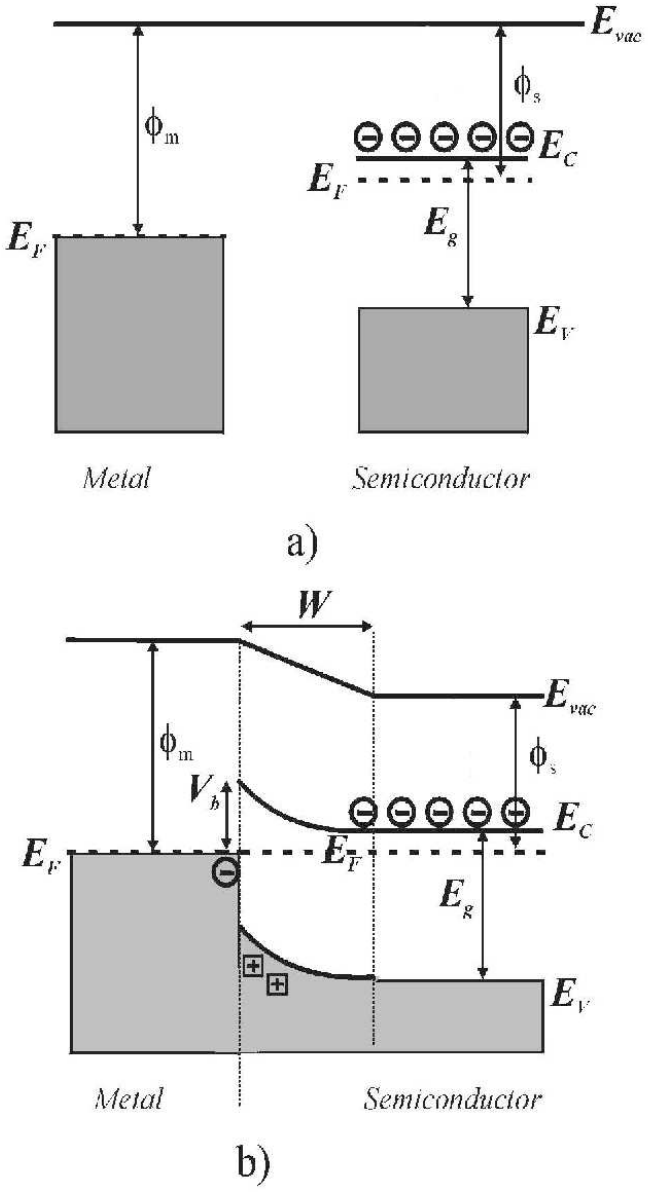

Figure 1.3: a) A schematic representation of energy bands of isolated metal and isolated n-type semiconductor. b) The band diagram at the contact between the metal and the semiconductor [4].

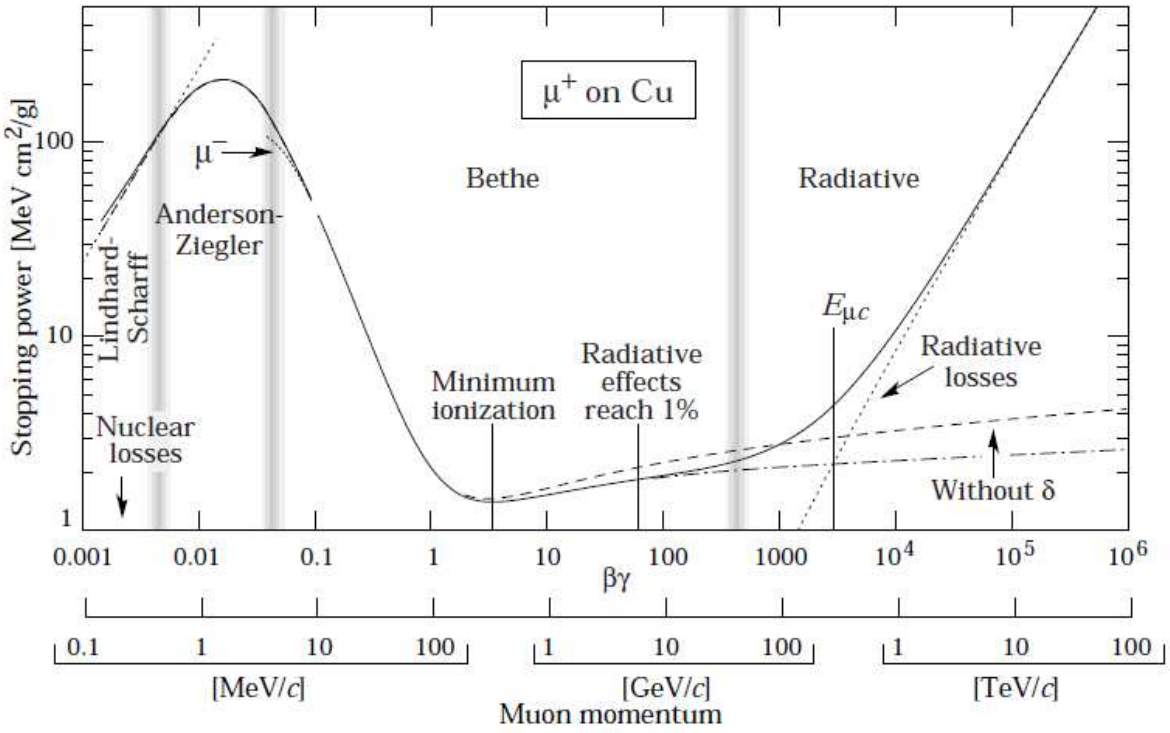

Figure 1.4: Mean energy loss for positive muons in copper as a function of $\beta\gamma = p/mc$ over nine orders of magnitude in momentum (12 orders of magnitude in kinetic energy). Solid curves indicate the total stopping power. Picture is taken from PDG [5].

β the velocity of the particle, $\beta = v/c$,
$\gamma = \frac{1}{\sqrt{(1-\beta^2)}}$,
Z the atomic number,
A atomic weight,
I the average ionization potential for the medium,
$\delta(p)$ is a small correction due to media polarization,
c is the speed of light and
T_{max} is the maximum kinetic energy that can be transferred to a free electron in a single collision.

As an example, the mean energy loss computed for muons in copper is shown as the "Bethe" region of figure 1.4 [5]. It decreases with $\frac{1}{\beta^2}$ until a minimum of is obtained for $3 < \beta \cdot \gamma < 4$. Because of the logarithmic term the energy loss increases again (relativistic rise) until a plateau is reached, called Fermi plateau. The relativistic rise saturates at high energies because the medium becomes polarized, effectively reducing the influence of distant collisions. Particles with $\beta \cdot \gamma \simeq 3.5$ have minimum loss and are called minimum ionizing particles (MIPs). Above $\beta \cdot \gamma = 100$ radiation losses due to Bremstrahlung and pair production become dominant.

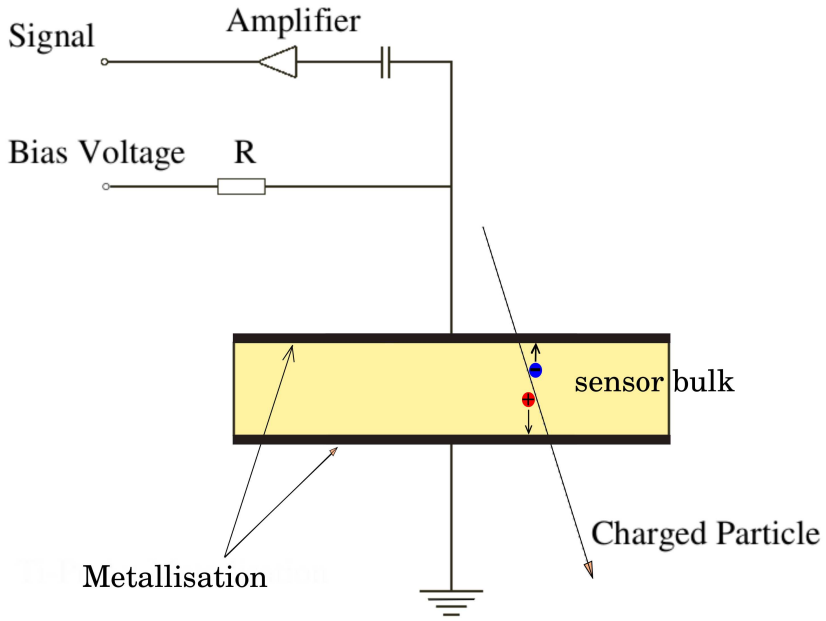

Figure 1.5: Principle of solid state ionisation chambers.

1.2.1 Signal Formation

Solid state detectors like diamonds and GaAs are operated as ionization chambers as shown in figure 1.5. This is possible due to their high resistivity of about 10^{13} Ωm. A charged particle crossing the medium deposits energy and some part of the deposited energy is going to create electron-hole pairs. Applying an electric field causes electrons and holes to drift to the positive and negative electrodes, and an electric current is induced in the external circuit. Electrodes can be segmented into pads, strips or pixels of different sizes, allowing the measurement of the position of the crossing particle. The charge created in the medium can be calculated by:

$$Q = \frac{E}{E_{ion}} e, \tag{1.1}$$

where E is the energy deposited in the medium, E_{ion} the energy required to create an electron-hole pair and e the electron charge.

The energy needed to generate an electron-hole pair is called *ionization energy*. It is proportional to the band gap. A lower ionization energy provides a larger charge for the same amount of deposited energy in the medium.

Without an external electric field, the created electron-hole pairs will diffuse and recombine. When an external electric field is applied, electrons and holes drift. The signal formation starts with the very first drift of electrons and holes. While electrons and holes are drifting to the electrodes, they induce charge in the electrodes, according to Ramo's theorem [6]. Only when the last electrons or holes reach the electrode or are trapped the signal formation stops. The velocities of the electrons and holes, $\vec{v}(x) = \mu\vec{E}(x)$, depend on the electric field $\vec{E}(x)$ in the medium and the mobility μ. The mobility is a characteristic

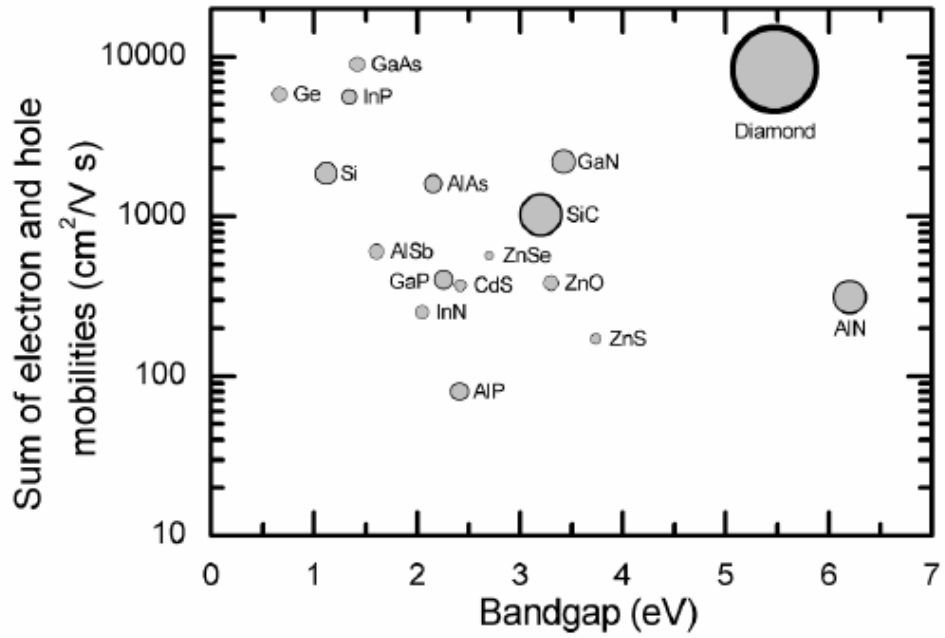

Figure 1.6: Electron and hole mobilities at room temperature. The mobility in diamond is taken from Isberg et al. (2002). Circles have an area proportional to the thermal conductivity.

of the material and connected to the diffusion constant D by Einstein equation [7]:

$$\mu = \frac{e}{kT} D.$$

Figure 1.6 shows the sum of electron and hole mobilities at room temperature for several materials. The sum of electron and hole mobilities for GaAs and diamonds is relatively large. The mobility for electrons and holes can be different, e.g. for GaAs the mobility for electrons is significantly higher than for holes ($\mu_{GaAs}(e)$ =8500 cm^2/Vs, $\mu_{GaAs}(h)$ =320 cm^2/Vs).

Table 1.1 compares the main characteristics of Si, diamond and GaAs.

1.3 Diamond Sensors

A single-crystal diamond has several important properties. It has the highest thermal conductivity at room temperature, high mechanical hardness and radiation tolerance and an ultra-wide optical transmission range. Diamond is an insulating material with a band gap of 5.7 eV. The low dielectric constant of diamond, $\varepsilon_C = 5.7$, leads to a small sensor capacitance for the front-end electronics.

1.3.1 Chemical Vapour Deposition Diamond Growth

Artificial diamonds were produced by the "high-pressure high-temperature (HPHT) growth" method [13]. Such diamonds contain a relatively large fractions of impurities making their use as sensors for radiation detection difficult. Diamond films with a lower fraction of

Characteristics	Silicon	GaAs	Diamond
Density, [g/cm^3]	2.32	5.32	3.52
Band gap, [eV]	1.12	1.42	5.45
Crystal structure	diamond cubic	zinc blende	diamond cubic
Lattice structure	diamond	sphalerite	diamond
Dielectric constant	11.9	12.9	5.7
Energy for e-h creation, [eV]	3.62 [8]	4.3 [9]	13.2 [10]
Mobility electrons,[cm^2/Vs]	1350	8500-8800	1800-4500 [11]
Mobility h,[cm^2/Vs]	480	320-400	1200-3800 [11]
Z	14	31, 33	6
Radiation length, X_0, [cm]	9.4	2.3	12.2
Resistivity, [Ω cm]	2.5 10^5	4 10^8	10^{13} - 10^{16}
Thermal conductivity, [W/cmK]	1.5	0.45	20

Table 1.1: Characteristics of materials used as sensors [9], [11] and [12]. The mobilities and the resistivity of diamond depend strongly on its purity.

impurities are produced by "Chemical Vapour Deposition (CVD)". The principle is to add carbon atoms one-at-a-time to an initial template. Thereby the tetrahedral bonds of the diamond lattice appear. As precursor a carbon-containing gas (often methane) is used, which is activated in a plasma by discharges or under temperatures higher than 2000° C [14].

In general the CVD diamond growth can be described by the following reaction:

$$CH_4(gas) \longrightarrow C(diamond) + 2H_2(gas).$$

The CVD diamond production process involves the following steps: activation of the gas phase, nucleation and diamond growth. Activation provides reactive radicals for further chemical reactions. Nucleation is the process when individual carbon atoms create nuclei on the template surface and form a sp^3 tetrahedral lattice. The proper choice of the initial template is important. The best template material is diamond (natural or HPHT), which provides the exact template for the diamond lattice. But also non-diamond substrates are used and the best non-diamond substrates are materials capable of forming carbide. Iridium substrates are under investigation since it has a lattice constant similar to diamond. They emerge in providing highly oriented films, significantly better than any other transition metals [15]. After the nucleation phase (clusters reached critical size and became stable) the growth phase starts in all three dimensions until the clusters reach each other and then they grow in one dimension and create a column like structure. This column structure creates crystal defects in the diamond bulk material. This can be a reason for non-homogeneous responses for polycrystalline diamonds [16].

The next step is to shape the diamond mechanically or by laser cutting and to metallize on both sides. For example, lithographically patterned metallization can be used.

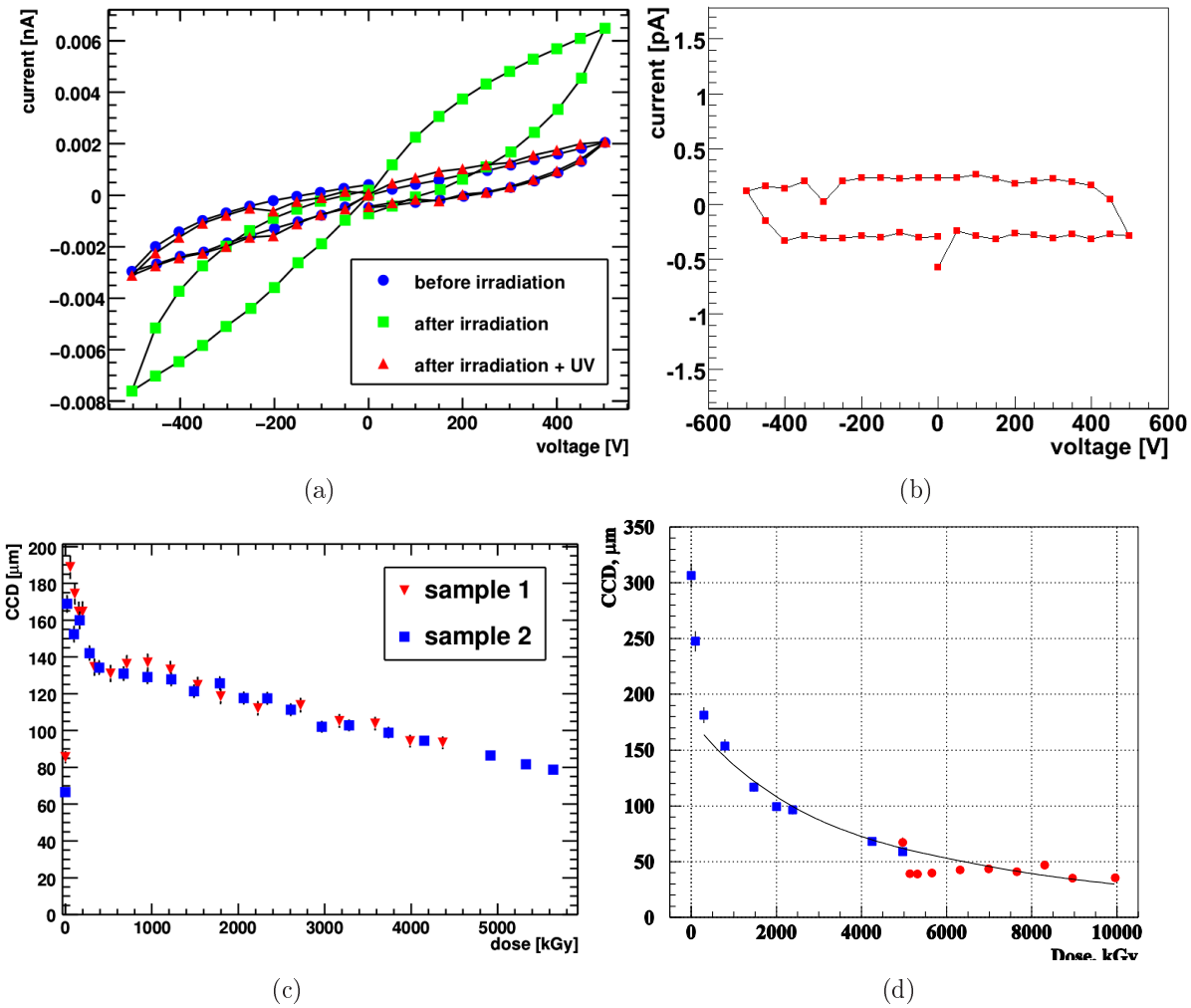

(a) (b)

(c) (d)

Figure 1.7: (a) The leakage current of pcCVD diamond as a function of applied voltage before *(blue)*, after *(green)* irradiation and after UV illumination *(red)* [17]. (b) The leakage current of scCVD diamond as a function of applied voltage after irradiation [18]. (c) Charge Collection Distance as a function of the dose absorbed for pcCVD diamond, measured using ^{90}Sr source. Triangles and squares represent two different samples [17]. (d) Charge Collection Distance as a function of the dose absorbed for scCVD diamond *(blue)* in 2007, *(red)* in 2008 [18].

1.3.2 Characterization

The leakage current of a polycrystalline CVD diamond as a function of the applied voltage is shown in figure 1.7(a). The sensor size is of about 12 mm x 12 mm x 500 μm with 10 mm x 10 mm metallization. The leakage current measured directly after irradiation exhibits a three times larger current. After applying an UV light illumination for about half an hour the leakage current became similar to the one before the irradiation [17]. The leakage current of single-crystalline diamond as a function of applied voltage is shown in figure 1.7(b). The leakage current was measured after the scCVDD was irradiated, before irradiation the leakage current was too small to measure. The studies scCVD diamond has a size of about 4 mm x 4 mm x 326 μm with round metallization of about 3 mm diameter.

The charge collection efficiency can be expressed by the mean drift distance, which is also called "charge collection distance", CCD. The charge collection distance as a function of absorbed dose decreases as shown in figure 1.7(c). In the first moment of irradiation the charge collection distance grows. This effect is called *Pumping Effect*. Since there are non-diamond atoms in the bulk, energy levels inside the band gap occur. These levels act as charge traps. During irradiation, they are filled and can not absorb electrons and holes anymore. After all traps are filled, the diamond is called *pumped*. By irradiating the diamond with UV light, trapped charges are released, which brings the diamond into the initial state. Figure 1.7(a) shows a reduction of the leakage current after irradiating diamond with UV light. This shows that diamond structure was not damaged after the irradiation. Figure 1.7(d) shows the charge collection distance of the scCVD diamond as a function of absorbed dose. The initial charge collection distance for scCVD diamonds is higher than for the pcCVD diamonds. The CCD for scCVDD drops in the beginning faster and then shows similar slope as for the pcCVD diamonds.

1.4 Gallium Arsenide Sensors

In collaboration with Joint Institute for Nuclear Research, JINR, and Tomsk State University several gallium arsenide GaAs wafers were produced. The crystals were grown by the Liquid Encapsulated Czochralski, LEC, method. The wafers of initial LEC GaAs material are doped by a shallow donor (Sn or Te). This doping is necessary to form a low-ohmic n-type semiconductor and to fill EL+ trapping centers with electrons. Then the wafers were annealed and compensated with a deep acceptor (Cr) by means of controlled diffusion at high temperature [19]. During annealing Cr diffuses through the wafer and compensates EL2+ traps. The specific properties of the GaAs:Cr wafers are the relatively large electron lifetime (5–10 ns) and the ability to produce a uniform electric field profile in structures with ohmic contacts. Due to the wide direct band gap and additional doping, GaAs is expected to be radiation tolerant. In addition it has high resistivity and can be operated similar to the diamond detectors. It is called a semi-insulating high-ohmic intrinsic material.

The wafer thickness is 500 μm. The final GaAs:Cr sensor has the form of a sector to allow circular assembly. Sensors are polished and metallized on both sides with Aluminum or Nickel. One side has a continuous metallization and the opposite side is segmented.

1.4.1 Liquid Encapsulated Czochralski

The growth starts with putting Gallium and Arsenic into a growth crucible. This is placed inside a high pressure crystal puller and heated up. At high temperatures the components melt. Adding boron trioxide creates a liquid boron oxide encapsulation to cover the melted GaAs [20]. This layer of boron trioxide, in combination with the pressure in the crystal puller, prevents sublimation of the volatile Group V element.

The materials melt until the compound synthesizes. Then a seed crystal is dipped through the boron trioxide layer into the melt. The seed is rotated and slowly withdrawn and a single crystal propagates from the seed.

1.4.2 Characterization

Measurement of the radiation tolerance of GaAs:Cr are shown in figures 1.8(a) 1.8(b) and 1.8(c) [21]. Several GaAs:Cr sensors were tested in an electron beam of up to 50 nA beam current at the "Superconducting Darmstadt Linear Accelerator"(S-DALINAC). One of the GaAs:Cr sensor sector pads was irradiated with 8.5–10 MeV electrons up to a dose of 1.5 MGy. The sensor performance was measured as a function of the absorbed dose.

In figure 1.8(a) GaAs the leakage current before and after the irradiation is shown as a function of the bias voltage applied. An increase of the leakage current by almost a factor of two is observed at room temperature after irradiation. However, the leakage current after irradiation is still small enough to operate a detector.

In figure 1.8(b) the charge collection efficiency, *CCE*, is shown as a function of the bias voltage applied. As it is seen, the CCE increases as the applied bias voltage increases and comes to a saturation. After irradiation the CCE is reduced and approaches saturation at larger voltages.

The CCE as a function of the absorbed dose is shown in the figure 1.8(c). For the two irradiated samples the CCE follows a similar decrease. The observed CCE dropped from 50% to 5% [22]. After irradiation the signal-to-noise ratio was still acceptable for MIP detection. All measurements were done at room temperature. The samples were kept under bias voltage of 200 V for the whole duration of the measurements.

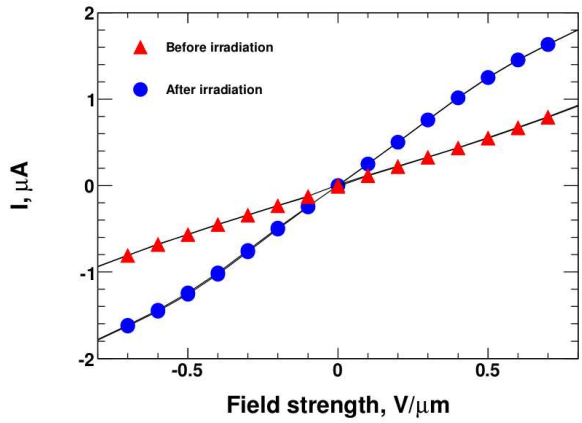

(a)

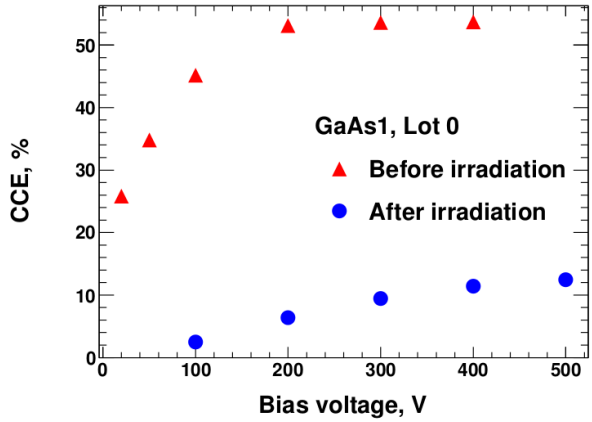

(b)

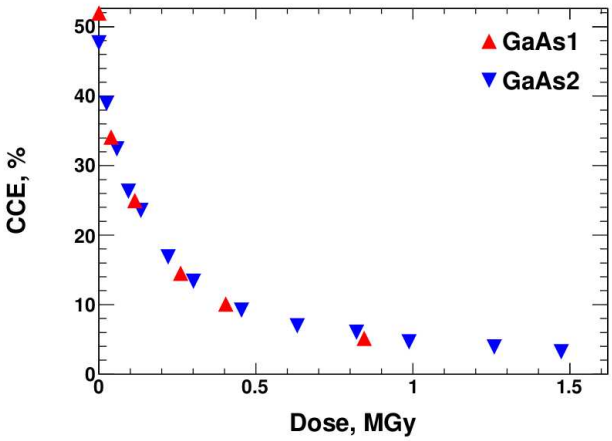

(c)

Figure 1.8: (a) The leakage current as a function of the bias voltage before (*red*) and after irradiation (*blue*). (b) The CCE as a function of the bias voltage before (*red*) and after irradiation (*blue*). (c) The CCE as a function of the dose absorbed for two GaAs sensors before (*red*) and after irradiation (*blue*) under bias voltage of 200 V [21]. One of the GaAs:Cr sensor sector pads was irradiated with 8.5–10 MeV electrons up to a dose of 1.5 MGy.

1.5 Devices for Data Taking

The size and shape of a signal depend on the number of electron-hole pairs created per μm inside the material and on the mobility of the charge carriers. Signals are amplified, shaped and transferred to the analysing electronics. Charge sensitive amplifiers are used for all studies in this thesis. They produce fast output signals. The shaper is slow in the operation and it makes an output signal of a standard shape.

The following devices for signal processing were used:

ADC The analog-to-digital converter converts an analog signal into a digital number, quantifying the amplitude of the signal. Some ADCs perform the conversions periodically with a sampling frequency. There are other ADCs, which work with an external trigger.

Here direct-conversion or flash ADCs were used for the signal processing. Such an ADC has a set of comparators sampling the input signal in parallel. Each comparator fires for its own voltage range. An advantage of a flash ADC is the high sampling rate.

TDC The time to digital converter. It is used to measure the exact time of signal arrival or its duration. On a generic approach, a TDC is a high-frequency counter that increments every clock cycle. When a signal occurs, the counter's value, representing the time, is saved to a buffer and can be read out. The clock cycle frequency defines the time resolution. The clock stability is important for the measurement accuracy.

Scaler is a device that counts the number of signals in a certain time interval.

Discriminator generates for each input signal above a certain threshold a standard output signal. Two kinds are used - fixed or constant fraction threshold.

DAQ Data acquisition is the process of sampling signals and converting the resulting samples into digital numeric values that can be analysed by a computer. The distinction is made between hardware and software DAQ.

The components of data acquisition systems include:

1. Sensors that convert physical parameters to electrical signals.
2. Circuits for analysing signals to convert sensor signals into a form that can be converted to digital values.
3. Analog-to-digital converters, which convert sensor signals to digital values.

The data acquisition hardware is controlled by software programs developed using various general purpose programming languages.

Chapter 2

Characterization of Radiation Hard Sensors

2.1 Beam Calorimeter Sensors

In test beams in 2010 and 2011 two GaAs:Cr sensors with different pad geometries have been investigated. The first one was subdivided in pads of about 5 by 5 mm^2, as shown in figure 2.1(a) and 2.2(a), denoted as type 1. The second one, type 2, has a geometry optimized by Monte Carlo simulation as described in chapter 7 and has different pad areas, depending on the radius, as shown in figure 2.1(b) and 2.2(b). Both GaAs sensors were grown by the Liquid Encapsulated Choralski method and doped with Cr, as discussed in the section 1.4. The sensor thickness was chosen to be 500 μm to ensure mechanical stability. The sensors are shaped as sectors to construct a ring. The sector angles are 45° and 22.5°, respectively. The inner and outer radii are given in Table 2.1. Each sensor was metallized on both sides and on one side the metallization is subdivided radially in 12 rings and each ring in pads. Sensors of type 1 were metallized by Aluminum and of type 2 with Nickel. The number of pads is 87 and 64, respectively. Some sensor parameters are summarized in the Table 2.1. The pad numbering uses the ring number, counted from bottom to top, and the pad number inside a ring, counted from left to right. All sensors of type 2 measured on a probe station are listed in the Table 2.2. Sensor characteristics were provided from the manufacturer. The characterisation of type 1 sensors (AG-66 No 7, AG-66 No 21, AG-66 No 26, AG-66 No 34 and AG-84 No 5) is summarized in Ref [23].

2.2 Measurement of Sensor Characteristics

For each pad of a sensor the capacitance and the leakage current are measured as a function of applied voltage. The measurements were done on a probe station. The side fully metalized was contacted to the chuck, the temperature controlled metal plate for sensor holding. Pads were contacted with needles. The probe station provided electromagnetic and optical shielding. The temperature control was provided together with dried air for humidity reduction. All measurements were done using a Labview program.

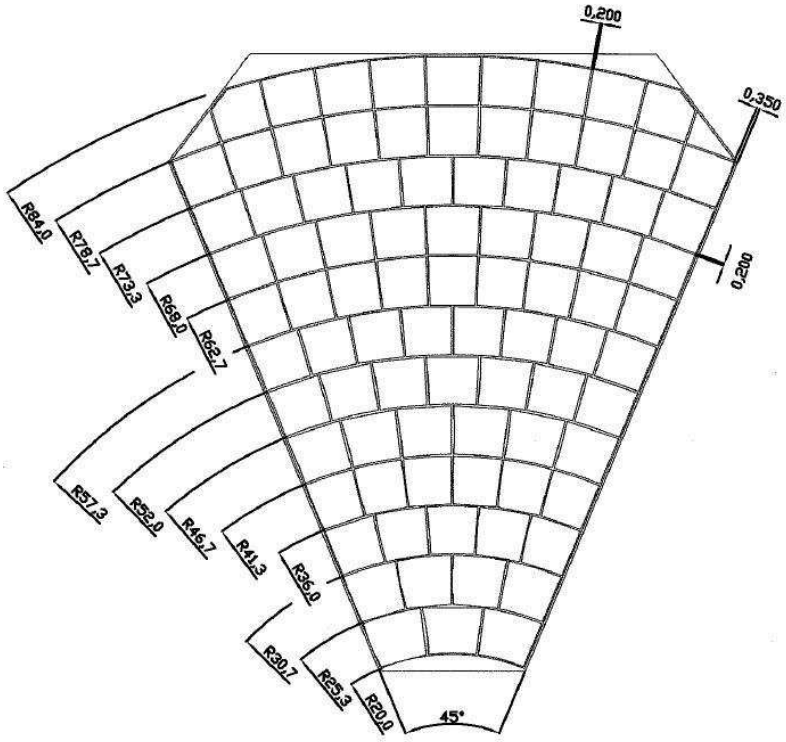

(a) type 1

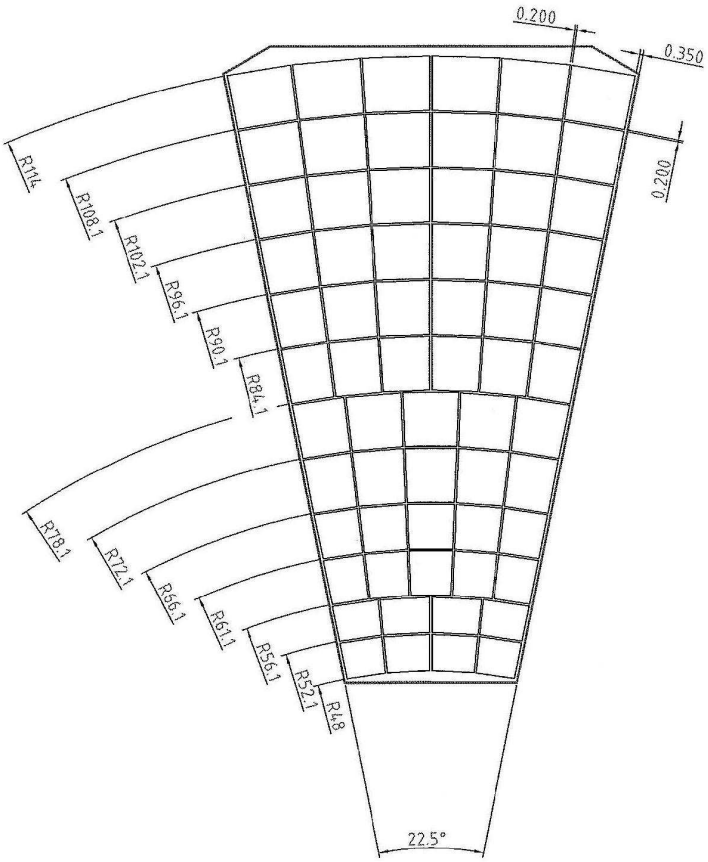

(b) type 2

Figure 2.1: (a) Equally segmented GaAs:Cr sensor sector layout (type 1). (b) Proportionally segmented GaAs:Cr sensor sector layout (type 2).

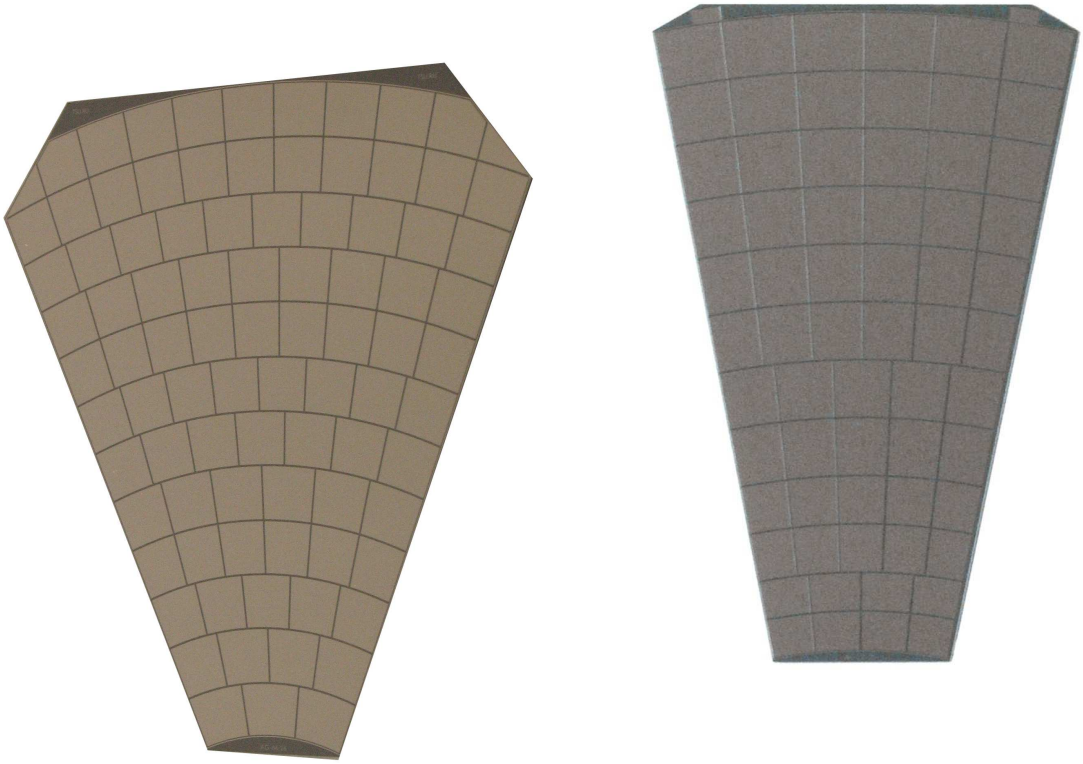

(a) type 1 (b) type 2

Figure 2.2: (a) Photo of a GaAs:Cr sensor sector of type 1. (b) Photo of a GaAs:Cr sensor sector of type 2.

Characteristic	Sensor type 1	Sensor type 2
Metallization	Aluminum	Nickel
Inner radius	20 mm	48 mm
Outer radius	84 mm	114 mm
Rings	12	12
Sector angle	45°	22.5°
Number of pads	87	64
Pad area	25 mm^2	from 16 to 42 mm^2
Pad gaps	0.2 mm	0.2 mm
Guard ring	0.35 mm	0.35 mm

Table 2.1: Parameters of the sensors of type 1 and type 2.

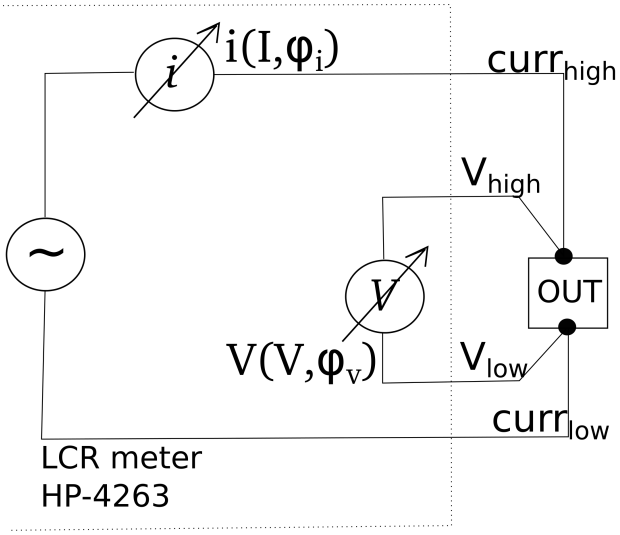

Figure 2.3: The principle scheme of the setup for the capacitance-voltage measurements.

2.3 Capacitance Measurements

The principle of the capacitance measurements is shown in figure 2.3. The LCR-meter feeds a pad of the GaAs sensor with an alternating current $i = i_a sin(\omega t + \phi_i)$ and measures the voltage amplitude u_a and the phase shift $\delta\phi_i$ of the voltage drop $u = u_a sin(\omega t + \phi_i + \delta\phi)$. Then the impedance is calculated. A constant DC voltage is applied with a Keithley 487 voltage supply through the coupling box. Capacitances of all sensor pads were measured with a HP-4263 LCR meter [24]. It allows to measure capacitances with voltages up to 450V. Measurements were made at 1 kHz frequency.

Figure 2.4(a) shows capacitance measurements as a function of pad size for one entire sensor of type 2. They are shown as grey triangles. The measurements were fit with a linear function. All neighboring pads were left floating. The middle line shows the calculated capacitances expected for a parallel plate capacitor $C = \frac{\epsilon A}{d}$, where ϵ is the dielectric constant, A the pad area and d the separation between the plates. The lower line are inter-pad capacitances, measured between two neighboring pads without connection to the backplane. All measured pad capacitances are in the range from 6 to 12 pF. Both the

Sample number	Manufacture number	Thickness, μm	Collected Charge, e	Comments
1	AG-84 No 7	490	38750	Guard Break
2	AG-84 No 13	498	38450	Bonded for tests
3	AG-84 No 19	495	38520	
4	AG-84 No 21	492	36550	Guard Break
5	AG-84 No 26	502	36490	Guard Break
6	AG-84 No 28	500	38590	Guard Break
7	AG-84 No 29	487	38420	
8	AG-84 No 32	502	38720	
9	AG-84 No 39	495	36450	
10	AG-84 No 41	487	37700	Guard Break
11	AG-221 No 25	492	41570	TB2011
12	AG-262 No 1	506	40570	
13	AG-262 No 3	512	41640	
14	AG-262 No 4	509	42690	
15	AG-221 No 6	498	37020	
16	AG-262 No 12	504	35630	
17	AG-262 No 13	517	37580	
18	AG-262 No 15	518	39190	
19	AG-262 No 16	509	37170	
20	AG-262 No 19	507	34490	
21	AG-84 No 23	492	37930	Guard Break
22	AG-84 No 24	485	38520	Guard Break

Table 2.2: 22 GaAs:Cr type 2 sensor characteristics given by the manufacturer.

measurements and predictions depend linearly on the pad size, but the slope is different. The measured pad capacitances differ from the calculated values by less than 1 pF. Other capacitance measurements are shown in appendix C.

By measuring capacitances, the metallization can be checked and crosstalk can be estimated. For several sensors different behavior of the capacitance as a function of bias voltage was observed and an example is shown in figure 2.4(b). The value of capacitances is higher than the maximum previously measured capacitance of 12 pF and is growing for pad and guard ring capacitance simultaneously at positive bias voltage applied. Such behavior was observed in less than 1 % of pads and only for the sensors of AG-84 series.

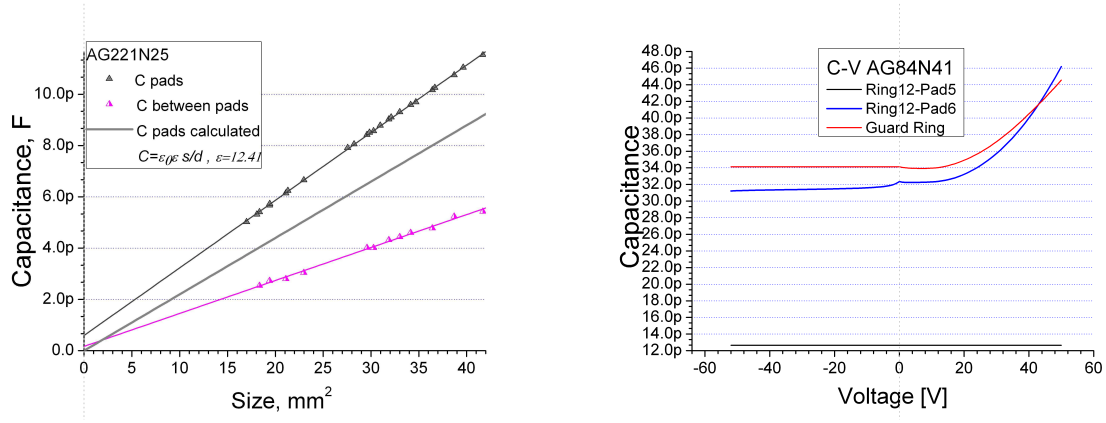

(a) (b)

Figure 2.4: (a) The capacitance measured as a function of the pad size between the back plane and each pad without grounding of neighboring pads - upper gray triangles line. The capacitance calculated – middle gray line. The capacitance measured between neighboring pads - purple triangles line. (b) Unexpected values from the measurement of the capacitance between pad and the back plane near to the guard ring and between the guard ring and the back plane as a function of the bias voltage.

2.4 Current-Voltage Characteristics

The leakage current as a function of the applied voltage was measured for all pads. An example is shown in figure 2.5(a). A Keithley 487 Picoammeter was used as a high voltage supply. Voltage steps were of 1 V up to 10V and of 10 V between 10 V and 350 V. All 22 sensors were measured at room temperature of 25°C. Figure 2.5(c) shows the zoom between -10 V and +10 V. It shows linear dependence between 10 V and 250 V and non-linear dependence between 0 V and 10 V. From the linear range the resistivity was calculated and is of the order 2.4x10^8 Ω.

The non-linear dependence of the leakage current from the applied voltage at the region around 0 V can be explained by a Schottky barrier. The energy diagram of GaAs:Cr sensor is shown in figure 2.6. There are two Schottky barriers on both sides of the pad shown in the energy diagram (b). On the interface between anode and GaAs a space charge appears. This region works as a hole source [25]. The current of holes is described by the formula [26]:

$$I_p = SA^*T^2 e^{[-\frac{q(\varphi_{B_p}+\varphi_{B_i})}{kT}]}[e^{(\frac{qV_1}{kT})-1]},$$

where S is the anode area, A^* Richardson constant, φ_{B_i} the bend of Schottky barrier, V_1 the decrease of voltage and φ_{B_p} the barrier height for holes.

The current component from electrons is obtained by the formula:

$$I = U/R_{eff} + I_n,$$

where U is the applied voltage, R_{eff} the effective resistance, and I_n the saturation current. The saturation current is the limiting current from metal to semiconductor through the Schottky barrier [25],[26],[27],

$$I_n = SA^*T^2 e^{(-\frac{q\varphi_{B_n}}{kT})},$$

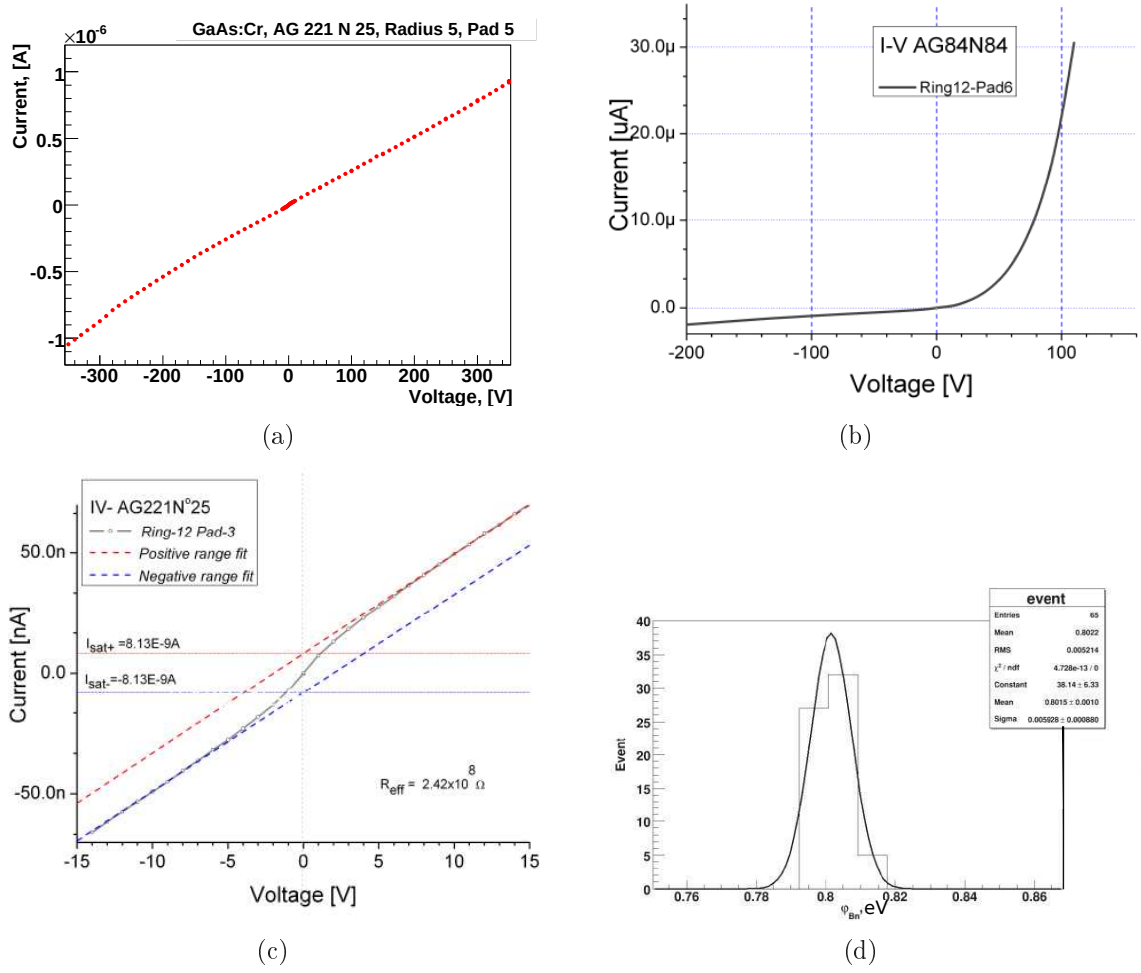

Figure 2.5: (a) The leakage current of a pad of the GaAs:Cr sensor as a function of the applied voltage in the range from -350 V up to +350 V. (b) An example of unusual leakage current measurement as a function of the bias voltage. (c) Zoom in the voltage region around zero, -10 V up to +10 V. (d) The Schottky barrier height measurement.

where φ_{B_n} is the barrier height for electrons. The leakage current for GaAs:Cr is non-linear up to 1 V due to larger hole current than electron current. In this way, from the leakage current measurements the sensor resistivity as was shown before and the Schottky barrier height can be obtained. The obtained Schottky barrier height is shown in figure 2.5(d). The barrier height of 0.8 eV is in the agreement with the information from the manufacturer [27].

The sensors used in the test beam were measured in the lab before bonding. Figure 2.7 contains leakage current measurements for each pad of a type 2 sensor at 100 V. It is plotted as a function of pad number from left to right as sketched in figure 2.1(b). The pads at the border have slightly lower leakage currents because of reduced pad area near to the guard ring. The plots for the remaining 11 sensors are shown in the appendix C. All together for 22 sensors of type 2 segmentation were measured. Figure 2.8(a) shows the current density calculated for the same sensor. The distribution was fit by Gaussian and the mean value is 7.15±0.19 nA/mm^2.

In addition, the leakage current was measured for several pads as a function of the

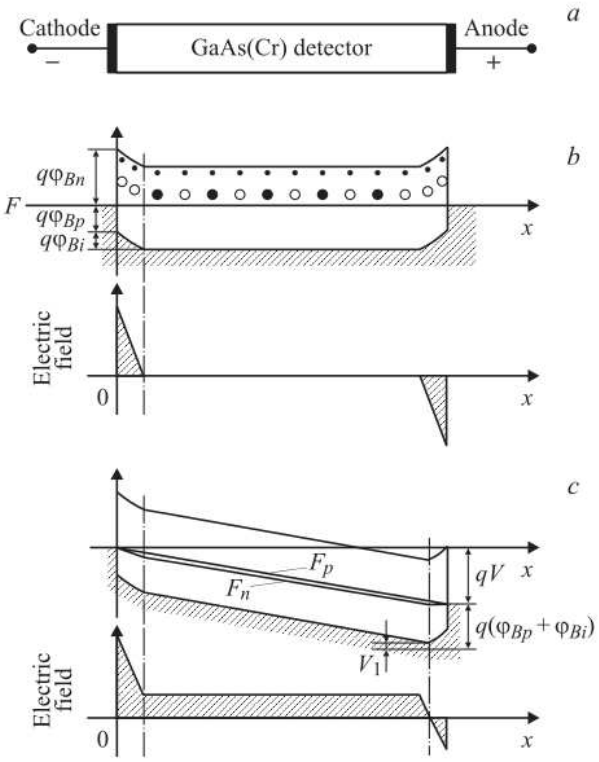

Figure 2.6: (a) The model of a GaAs pad, (b) energy diagram and electric field distribution in the sensor without applied voltage, (c) energy diagram and electric field distribution in the sensor with applied voltage. b - shows small donor levels and deep Cr impurities [25]. $F_{n,p}$ are the quasi Fermi levels for electrons and holes, respectively. $V_1 = V - I_p R$, where V is applied voltage and R is a pad resistivity.

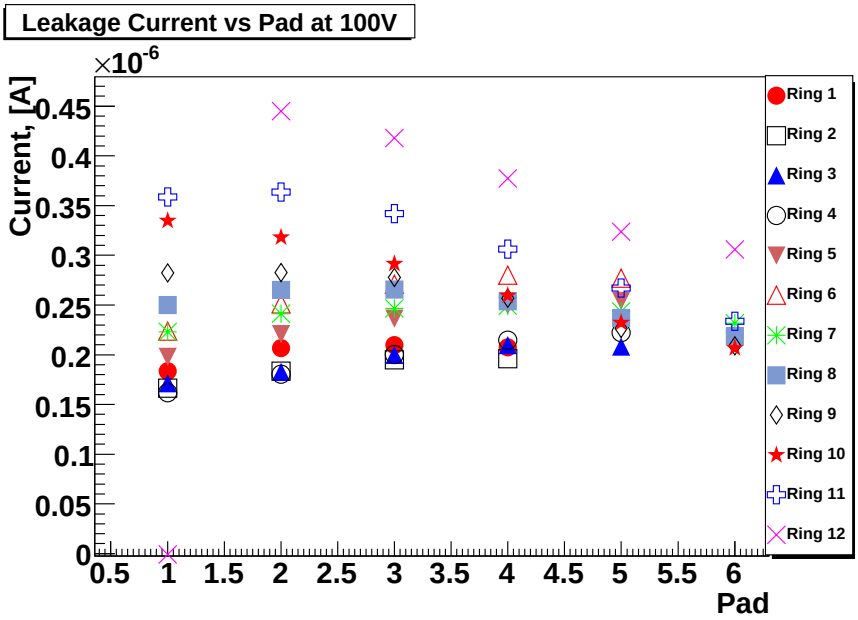

Figure 2.7: The leakage current of all GaAs:Cr sensor pads of a type 2 sample at 100 V bias voltage as a function of the pad number from left to right. See the layout in figure 2.1(b).

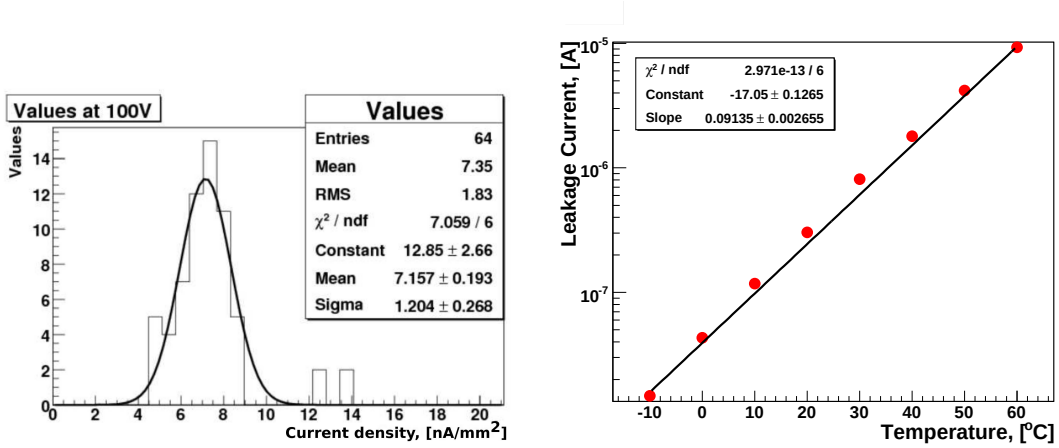

(a) (b)

Figure 2.8: (a) The current density of a GaAs:Cr sensor pads at 100 V bias voltage. (b) The leakage current of a GaAs:Cr sensor pad at 100 V bias voltage as a function of the temperature.

temperature. Figure 2.8(b) shows the leakage current at 100 V from −10° C up to +60° C. The leakage current increases exponentially with the temperature increase by a factor of 2.5 for each 10°C. For the semiconductors the leakage current is explained by the number of charge carriers [26]

$$n = n_i e^{[\frac{E_F - E_i}{kT}]},$$

where n_i the intrinsic carriers concentration, E_i the intrinsic Fermi level and E_F the Fermi level. The leakage current then depends on the temperature:

$$I_L \propto e^{-\frac{E_g}{2kT}}, \tag{2.1}$$

where E_g the band gap. The temperature can be used for reducing the leackage current.

Application of Radiation Hard Sensors at LHC

Chapter 3

Experiments at the LHC

Introduction

The Large Hadron Collider, LHC, is an accelerator and storage ring for protons and ions. It uses superconducting dipole magnets to force particles on a circular orbit. It is installed in the former LEP [28] tunnel of 27 km circumference and was designed to provide proton-proton collisions with beam energies of up to 7 TeV. Two separate beams are accelerated in opposite directions in separate beam pipes. There are four major experiments placed along the ring. Their locations are shown in figure 3.1. Two of them are large multipurpose experiments, ATLAS (A Toroidal LHC Apparatus) [29, 30] and CMS (Compact Muon Solenoid) [31, 32, 33]. Both detectors have a cylindrical structure with end-caps at both sides. ATLAS is instrumented with a small solenoidal and superconducting toroids for precise momentum measurements of muons. CMS has a solenoidal magnetic field with all calorimeters installed inside the coil. CMS was constructed in a hall on surface and fully assembled parts were lowered into the cavern and assembled together. This makes the CMS detector easily maintainable and easy to handle in future upgrades. The two other experiments are smaller and dedicated to specific physic topics, LHCb [34] for b-physics and the study of CP–violation, and ALICE (A Large Ion Collider Experiment) [35] for heavy ion physics, for example, the study of the quark-gluon plasma.

Goals of the LHC and the experiments are [32]:

- to explore physics at the TeV scale.
- to study the mechanism of electroweak symmetry breaking (e.g. the Higgs particle search).
- to look for phenomena beyond the Standard Model, SM, (e.g. the search for super-symmetric partners of the SM particles).
- to investigate new form of baryonic matter.
- to understand the asymmetry between matter and antimatter in the universe.

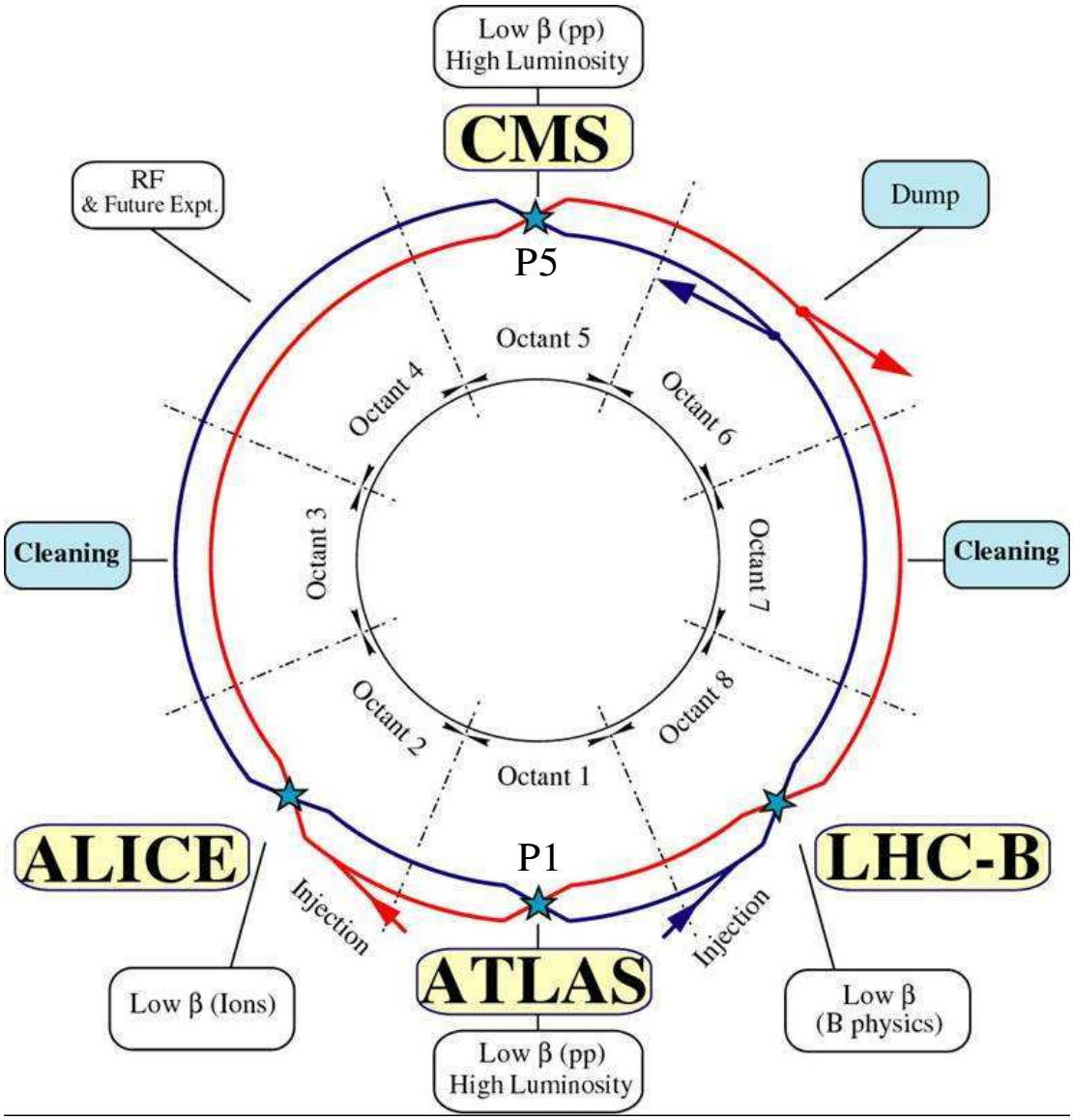

Figure 3.1: Schematic layout of the LHC ring with its 8 octants, two-beam pipe design and its four insertion regions for experiments [36].

For two colliding beams, the number of scattering events per second is given by the relation:

$$N = \sigma L.$$

The cross-section, σ, is coming from the process nature, but the factor, called *luminosity*, determines the performance of the accelerator. The luminosity is defined as:

$$L = \frac{f_{rev} N_1 N_2 n_b}{4\pi\sigma_x\sigma_y} F,$$

where f_{rev} is the LHC revolution frequency,$N_{1,2}$ number of particles per bunch, n_b is number of bunches in one orbit, $\sigma_{x,y}$ are the RMS beam widths and F is the reduction factor due to the crossing angle. The design luminosity is $L = 10^{34} cm^{-2} s^{-1}$. To study rare events a large L value is necessary. The luminosity can be increased by the number of particles in the beams and by reducing vertical and horizontal beam sizes.

3.1 The CMS Experiment

The CMS experiment is designed to measure the energy and momentum of all particles, created in a proton-proton collision. It is placed in the interaction region 5, P5, in the fifth octant as shown in figure 3.1. The CMS layout is shown in figure 3.2. CMS is 21.6 m in length and 14.6 m in diameter and the total weight is 14 500 tonnes. According to Ref. [31], CMS was designed for getting the best possible scientific results, and therefore to look for the most efficient ways of finding evidence for new physics phenomena.

CMS is an example of a multipurpose detector system used for collider experiments. It has an onion structure, where each sub-detector layer is surrounded by another layer. It comprises the following sub-detectors from the innermost layer to the outside: a vertex detector, a tracker, an electromagnetic calorimeter, a hadron calorimeter and a muon system. A solenoidal magnetic field of 4 T ensures excellent particle momentum measurement.

CMS was designed to match the following general requirements:

- precise vertex and secondary vertex reconstruction
- a high resolution electromagnetic calorimeter for detection and measurement of electrons and photons
- a hermetic hadronic calorimeter
- highly precise measurement of jets
- a high performance system for muon detection and measurements,

Additionally, for the diffractive and heavy-ion physics programs, forward detectors are installed:

- the CASTOR electromagnetic and hadronic calorimeter around the beam pipe,
- Zero Degree Calorimeter (ZDC) for neutrons and very forward photons measurement.

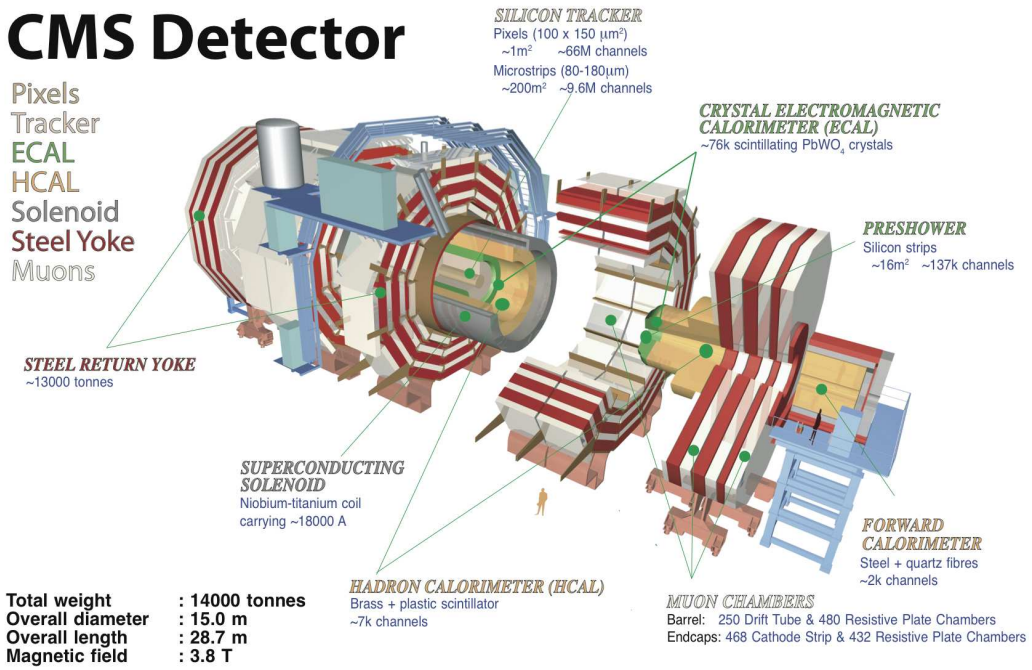

Figure 3.2: Schematic of CMS [31].

Detectors for beam conditions and radiation monitoring (BRM) are installed at several locations inside and around CMS. Near to the beam pipe inside the tracker volume the Fast Beam Condition Monitor (BCM1F) is installed. It will be described here in more details below.

Each beam may contain 2808 bunches with 25 ns separation. Up to now LHC was operated with 1380 bunches per beam and 50 ns separation. One turn of the beam is called *orbit*. Some of the bunches can be left empty. 25 ns bunch spacing may be a challenge for the electronics design.

LHC provides up to 20 inelastic collisions superimposed within one bunch crossing. The number of inelastic events requires a high-performance trigger system to select and store events interesting for physics analysis. The high flux of particles penetrating CMS required high radiation tolerance of the inner detectors and their electronics.

3.1.1 Tracking System

The tracking system of CMS is composed of silicon pixel and strip detectors, which cover several concentric cylinders around the beam pipe and disks in the forward - backward directions [37]. The whole tracker is 5.8 m long and 2.6 m in diameter. Starting from the beam pipe, the first 3 layers are silicon pixel detectors followed by 10 layers of silicon micro-strip detectors at larger radii. The position close to the interaction point, IP, leads to a large amount of particles crossing the pixel detector, requiring fine granularity for good

tracking and secondary vertex reconstruction. The pixel size is 100 by 150 μm and microstrip size is 80 - 180 μm. Pixel detectors were optimized for the position resolution, rate capability and radiation tolerance with minimal amount of material. The tracker detector measures charged particles within the pseudorapidity range $|\eta| < 2.5$. The pseudorapidity is a variable used as spatial coordinate describing the angle of a particle relative to the beam axis. It is defined as

$$\eta = -\ln\left[\tan\left(\frac{\theta}{2}\right)\right],$$

where θ is the angle between the particle momentum $\mathbf{p}$ and the beam axis. The tracker provides an impact parameter resolution or approximately 15 μm and a resolution on transverse momentum (p_T) of about 1.5% for 100 GeV particles. The tracker was designed for operation with a maximum luminosity of $1 \cdot 10^{34}$ cm^{-2}s^{-1} and will be upgraded for the high luminosity operation of LHC after 2020 to a higher number of pixel detectors for better track resolution.

3.1.2 Electromagnetic Calorimeter

The electromagnetic calorimeter (ECAL) consists of 61200 lead tungstate ($PbWO_4$) crystals in the central barrel and 7324 crystals in each of the two end-caps. It covers a pseudorapidity range $|\eta| < 3.0$. To detect and readout the scintillation light from the crystals, silicon avalanche photo detectors (APD) are used for the barrel part and vacuum phototriodes for the end-caps. The photo detectors are required to operate in the magnetic field. The lead tungstate scintillating crystals have a short radiation length, X_0=0.89 cm, and a Moliere radius of 2.2 cm. They are fast (80% of the light is emitted within 25 ns) and radiation hard (up to 10 Mrad) [31]. However, they provide a relatively low light yield of 30 γ/MeV. Both, the crystals and the APD are sensitive to temperature changes and need good temperature stabilization.

In front of the end-caps, a preshower detector is installed for improving electron-photon separation and π° identification. Moreover, it improves the position measurement of particles before they enter the ECAL end-caps. The preshower detector can be considered as a sampling electromagnetic calorimeter consisting of two layers. Each layer contains lead as absorber and silicon strip detectors as sensitive layer placed behind the lead.

3.1.3 Hadronic Calorimeter

The hadronic calorimeter (HCAL) [38] is a sampling calorimeter containing 3.75 mm thick layers of plastic scintillators and of 5 cm thick brass absorbers in the barrel and 8 cm thick absorbers in the end-caps [38]. Brass is a non-magnetic material with a short interaction length. The scintillator tiles are read out with silicon hybrid photodiods, HPD, via wavelength shifting fibers. HCAL is subdivided into barrel (HB), outer (HO) and end-cap(HE) HCAL parts. In addition, a forward HCAL (HF) is installed in the forward region, as shown in figure 3.2. It is using quartz fibers as active media and steel absorber. All HCAL parts except HO are located in the solenoid. HCAL has been designed to minimize dead regions to maintain the missing energy measurement performance.

In future upgrade, the HCAL avalanche photodiods, APD's, will be replaced by a new photodetectors called Silicon Photo Multiplier (SiPM) [39, 40, 41]. A SiPM is a

pixel array of Avalanche Photodiodes operating in Geiger mode. Each pixel that has fired due to a converted photon creates a single pulse of charge with uniform amplitude. In the end all signals from all pixels are added together inside the chip to give a single output being proportional to the number of photons. In comparison to APD and hybrid photodiods, SiPMs have a high quantum efficiency, high gain and good signal-to-noise ratio. Furthermore, they are not affected by the magnetic field.

3.1.4 Forward Calorimeters

CASTOR is a very forward Cherenkov sandwich calorimeter located 14.3 m from the CMS interaction point [42, 43]. The main physics goals for operating CASTOR are soft QCD and exotic physics studies. CASTOR consists of tungsten absorber layers and fused silica (quartz) plates as active medium. The plates are inclined at 45° with respect to the crossing particles to increase the collection of Cherenkov light. The readout is realized with light-guides transporting the light to radiation hard photomultiplier tubes. CASTOR has a cylindrical design with a length of 1.5 m and a diameter of 60 cm and covers a pseudorapitidy range from $5.1 < \eta < 6.6$.

ZDC is the Zero Degree Calorimeter which is compact, fast, highly radiation resistant with good energy and position resolution [44]. It uses tungsten as absorber planes and quartz fibers as active medium. It consists of an electromagnetic calorimeter part with tungsten planes located perpendicularly to the beam particles followed by a hadronic calorimeter part with tungsten planes tilted at 45°.

ZDC is intended to measure neutrons and photons at very low angles. The ZDC is located at the end of the straight section of the beam at P5.

3.1.5 Magnet and Muon System

The CMS magnet is a superconducting solenoid of 13 m length and 5.9 m diameter. It generates an almost homogeneous magnetic field of 4 T in the barrel region of the CMS detector. The tracking system and the calorimeters are included in the coil. The iron yoke outside of the magnet returns the magnetic field, yielding a field strength of about 2 T inside the iron.

The slots in the iron yoke are instrumented with the following detectors:

- Drift tubes (DT) in the barrel cover the pseudorapidity range $|\eta| < 1.2$.
- Cathodic strip chambers (CSC) in the end-cap covering the range of the pseudorapidity $0.9 < |\eta| < 2.4$. They are chosen due to robust operation in a magnetic field, high rate capability and good spatial and time resolution.
- Resistive plate chambers (RPC) in the barrel and in the end-caps cover up to $|\eta|$=1.6. The RPC are used for the first level trigger due to their fast response.

Muon detectors are used to identify and measure the momentum of muons. They are also essential for bunch crossing tagging and triggering. The full system is described in Ref. [31].

Chapter 4

The Beam Conditions and Radiation Monitoring System of CMS

At the LHC each proton beam stores an energy of more than 330MJ at nominal parameters at 7 TeV [45]. This energy in case of a beam loss can cause serious harm to LHC equipment and the CMS detector. The damage on material due to 450 GeV proton beam was tested in [46]. The observed radius of damage reached few mm in copper.

To be able to extract the beam without danger to the equipment into the graphite absorber (beam dump), abort kicker magnets are installed in the LHC ring at P6. Their rumping time is 3 μs, requiring so called abort gap in the bunch filling scheme.

The Beam Conditions and Radiation Monitoring System, BRM, [47, 48, 49] aims to measure beam conditions in the CMS experiment and initiate protection procedures in case of dangerous scenarios for the operation of the CMS and LHC. It delivers data with time resolution from ns to several months. BRM subsystems are working independently from central CMS power and data acquisition. The following BRM subsystems are located around the CMS cavern and near the beam pipe.

BPTX - The Beam Pick-up Timing System for Experiments. It consists of two LHC beam position monitors (BPM) each comprising four electrostatic button electrodes around the beam-pipe [50]. The time resolution is about 50 ps and the amplitudes are proportional to the bunch charge. The combination of amplitude and timing information provides a bunch pattern measurements. The BPTX system is the primary reference for triggering on bunches passing through CMS. It is also used for triggering several subsystems including the BRM detectors and contributes to the global CMS trigger system.

RADMON - RADiation MONitor is an extension of the LHC-wide radiation monitoring system for measurements of the ambient radiation dose. RADMONs measure doses and dose rates by using Radiation-sensitive Field-Effect Transistors, RadFETs, and Static random-access memory, SRAM. A RadFET measures the hadron flux and a SRAM measures the rate of single events upset (SEU) in the memory.

BCM1L - Beam Condition Monitor 1 are current monitors installed in the tracker volume at a radius of about 5 cm around the beam pipe. Each of eight monitors contains a polycrystalline CVD diamond sensor of 1 cm^2 area. It is placed at about 5 cm

radius around the beam pipe to measure the particle flux. The current through the sensors is proportional to the flux of particles. In case the measured current is above the abort threshold, it will initiate the abort signal, which will be sent to the control room to trigger a beam dump.

BCM2L - Beam Condition Monitor 2 has 4 diamonds mounted at about 5 cm radius, and 8 diamonds at 28 cm radius at the rear side of HF. All diamonds are polycrystalline CVD diamond and the current through the sensors is monitored as in BCM1L. The BCM2L is providing also the beam abort signal [51].

BSC - Beam Scintillator Counters are scintillator tiles located on the front and rear of HF. This system was installed to provide a crosscheck of the beam timing and a trigger for p-p scattering events at low luminosity. The scintillators are not radiation hard and the system will be replaced with BHC.

BHC - Beam Halo Counter - scintillator counter under development for the BSC replacement after the LHC shut down 2013-2014.

BCM1F - Fast Beam Conditions Monitor 1 uses single crystal CVD diamond sensors with a fast amplifier for bunch by bunch monitoring of beam halo particles and collision products.

A table with the location of the BCM subsystems is shown below.

Subsystem	Position Z	Function	Sampling time	Material
BPTX	175 m from IP		50 ps	electrostatic electrodes
RADMON	Throughout the CMS cavern	Monitoring	1 s	RadFET and SRAM
BCM1L	Pixel Volume, ±1.8 m	Protection	5 μs	pCVD diamond
BCM2L	At the rear of HF, ±14.4 m	Protection	40 μs	pCVD diamond
BSC (old)	In front of HF, ±10.9 m, 14.4 m	Monitoring	bunch by bunch	Scintillators
BHC (new)	In front of HF	Monitoring	bunch by bunch	Scintillators
BCM1F	Pixel Volume, ±1.8 m	Monitoring	bunch by bunch	sCVD diamond

For one of the subsystems, the Fast Beam Condition Monitor - BCM1F, the operation was monitored during 2011-2012. The performance of the full system is reviewed in the following chapter. Studies for the use of BCM1F as a luminosity monitor will be shown in the chapter 5.

4.1 The Fast Beam Conditions Monitor at CMS

Beam Conditions Monitors are used to prevent damage in the inner detector system in case of dangerous beam conditions. Previous experiments at KEK, SLAC and Fermilab

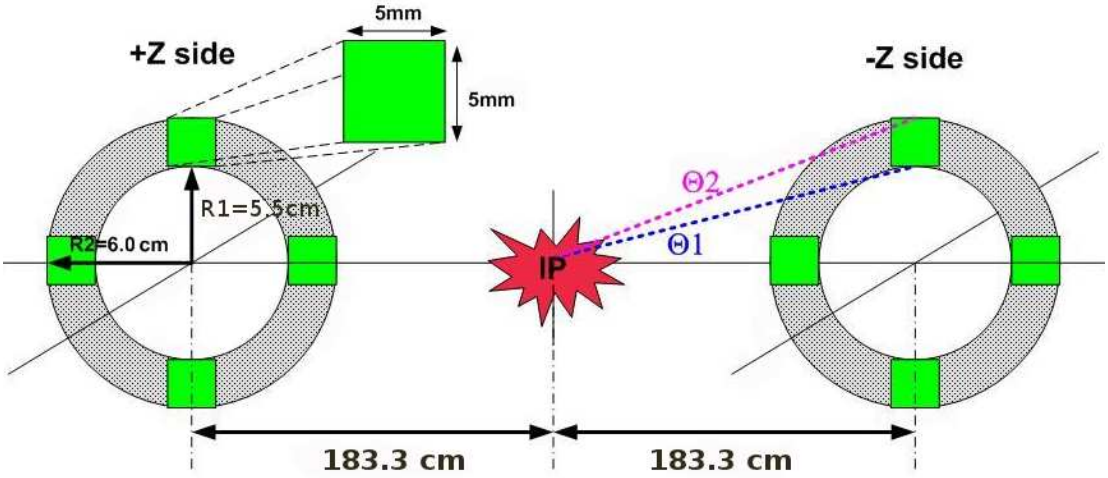

Figure 4.1: Location of the BCM1F diamonds inside the CMS tracker volume

used current monitors similar to BCM1L and BCM2L [52], [53]. Single crystal diamond counters were investigated for the first time in the ZEUS experiment at HERA [54].

BCM1F at CMS was developed for measuring both beam losses and collision products [55]. For the first time single crystal diamond sensors are used.

The size of the diamonds is small, what allows to install them near to the beam pipes at 5.5 cm radius, as shown in figure 4.1. Two subsystems of four modules were installed on both sides of the IP at the distance of 1.8 m from the IP. Each module contains a scCVD diamond sensor, radiation hard front-end electronics and an analog optical readout of the signals. All modules are positioned in a plane perpendicular to the beam-pipe as shown in figure 4.1. Each module is shielded by an aluminum box. The boxes are mounted on carbon fiber carrier structures shown in figure 4.2. The module locations are marked as up, down, far and near with respect to the LHC plane. These abbreviations are used for labeling of the modules.

Incoming and outgoing particles are considered as relativistic and circulate around the LHC with speed of light. The time of flight of relativistic particles between the IP and each sensor plane is of about 6 ns and between the two planes 12 ns. The position of the BCM1F is chosen to be optimal in terms of time separation between incoming and outgoing particles of the beam halo [56].

4.1.1 scCVD Diamond Sensors

BCM1F comprises 8 single-crystal CVD diamond sensors (scCVD). The dimensions of the sensors are 5x5x0.5 mm^3. The square metallization size is 4.7x4.7 mm both sides. In addition, they also fulfill the time resolution requirements for resolving bunches.

In the table 4.1 a mapping is given between the positions of the modules, the labeling of the transmission lines and the ADC channels.

The system has to be robust and simple because there is no cooling and access to the BCM1F during operation.

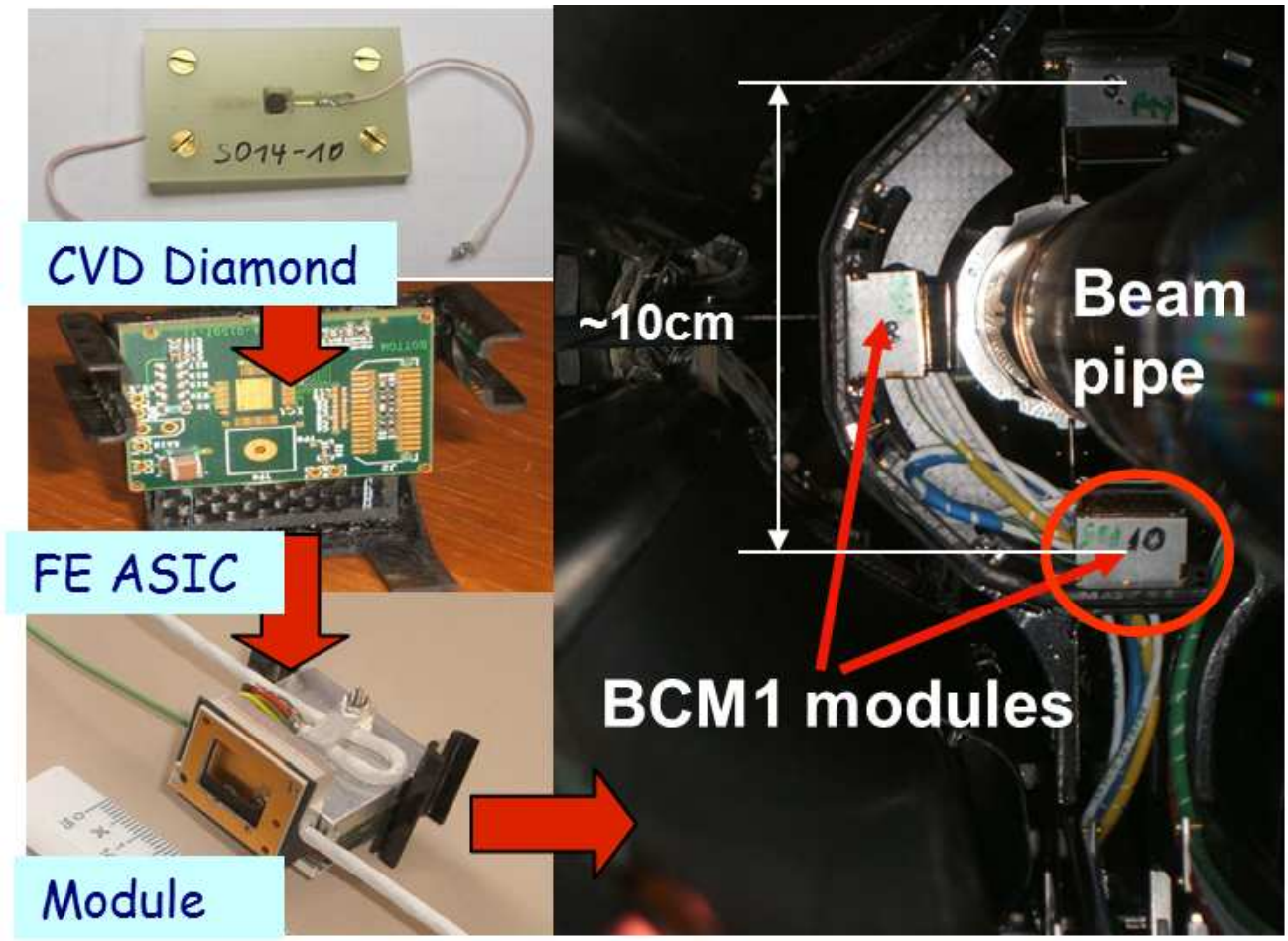

Figure 4.2: Left: The components of a BCM1F module. A single crystal diamond sensor (top), a front-end ASIC (middle) and a complete module (bottom). Right: Photo of the installation of BCM1F modules around the beam-pipe inside the CMS detector.

ADC Channels	Position	Side/Num.
0	-Z top	1/1
1	-Z far	1/2
2	-Z bottom	1/3
3	-Z near	1/4
4	+Z top	2/1
5	+Z far	2/2
6	+Z bottom	2/3
7	+Z near	2/4

Table 4.1: The position of the BCM1F modules, the label of the transmission lines and ADC channels.

4.1.2 BCM1F Electronics

Each diamond is connected to a radiation hard charge sensitive preamplifier JK16 [57], produced using 0.25 μm CMOS technology. The front-end has of about 1 nF input virtual capacitance and a 60 mV/fC charge gain. For a 5 pF detector capacitance, the measured noise is about 700 e^- equivalent noise charge (ENC). The JK16 single ended output is AC coupled to the custom-designed Linear Laser Driver ASIC (LLD) [58]. The peaking time was measured to be 22 ns [56]. The gain and the laser driver bias current cannot be programmed. The input polarity and the laser driver bias setting were set to obtain the best dynamic range on each module.

The output signal is transmitted to the counting room over an analog optical chain [59] developed for the CMS tracker. Single fibers from the lasers are connected to an interconnecting patch panel and afterwards single fibers merges into a 12-fiber ribbon cable which is going to the counting room. There each ribbon connects directly to a 12-channel analog optical receiver, which is converting optical signals back to electrical. From the optical receiver, the signals are split by a fan-out module and the copies are sent to an ADC and to discriminators. An ADC of the type CAEN V1721 is used. It contains 8-channels, each containing a flash ADC with 500 MSamples/s sampling frequency. The memory per channel is 2 MB. The ADC can be triggered internally or externally. It can read out up to 45 consecutive beam orbits or a corresponding number of user definable time intervals. The information is read out via an on-board optical link and data is processed in a PC. Since the ADC has fast sampling, precise time measurements are possible, for example, to emulate a TDC, as it will be described in the following section.

The signals after the discriminators are split again and counted with a V560 scaler from CAEN and digitized with multi-hit capable TDC V767 from CAEN with 20 bit dynamic range and 0.8 ns least significant bit, LSB, resolution. The TDC and the scalers are read out via a VME-bridge.

Test pulses feeded in the preamplifier were used for a system functionality check and performance monitoring.

A schematic of the complete back-end is shown in figure 4.3. The scaler deliver on-line count rate for each channel which are displayed in the CMS and LHC counting rooms. The TDC arrival time is mapped in an orbit time interval. Data is collected over several

10 minutes to obtain count rates for colliding and non colliding bunches. A lookup table, LUT, is located between TDC and scalers and provides each of them with a copy of signals and veto signals to stop reading signals when the TDC buffer is readout. I future a new readout histogramming unit, RHU, will be used. It histograms hits in bins of 6.25 ns (4 per 25 ns bx) over the entire orbit for a configurable number of orbits, for each channel. It also collects postmortem information to analyze signals recorded before the beam dump signal appeared. It is being developed to be a part of the BCM1F DAQ system after the upgrade. The documentation is available in Ref. [60]. The NIM to ECL converter is providing a change of signal from standard NIM to ECL and opposite. The box with the so called beam-gas logic contains Multiple Gate & Delay Modules, MGD, and scalers. The MGD modules has been developed to measure beam halo and albedo rates. The gating selects detector signals in specific time slots relative to the bunch clock: collision products 6.25 ns after bunch crossing, beam gas for each beam 6.25 ns before/after non-colliding bunches and albedo rate just before start of a bunch train.

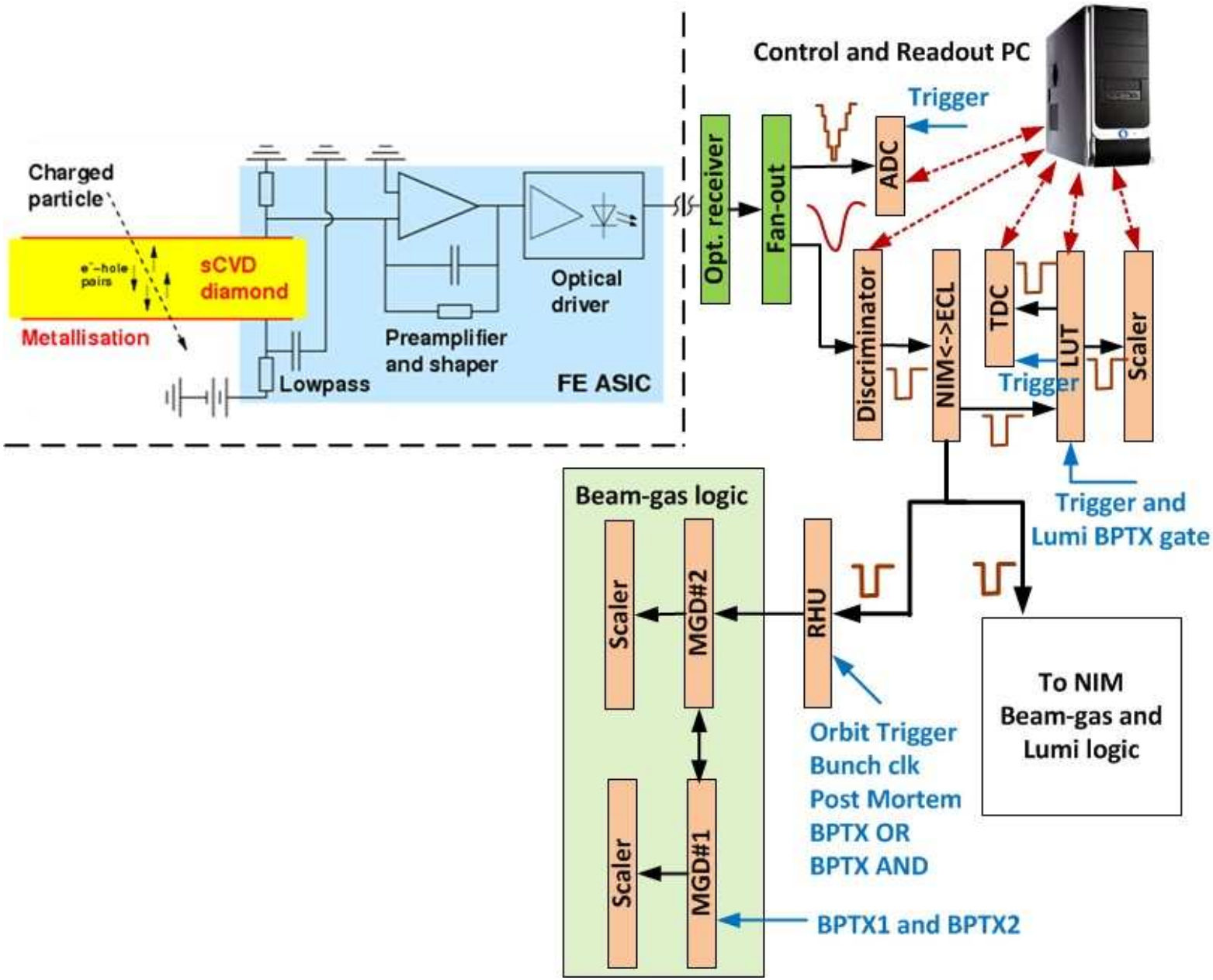

Figure 4.3: Structure of the BCM1F readout electronics and data acquisition.

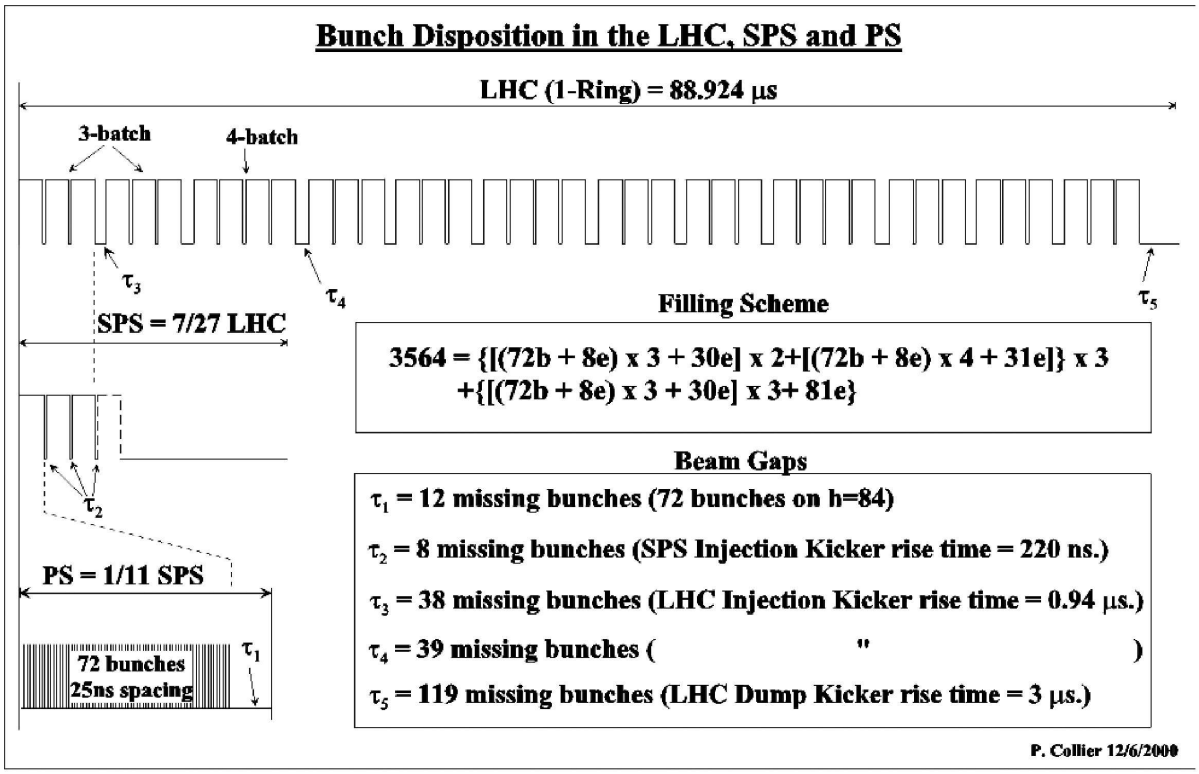

Figure 4.4: LHC proton filling sheme

4.2 Bunch Structure

The filling scheme of LHC, mapped on one orbit, is shown in figure 4.4. Each proton beam at full intensity will contain 2808 bunches. Each bunch contains 1.15x10^{11} protons at the start of a nominal fill. The LHC is filled with bunches using the pre-accelerators PS and SPS. The 72 bunches from Proton Synchrotron, PS, are combined into a batch and injected into the Super Proton Synchrotron, SPS. Then three or four batches from the SPS are injected into the LHC and form trains. Gaps between the trains and batches are specified with $\tau_{1,2,3,4,5}$ in figure 4.4. The filling scheme allows a maximum of 3564 bunches to circulate in one orbit. In 2010-2012, LHC was operated with 50 ns bunch spacing and 1380 bunches were colliding in CMS.

BCM1F is fast enough to distinguish between particles originating from consecutive bunches. In addition BCM1F allows to detect halo particles and collision products. Since the time difference between halo particles of incoming bunches and collision products is about 12 ns, for their separation a time resolution of a few ns is needed. The intrinsic time resolution of BCM1F will be discussed in the section 4.6.

The ADC with fast sampling can provide timing information. The orbit clock is used as a trigger to read out the ADC. Each recorded signal is analyzed by applying a fixed threshold and a number of the samples over threshold. The first sample over threshold defines time of signal arrival. The number of samples over threshold times sampling frequency define time over threshold. Figure 4.5(a) shows a distribution of the arrival time obtained from the ADC data mapped on a full orbit. This time structure allows to see the LHC bunch structure. Figure 4.5(b) shows a zoom into a batch of 36 bunches separated by

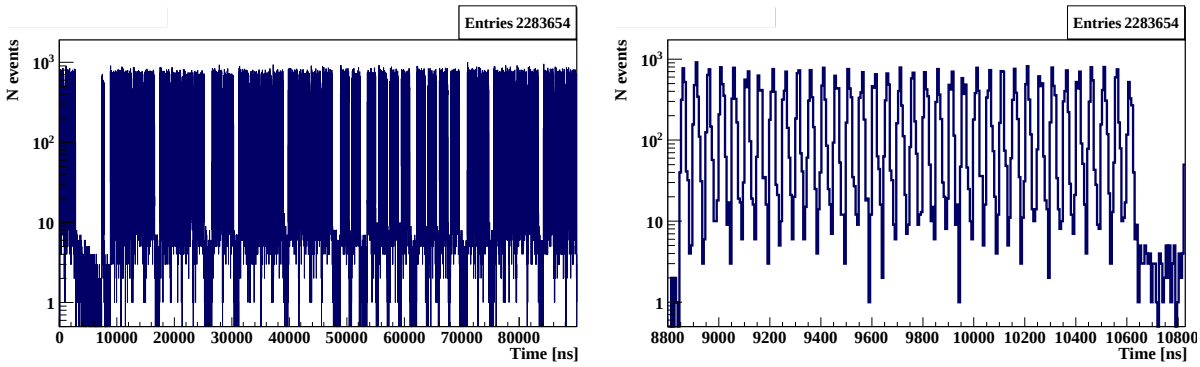

(a) (b)

Figure 4.5: Example of the bunch structure of LHC, observed with ADC at 17.08.2011, Fill 2030. Right - zoom into a batch comprising 36 bunches.

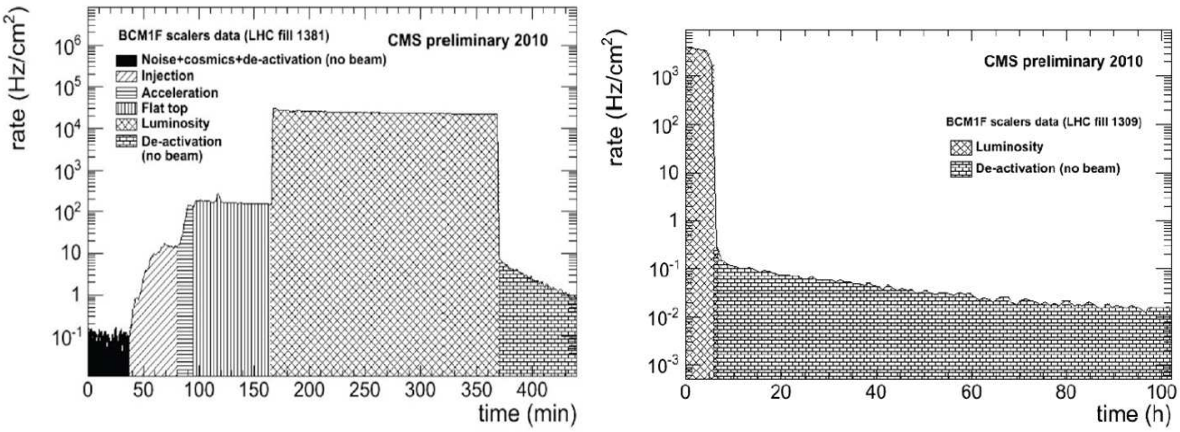

(a) (b)

Figure 4.6: (a) The BCM1F scaler rate as a function of time, showing LHC stages. (b) The BCM1F scaler rate as a function of time after the beams were dumped.

50 ns. Each peak is a combination of particle measured by BCM1F originating from halo particles from incoming and outgoing bunches and from collision products. In figure 4.5(a) the train structure of the LHC over 2011-2012 as a combination of two and four batches. The gap at the left side in figure 4.5(a), around 5000 ns, is the so called abort gap of 3 μs. The measurements were done at 13-th September 2011 with 1380 bunches in the LHC and 50 ns between bunches.

Every LHC fill follows an order of sequences [61]. The tasks within a sequence that are related to a specific activity are grouped into sub-sequences. The main sequences are called: injection, ramp, flat top, squeeze, stable beams, unstable beams and dump.

After injection the beams are accelerated, whereas the magnets are ramped up to keep the beams on the nominal orbit. The sequence flat top is the interim period when the acceleration is finished and all injected bunches are circulating in the rings, but not colliding jet. The next sequence are squeeze and stable beams. In this sequences the beams start to collide.

In figures 4.6(a) and 4.6(b) the BCM1F rates are shown for the successive LHC se-

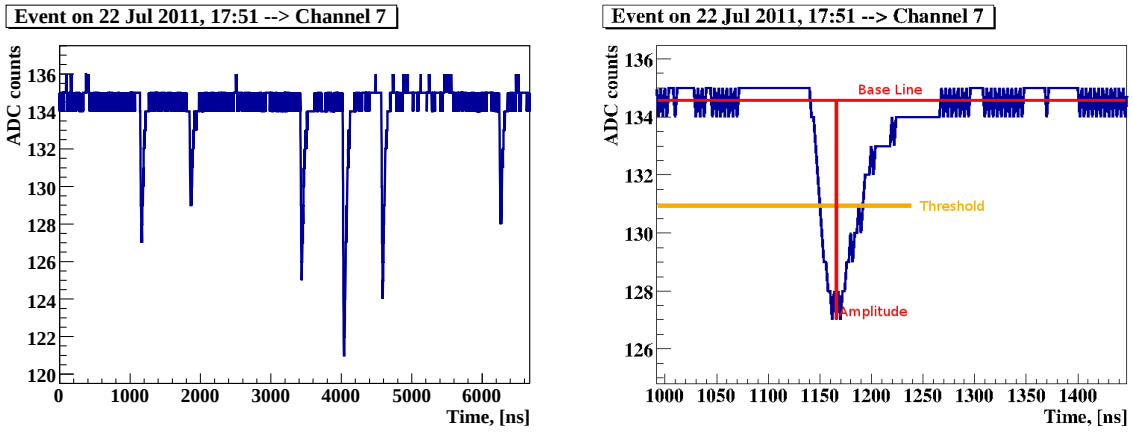

(a) (b)

Figure 4.7: (a) Part of one LHC orbit measured by the flash ADC of BCM1F. (b) Example signal observed with the ADC.

quences [62]. Data from the flat top sequence will be used later for intrinsic time resolution measurements of BCM1F. The stable beams sequence, in figure 4.6(a) called "luminosity", is used for taking data in the CMS experiment. The count rate of BCM1F jumps up by two orders of magnitude since the collision products appear. The count rate as a function of time decreases, as expected, during the stable beam phase, since the transverse sizes of the beam grow, leading to a decrease of the luminosity. Figure 4.6(b) shows the count rate after the beams were dumped. The slight drop with time attributed the de-activation of the material. It was fitted with two exponentials, obtaining effective decay constants of 34 minutes and 40 hours.

The count rate was forwarded to the LHC control room as so called background 1.

4.3 Signal Processing with the ADC

The ADC data offline analysis provides the understanding of the performance of the full system. Each signal is recorded with 2 ns sampling. An example of BCM1F data recorded in 2011 with the ADC is shown in figure 4.7(a). It contains signals from the particles that crossed the diamond sensor in the displayed time interval. Signals are appearing not each 50 ns due to the small area of the diamond sensor. In figure 4.7(b) one particular signal is shown with baseline, signal amplitude and threshold definitions.

For the signal processing several steps are defined. Firstly, the baseline has to be determined when there are no signals from particles crossing the detector. During LHC operation the baseline is determined in the time window of the abort gap. It is obtained as the mean value of a certain amount of samples. Then an algorithm for peak finding is applied [63]. When the ADC values in several samples are over the predefined threshold, the signal candidate is found. Then the number of ADC samples over the threshold is counted and the **signal length** is defined. Only signals above a predefined length are accepted, what rejects noise. The signal amplitude is defined as the difference between the signal maximum and the baseline value.

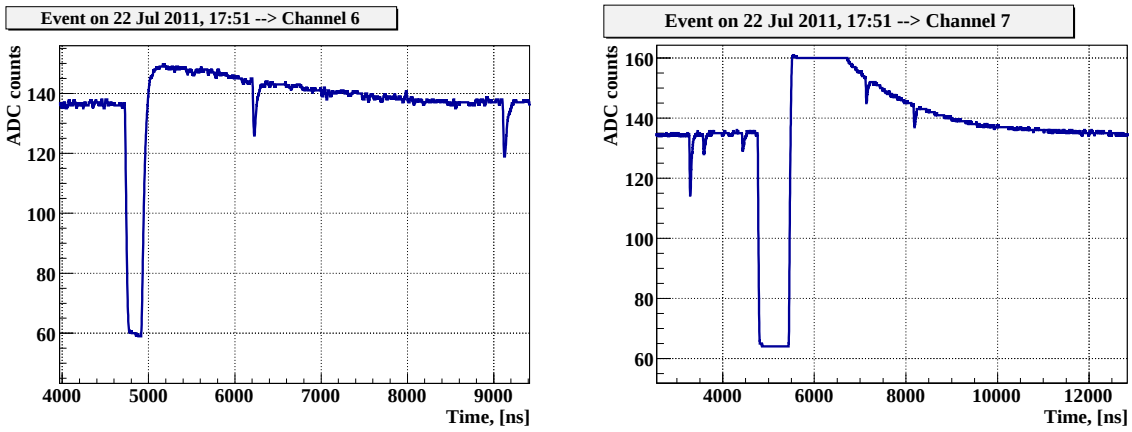

(a) (b)

Figure 4.8: Examples of saturated signal observed with the ADC, proton run, Fill 1966

In figures 4.8(a) and 4.8(b) are shown examples of saturated signals recorded from different channels. The saturation is caused by the limited dynamic range of the laser diode. The fraction of such signals is only a few percent.

The data recording is made via ROOT Trees. ROOT is an object-oriented program and library developed by CERN. The ROOT file contains the following information:
Event - a number of an orbit clock trigger or a self trigger or of any other pulse given as a trigger for the ADC.
Channel - is the channel number from 0 to 7, as described in table 4.1.
EventHeader - are variables storing headers of each trigger.
BaseMean and BaseSigma are the calculated mean and standard deviation values of the baseline.
N - the number of samples measured with the ADC.
Data - is an array containing the ADC values for N samples.

4.3.1 Signal Shape Function

For the signal description a signal shape function for a CR-RC shaper can is used. CR-RC pulse shaping is the most used technique, for the BCM1F preamplifier JK16 and later to the FE ASIC for the forward calorimeters, and is performed by sending the signal through a cascaded CR differentiator and CR integrator. In this way the signal is filtered at low and high frequencies, what results in an improvement in signal-to-noise ratio. The high-pass filter is often implemented by a CR component and the low-pass filter by a RC. The duration of the pulse is defined by the CR-RC shaper components and differentiator, τ_d, and integrator, τ_i, time constants. The signals recorded by the ADC can be parametrized as [64]

$$s(t) = V_0 \frac{\tau_d}{\tau_d - \tau_i}[e^{\frac{-t}{\tau_d}} - e^{\frac{-t}{\tau_i}}],$$

where V_0 - is proportional to the signal amplitude. For equal time constants $\tau_d = \tau_i = \tau$

$$s(t) = -V_0 \frac{t}{\tau} e^{\frac{-t}{\tau}}, \tag{4.1}$$

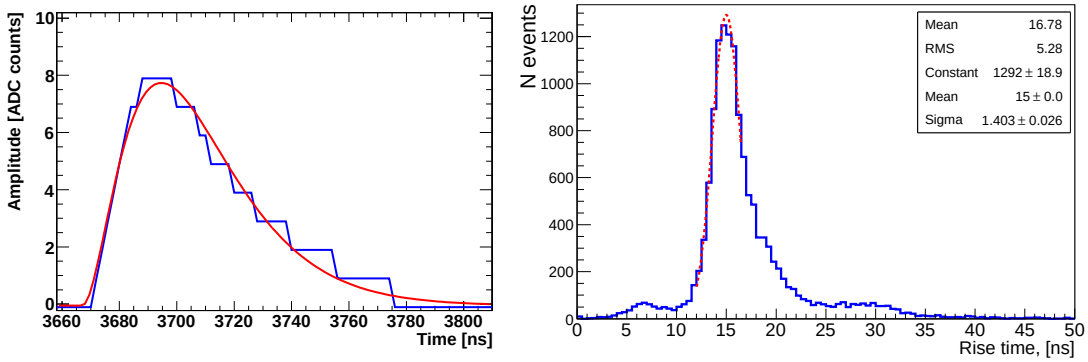

(a) (b)

Figure 4.9: (a) A MIP signal example in blue and fit by the function of equation 4.1, in red. (b) The rise time obtained from the fitted signals with the signal shape function.

where τ is the rise time of the signal. An example of a fit using equation 4.1 for a signal sampled by the ADC is shown in figure 4.9(a). More detailed calculations are shown in apendix B. This method was applied for the BCM1F signal fitting and later for the test beam data analysis. This method is not sensitive to baseline shifts. The resulting time rise of signals for the BCM1F are shown in figure 4.9(b). The mean rise time was obtained to be 15 ns. It is slightly less than it was given in the description of the BCM1F JK16 ASIC before.

4.3.2 Signal Baseline

The baseline is determined from the samples taken during the 3 μs abort gap, where no signals are expected. In this time window, the baseline is calculated as the mean value of 100 samples. Calculating the baseline for each event separately results in the blue dashed distribution of figure 4.10(a). Averaging the baseline over 100 events, the red full line distribution is obtained. The latter shows a narrower distribution. This affects the amplitude calculations too, what can be seen in figure 4.10(b). The pedestal, MIP and saturation peaks are sharpened and the MIP peak can be better determined for the baseline calculated for 100 events. This is explained by reducing influence from the rarely appearing signals in the abort gap e.g. due to activation of the material in the CMS. Hence, mean baseline is defined as the mean value of the baselines from the last 100 events.

4.3.3 Baseline Monitoring Tool 2011

A special DAQ program, called Baseline Monitoring Tool (BMT), was developed [63]. The average value over a full ADC buffer of about 4 Msamples is calculated. The result is saved in a text file. A histogram is created showing the baseline as a function of time over a period of several months as shown in figure 4.11. The baseline value is send every 5 minutes to the CMS control room. Baseline measurements in presence of collisions are shifted due to signals measured in the 4 μs window. A decrease of 5% is seen in this time

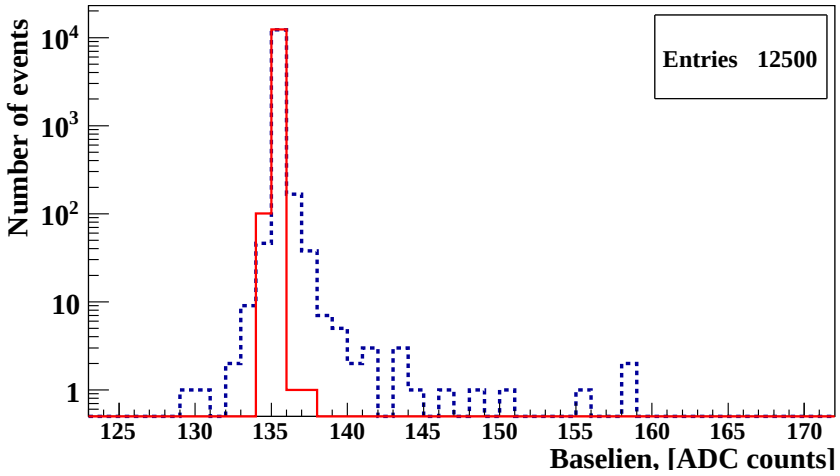

(a)

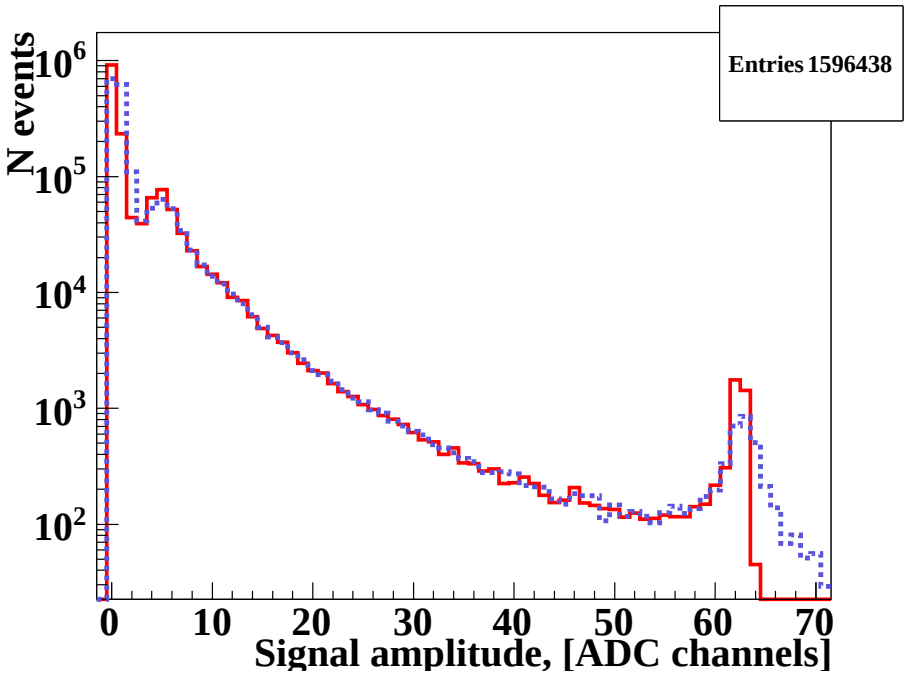

(b)

Figure 4.10: (a) Distribution of baseline values, *blue* - single event baseline, *red* - averaged baseline over 100 events. (b) The amplitude spectra for different baseline definitions: *blue* - single event baseline, *red* - averaged baseline over 100 events.

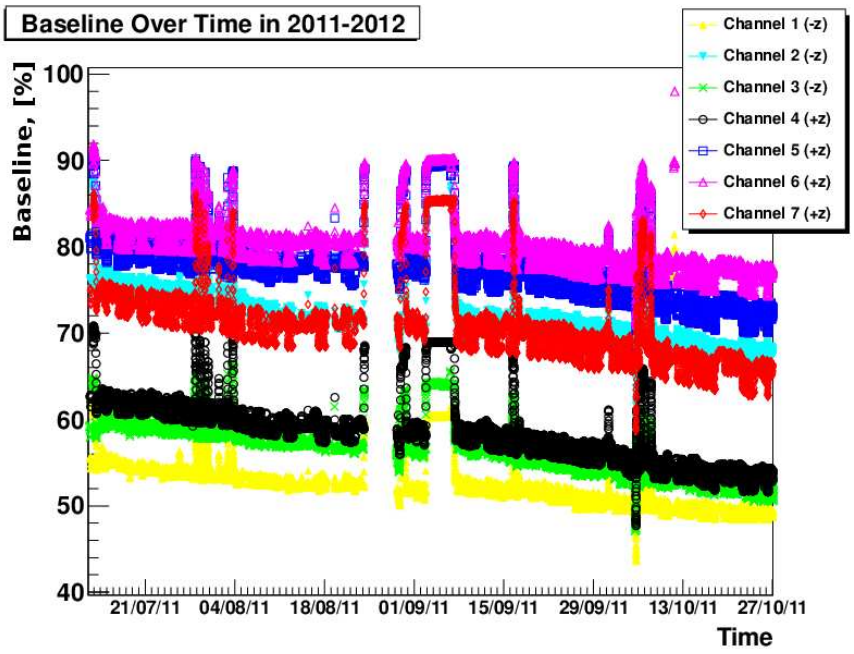

Figure 4.11: The baseline monitoring results examples over 2011.

window. Breaks between measurement were due to DAQ updates and power cuts in CMS. A decrease of the baseline by about 5 % is observed in a time period of three months.

There are studies done to investigate the dependence of the baseline on the temperature. An example of this dependence is shown in figure 4.12 [65]. The baseline of 8 channels and the temperature measured in the pixel detector are shown as a function of time for about 10 days. One can see that the baseline value is anti-correlated with the temperature.

4.4 Spectra of Signal Amplitudes

In figure 4.13 an amplitude spectrum is shown for channel 0, measured in May 2011. It shows a sharp pedestal, a peak corresponding to the expectation for a relativistic particle, hereafter called *MIP signal*, and a saturation peak due to the limited dynamic range of the laser diode. The minimum amplitude, measured by the peak finding algorithm is 0.1 ADC counts.

The length of signals is defined as the time the signal exceeds a certain threshold. It is used to discriminate noise from signals by applying an appropriate threshold. Another quantity to reduce the noise is the signal amplitude.

Figure 4.14(a) shows the signal amplitude as a function of the signal length for low amplitude and signal length thresholds. The red spot around 70 ns signal length corresponds to MIP particles. At larger signals the signal length increases. The amplitude is saturated for some signals longer than 150 ns. Figure 4.14(b) shows a zoom in figure 4.14(a), where three spots of enhanced signal density are visible with similar amplitude, but signal lengths of about 70, 125, 175 ns. The spots correspond to cases where two or three signals, arriving each 50 ns, overlap. Similar figures for other channels are shown in appendix A.

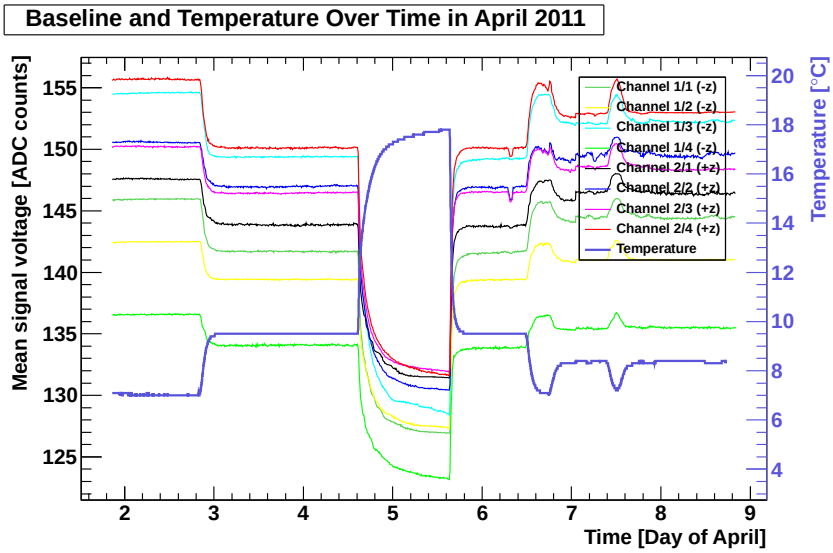

Figure 4.12: The baseline and the temperature measured simultaneously at the pixel detector as a function of time.

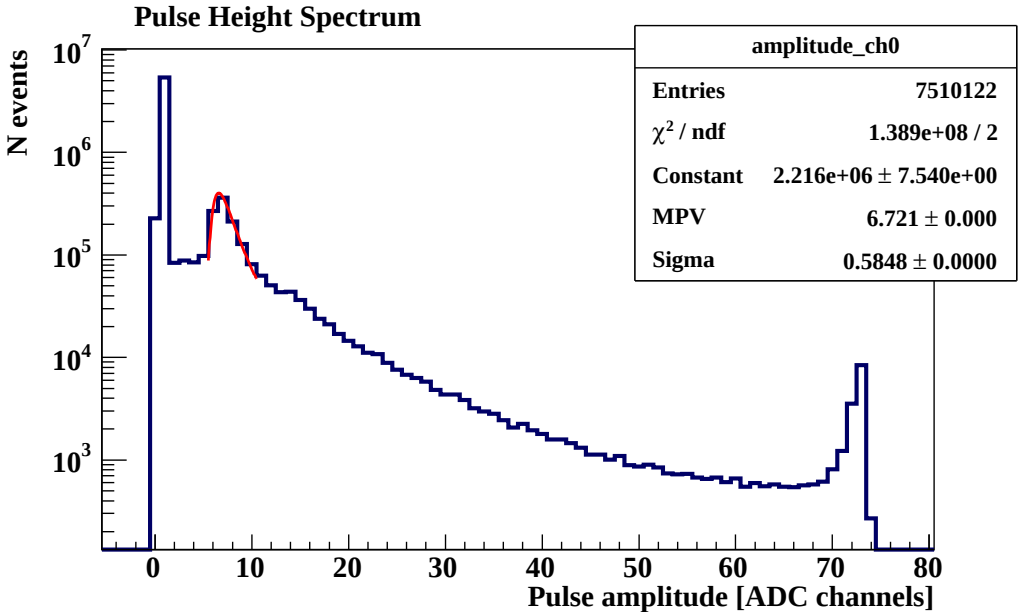

Figure 4.13: Example of signal amplitude spectrum observed with ADC, channel 0, May 2011

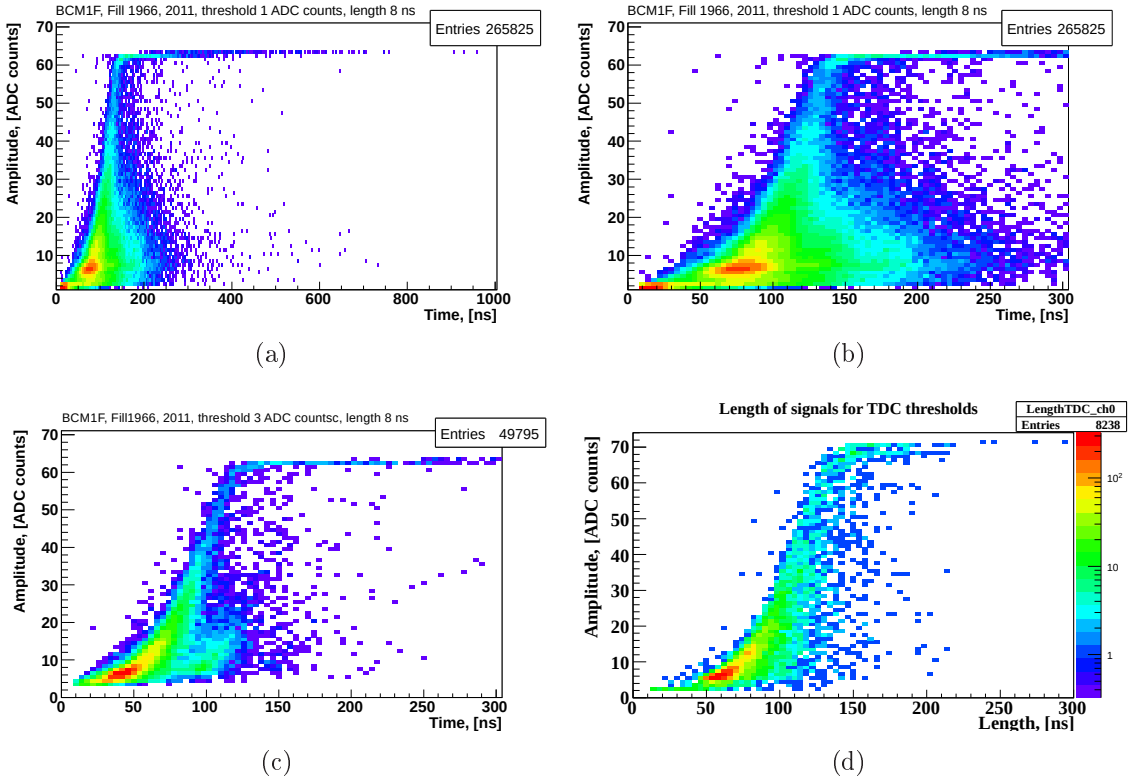

Figure 4.14: Example of signal amplitude vs length of the signals observed with ADC in channel 0 (a) at full range, (b) first zoom in signal length. (c) Example of the signal amplitude vs length for amplitude threshold of 3 ADC counts. (d) The signal amplitude as a function of the signal length for flat-top LHC sequence.

Figure 4.14(c) was obtained with an amplitude threshold of 3 ADC counts and 10 ns signal length threshold. The increase of the signal amplitude threshold reduces the signal length. The red spot on figure 4.14(c)shows that the MIP signal length is around 40 ns. Increasing the threshold of the signal amplitude also the amount of overlapping signals is reduced.

Using data from the flat-top sequence of the LHC, as shown in figure 4.14(d), overlapping signals are not visible since the count rate is low, and hence also the probability for overlapping signals.

4.4.1 Constant Fraction Discriminator Emulation

A constant fraction discriminator, CFD, is an device to process signals and is replacing mathematical operation of finding maximum and then finding a fraction of the maximum of the signal. CFD are used in order to reduce the time walk. Time walk appears for fixed threshold discriminators when the amplitude of signals varies. The principle of CFD is splitting the input signal in two parts. One part is attenuated by a factor N and subtracted from the delayed input pulse. The amount of delay can be adjusted. The resulting bipolar signal crosses the baseline at a constant time with respect to the start of the pulse.

To improve the time resolution of the BCM1F system a constant fraction discriminator was emulated using ADC data. The signal amplitude was determined first with the peak finding algorithm and the amplitude was used to define the arrival time when the signal reaches higher than 50% of the full amplitude. Figure 4.15(a) shows the signal amplitude as a function of signal length for the constant fraction discriminator emulation. With increase of the signal amplitude, the signal length is staying constant up to an amplitude of 60 ADC counts. Then signal length increases due to signal amplitude saturation. Figure 4.15(b) shows a histogram of the signal length with mean value 43.96 ns and sigma 3.63 ns. All plots shown are for channel 0 of the ADC. The other channels exhibit similar behavior.

4.5 Comparison of ADC and Discriminator Threshold Scans

Threshold scans are used to find a threshold for the discriminators to count efficiently signals and not, or only little, noise. The scalers are counting the number of signals per second, hereafter called rate, for all 8 channels. The discriminator thresholds were varied with 2 mV step and the rates were measured for each threshold.

A threshold scan using discriminators is shown in figure 4.16(a). It shows for the 8 BCM1F channels the rate as a function of the applied threshold in the discriminators. The rates are slightly growing with reducing thresholds and at low thresholds are growing fast due to noise. The threshold values just above the noise is used for the discriminators to count rates in BCM1F are presented in table 4.2.

An independent determination of the thresholds is done using the signal spectra obtained from the ADC as shown in figure 4.13. The spectra were integrated from the maximum to zero ADC counts. The distributions obtained are shown in figure 4.16(b) for all BCM1F channels. There are similarities in the behavior of all channels, especially in channel (-Z far and +Z bottom). The calibration factor used for comparison of ADC measurements and discriminator measurements is 4.6 mV per 1 ADC count [66].

The results for the optimum thresholds of the discriminators performs obtained with a threshold scan or using the ADC spectra are listed in the table 4.2. The values obtained are almost equal. Small difference are due to the rough ADC binning of 4.6 mV. There is an offset between the values set by the software and by the hardware of the discriminators. These offsets are also presented in table 4.2.

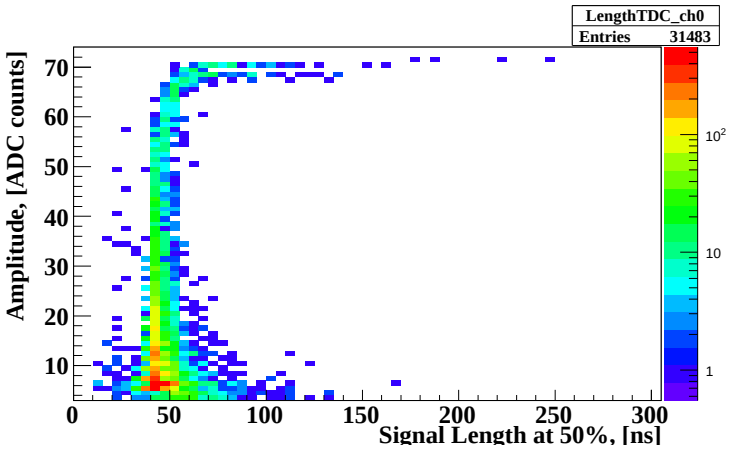

(a)

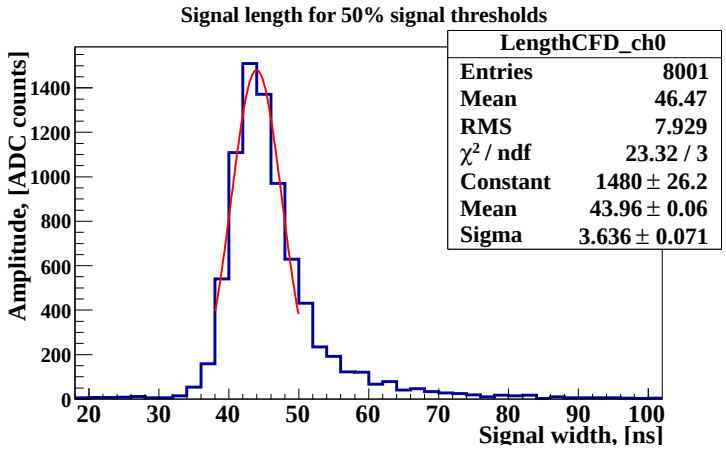

(b)

Figure 4.15: (a) Example of signal amplitudes as a function of the length at 50% of the amplitude using ADC, channel 0. (b) The signal length at 50% of the signal amplitude.

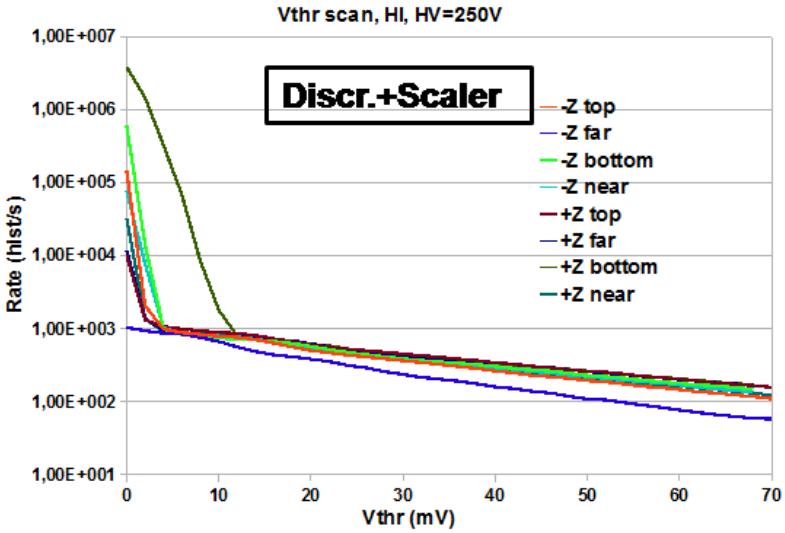

(a)

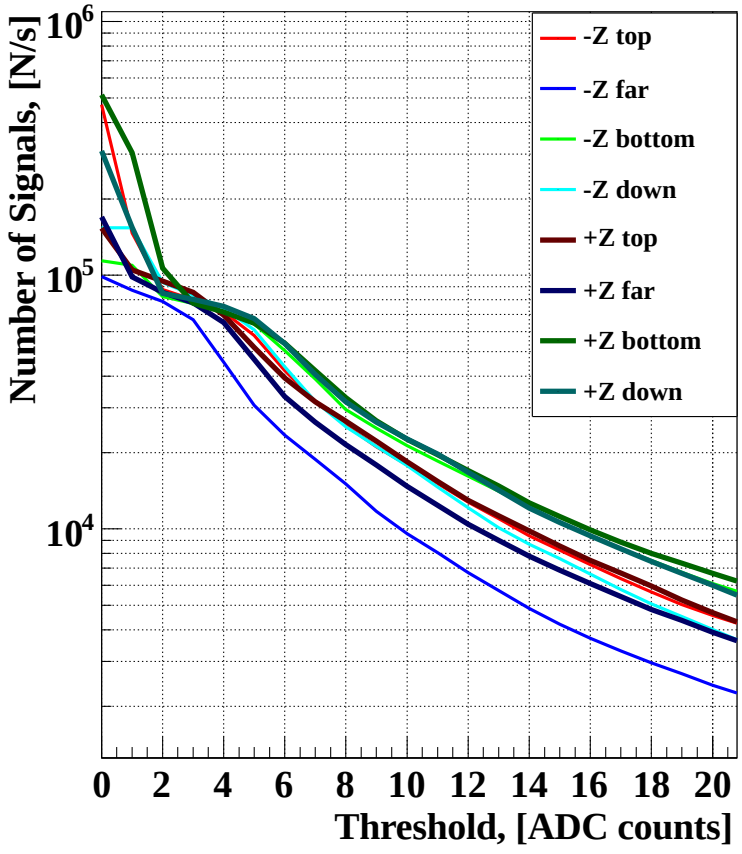

(b)

Figure 4.16: (a) Threshold scan results using discriminators and scaler [67]. (b) Threshold scan obtained from the ADC data analysis. Measurements were performed in November 2011.

Position	-Z top	-Z far	-Z bott.	-Z near	+Z top	+Z far	+Z bott.	+Z near
Discr. settings	-10	-8	-8	-8	-8	-8	-14	-8
Discr. offset	-7	-7	-7	-7	-6	-6	-7	-6
Discr. real	-17	-15	-15	-15	-14	-14	-21	-14
ADC thr.	14	14	14	14	14	14	19	14

Table 4.2: The threshold values obtained from the threshold scan for the discriminators and from the ADC signals amplitudes. Thresholds are given in mV.

4.6 Intrinsic Time Resolution

An essential feature of BCM1F is the possibility to assign halo particles and collision products to a single bunch. For this purpose a time resolution of about few nanoseconds is needed. For measuring the time resolution of BCM1F usually halo particles are used from non-colliding bunches. In 2008 this measurement was done with low statistics [56]. The intrinsic time resolution was found to be 1.3 ns. The measurement was done using two BCM1F modules on the opposite sides of interaction point at the same azimuthal angle. To repeat the measurement of the time resolution, several techniques were used and will be explained below.

4.6.1 Test Pulses Measurements

Firstly, measurements were done with test pulses injected into the input on the FE-electronics. The test pulse, generated by a pulse generator, has rectangular shape with a duration of 1 μs and 1 V amplitude. The response signals were digitized by the ADC. An example of a response signal is shown in figure 4.17. Test pulses were applied to all BCM1F channels and the arrival time of the response signal was measured. The measured arrival time distribution for one channel is shown in figure 4.18(a). The distribution is fitted with Gaussian and the standard deviation was measured to be 6.14 ns. Then the test pulse itself was fed into the ADC and digitized, and the arrival time of the digitized test pulse was determined. The distribution of the difference between the test pulse response signal arrival time and the test pulses reference time is shown in figure 4.18(b). The distribution is fitted with Gaussian. The standard deviation was measured to be 1.34 ns. The difference to the result in figure 4.18(a) is explained by the jitter appearing due to the randomly arriving trigger in respect to the ADC internal clock.

4.6.2 Measurements with Halo Particles

To measure the time resolution including the sensor, halo particles from non-colliding bunches circulating in LHC parallel to the beam pipe were used during the flat top sequence. The constant fraction discriminator emulation was applied to determine signal arrival times as described in section 4.4.1.

Using the orbit trigger, signals in two sensors at the same azimuthal angle and different sides almost in coincidence are searched for. The difference between the two time measurements must be about 12 ns as estimated from the distance between modules of 3.6 m.

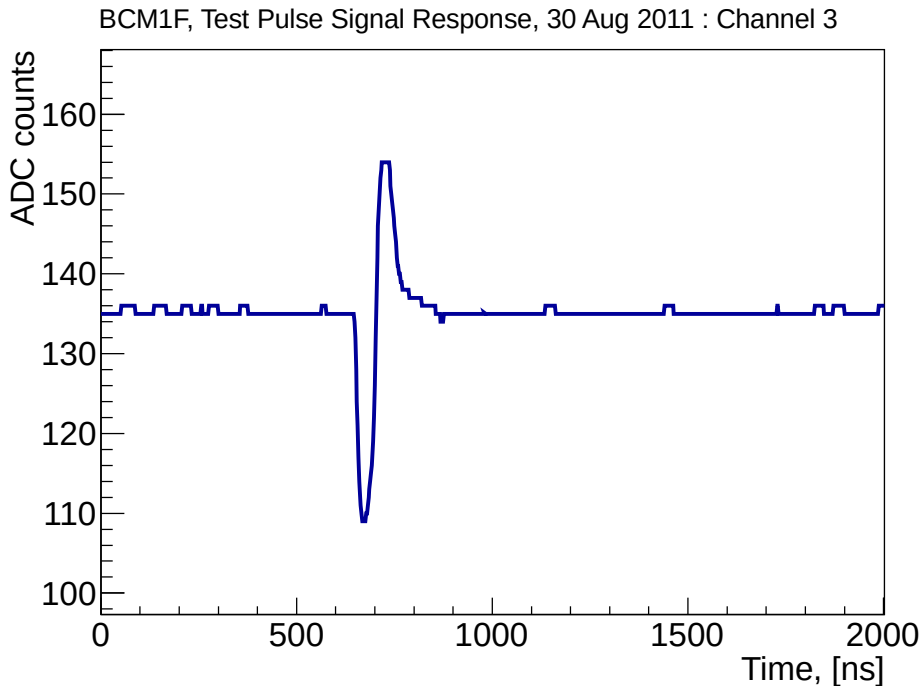

Figure 4.17: Test pulse signal digitized by the ADC, 2011, channel 3.

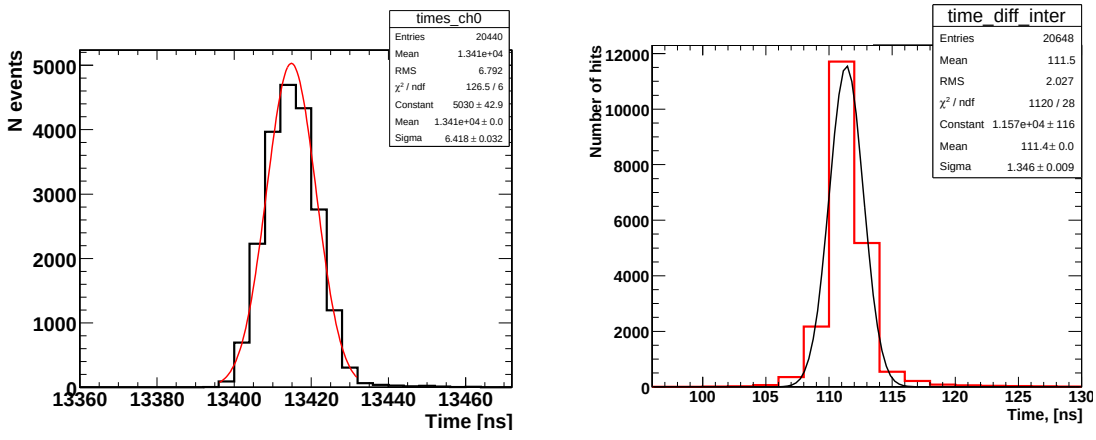

(a) (b)

Figure 4.18: (a) Test pulse response signal arrival time distribution for one channel, measured with respect to the ADC trigger. (b) Difference between the arrival times of the test pulse and the response signal, both fed into ADC inputs.

The quantity, $\triangle t$,

$$\triangle t = t_2 - t_1,$$

was calculated, where t_1 and t_2 are arrival times of halo particles in the two BCM1F channels in the same azimuthal angle on opposite sides of IP, and filled in a histogram. The result is shown in figure 4.19. Since halo particles are circulating in both directions, two peaks are observed at -12 ns and +12 ns.

The distributions of $\triangle t$, as shown in figure 4.19, were fitted with a Gaussian. The width is obtained to be $\sigma(\triangle t) = 2.2$ ns. $\sigma(\triangle t)$ can be expressed as

$$\sigma(\triangle t) = \sqrt{\sigma_{t_1}^2 + \sigma_{t_2}^2}.$$

With the assumption that the two channels have the same time resolution, $\sigma_{t_1} = \sigma_{t_2} = \sigma_t$, the time resolution for each channel is

$$\sigma_t = \frac{1}{\sqrt{2}}\sigma(\triangle t).$$

The intrinsic time resolution of BCM1F results to 1.55 ns, slightly larger than the value obtained using test pulses.

4.7 Aging Monitoring

The performance of the readout chain was investigated using test pulses. Test pulses are fed into the FE-electronics with a pulse shape described in section 4.6.1. The ADC is triggered with a pulse delayed by a constant time with respect to the test pulse and signals from all channels are digitized. These measurements were done in 2011-2012 and compared with measurement in 2009. The amplitudes of the test pulse response signals are calculated as the difference between the signal minimum and the baseline. Firstly, the baseline was calculated in the window before the test pulse response signals and then the minimum of the signal was determined. In figure 4.20(a) the test-pulse response signal amplitude is shown as a function of the integrated luminosity in 2011 for all BCM1F channels. In 2011 the decrease for BCM1F channels was only a few ADC counts.

Figure 4.20(b) shows the result of the measurements including data from 2012 for channel 3. In addition in figure 4.20(b) the baseline for the same channel is displayed. The test pulse response signal amplitude decreased by 15% and the baseline decreased by 22% at an integrated luminosity of 30 fb^{-1} recorded by CMS.

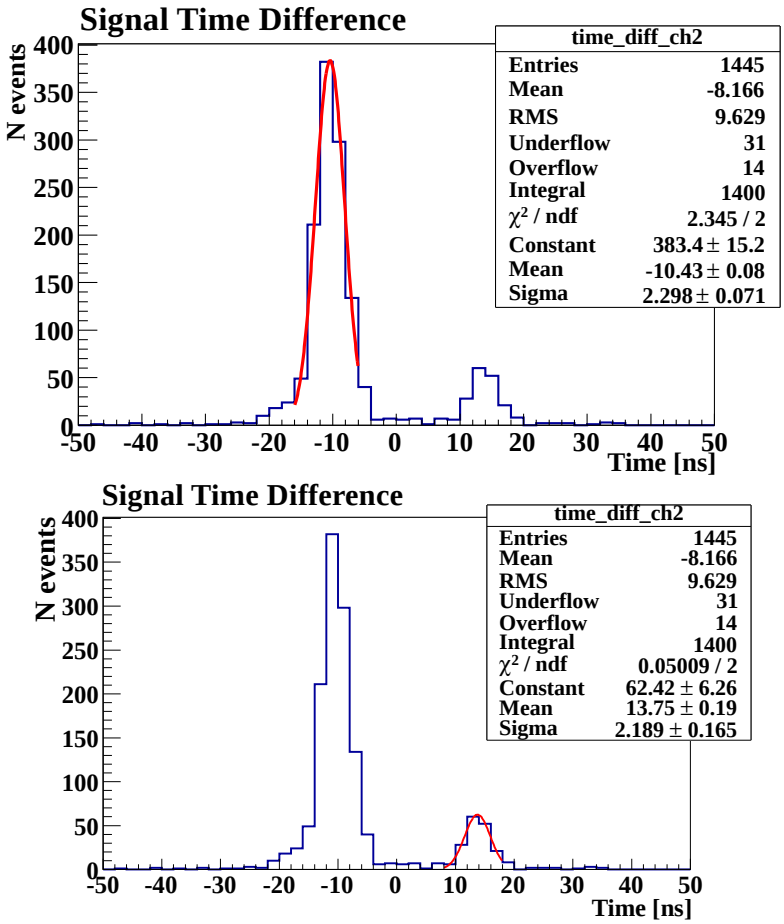

Figure 4.19: The time difference between signal from two sensors of equal azimuthal angle measured using beam halo particles during the flat top sequence of LHC in 2011.

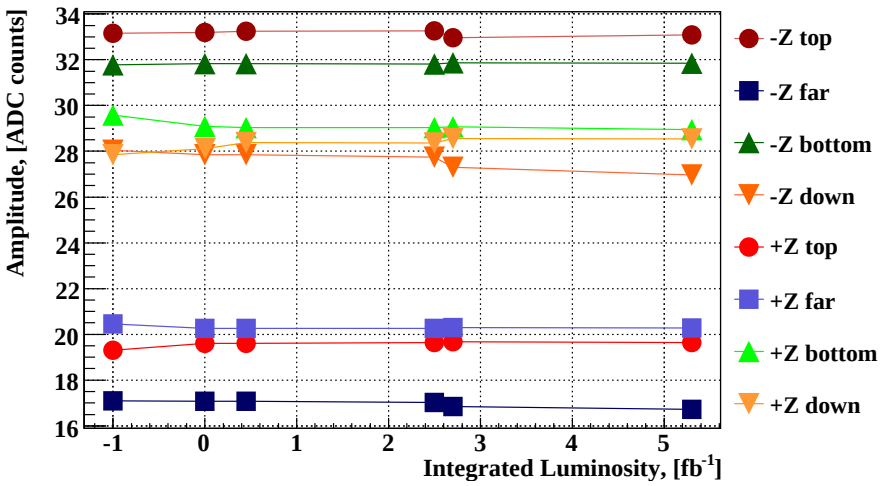

(a)

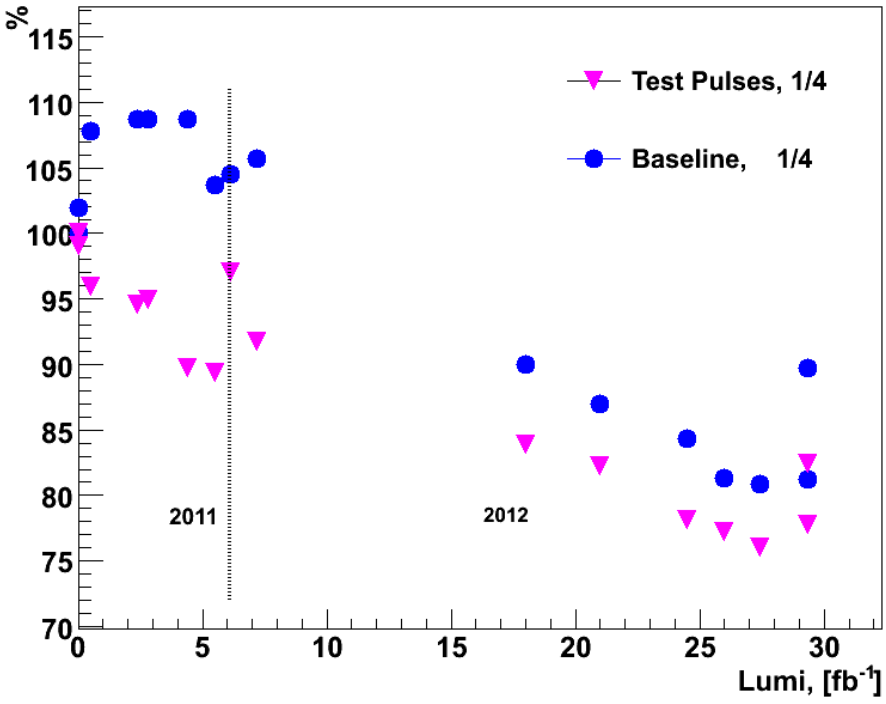

(b)

Figure 4.20: (a) Amplitudes of signals as response to constant test pulses as a function of the integrated luminosity in 2011 for all channels. (b) The amplitudes of signals as response to constant test pulses as a function of the integrated luminosity in 2011-2012 overlayed with the baseline values for ADC channel 3.

Chapter 5

Luminosity Measurements with BCM1F

Introduction

The measurement of luminosity is important for all high energy experiments. It is firstly a characteristic of the accelerator performance. But, secondly, the luminosity is needed to determine the cross sections of physics processes. In this chapter the luminosity measurements in CMS will be described and the measurement of the luminosity bunch by bunch with BCM1F will be introduced. Systematics effects found in studies of the ADC data will be shown.

5.1 Luminosity at CMS

At the LHC the luminosity is measured to monitor the LHC's performance in real time and to provide an overall normalization for physics analyses. The design goal for the real time measurement is to determine the average luminosity with a 1% statistical accuracy in 0.1 s [32]. For the offline analyses, a design goal for the systematic accuracy of less then 5% was given.

For the luminosity measurements processes with known cross section can be used. At the LHC the pp total cross section or the production rates for W's and Z's are examples. However, to calculate these cross sections models are used with large uncertainties. Therefore van der Meer scans were used to calibrate the luminosity, by measuring σ_x, σ_y, the transverse beam widths, and the number of interactions per BX, corresponding to a certain luminosity. Then, once it is calibrated, from the number of interactions per BX, the absolute actual luminosity can be obtained. This method is used for HF, BCM1F and the pixel detector to measure the luminosity.

The three main measurement techniques for the off-line luminosity are:

1 measuring the flux of collision products in the very forward region using the forward hadron calorimeter, HF.

2 counting pixel clusters in the pixel detector [68]

3 counting the number of reconstructed vertices using the pixel and strip tracker detectors [68]

CMS provides both "delivered" and "recorded" luminosity. The delivered luminosity refers to the luminosity delivered by the LHC. The recorded luminosity includes only the luminosity used by CMS. The delivered and recorded luminosities are ideally equal, but in case the CMS detector is unable to take data for a short time, the recorded luminosity is lower, as shown in figure 5.1(a) for 2012. Figure 5.1(b) shows the delivered luminosity by LHC in the years 2010-2012, illustrating the enourmous improvement of the LHC performance with time.

For a real time luminosity measurement up to 2011 only the HF was used. The pixel detector can not be used for the on-line luminosity measurements, because it is slow. In addition, a bunch-by-bunch monitoring, which is useful for accelerator diagnostics, is important. This needs a system to provide information in real-time and independently from the CMS DAQ operation.

Since BCM1F counts collision product rates, it is potentially able due to its excellent time resolution for the luminosity measurement in the bunch by bunch mode. In addition, it allows to determine the luminosity in short time intervals, e.g. minutes or seconds. The final normalization of the luminosity for BCM1F is based on van der Meer scans, which determine the size of the colliding beams and thus the luminosity with minimal reliance on simulation.

5.1.1 HF Luminosity Measurements

The CMS forward hadronic calorimeter provides on-line and off-line luminosity measurements. The on-line technique is based on "zero counting", described later in section 5.1.3. In this method the average fraction of empty calorimeter towers is used to infer the mean number of interactions per bunch crossing. The off-line measurement exploits the linear relationship between the average transverse energy per tower and the luminosity. To avoid non-linearities the HF is limiting the coverage to four azimuthal (2π) rings in the range $3.5 < |\eta| < 4.2$ [70].

As a cross check on the HF-based online luminosity monitor, three offline methods are used. The first one is based on transverse energy in the HF. The second is using tracking and vertex information and the third is counting pixel clusters.

5.1.2 Pixel Luminosity Measurements

The "Vertex Method" requires that at least one vertex with at least two tracks to be found in the event. The z-position of the vertex is required to lie within 150 mm of the center of the interaction region. This method provides good efficiency for minimum bias (MB) events, while suppressing non-collision backgrounds to the few per mil level. [71].

The pixel cluster counting (PCC) method uses pixels in the inner part of the CMS detector [72]. The number of pixels is of about 7 x 10^7. Only a small fraction of pixels is fired even at 'pile up' of several events per bunch crossing. Each p-p interaction results in a certain number of pixel clusters, $N_{pixel/inter}$. Then the number of clusters after a bunch crossing can be expressed as:

$$\langle N_{cluster} \rangle = \langle N_{pixel/inter} \rangle \langle N_{interaction} \rangle \equiv \langle N_{pixel/inter} \rangle \mu_p,$$

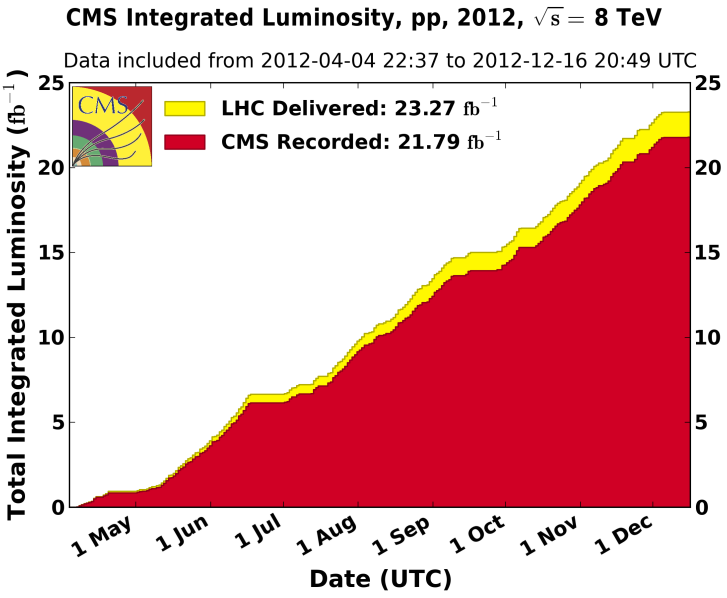

(a)

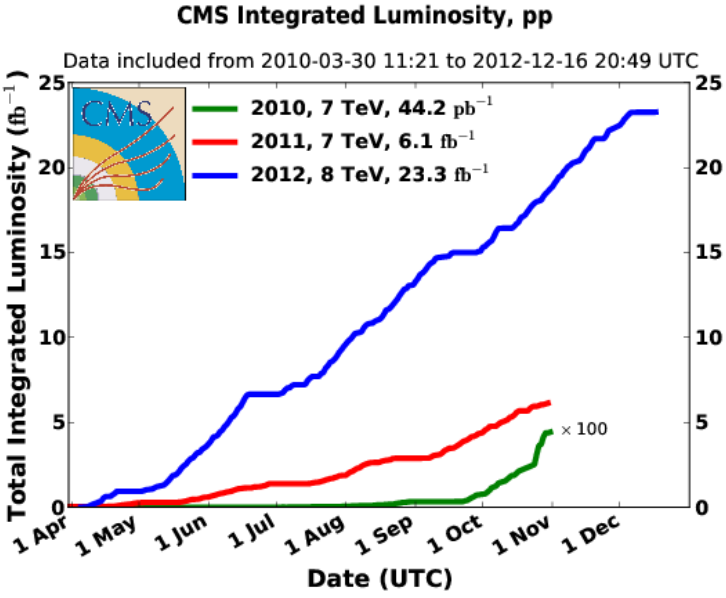

(b)

Figure 5.1: (a) The delivered luminosity in 2012 versus time (yellow), and the recorded one by CMS (red) during stable beams and for p-p collisions at 8 TeV centre-of-mass energy. (b) The delivered luminosity versus time in 2010, 2011, 2012 (p-p data only). [69].

where the average number of interactions per bunch crossing is denoted by μ_p [73]. The relationship between the interaction cross section, $\sigma_{interaction}$, the instantaneous luminosity, dL/dt, and μ_p is

$$\mu_p = \frac{\sigma_{interaction}}{f}\frac{dL}{dt},$$

where f = 11,246 Hz is the LHC orbital frequency.

Then the definition of an effective pixel cross section is defined as:

$$\sigma_{cluster} = \sigma_{interaction} = \langle\ N_{cluster}\rangle\ f\ (\frac{dL}{dt})^{-1}.$$

The van der Meer scan, described in the section 5.1.4, is used for the calibration of the method.

5.1.3 Zero Counting Algorithm

The number of interactions per bunch crossing for a given set of beam parameters follows a Poisson distribution. Then the probability of a number of interactions, n, is given by,

$$p(n) = \frac{\mu^n\ e^{-\mu}}{n!}.$$

This relation allows to determine the average number of interactions when the probability that there is no interaction, $p(0)$, is measured,

$$\mu\ =\ -\ ln[p(0)]\ =\ -\ ln[1-p(>0)]$$

For the case of BCM1F, p(0) is defined as the probability that there is no hit in the eight diamond sensors.

There are several other combinations which can be considered:
XOR+: Requires hits on the +z end and no hits on the -z side.
XOR-: Requires hits on the -z end and no hits on the +z side.
AND : Requires hits in both the +z and -z sides.
OR : Requires hits in the +z or -z sides.

From each of these logics a quantity μ is defined. The following expression is fullfilled.

$$\mu_{OR} = \mu_{AND} + \mu_{XOR-} + \mu_{XOR+}$$

The advantage of using different logics is that each has a maximal sensitivity in a different luminosity regime.

5.1.4 Van der Meer Scan

The luminosity of an accelerator is given by

$$L\ =\ f_{LHC}\ N_1N_2K\ n_b\ \int\ \rho_1^{lab}(\vec{r}-\Delta\vec{r},t)\rho_2^{lab}(\vec{r},t)\ d^3\vec{r}dt, \tag{5.1}$$

where $K = \sqrt{(\vec{v_1}^2 - \vec{v_2}^2)^2 - \frac{(\vec{v_1} \mathrm{x} \vec{v_2})^2}{c^2}}$ is the Moller kinematic relativistic factor [74], c is the speed of light, $N_{1,2}$ are the number of particles in the colliding bunches all moving with the common velocities $\vec{v_{1,2}}$, f_{LHC} is the frequency of collisions and $\rho^{lab}_{1,2}(\vec{r}, t)$ are the normalized particle densities in the laboratory frame. The absolute value of the luminosity or the cross section can be measured by separating the beams in the transverse plane by $\Delta\ \vec{r}$ and by monitoring a collision rate as a function of $\Delta\ \vec{r}$. This method was proposed by van der Meer more than 40 years ago and was originally proved in Ref. [75] for arbitrary beam shapes and parallel beams.

In ideal circumstance with n_b colliding bunches circulating in the accelerator the following relation can be used:

$$L = \frac{n_b f_{LHC} \mu}{\sigma_{inelastic}},$$

where $\sigma_{inelastic}$ is the inelastic scattering cross-section, f_{LHC} is the revolution frequency and μ is the average number of interactions per bunch crossing:

$$\mu = \frac{\langle N \rangle}{n_b},$$

where $\langle N \rangle$ is the average number of interactions per orbit.

The average number of interactions per BX can be measured, but inefficiencies might occur and $\mu_{measured} = \epsilon\ \mu$, where the efficiency, ϵ, allows for detector effects.

The luminosity calibration is necessary for converting the measured $\mu_{measured}$ value to a luminosity. For this purpose, the van derMeer scan is used. It relies on making measurement of μ as a function of the horizontal and vertical beam displacement. Equation 5.1 can be rewritten in the following form:

$$L\ =\ f_{LHC}\ N_1 N_2 K\ n_b \int\ \rho_1(x,y)\rho_2(x,y)dxdy,$$

where $\rho_{1,2}(x, y)$ is the particle density of the beams as a function of the transverse distance from their respective centers. Assuming that there is no correlation between the beam density in the x and y directions, the above equation can be re-parametrized in terms of the effective beam width,

$$\Sigma_x = [2\pi \int \rho_1(x)\rho_2(x)dx]^{-1},$$

$$\Sigma_y = [2\pi \int \rho_1(y)\rho_2(y)dy]^{-1},$$

and the luminosity reads in the following form:

$$L = \frac{f_{LHC}\ N_1\ N_2}{2\pi \Sigma_x \Sigma_y}.$$

BCM1F was used in all van der Meer scans in 2012 to determine Σ_x and Σ_y. An example of the results observed in April is shown in figure 5.2. Three separate scans were performed independently in the x and y directions. For each step of the beam separation, the rate at the detector is measured giving the dependence of the value μ on the beam separation. The distribution is fitted with two Gaussians, from which the quantities Σ_x and Σ_y are derived.

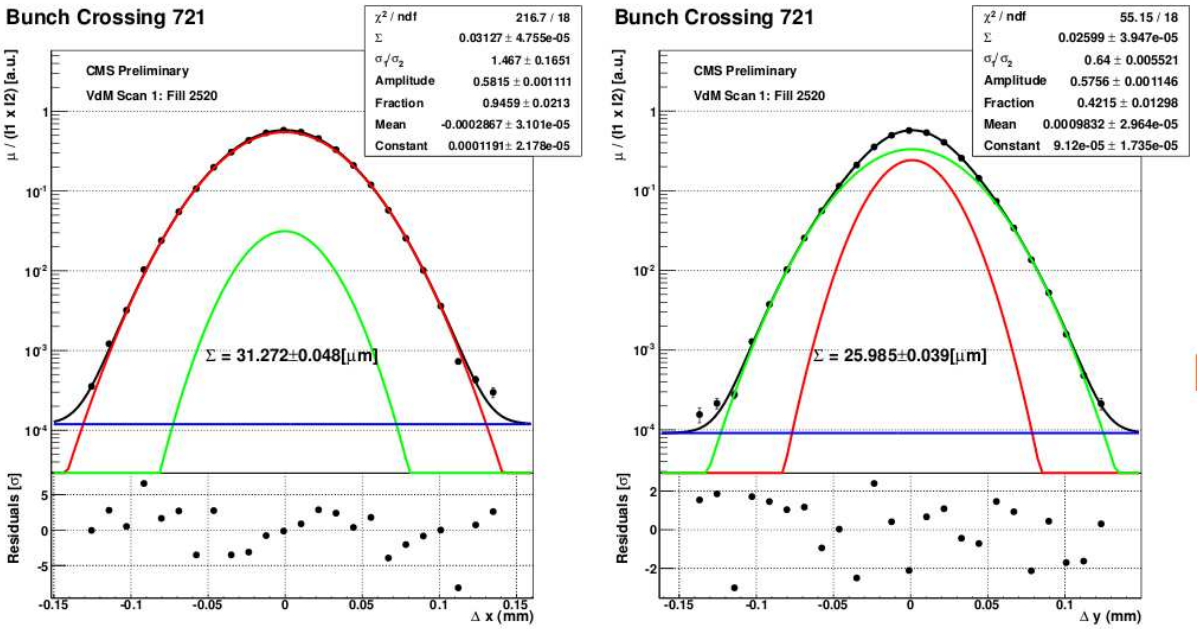

Figure 5.2: Data gathered during the April 2012 VdM scan. The data is fit with a double Gaussian plus a constant where the single Gaussian components are shown in red and green, the constant in blue, and the combined result is in black [76].

5.2 Systematics due to the Detector

In the discriminators used in BCM1F constant thresholds were set [77]. If a fast shift in the signal baseline occurs, the next signal might be not be seen by the system as it will not have sufficient amplitude to pass the threshold. Therefore the number of hits in the detector can be underestimated. The following effects will be discussed:
Time under threshold, TUT: The front-end ASIC needs a certain time to return to the baseline after a signal is amplified. This time is dependent on the signal amplitude and whether the front-end electronics was saturated. In addition, the overlapping of several consecutive signals makes the time under threshold longer, and the discriminator generates only one output pulse. This will be discussed in the section 5.2.1.
Overshoot signals: There were signals with a large amplitude above saturation found. For these signals an overshoot was observed. In case an overshoot occurs, signals during the overshoot have a reduced probability to be detected. To estimate this effect, high amplitude signals were studied in the laboratory to parametrize the shape of the overshot signal.

5.2.1 Characterization of Saturated Signals

There is a small fraction of **Saturated Signals** as shown in section 4.3 in figures 4.8(a) and 4.8(b). These are high amplitude signals appearing in the diamond sensor and saturate the front-end electronics. Saturated signals cause overshoot and shift the baseline for a few microseconds. During this time the system can become blind for the following MIP signals. This decreases the hit counting efficiency.

To model the overshoots of signals measurements in the laboratory have been done with one module of BCM1F. Test pulses with an amplitude of 0.22, 0.44, 0.88, 1.34, 1.94, 2.76, 3.46 V were applied. The signals obtained are shown in figures 5.3(a), 5.3(b), 5.3(c), 5.3(d) and 5.3(e).

The tail of the overshoot signal was fitted with exponential function using the formula $Y(t) = a + b\, e^{c*t}$. The decay time constant is determined to be between -0.0005 and -0.0007, corresponding to 1.4 - 2 μs.

The amplitude of the overshoots is correlated to the time over threshold measured as shown in figure 5.4(a). In addition, the overshoot signal length as a function of the saturated signal length is shown in figure 5.4(b). Above a certain signal length the overshoot amplitude grows almost linearly with the pulse length of the signal in saturation. Due to the limited dynamic range of the laser driver, the overshoot amplitude also saturates. This effect also causes dead time of the system due to a large shift of the baseline.

5.2.2 Dead Time vs Luminosity

The fraction of long signals is determined and the dependence on the luminosity is estimated. In figure 5.5(a) the definition of the time under threshold, TUT, and the time over threshold, TOT, is illustrated. In figure 5.5(b) the sum of time over threshold and time under threshold is shown as a fraction of one LHC orbit as a function of the collision rate. It shows a linear dependence, hence it is concluded that also the dead time of BCM1F depends linearly on the luminosity.

5.3 One Bunch Detection Probability

The probability to detect a hit from a certain bunch depends on the detector geometry, the radiation degradation and the luminosity. It is defined as the number of detected particles in the chosen bunch divided by the number of orbits. To reduce the effect of a baseline shift due to overshoots only the first bunch in the first and second train are considered. These bunches arrive after the abort gap and are therefore much less affected by inefficiencies caused by the large signals from preceding bunches.

Figure 5.6 shows the one bunch detection probability for one BCM1F channel as a function of the instantaneous luminosity measured by HF. The data was fitted with a linear function and the residuals between the data and linear fit are shown below. The linear fit corresponds to the dependence with the 0.2 % residual. The measurement was done over a long LHC fill to cover a large range of luminosities. Figure 5.7 shows for the remaining 7 BCM1F channels the one bunch detection probability fitted by a linear functions. This measurement demonstrates that BCM1F can measure the luminosity in a very large range.

5.4 Luminosity Measurement Using BCM1F

BCM1F performed successful measurements of instantaneous luminosity in 2012. The systematics effects described before were taken into account and corrections were applied.

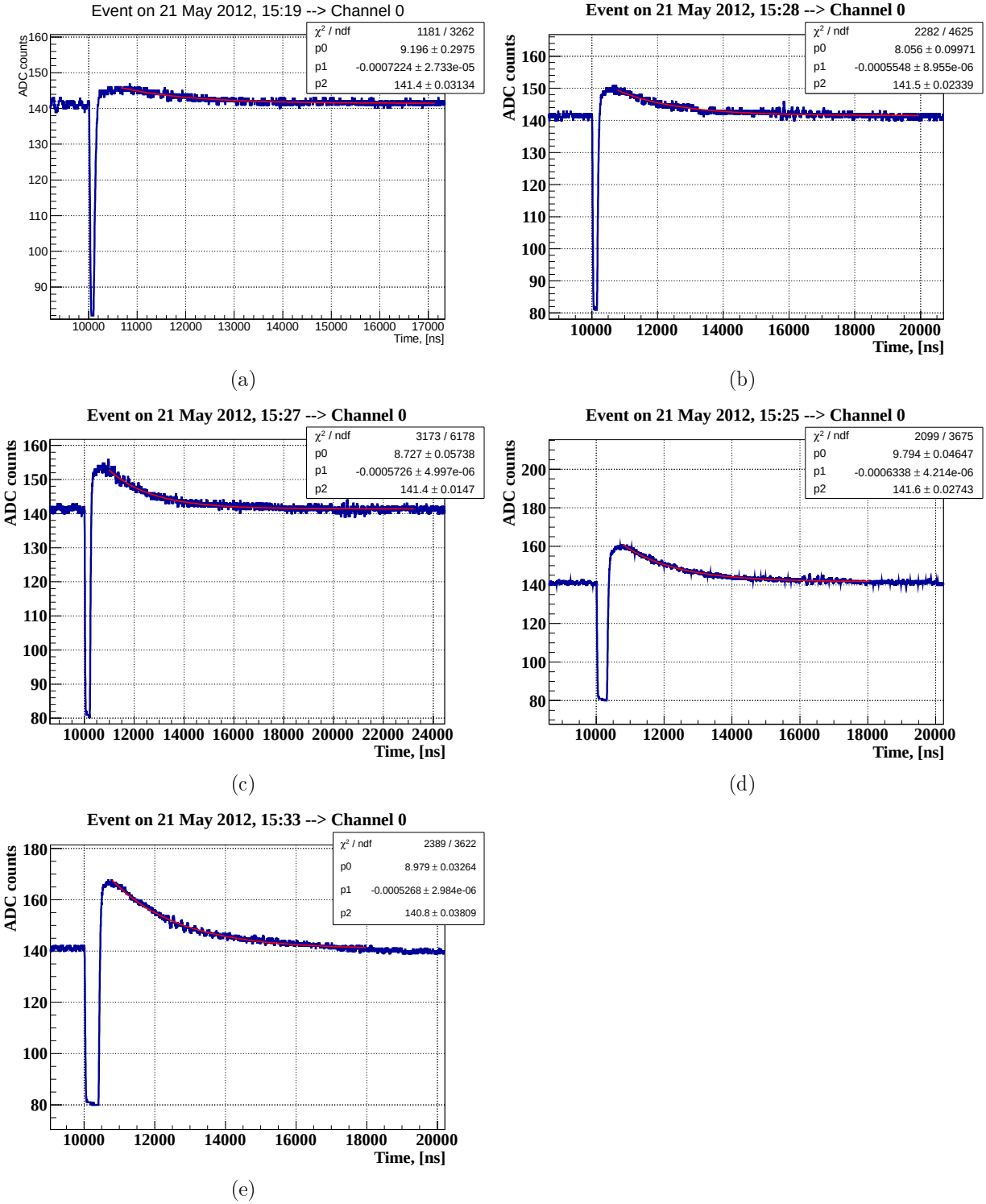

Figure 5.3: Test pulse response signal shapes measured in the laboratory for test pulses of 0.22, 0.44, 0.88, 1.34, 1.94, 2.76, 3.46 V amplitude. The baseline overshoot tails were fitted with an exponential function.

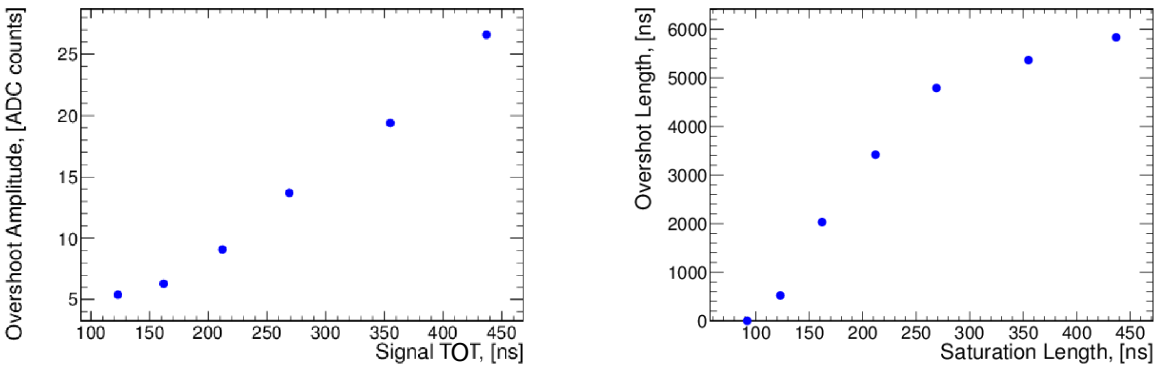

(a) (b)

Figure 5.4: (a) The overshoot signal amplitude as a function of the saturated signal length, defined as a time over threshold. (b) The overshoot signal length as a function of the saturated signal length, defined as a time over threshold.

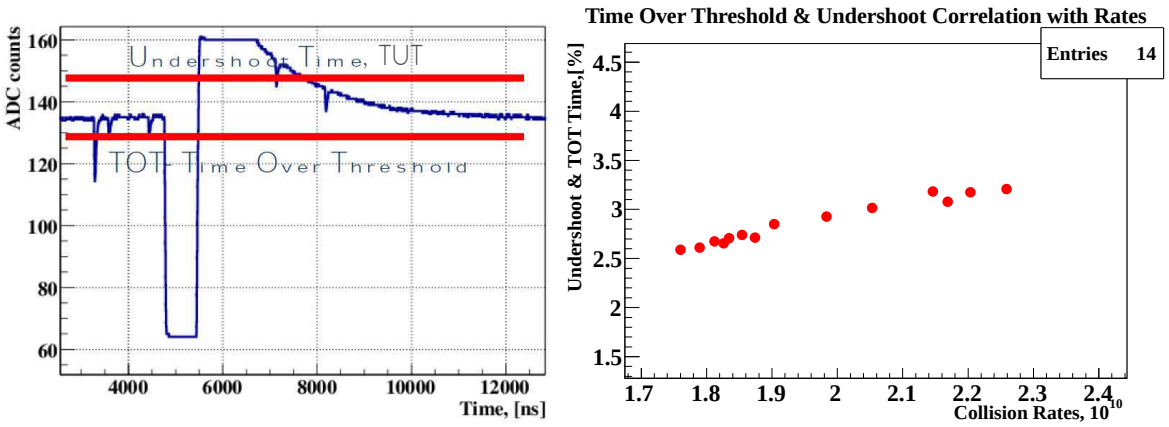

(a) (b)

Figure 5.5: (a) Example of a saturated signal with TUT and TOT definitions. (b) Undershoot and TOT fraction of the LHC orbit as a function of the collision rate obtained from HF.

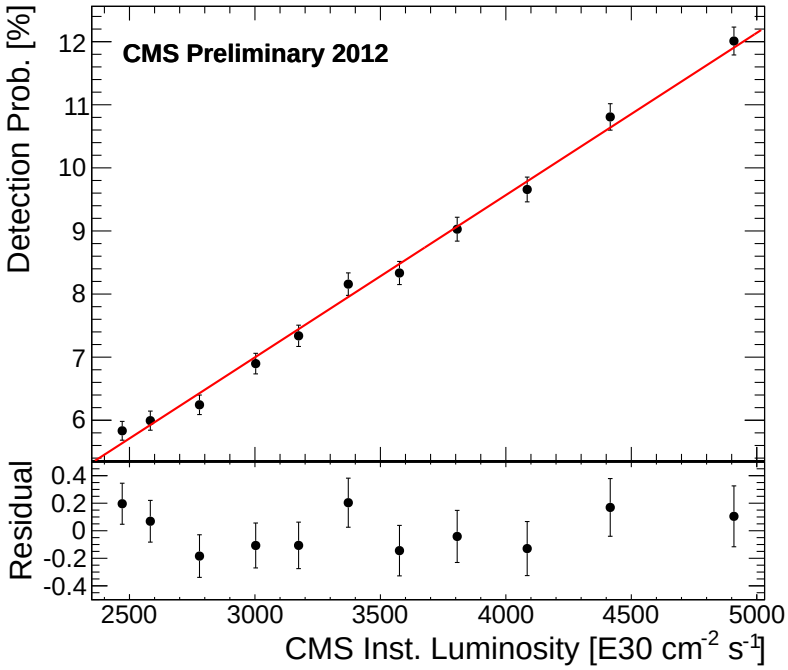

Figure 5.6: One bunch detection probability as a function of the instantaneous luminosity measured by HF. The detection probability is measured for the leading bunch in each orbit.

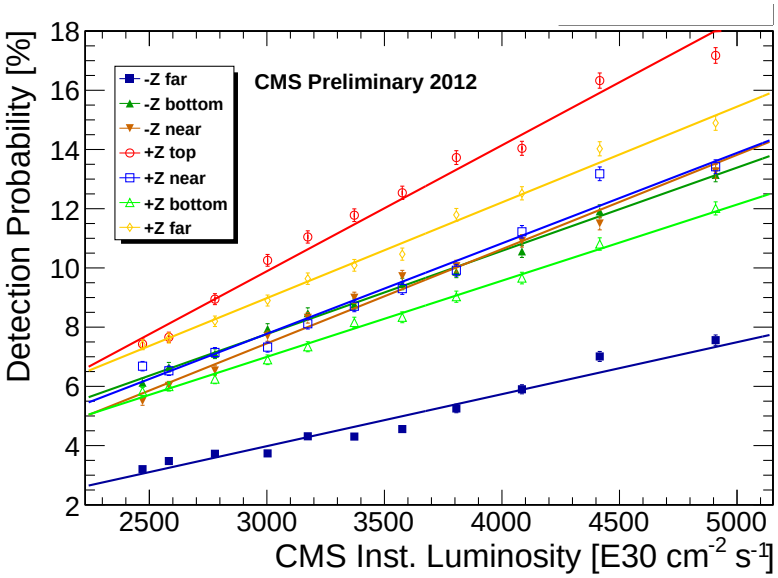

Figure 5.7: One bunch detection probability for all BCM1F modules as a function of the instantaneous luminosity measured by HF. The hit probability is measured for the leading bunch in each orbit.

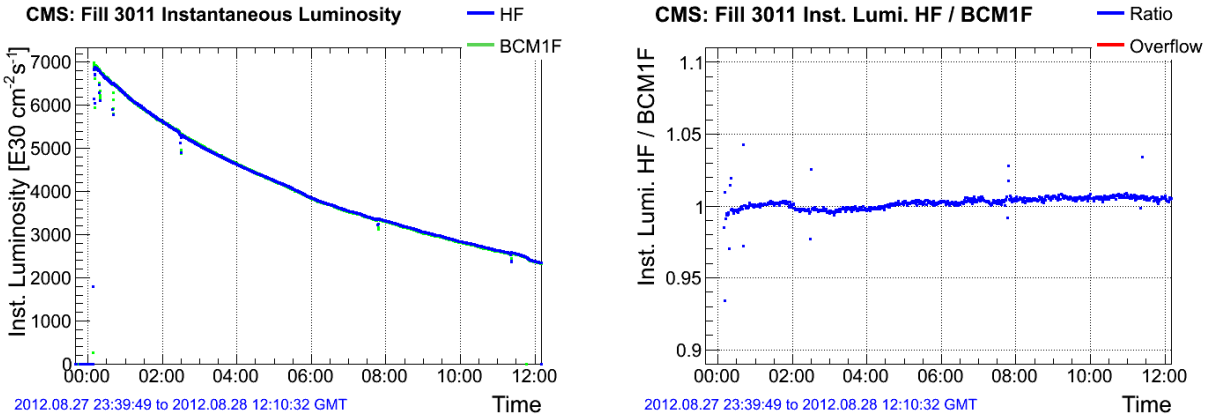

(a) (b)

Figure 5.8: (a) Example of the instantaneous luminosity as a function of time measured by HF (blue) and BCM1f (green). (b) The ratio between measured instantaneous luminosity by HF and BCM1f as a function of time.

Figure 5.8(a) shows the instantaneous luminosity measured as a function of time by HF and BCM1F. The ratio between these two measurements is shown in figure 5.8(b). In the beginning of the fill BCM1F shows a slight overestimation of the luminosity. This effect is still under investigations and will be taken into account for the BCM1F upgrade.

There is a new BCM1F system under preparation to be installed in the 2013-2014 shut down of LHC. The new BCM1F system will contain 24 diamond sensors, which will be possibly metallized with two pads. The final number of channels will be 48. A dedicated front-end ASIC will be developed to reduce inefficiencies due to overshoot signals. The laser driver will be shifted away from the beam pipe to reduce radiation damage. In addition, a temperature sensor will be installed to correct the gain due to temperature jumps. The back-end electronics will be upgraded too. The fixed threshold discriminators will possibly be replaced by the constant fraction discriminators to get better time resolution. The new readout histogramming unit, RHU, discussed in section 4.1.2 is now under development for histogramming a full orbit without any dead time. In the end, the new BCM1F system will provide CMS with luminosity measurements with reduced inefficiencies, and hence with reduced systematic uncertainties.

Application of Radiation Hard Sensors in a Future Linear Collider

Chapter 6

Very Forward Calorimeters for a Detector at the International Linear Collider

The International Linear Collider, ILC, will be the next generation collider for high energy physics experiments [78]. It will consist of two superconducting linear accelerators to accelerate and collide electrons and positrons at 500 GeV center of mass energy with the opportunity to go down to 200 GeV. An energy upgrade would allow ILC operation up to 1 TeV. The aim is to measure very precisely the properties of the Higgs boson and any other new particles that may be discovered by the LHC.

These discoveries are expected to lead to a new understanding of what the universe is made of and how it works. The ILC will give cleaner signatures with less background for the relevant processes than the LHC. This chapter describes the two experiments SiD and ILD. In detail the forward region of the ILD will be discussed. Two calorimeters, LumiCal and BeamCal will be introduced.

6.1 The SiD and ILD Detectors for ILC

Two detectors, called ILD and SiD, shown in figure 6.1, are designed using complementary technologies. Only one of them can be placed in the interaction region. Hence a push-pull regime is foreseen for data taking. When one detector takes data maintenance can be done for the other. To match the requirements from physics both detectors are designed for unprecedented performance for vertexing, tracking and jet measurement. They will apply the particle flow concept for jet energy measurement.

6.2 The Requirements on the ILC Detectors

The ILC provides a broad spectrum of physics opportunities, which the detector must be prepared to address. These include detailed studies of the Higgs sector, Top production at threshold, di-boson production, measurement of SUSY particle features, and other new physics often motivated by alternative models. Each of these creates its own particular set

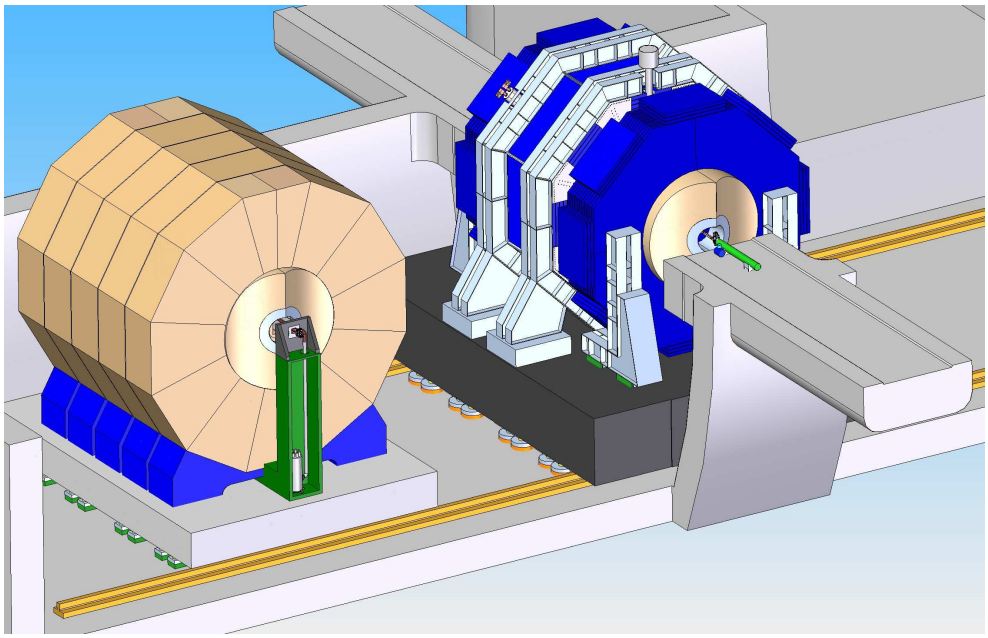

Figure 6.1: ILD and SiD detectors in push-pull mode.

of requirements. In general, the detectors have been designed to cover the requirements for all such possibilities, over the full range of center of mass energies [79].

These requirements for are summarized in the following:

- Jet Energy Resolution
  Excellent jet energy resolution is required for ILC detectors. For this purpose, the Particle Flow Algorithm, PFA, was developed. This technique is taking into account that charged particles can be measured with superior precision in the tracker. The depositions from the charged particles in the calorimeters will be removed and the remaining depositions are assigned to the neutral particles, e.g.photons and neutrons. The jet energy and direction is then obtained from the tracks and the neutral particle depositions in the calorimeter. The PFA needs highly segmented calorimeters to avoid confusion between individual particle depositions. New detector technologies and new reconstruction algorithms enable the needed energy measurement precision of 3 to 4 percent for 100 GeV jets, set by the requirement to separate W and Z di-jet final states [79]. This requirement leads to 1000-times higher granularity and 2 times better resolution of calorimeters in comparisson to the LHC calorimeters.

- Track Momentum Resolution

  To reconstruct the Higgs boson, in the Higgs-strahlung process, requirements are set to the charged track momentum resolution. The recoiling Higgs boson mass is reconstructed from the Z boson decaying into a lepton pair. In Ref. [79], the recoiling Higgs boson mass was shown to be reconstructed precisely with $\delta\ p/p^2 \approx 5\ \cdot\ 10^{-5}\ \mathrm{GeV}^{-1}$. To reach this resolution, a high magnetic field and a high precision tracker with a minimum of material is required. Compared with a LHC tracker, this requirement

leads to 6 times less material and 10 times better resolution than the tracker of the LHC experiments.

- Vertex Resolution

  A new generation of vertex detector is required for the flavor tagging and the quark charge tagging. For this purpose new highly granulated and thin sensors were designed and developed. A fast read out is important due to high occupancy of the vertex detectors leading to high power. In addition, low mass for detectors and their support structure are required. An advantage of ILC is the low duty cycle and this allows power pulsing reducing the heat load and the need for the cooling. For most of the technologies air cooling is considered to be sufficient.

As a result, Higgs branching fractios and quark asymmetries will be measured with sufficient accuracies to test the Yukawa couplings of the Standard Model.

A large amount of soft e^+e^- pairs is produced at the interaction point due to beamstrahlung at small polar angles. A special Detector Integrated Dipole magnet is used, called anti-DID, to guide a large fraction of particles out of the detector.

These e^+e^- pairs are a challenge for the very forward calorimeters. The depositions near the beam pipe approach a MGy per year. Hence radiation hard sensors are needed. In addition, high energy electrons and positrons must be detected in the forward calorimeters for background suppression in new particle searches. This feature will be discussed later in detail.

6.2.1 SiD Detector Concept

The SiD detector is shown in figure 6.1 on the right side. It is a compact detector for precision measurements. The name points to the choice of a full silicon tracker. To obtain the necessary particle momentum measurements precision a solenoidal magnetic field of 5 T is foreseen. The tracker is followed radially by a finely segmented silicon-tungsten sandwich electromagnetic calorimeter, which is surrounded by a highly segmented sandwich hadronic calorimeter with steel absorbers and glass resistive plate chambers as sensors. Both tracker and calorimeters are located within the magnet. The the magnetic field is returned by the iron yoke, which is instrumented with muon detectors. The forward region will be instrumented with two special semiconductor-tungsten sandwich calorimeters LumiCal for precise measurement and BeamCal for fast estimation of the luminosity.

6.2.2 ILD Detector Concept

The ILD detector is shown on the left side in figure 6.1. It is a slightly larger detector, since at larger radii particles within a jet can be better spatially separated [80].

The tracker is a combination of a large-volume time projection chamber (TPC) and a silicon tracker. The TPC will provide up to 224 space points per track. It efficiently separates tracks and precisely reconstructs particle momenta. The silicon tracking detectors

will be located inside and outside of the TPC. This will increase the momentum resolution and helps in linking the vertex detector to the TPC and in predicting the impact point of a track in the ECAL.

The calorimeters are also located inside the magnet. The ECAL is a highly segmented sensor-tungsten calorimeter with small cell size to provide up to 30 samples in depth. Two sensor technologies are considered: silicon or scintillator. The HCAL is also highly segmented sandwich calorimeter with steel absorber and small cell size of two possible technologies, scintillator tiles or gaseous detectors. Calorimeters are surrounded by a large volume superconducting coil.

The magnet flux is returned through the iron yoke is also instrumented with muon detectors. An iron yoke, instrumented with scintillator strips or RPCs, returns the magnetic Flux of the solenoid, and at the same time, serves as a muon filter, muon detector and tail catcher, [81].

In addition, the detector is completed by two cylindrical and radiation hard calorimeters in the very forward direction. The Forward calorimeters are used to make the ILD hermetic. They measure precisely the luminosity and provide an on-line luminosity measurements for the collider.

6.3 Calorimeter Technologies

Calorimeters are divided into electromagnetic and hadronic ones. Both types use particle showers for detection and energy and position measurement of particles. Showers initiated by hadrons (protons, pions etc.) are distinctly different from electromagnetic showers initiated by electrons or photons.

6.3.1 Types of Calorimeters

There are several techniques to build calorimeters driven by the detectable signal, which are scintillation, ionization and Cherenkov radiation. The generated signal should be proportional to the energy of the initial particle. By the sensor material, calorimeters can be divided to following types:

- Solid-State calorimeters: charged particles create electron-hole pairs in sensors. Examples are germanium and silicon crystals.
- Cherenkov calorimeters: The medium is a transparent material and relativistic electrons and positrons in the shower generate Cherenkov photons. To obtain an electrical signal photo-sensors are needed. An example is a lead-glass calorimeter.
- Scintillation calorimeters: The medium is a material in which charged particles produce light via fluorescence. Examples are BGO, CsI and PbWO4.
- Noble-liquid or gas calorimeters: The medium is a noble gas (Ar, Kr, Xe) operated at low temperature. Both ionization and scintillation signals can be collected.

Calorimeters are distinguished between homogeneous and sampling calorimeters. A **homogeneous calorimeter** is one in which the entire volume is sensitive and contributes a signal. A **sampling calorimeter** is one in which the material that produces the particle shower is distinct from the sensors that measures the deposited energy. Typically absorber and sensor alternate in depth. For sampling calorimeters heavy absorbers are used to obtain small X_o and Moliere radius. Although their energy resolution is worse than the one of homogeneous calorimeters, they are relatively easy to segment longitudinally and laterally. In addition, they allow better position resolution and particle identification.

6.3.2 Electromagnetic Showers Development

BeamCal and LumiCal are electromagnetic calorimeters. The processes essential for the shower development are bremstrahlung and pair creation. For example an electron radiates a bremstrahlung photon, which converts to an e^+e^- pair, which then also radiate bremstrahlung photons and so on.

The longitudinal development of a shower is governed by the high-energy part of the cascade. When the particle energies are below the critical energy the bremstrahlung cross section drops and the number of particles in the shower starts to decrease. The remaining particles dissipate their energy by ionization and excitation.

The Critical Energy , E_C, of an electron is the energy at which the main energy loss mechanism changes from radiation losses to ionization losses. Above the critical energy, bremdstrahlung is the dominating process for the electron energy loss.

For the shower development, the following variables are essential:

Radiation Length - X_o - is a characteristic of a material. It is the distance over which a high-energy electron loses $1 - \frac{1}{e}$ of it's energy by bremstrahlung. It is equal to 7/9 of the mean free path of a photon for pair production [5]. Tungsten is characterized by a very small radiation length, X_o=0.3504 cm.

Moliere Radius - R_m - is a characteristic of a material defining the transverse dimension of the electromagnetic showers. It is the radius of a cylinder containing on average 90 % of the shower energy and is related to the radiation length of X_o by:

$$R_m = 0.0265 X_\mathrm{o}(Z + 1.2),$$

where Z is the atomic number of the material. A small R_m is important for the shower position measurement and the shower separation. For a sampling calorimeter the Moliere radius estimation can be done by simulation.

Shower depth - is approximately parametrized as:

$$X = X_\mathrm{o}\frac{ln(E_0/E_c)}{ln(2)}.$$

Shower maximum - the depth in the material, where the number of particles in the shower stops increasing.

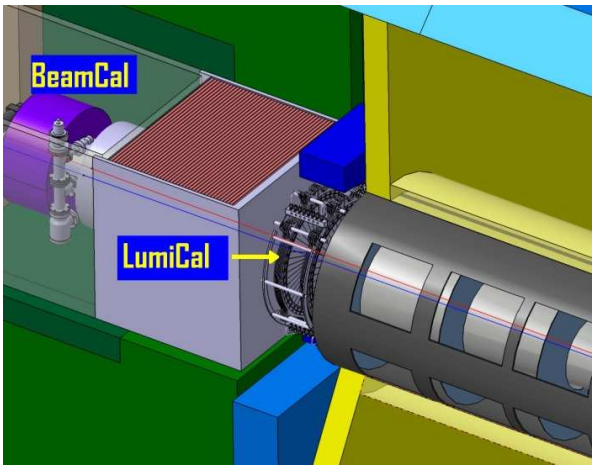

Figure 6.2: ILD very forward region with LumiCal and BeamCal.

6.4 Very Forward Region of Detectors

In the very forward region of both detectors at ILC two calorimeters are foreseen - The Luminosity Calorimeter (LumiCal) for the precise luminosity measurement and the Beam Calorimeter (BeamCal) for the fast estimate of the luminosity and for beam tuning. Both calorimeters extend the polar angular coverage of the detector, important for example for single high energy electron or positron detection. They are designed as cylindrical sensor-tungsten sandwich electromagnetic calorimeters centered around the outgoing beam-pipe [82]. The scheme of the forward region of the ILD is shown in figure 6.2. The BeamCal also shields the inner detector systems from back scattered low energy electrons and photons.

The luminosity measurement is based on Bhabha scattering, $e^+e^- \rightarrow e^+e^-(\gamma)$. To match the physics benchmarks, an accuracy of better than 10^{-3} is needed at a center-of-mass energy of 500 GeV [80] and of better than 3 x 10^{-3} at 3 TeV. For the GigaZ option of the ILC an accuracy of 10^{-4} is needed, [83]. To reach these accuracies particularly challenging requirements on the mechanics and position control for LumiCal arise. The small Moliere radius allows a robust electron shower reconstruction. For BeamCal single high energy electrons and positrons have to be reconstructed on top of a large background of low energy electrons and positrons originating from the Beamstrahlung.

The forward calorimeters nees special FE electronics. Due to the high occupancy they must be readout after each bunch crossing. At the ILC, each bunch train comprises 2820 bunches separated by 308 ns and followed by a 199-ms idle period.

6.5 Luminosity Calorimeter

6.5.1 Luminosity Measurement

LumiCal will provide the experiment with a precise luminosity measurement. The luminosity is necessary to perform cross-section measurements. If for an investigated process a

number of events, N_B, is counted, the cross section, σ_B, is obtained as:

$$\sigma_B = \frac{N_B}{L}, \tag{6.1}$$

where L is the luminosity.

The luminosity at colliders was treated in the section 5.1.4. The precision of the beam parameters, Σ_x and Σ_y, and the number of particles in the bunch is not sufficient to reach a precision of the luminosity measurements of 10^{-3}. Therefore a gauge process, Bhabha scattering, is used. Its cross section can be precisely calculated from the theory. The luminosity can be calculated from counting the number of Bhabha events, N_B, and using the calculated Bhabha cross section, σ_B, using equation 6.1.

Bhabha scattering $e^+e^- \to e^+e^-$ includes γ and Z^0 exchange in s- and t-channel.

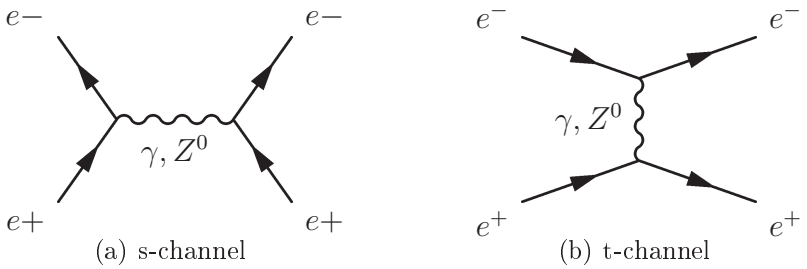

(a) s-channel (b) t-channel

Figure 6.3: The leading order Feynman diagrams of Bhabha scattering.

It's differential cross-section at Born level reads:

$$\frac{d\sigma_B}{d\Omega} = \frac{\alpha^2}{2s}\left[\frac{1+cos(\theta/2)}{sin^4(\theta/2)} - 2\frac{cos^4(\theta/2)}{sin^2(\theta/2)} + \frac{1+cos^2\theta}{2}\right],$$

where $\sqrt{s}$ is center-of-mass energy, α the fine structure constant and θ the scattering angle with respect to the electron beam direction.

For low scattering angles this expression can be approximated as:

$$\frac{d\sigma_B}{d\theta} = \frac{2\pi/\alpha^2}{s}\frac{sin\theta}{sin^4(\theta/2)} \approx \frac{32\pi\alpha^2}{s}\frac{1}{\theta^3}.$$

Due to the steep drop of the cross section as a function of θ the lower threshold must be controlled very precisely.

6.5.2 LumiCal Design

Two LumiCal detectors will be located on both sides of the interaction point. Each calorimeter is a barrel silicon-tungsten sandwich calorimeter consisting of 30 layers. Each tungsten plate will be of one radiation length thickness. The LumiCal sensors have been designed and manufactured by Hamamatsu Photonics. The sensor thickness is 0.320 mm. It is made of n-type silicon bulk material. The pitch of the concentric p+ pads is 1.8 mm and the gap between two pads is 0.1 mm. The sensitive region is from 80 mm up to 195.2 mm in radius. The bias voltage for full depletion ranges between 39 and 45 V,

and the leakage currents per pad are below 5 nA. Pad capacitances were measured to be between 8 pF for the smallest pads and 25 pF for the largest pads [84]. The front-end electronics will be located at the outer radius near to the sensors. There are also space for readout cables, cooling and alignment system foreseen. A sketch of the proposed design overview is presented in figure 6.4(a).

6.6 Beam Calorimeter - BeamCal

BeamCal is a sensor tungsten sandwich calorimeter, positioned just outside the beam-pipes. Due to crossing angle of the beams, the beam-pipe is split for the incoming and outgoing beams. Hence two holes in the center of the BeamCal are needed. BeamCal is positioned behind LumiCal about 3.45 m from the IP, as shown in figure 6.2.

At ILC we have to tackle a new phenomenon - the beamstrahlung. Beamstrahlung is generated when electron and positron bunches cross and squeeze due to their magnetic field, the so called pinch effect. It enhances the luminosity. However, electrons and positrons radiate photons. A fraction of these photons converts in the Coulomb field of the bunch particles creating low energy e^+e^- pairs. The photons and a large fraction of the pairs are radiated at very low polar angle and escape in the beam pipe. The remaining pairs escape at larger polar angle and deposits their energy after each bunch crossing in BeamCal. An advantage is that these depositions may be used to estimate the beam parameters [85, 86]. The disadvantage is in the high radiation dose of about one MGy per year in the sensors close to the beam-pipe.

The design of the BeamCal was optimized by Monte Carlo simulations [14]. BeamCal has a sandwich structure of 30 layers with cylindrical geometry. Each layer consist of 3.5 mm thick tungsten and a 500 μm pad sensor made of GaAs or diamond. A fan-out is used for tracing signals from sensor pads to the FE electronics, positioned at the outer radius.

In front of each BeamCal a 10 cm radius cylindrical graphite block is located for shielding the inner detectors from back scattered low energy electrons and photons.

The requirements on the sensors are stable operation under high electromagnetic dose, good linearity over a dynamic range of about 10^4, very good homogeneity, and fast response.

6.7 Front-End Electronics

All detectors in the very forward region have to tackle relatively high occupancy, requiring dedicated front-end electronics. At the ILC subsequent bunch crossings, separated by 300 ns, have to be read out and resolved. A power dissipation can be reduced by readout the calorimeters within 300 ns and to switch off the power between bunch trains. The front-end electronics will work in two modes, the standard data taking (SDT) mode, used for normal data taking for the shower readout, and the detector calibration (DCal) mode, used to measure MIP signals. There are two ASIC developments for the forward calorimeters. Both of them can be applied both for the LumiCal and BeamCal. They will be discussed below. As the front-end technology for the LumiCal is more advanced, it was used for the prototype development and was tested on the test beams, as described in chapter 8.

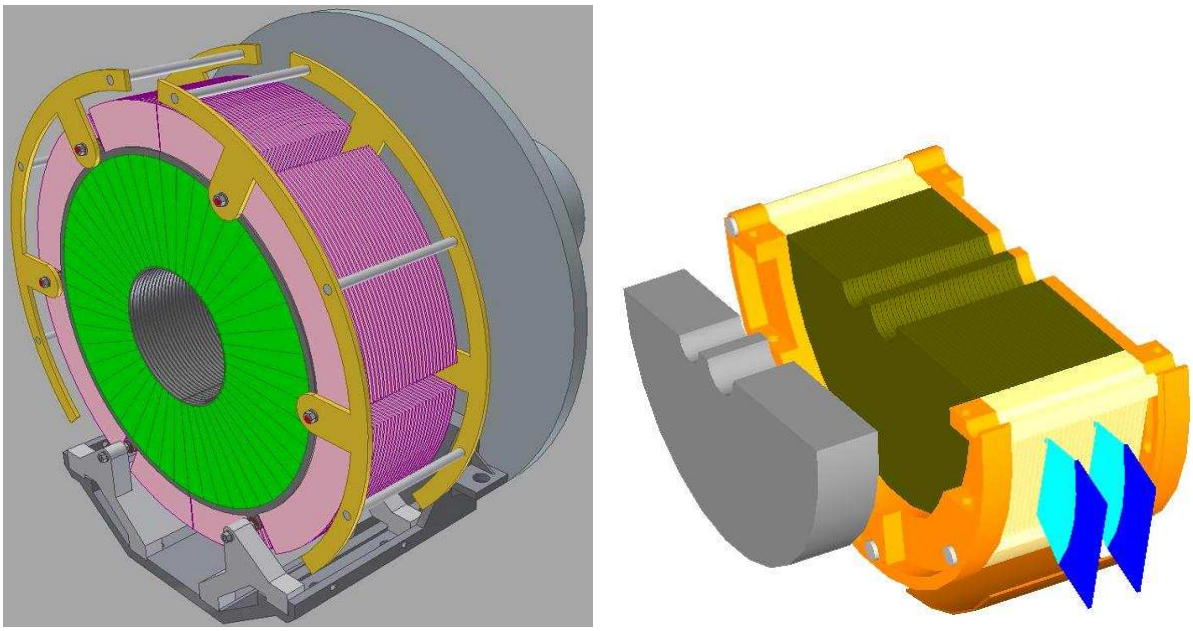

(a) (b)

Figure 6.4: (a) - LumiCal design with silicon sensor segments shown in green, tungsten structure in purple and, in yellow, the mechanical frame for the required stability. (b) - BeamCal design - half cylinder with graphite block in front in grey, sensor segments shown in cyan and readout electronics in blue. In orange, the mechanical support is shown.

6.7.1 LumiCal Front-End

Figure 6.5(a) shows the scheme of the Front-End ASIC. The ADC ASIC block diagram is shown in figure 6.5(b). Both FE ASIC and ADC ASIC were developed in 350 nm AMS technology [87, 88].

The FE ASIC comprises a charge sensitive amplifier, a pole-zero cancellation circuit and a shaper. The peaking time is 60 ns. There are switches allowing to change the resistor and capacitance values of the feedback circuit leading to different gains. The preamplifier and shaper can work in two gains, called "High" and "Low". This leads to four combination of gains later investigated in the test beam and called "HighHigh", "HighLow", "LowHigh" and "LowLow".

In each prototype FE ASIC chip 8 channels are included, where the first 4 channels have a passive feedback with resistors R_f, R_p, and the second 4 channels use MOS transistors [89] for the feedback.

The electronics is placed on 2 mm aluminium plates working also as a heat sink.

6.7.2 BeamCal Front-End

The front-end and ADC ASIC of BeamCal are designed and developed in 180 nm mixed-signal technology following a different readout concept. Since a train of about 3000 bunches within 1 ms is followed by a 199 ms idle period at ILC, the signals from all pads are stored in an analog memory and digitized and readout after the train is over.

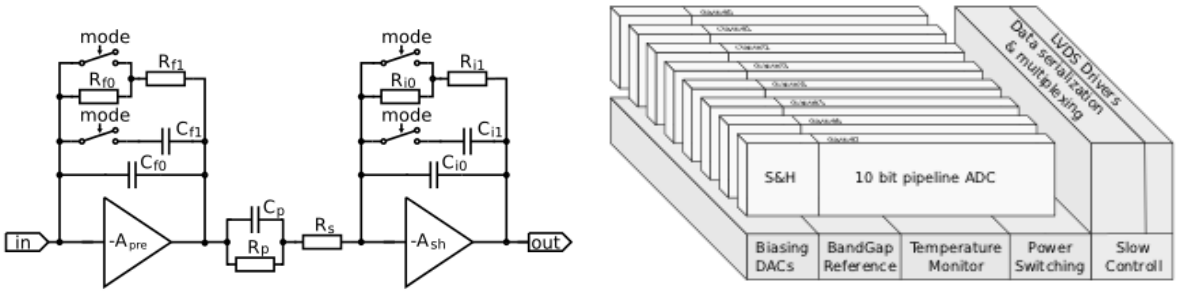

(a) (b)

Figure 6.5: (a) The schematics of one FE ASIC channel. (b) The block diagram of one ADC ASIC chip for LumiCal.

For the BeamCal front-end electronics the expected pad capacitance were estimated to be about 9 pF for a pCVD diamond or 20 pF for Silicon or GaAs sensors [90]. Additional capacitances will come from the copper traces on the fan-out that connect pads to the front-end electronics. In the initial BeamCal specifications, the maximum input signals were estimated to be about 36.9 pC in the SDT mode, and 50 times smaller in the DCal mode.

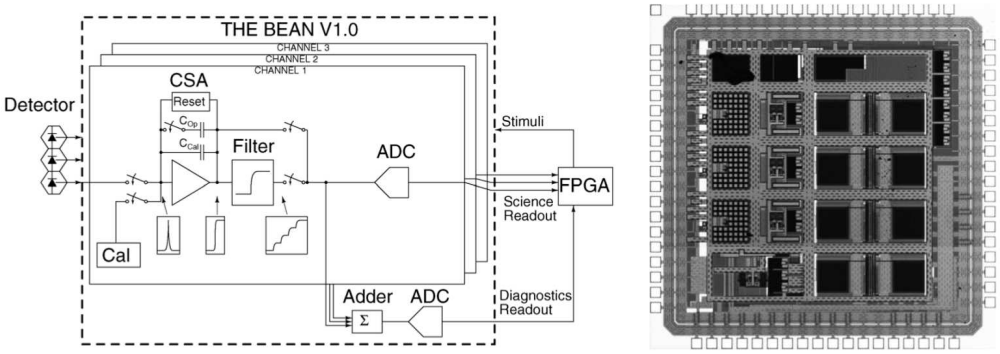

(a) (b)

Figure 6.6: (a) - The scheme of the Bean prototype [91]. (b) - Microphotography of the Bean prototype of BeamCal.

The BeamCal instrumentation integrated circuit, Bean, is designed and prototypes are available. The scheme of the Bean prototype is shown in figure 6.6(a), [90]. Each channel has a 10-bit output for standard data taking, and an additional 8-bit output with the sum of the outputs of all channels to be used for beam diagnostic purposes. A microphotography of the Bean prototype is shown in figure 6.6(b).

To process the signal charge at the ILC pulse rate, the Bean uses switched-capacitor filters and a slow reset-release technique. Each channel has a 10-bit successive approximation analog-to-digital converter. The Bean also features a fast feed-back adder capable of providing a low latency output for beam diagnostic purposes. Currently there are studies ongoing for 3-channel prototype of the Bean built to validate the concept. The final goal is to build the final device with 32 channels.

Chapter 7

Simulation Studies of the Beam Calorimeter

One goal of the BeamCal is the detection of high energy electrons on top of the large background from beamstrahlung pairs. A high detection efficiency is important for new physics searches at ILC [92]. The high background in the low polar angle region of BeamCal requires an optimisation of the sensor segmentation to obtain the highest efficiency for single electrons shower reconstruction.

To estimate the efficiency of single electron reconstruction, a cluster finding algorithm was written and applied for two segmentation schemes. This chapter is summarizing the BeamCal simulation studies for different ILC beam parameters.

7.1 ILC Beam Parameters

Beam parameters of the ILC are under continuous discussions since years. Modifications are the result of considering cost reduction, improved understanding of system functionality, a more robust design and progress in accelerator. The current parameter set was optimized at a center-of-mass energy of 500 GeV to reach the design luminosity of 2 x 10^{34} cm^{-2} s^{-1} with low cost. Two recent sets of machine parameters are given in table 7.1, which are called RDR and SB2009.

The **Emittance** is a property of a charged particle beam in a particle accelerator and is a measure of how much phase space a beam takes. The vertical and horizontal emittances are Y and X projection of the ellipse size of the beam.
The **Beta Function** is related to the transverse size of the particle beam as a function of the coordinate along the nominal beam trajectory.

The SB2009 has two parameter sets for 500 GeV center-of-mass energy:

No TF : Strong focusing the bunches before crossing leads to high-disruption, which results in a luminosity of approximately 1.5 x 10^{34} $cm^{-2}s^{-1}$. The energy loss due to beamstrahlung of 4% is higher than the RDR nominal value by a factor of 1.6 but is still significantly less than the maximum RDR value of 5.5%.

500 GeV		RDR			SB2009	
		min	nominal	max	with TF	no TF
Bunch population	x 10^{10}	1	2	2	2	2
Number of bunches		1260	2625	5340	1312	1312
Linac bunch interval	ns	180	369	500	530	530
RM bunch length	μm	200	300	500	300	300
Normalized horizontal emittance at IP	mm-mrad	10	10	12	10	10
Normalized vertical emittance at IP	mm-mrad	0.02	0.04	0.08	0.035	0.035
Horizontal β function at IP	mm	10	20	20	11	11
Vertical β function at IP	mm	0.2	0.4	0.6	0.48	0.2
RMS horizontal beam size at IP	nm	474	640	640	470	470
RMS vertical beam size at IP	nm	3.5	5.7	9.9	5.8	3.8
Vertical disruption parameter		14	19.4	26.1	25	38
Fractional RMS energy energy loss to beamstrahlung	%	1.7	2.4	5.5	4	3.6
Luminosity	$10^{34} cm^{-2} s^{-1}$	2			1.5	2

Table 7.1: Beam parameters of the ILC. The RDR parameters are compared to the SB2009 parameters. TF refers to Travelling Focus.

With TF : A second approach relies on a technique known as a traveling focus [93], where the focus at the interaction point is adjusted along the bunch length. It allows the vertical beta function to be reduced below the bunch length, which leads to higher luminosity, and compensating for the factor-of-two reduction due to the lower bunch number. Crucial for the BeamCal is that the beamstrahlung is higher than for the RDR nominal parameter values.

7.2 Simulation tools

7.2.1 Beamstrahlung at the ILC

At the ILC the beamstrahlung will be crucial for the forward detectors. Beamstrahlung is a radiation from particles deflected by the magnetic field when two bunches cross each other. The power radiated by a beam electron is [94]

$$P_e = \frac{2}{3}\frac{e^2}{m^2c^3}\gamma^2 F^2,$$

where $F = e(E + c\beta B)$ is the Lorenz force.

There are several variables to describe beamstrahlung:

1. Often a parameter Υ, which is ratio of the critical photon energy, $\hbar\omega_c$, to the beam energy E_{beam}, is used instead.

$$\Upsilon = \frac{2}{3}\frac{\hbar\omega}{E_{\mathrm{beam}}} \approx \frac{5}{6}\frac{Ne_e^2\gamma}{\alpha\sigma_z(\sigma_x+\sigma_y)},$$

where $\sigma_z, \sigma_x, \sigma_y$ are the bunch dimensions and N the number of electrons in the bunch.

2. Critical Frequency

$$\omega_c = \frac{3\gamma^3 c}{2\rho},$$

where ρ the bending radius of the beam particles trajectory and γ is the relativistic factor

$$\gamma = \frac{E_{Beam}}{m_e}.$$

3. Averaged number of beamstrahlung photons per incoming beam particle -

$$N_\gamma \approx 2.12\frac{\alpha N r_e}{\sigma_x+\sigma_y}\frac{1}{\sqrt{1+\Upsilon^{2/3}}}$$

.

4. And averaged energy loss per incoming particle -

$$\delta_B \approx \frac{r_e N^2\gamma}{\sigma_z(\sigma_x+\sigma_y)}\frac{1}{(1+1.5\Upsilon^{2/3})^2}$$

Real beamstrahlung and virtual photons can interact with individual particles inside the bunch to produce incoherent e^+e^- pairs by

1. the Breit-Wheeler process $\gamma\gamma \to e^+e^-$
2. the Bethe-Heitler process $\gamma e \to eee$.
3. the Landau-Lifshitz process $ee \to eeee$.

In figure 7.1 the feynman diagrams for these processes are shown.

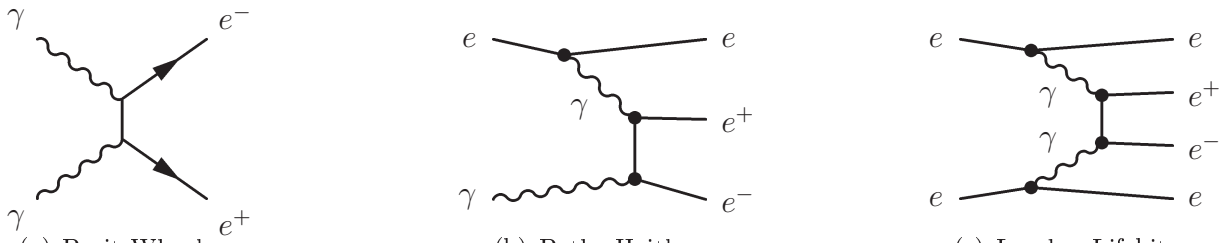

(a) Breit-Wheeler (b) Bethe-Heitler (c) Landau-Lifshitz

Figure 7.1: Processes of incoherent pair creation.

By interaction with the collective field of the opposite bunch also coherent pairs are produced. The latter process strongly depends on Υ and plays a role at multi-TeV colliders.

In the magnetic field of the bunch e^+e^- pairs are deflected and hit BeamCal.

The generation of beamstrahlung pairs is provided by the software package guinea pig described below. Studies on the beamstrahlung pair distributions are discussed in Ref. [14].

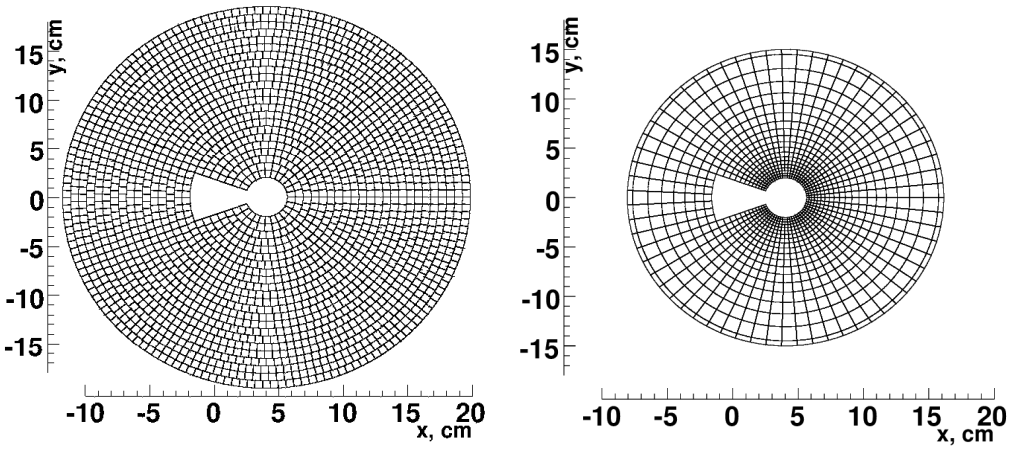

(a) (b)

Figure 7.2: (a) BeamCal segmentation with 23 rings of pads of almost equal size. (b) BeamCal segmentation with 20 rings of pads growing with radius. BeamCal is centered around outgoing beam pipe - the key hole in the center leaves space for the incoming beam pipe.

7.2.2 Guinea Pig

For the simulation of the bunch crossings guinea pig (GP) software is used [95]. Input parameters for GP are the number of particles per bunch, the energy of the particles, vertical, horizontal and longitudinal beam-sizes, emittances and offsets. The output file "pairs.dat" contains e^+e^- pairs created by beamstrahlung: the energies, momenta and initial coordinates of each particle at the interaction region of the ILC.

An example of the input parameters in the *acc.dat* file is shown below:

$\$ACCELERATOR :: ilcSB2009$
$\{energy = 250.0; particles = 2.0;$
$\sigma_x = 470.0; \sigma_y = 5.8;$
$emitt_x = 10.0; emitt_y = 0.035;$
$\sigma_z = 300.0;$
$f_{rep} = 5.0; n_b = 1312;$
$charge_{sign} = -1.0; dist_z = 0.0;$
$offset_x = 0.0; offset_y = 0.0;$
$waist_x = 0.0; waist_y = 0.0;\},$
where $energy$ is energy of the particles in GeV, $particles$ is number of particles per bunch in units of 10^{10}, σ_x, σ_y and σ_z are horizontal, vertical and longitudinal beam sizes, $emitt_x$ and $emitt_y$ are normalized horizontal and vertical emittances, f_{rep} is the repetition frequency of collider, n_b is the number of bunches per bunch train, $charge_{sign}$ is the relative charge of two beams, -1 is for e^+e^-, $dist_z$ is the longitudinal charge distribution, $offset_x$ and $offset_y$ are horizontal and vertical beam offsets and $waist_x$ and $waist_y$ are the shifts of the horizontal and vertical waists with respect to the plain of collision.

7.2.3 Beam Calorimeter Simulation Tool - BeCaS

For the fast simulation of BeamCal a software package, BeCaS [96], was used. BeCaS is based on Geant4 [97] and includes a detailed geometry and material description of sensors and absorbers and a simplified description of the surrounding detectors. A solenoidal magnetic field including an anti-DID field [98, 99] inside and around the detector is applied for particle tracking. The beam crossing angle is 14 mrad. The BeamCal is positioning at z=3550 mm centered around the outgoing beam. The inner and outer radii are 20 and 165 mm, respectively. In depth, the calorimeter comprises 29 absorber disks of 1 X_o thickness interspersed with sensor planes. A 10 cm thick graphite block is positioned just in front of BeamCal. An additional sensitive layer in front of the calorimeter is called Pair Monitor. The sensor planes are made of 0.3 mm diamond with gold metallization, a kapton foil of 0.1 mm thickness and a 0.05 mm air gap. The tungsten disks outer radius is equal to the sensor outer radius.

A sketch of two sensor segmentations studied is shown in figures 7.2(a) and 7.2(b). The segmentation with equal pad size uses the following relations.
The inner, R_{i-1}, and outer, R_i, radii dimensions of pads are calculated as:

$$R_i = R_{i-1} + dR,$$

where i is the number of the ring and dR is the constant radial pad size. It is calculated by the following expression:

$$dR = \frac{R_{\text{outher}} - R_{\text{inner}}}{N_{\text{rings}}},$$

where N_{rings} is a number of rings in the radial dimension of the BeamCal. The azimuthal angle is calculated differently for each ring depending on the number and sizes of pads. In the second segmentation the radial pad size is growing with the radius following the relation:

$$R_i = R_{i-1} + dR,$$
$$dR = aR_1^i,$$

where a=1.1099 and R_1 is the innermost radius of the BeamCal. The angular segmentation is constant, $d\theta = const$. The equal sized segmentation has 73620 pads for two calorimeters and the radially growing segmentation 70560 pads.

An example of one bunch crossing simulation is shown in figure 7.3(b) for 500 GeV RDR nominal beam parameters and 7.3(a) for the 500 GeV SB2009 beam parameters. The deposited energy from the beamstrahlung pairs in the sensors of the calorimeter is summed over 30 BeamCal layers and shown using the color scale given in the figure. Also the energy deposited by a single electron of 250 GeV in the sensors of BeamCal is summed over 30 layers and superimposed on top of the beamstrahlung pairs depositions from one bunch crossing.

7.3 Cluster Reconstruction Algorithm

Typical longitudinal distributions of the energy deposited in the calorimeter are shown in figure 7.4(a) for pairs and a single high energy electron. The deposited energy was simulated

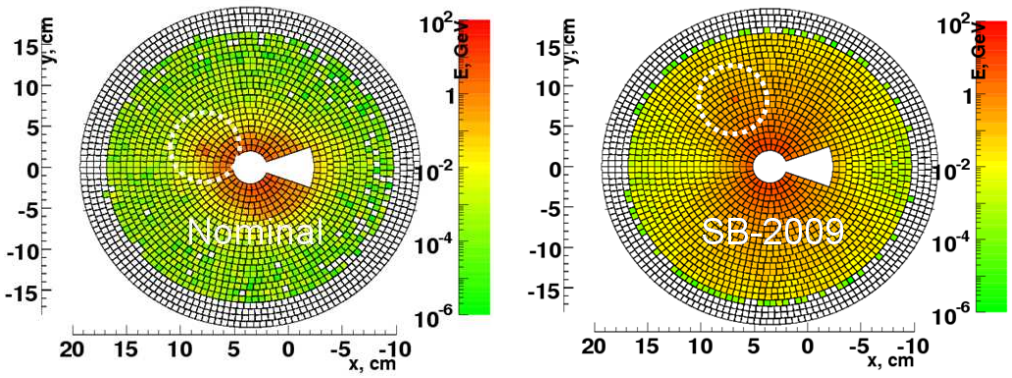

(a) (b)

Figure 7.3: (a) The deposited energy of one bunch crossing from the beamstrahlung pairs with an overlayed 250 GeV electron shower using nominal RDR beam parameters. (b) The result of BeCaS simulation of one bunch crossing. The deposited energy from the beamstrahlung pairs with SB2009 ILC beam parameters with an overlayed 250 GeV electron shower deposited energy is shown. Both plots show the sum of deposited energy in 30 layers of BeamCal.

for one bunch crossing as a function of the sensor layer number for two beam parameter sets: SB2009 in blue, RDR nominal in black color. The maximum of the longitudinal development of electromagnetic showers of beamstrahlung pairs for both parameter sets is around the 6^{th} layer. A typical energy spectrum of the electrons and positrons in the shower is shown for one bunch crossing inside the sixth sensor layer in figure 7.4(b). A typical energy of the shower particles is about 10 MeV. For SB2009 beam parameters more beamstrahlung pairs are created and the deposited energy in BeamCal is higher for SB-2009 than for nominal RDR beam parameter set.

In addition, the deposited energy from a single electron of 250 GeV is shown in red with the scale on the right side. The single high energy electron or positron showers are propagating almost parallel to the axis of the detector. The maximum of the shower development, as can be seen from figure 7.4(a) for a single electron is around the 11^{th} layer.

For the search of a shower, pads in different layers, but at the same radius and azimuthal angle are grouped into rows of up to 30 pads called **towers**. To accept a tower 10 and more consecutive pads with non-zero deposited energy after the 5^{th} layer of the BeamCal are required. The tower with the maximum deposited energy is called a **seed tower**. Surrounding towers of the seed tower are attached to it to form a cluster candidate. A cluster candidate is accepted if it contains two and more neighboring towers. In case of a shower core development on the border between two or more towers and if one of the neighboring towers contain 90% or more of seed tower energy, further neighboring towers are searched for and added to the cluster. For every cluster, the deposited energy and radial and polar angle coordinates are calculated as an energy weighted average of the tower positions. In case a cluster candidate is found, the algorithm starts to look for additional cluster candidates.

Figure 7.5 shows the number of towers found for 100, 150, 200 and 250 GeV electron showers, requiring a different number of subsequent pads in the tower for the segmentation with the equal pad size, when no pair depositions are in the calorimeter. The upper dark

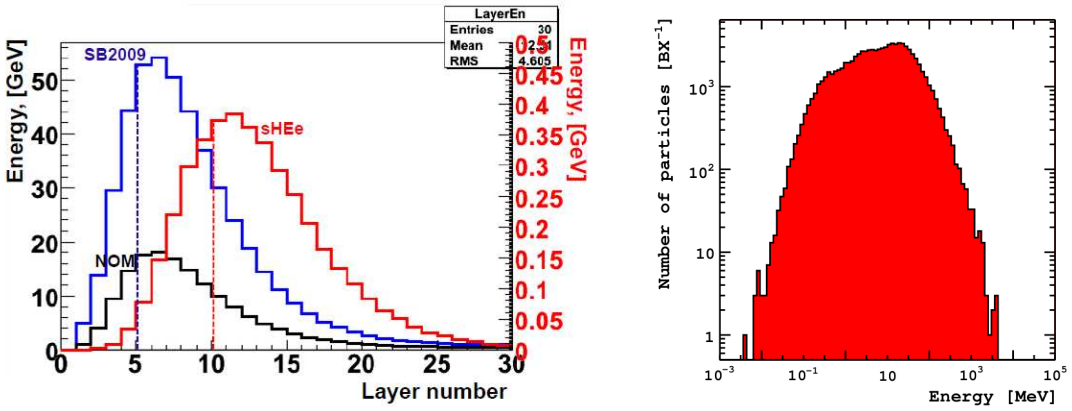

(a) (b)

Figure 7.4: (a) Longitudinal distributions of the energy deposited in the calorimeter. The energy deposition in the diamond layers caused by the background from ILC Nominal beam parameters (black), SB2009 ILC beam parameters (blue) and by the 250 GeV (red) are shown [100]. (b) The spectrum of the shower electrons and positrons at $6X_0$ for one bunch crossing [101].

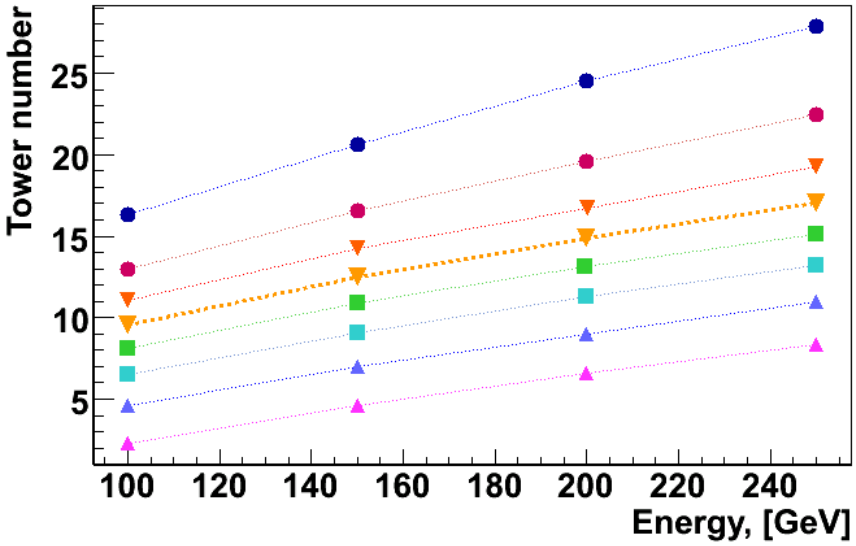

Figure 7.5: Number of towers found with different requirement on the number of consequent pads (the upper line correspond to 4 pads, then each line down was obtained with 2 pads more required to be in the tower)

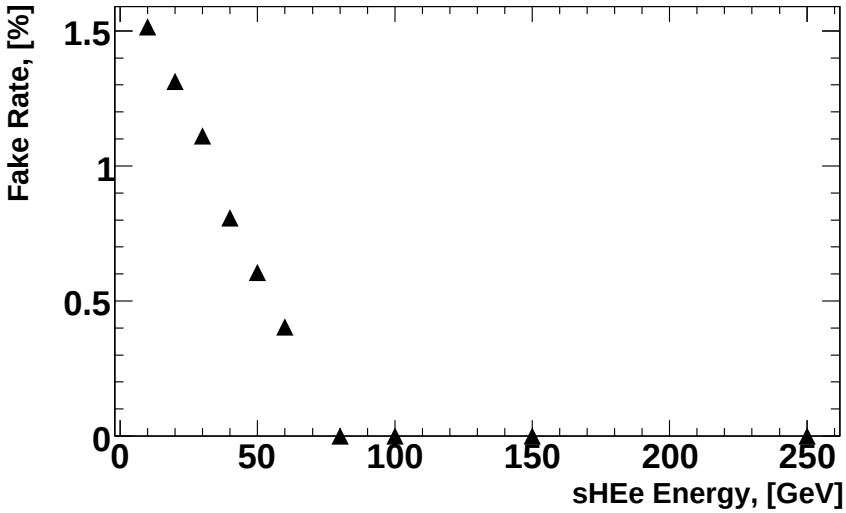

Figure 7.6: The fake rate of the cluster finding algorithm for nominal beam parameters.

blue line (dots) corresponds to the number of towers in the showers with 4 subsequent pads in the tower. The following lower lines correspond to 6, 8, 10, 12, 14, 16 and 18 subsequent number of pads with non-zero deposited energies in the towers. With increasing the threshold on the number of pads in the towers the number of found towers is decreasing. The number chosen in the algorithm used is shown with bold dotted yellow line in the middle.

To find electron showers on top of the beamstrahlung pairs, the 10 last consecutive bunch crossings are taken into account. The mean and the RMS values for each individual pad were calculated and subtracted from 11^{th} bunch crossing which contains a superimposed high energy electron shower. Then the cluster reconstruction algorithm was applied to find clusters.

7.3.1 Fake Rate

The beamstrahlung depositions from a bunch crossing simulation for nominal beam parameters and SB2009 were shown in figures 7.3(a) and 7.3(b). Fluctuations of the background can be recognized by the cluster finding algorithm as a shower. These events are called **fake electrons**. The number of found fake electrons normalized to the total number of generated bunch crossings without high energy electrons is called **fake rate**.

By applying the clustering algorithm to samples of pure background events the fake rate was determined. As the beamstrahlung pairs have higher density in the central region of the BeamCal the most fake showers were found at the inner BeamCal radius. Figure 7.6 shows the fake rate as a function of the energy of the clusters found. The fake rate was shown to be less then 1.5% even for very low cluster energy.

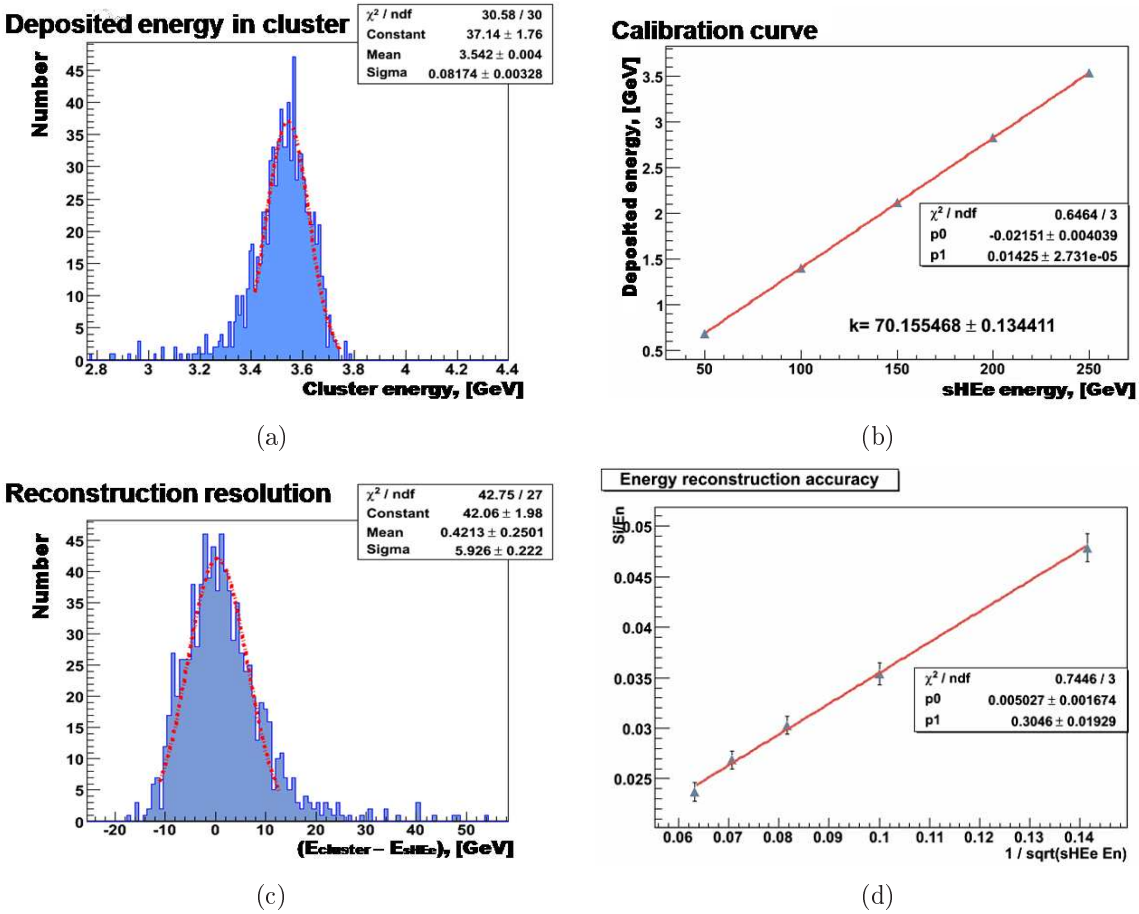

Figure 7.7: (a) The deposited energy in the BeamCal sensors from a 250 GeV electron shower. (b) The deposited energy in the BeamCal from electron showers as a function of the electron energy. (c) An example spectrum of the difference between the reconstructed energy of the electron from the found cluster and the initial energy of electrons of 250 GeV. (d) The energy resolution of the BeamCal as a function of the square root of the energy of initial electrons.

7.3.2 Calorimeter Response and Energy Resolution

Electrons of different energies are traced to the calorimeter and the shower is simulated. The deposited energy in each pad is used to reconstruct the total energy of the shower. Figure 7.7(a) shows an example of the recorded energy in the pads from showers of 250 GeV electrons. The mean value of the Gaussian fit is plotted as a function of the initial electron energy in figure 7.7(b).

The relative energy resolution of a calorimeter, σ_E/E, can be parametrized as [102]:

$$\frac{\sigma_E}{E} = \frac{p_0}{\sqrt{E}} \oplus \frac{p_1}{E} \oplus \ p_2, \tag{7.1}$$

where the right side is the square root of the quadratic sum of the tree terms. The stochastic term $p_0/\sqrt{E}$ represents the statistical fluctuations in the shower development. The second term p_1/E includes effects from the instrumentation of the calorimeter like electronics noise

and pedestal fluctuation. The third term p_2 appears due to systematic effects like detector non-uniformity or calibration uncertainty.

Below the first term of the equation 7.1 is explained and calculated for the BeamCal. If there is no leakage of the showers in the calorimeter the obtained energy resolution is called intrinsic energy resolution of the sampling calorimeter. The energy measured by a sampling calorimeter in the active layers of the calorimeter, called visible energy, E_{vis}, is a small fraction of the total deposited energy of the shower, E. The visible energy is proportional to the total energy E. The intrinsic energy resolution is defined by fluctuations of the visible energy:

$$\frac{\sigma_E}{E} = \frac{\sigma_{E_{\mathrm{vis}}}}{E_{\mathrm{vis}}}.$$

In addition, the visible energy is proportional to the mean energy loss $\overline{E_{\mathrm{loss}}}$ of shower particles (electrons and positrons) in the active layers:

$$E_{\mathrm{vis}} = \overline{N_{\mathrm{act}}}\,\overline{E_{\mathrm{loss}}},$$

where $\overline{N_{\mathrm{act}}}$ is the average number of shower particles passing through the active layers. Fluctuations of the visible energy are dominated by fluctuations in the number of particles in a shower, N_{act}, and the intrinsic energy resolution can be described as:

$$\frac{\sigma_{E_{\mathrm{vis}}}}{E_{\mathrm{vis}}} \approx \frac{\sigma_{N_{\mathrm{act}}}}{N_{\mathrm{act}}}.$$

The number of shower particles follow a Poisson distribution. However, since $N_{\mathrm{act}} >> 1$, the distribution is becoming similar to the Gaussian distribution and the following expression appears:

$$\frac{\sigma_{N_{\mathrm{act}}}}{N_{\mathrm{act}}} \approx \frac{1}{\sqrt{N_{\mathrm{act}}}} \propto \sqrt{\frac{\tau}{E}},$$

where τ is the calorimeter sampling frequency. Then the calorimeter intrinsic energy resolution can be expressed as:

$$\frac{\sigma_E}{E} = \frac{p_0}{\sqrt{E}}.$$

Figure 7.7(b) shows the linear dependence between the deposited and primary energy for single high energy electron. The data points are fitted and the parameters of the fit are used for the reconstruction of the primary electron energy from the cluster energy. An example spectrum of the difference between the reconstructed energy of the electron from the cluster and the initial energy of electrons of 250 GeV energy is shown in figure 7.7(c). The distributions are fitted with a Gaussian. The standard deviation of the Gaussian is plotted in figure 7.7(d) as a function of $1/\sqrt{E_{\mathrm{shower}}}$. As expected a linear dependence is found.

The showers were reconstructed without background. The intrinsic resolution is parameterized to be

$$\frac{\sigma_E}{E} = \frac{(30 \pm 2)\%}{\sqrt{E}},$$

where the energy E is expressed in GeV.

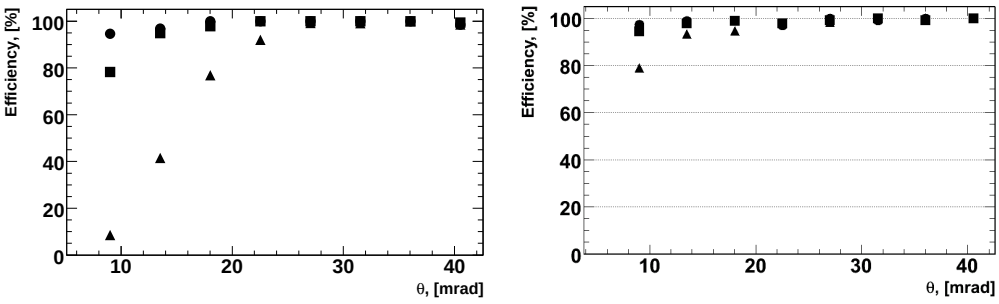

(a) (b)

Figure 7.8: (a) The electron reconstruction efficiency in the presence of pair depositions for the BeamCal segmentation with equal pads as a function of the polar angle. The energies of the initial electrons are 50 GeV (triangle), 150 GeV (square) and 250 GeV (dots). (b) The electron shower reconstruction efficiency on top of the background for the BeamCal segmentation with radially increasing pads size. The energy of the initial electrons are 100 GeV (triangle), 150 GeV (square) and 250 GeV (dots). All beamstrahlung background were simulated with the nominal RDR beam parameter set at a cms energy of 500 GeV.

7.3.3 Electron Reconstruction Efficiency

To define how efficient the cluster finding algorithm finds electron showers on top of the pair background the parameter ε is introduced as the ratio between the number of reconstructed to the number of generated electrons

$$\varepsilon = \frac{N_{reconstructed}}{N_{generated}}.$$

In figure 7.8(a) the reconstruction efficiency for electrons with energies of 50, 150, 250 GeV is shown as a function of the polar angle for the segmentation with equal pads, and in figure 7.8(b) for the segmentation with radially increasing pad size. The efficiency at small polar angles is lower in both cases due to high beamstrahlung background fluctuations. At larger polar angles the efficiency approaches 100%. Near the maximum polar angle it is slightly reduced due to leakage of part of the showers. Reducing the pad sizes in the central region of the BeamCal leads to an increase of the shower finding efficiency as shown in figure 7.8(b). For example, electrons with energy of 150 GeV are reconstructed at the inner radii with 20% larger efficiency.

7.3.4 Expected Doses

The BeCas simulation program was used to simulate beamstrahlung pairs and calculate the dose in the sensors of BeamCal using the deposited energy in each pad. The dose was obtained by the following equation:

$$Dose = \frac{E_{\mathrm{Dep}} Dose_{\mathrm{Scale}}}{V_{\mathrm{pad}} D_{\mathrm{pad}}},$$

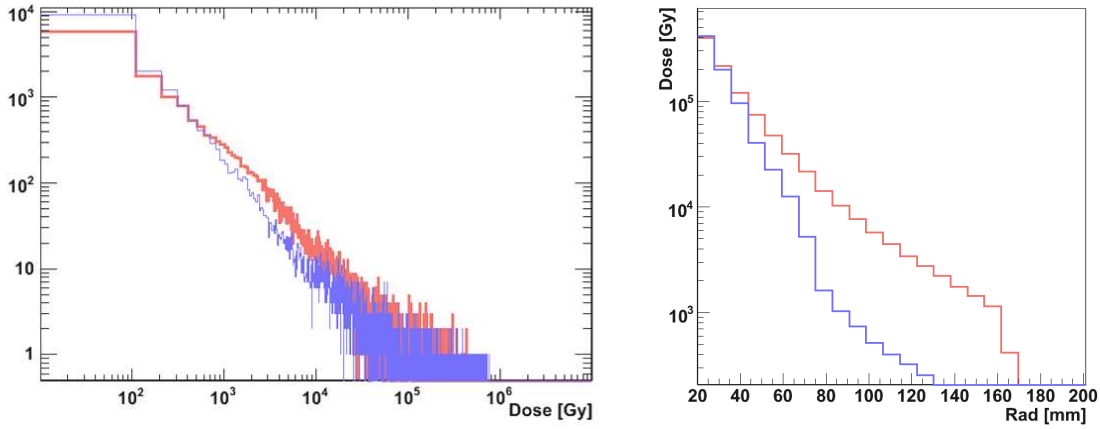

(a) h (b)

Figure 7.9: (a) Dose spectrum in BeamCal at 6^{th} layer for SB2009 (red) and nominal (blue) parameter sets. (b) Dose as a function of BeamCal radius for SB2009 (red) and Nominal beam parameters (blue) at 500GeV at center mass energy.

where $Dose_{\text{Scale}}$ is a factor equal to the number of bunch crossings per year for each beam parameter set, V_{pad} the pad volume and D_{pad} the mass density of the sensor. In figure 7.9(a) the dose obtained for each pad is distributed. The maximal dose per pad is nearly 1 MGy per year. The highest doses are in the 6-th layer at small radii. Due to the lower number of bunch-crossings in the SB2009 beam parameters set the obtained doses are similar to the one obtained with nominal beam parameters.

In figure 7.9(b) doses calculated for each radius of the 6^{th} layer are shown for the two beam parameters sets. At larger radii higher doses are obtained for SB2009 beam parameters.

Chapter 8

Test Beams Studies for Sensor Plane Prototypes

Introduction

The purpose of the beam test was to measure the performance of fully assembled sensor planes. The electron beam of the DESY II accelerator was used. Three test beam campaigns were organized in the years 2010-2011. In the first campaign the readout chain contained sensor, fan-out, FE ASICs and a stand alone ADC. The second and the third test beams included FE ADC ASICs in the readout chain. In the following chapter the test beam setup and the preparation for the test beam are described.

8.1 Test Beam

8.1.1 The DESY Beam Test Facility

DESY II is an electron synchrotron. It accelerates in sinusoidal mode with a frequency of 12.5 Hz. One DESY II magnet cycle takes 80 ms. The revolution frequency is 1 MHz, the RF frequency 500 MHz, and the bunch length around 30 ps.

The DESY II test beam infrastructure provides electrons or positrons. In figure 8.1 is shown the schematic layout of a test beam. Firstly, a bremstrahlung beam is generated by a carbon fiber inserted in the circulating electron beam. Using metal plates (converter in the figure), the beamstrahlung photons are converted to e^- e^+ pairs. Converters can have different thicknesses and consist of different metals. For the selection of a certain energy, a system of dipole magnets is used. The beam is spread out into a horizontal fan. Collimators in the fan cut out the final beam [103]. The magnet is used to control the energy of the beam. Electron energies from 1 to 6 GeV are provided. In this range the electrons have an energy loss similar to minimal ionising particles (MIPs). In the 2010 campaign a beam of 4.5 GeV was used and in 2011 beams of 2 and 4 GeV.

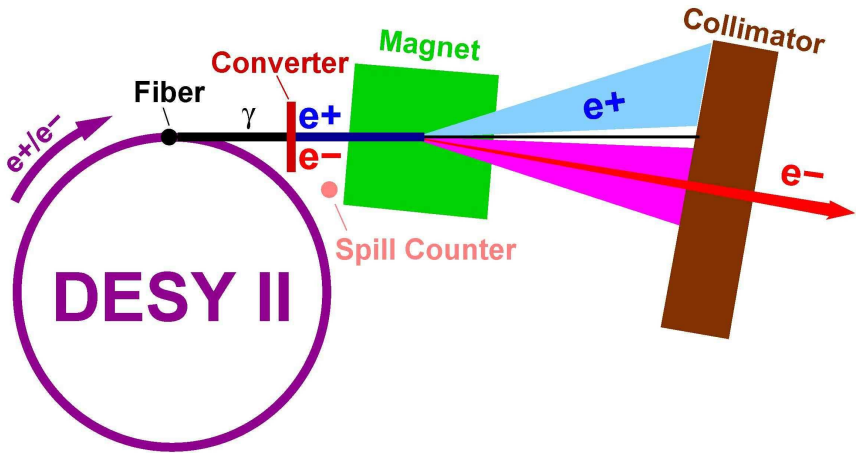

Figure 8.1: Schematic Layout of a Test Beam at the DESY facility DESY II [104]

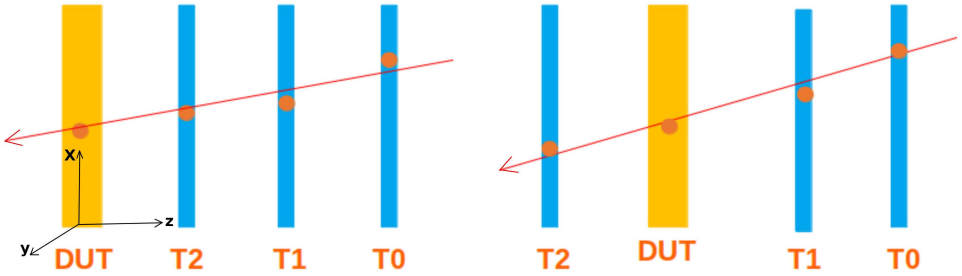

Figure 8.2: A sketch of the test beam setup. Particle trajectories are defined by linear approximation using telescope plane signals. The impact point in DUT is reconstructed, left using the three telescope planes in front of the DUT and right telescope planes in front and behind the DUT.

8.1.2 The Beam Telescope

The DESY II test beam area was equipped with a beam telescope which provides tracking for beam particles [105]. The beam telescope, build previously for the ZEUS micro vertex detector, MVD, beam tests, consists of 3 modules. Each module comprises two 300 μm thick single-sided silicon sensors of 32 by 32 mm area with a strip pitch of 25 μm. The read out pitch is 50 μm. The sensors are turned by 90° to have strips in X and Y directions. For each silicon strip sensor 640 strips are read out. The signal to noise ratio for all strips is between $80 < S/N < 130$. Each of telescope planes provides for each hit transverse coordinates x and y and a z coordinate. The spatial resolution of each plane, reported by ZEUS, was 25 μm [106]. Reconstruction of tracks is made after alignment of three telescope planes by linear approximation as shown in figure 8.2. A sketch of the setup, a photo and a drawing with the dimensions between telescope planes are shown in figures 8.2, 8.3(a) and 8.3(b).

The telescope planes can be moved in Z directions on a mechanical bench. Two detectors under test, DUT, locations were used, one with the DUT installed in between telescope planes and one behind all telescope planes. Data are taken in 2010 and 2011 with telescope planes in locations, optimized for different studies.

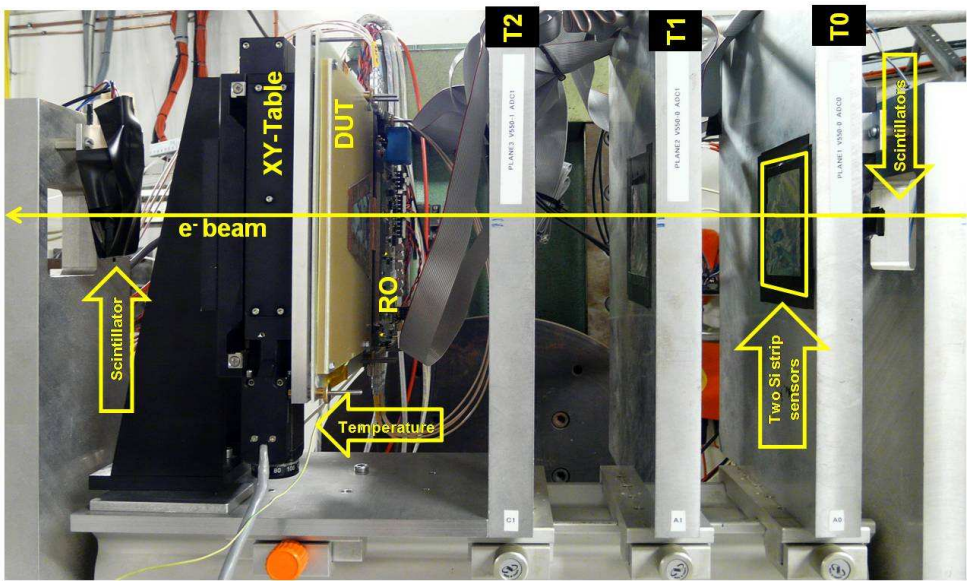

(a)

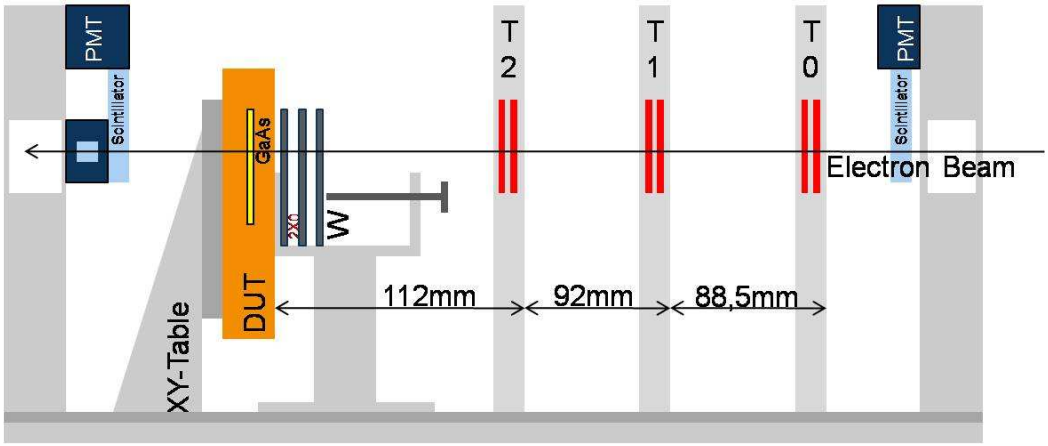

(b)

Figure 8.3: (a) - Test Beam Setup Photo with explanations. (b) - Test Beam Setup Drawing with the telescope plane locations in 2011.

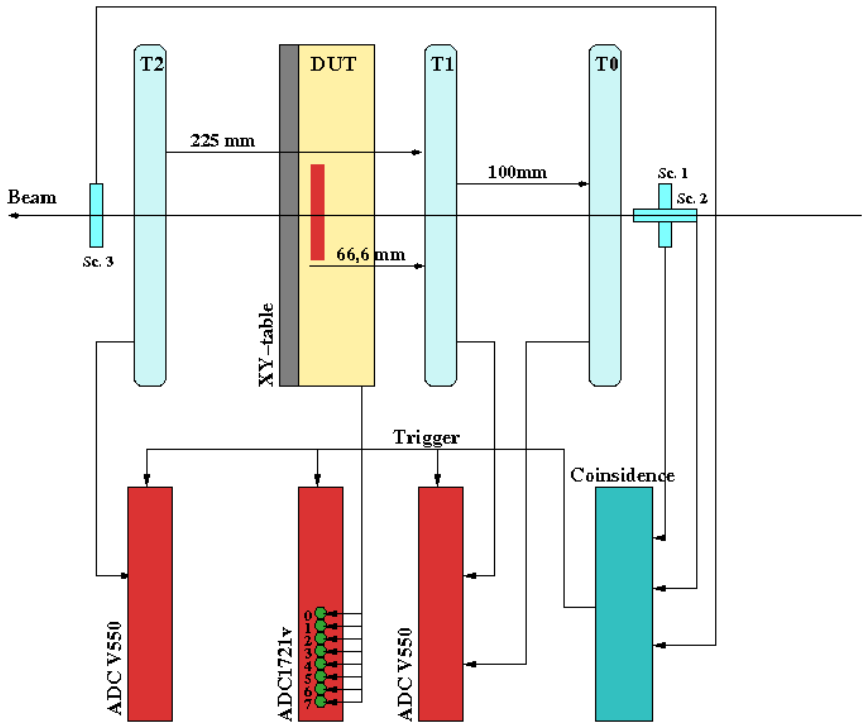

Figure 8.4: The test beam setup readout with telescope plane locations in 2010.

In figure 8.4 the test beam layout is shown including 3 telescope planes, DUT, 3 scintillators and read-out ADC modules. There are 3 finger scintillators of 7 mm width, two of them are located in front of the telescope and are perpendicular to each other. The trigger for the read out of the telescope and the DUT is obtained using the scintillator signals. The sensor box containing the sensor plane was mounted on a XY-table. It allows remotely moving the DUT in the beam. The distances between the telescope planes and the DUT are measured between the front edge of each plane.

8.1.3 The Prototype

The prototype of a sensor plane consists of a GaAs:Cr sensor, as described in chapter 1, attached to a fan-out and connected to a PCB comprising the FE ASICs and auxiliary electronics. Photos of the boards as used in 2010 and 2011 are shown in figure 8.5 and 8.6, respectively.

Four FE ASICs with 8 preamplifiers each were connected to sensor pads. In 2010 the amplified signals were fed into a standalone ADC (CAEN v1721). Two regions of 8 pads each were read out. In 2011 the read out chain was completed with four 8-channel 10-bit ADC ASICs, an field programmable gate array, FPGA, (Xilinx Spartan3), a microcontroller (Amtel AVR ATXMEGA128), memory cards, a temperature monitor and voltage regulation. Details on the electronics board are given in Ref. [107].

Two GaAs:Cr sensor types were investigated in the test beams. The sensors were glued to fan-outs, as shown in figure 8.7(a). The fan-out used in 2011 was instrumented with resistors and capacitances to provide AC coupled signals from the pads to the ASIC inputs. The fan-out itself was screwed to an additional PCB carriage with a window corresponding

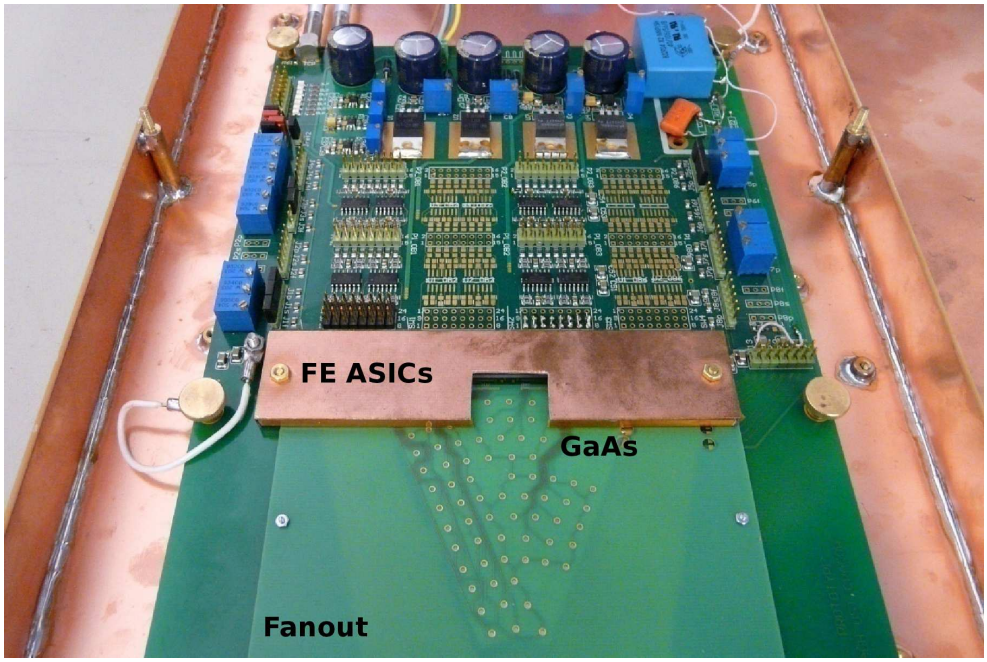

Figure 8.5: The assembled sensor plane used in 2010 test beam studies. GaAs denotes the GaAs sensor, placed below the fan-out. The pads are bonded to the readout traces through the holes.

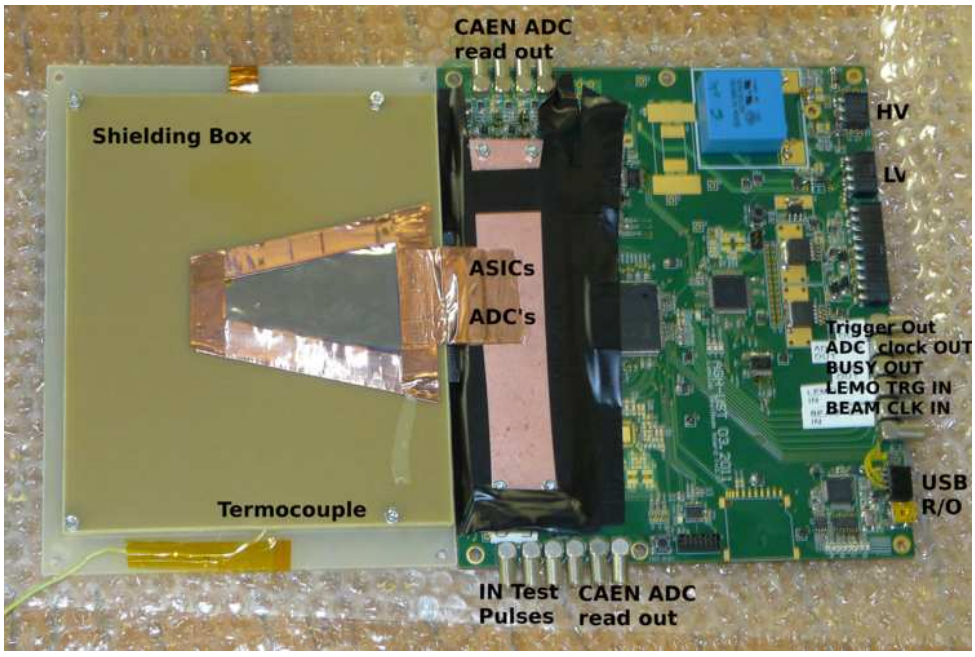

Figure 8.6: The assembled sensor plane used in 2011 test beam studies. GaAs sensor is located in the shielding box. On the top and bottom there are 8 connectors to read out FE ASICs by CAEN ADC in parallel to ADC ASIC.

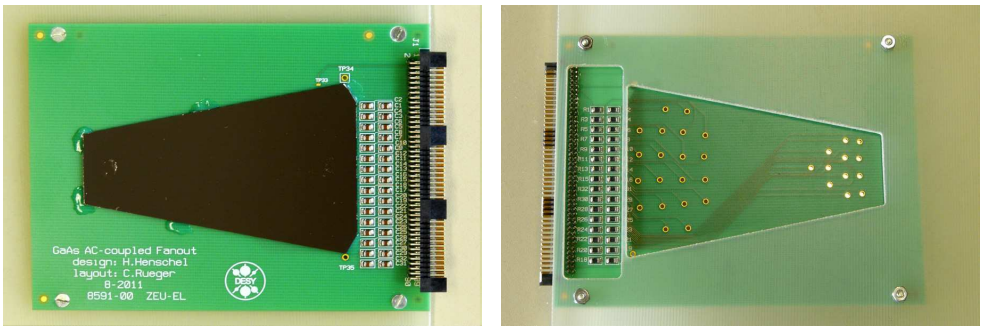

(a) (b)

Figure 8.7: (a) The sensor glued on the fan-out bottom side. (b) Fan-out screwed to the PCB carriage with bonded sensor pads, top side.

to the sensor shape as shown in figure 8.7(b). Fan-out traces at one end were bonded to a connector to the read-out electronics board and at the other end to the pads through small holes seen in figure 8.7(b). High voltage was applied to the fully metalized side of the sensor as shown in figure 8.7(a). In the end the fully assembled prototypes were put into a shielding box as shown in figure 8.6. The operation bias voltage was set to 60 V in 2010 and up to 200 V in 2011.

The 8 channels readout in addition by an external ADC in 2011 are labeled "CAEN ADC read out" in figure 8.6. The first 4 channels of the CAEN ADC are connected to the bottom ASIC and the other 4 channels to the top ASIC. Inside ASICs each second channel was chosen to be read out simultaneously by two ADCs.

Figure 8.8 shows the pads which were irradiated in the test beam in 2011. The purple circles indicate the pads, which are in addition readout by an external ADC.

8.1.4 Measurement Plan

The goal for the test beam was to measure the performance of a GaAs:Cr sensor plane with different segmentations as explained in chapter 2. The full chain of sensor, fan-out, FE ASICs and ADC ASICs was intensively tested. All together 32 pads of the sensor were connected to the ASICs and simultaneously read out. An FPGA was used for the communication between the ADCs and the computer. In addition, for 8 out of 32 channels, the analog signal was fed into an external ADC. The measurements aimed to obtain the following characterizations:

- stability for all investigated channels,
- the signal-to-noise ratio,
- different modes of preamplifier and shaper settings [108],
- baseline stability,
- uniformity of the sensor response and edge effects,
- signal amplitude dependence on the bias voltage,

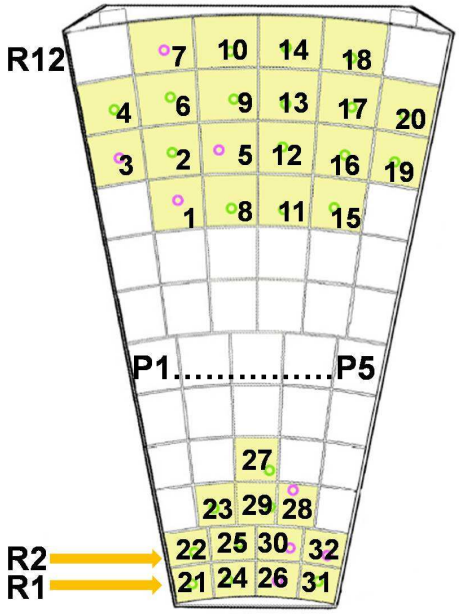

Figure 8.8: The 32 channels irradiated in the test beam 2011.

- ability of multiple particle detection.

8.1.5 Calibration

For a given readout chain the maximum of a signal is proportional to the charge created in the pad. Signals readout from the ADC are expressed in ADC counts. In order to convert the amplitude maximum to the charge, a calibration coefficient, k_{Cal}, has to be determined:

$$k_{\mathrm{Cal}} = \frac{Q}{S_{\mathrm{ADC}}},$$

where S_{ADC} is the amplitude maximum measured in ADC counts and Q is a known injected charge.

To calibrate the readout chain the known charge is created via a capacitance at the input of the FE ASICs. Capacitors of 0.5 pF were used in the first channels and 0.23 pF in the second four channels in 2010. In 2011 test capacitances of 0.5 pF were in addition implemented in the readout board. A rectangular pulse with an amplitude of 1 V is applied to the capacitors, C, via an attenuator. The injected charge is calculated using

$$Q = CV.$$

Test pulses can be applied simultaneously either to odd or even channels and readout by the full chain. An example of the calibration for channel 0 of the first chip is shown in figure 8.9. Pulses of different amplitude were fed into the front-end electronics and the response signal size was measured with a stand alone ADC. Four different measurements were performed for each combination of the FE ASIC gain settings.

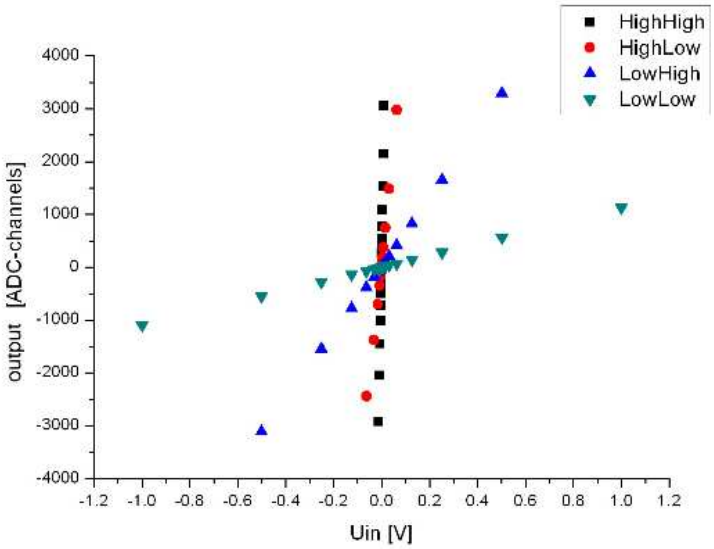

Figure 8.9: Results of the calibration measurement for channel 0 of chip 1 [23]. Test pulses of different amplitude, U_{in}, are compared to the output signal size measured in ADC counts. Different settings of the preamplifier and shaper amplifications are used.

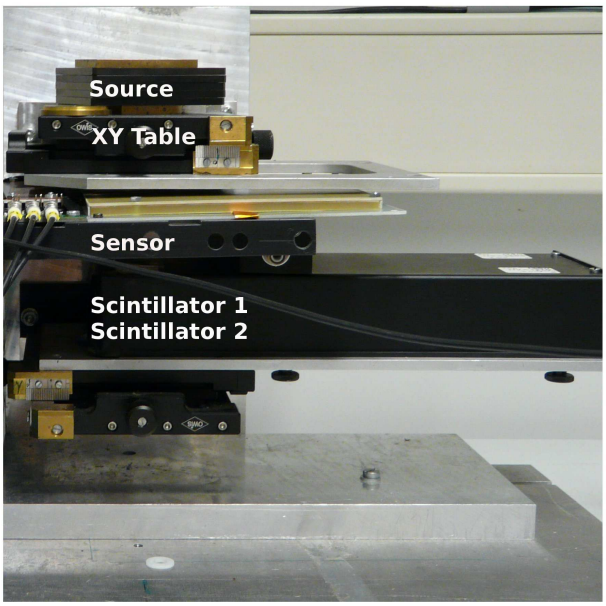

Figure 8.10: ^{90}Sr setup with a GaAs:Cr sensor plane under test.

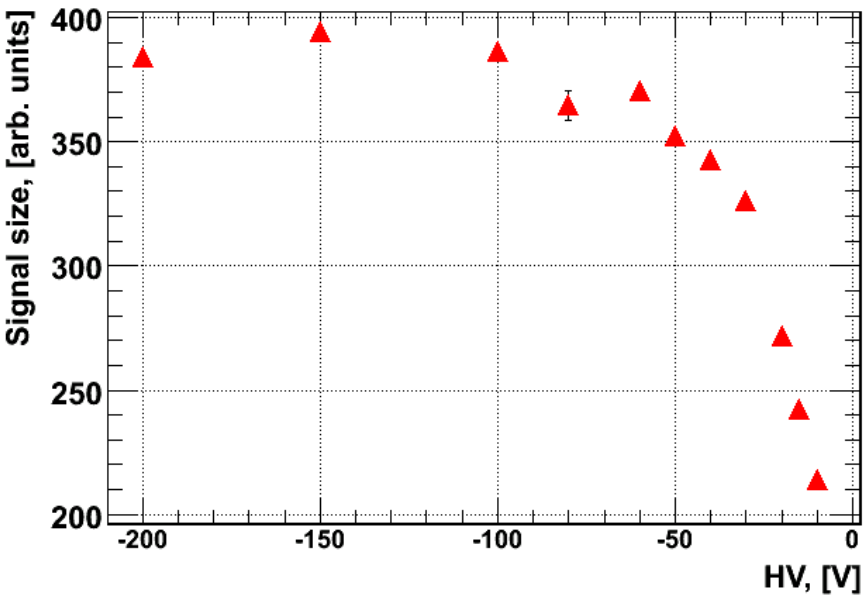

Figure 8.11: The size of the integrated signal as a function of the bias voltage.

8.1.6 Laboratory Setup

The fully assembled sensor plane was firstly investigated with a ^{90}Sr source. Figure 8.10 shows the setup with a ^{90}Sr source on top, a XY-table to move the prototype with respect to the source in the middle, and a trigger box at the bottom. The trigger box contains two scintillators with photomultipliers attached. A coincidence from two scintillator signals is required to generate a trigger to readout the sensor plane. The trigger selects electrons with sufficient energy crossing the sensor and two scintillators. The functionality of all channels was tested before the installation of the sensor plane in the test beam.

The size of the signal from an electron depends on the voltage applied to the sensor, as seen in figure 8.11. It is growing fast by up to 60 V and saturates at about 100 V. The result is in agreement with the measurement, described in the section 1.4. The bias voltage used at the test beam was 60 V.

8.2 Simulation of the Deposited Energy in GaAs

To estimate the deposited energy of relativistic particles in the sensor, simulations using GEANT were done. Two kinds of electron beams were generated. Firstly, a beam with the energy spectrum of a ^{90}Sr source, and secondly mono-energetic electron beams of 2, 4 and 4.5 GeV. The simulation was done for a GaAs sensor of 500 μm thickness. The values of the deposited energy for each particle are distributed as shown in figures 8.12(a), 8.12(b), 8.12(c) and 8.12(d) as red lines. The black lines are a fit with the Landau distribution. The most probable value of the fits are summarized in the Table 8.1. Divided by the averaged energy for the creation of an electron-hole pair of 4.3 eV, the expected number of the e-h pairs is obtained.

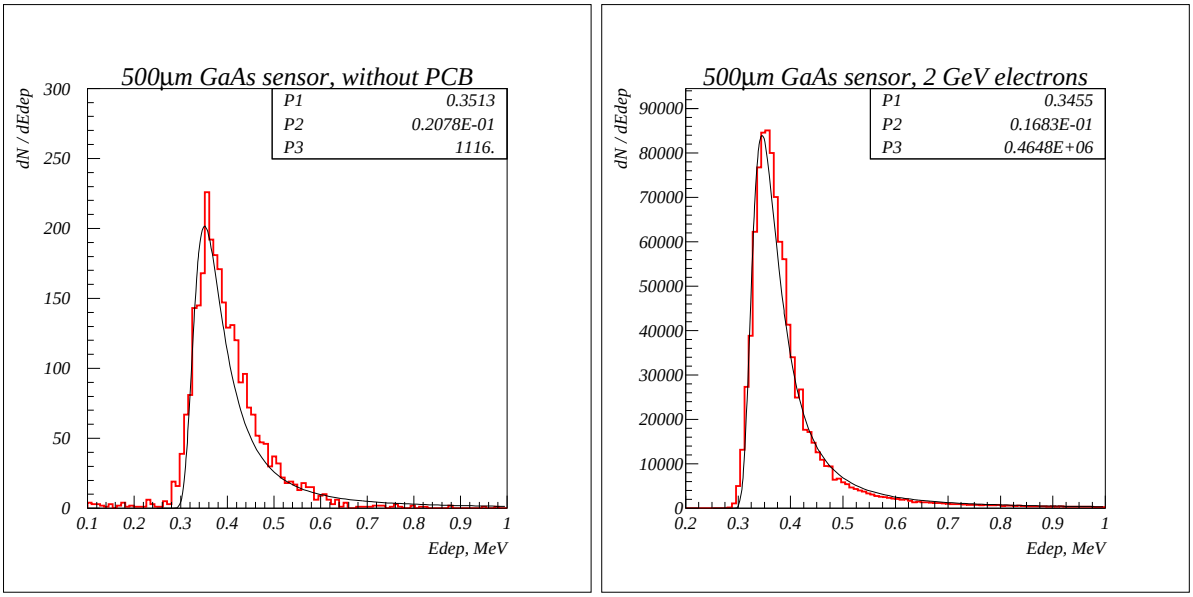

(a)

(b)

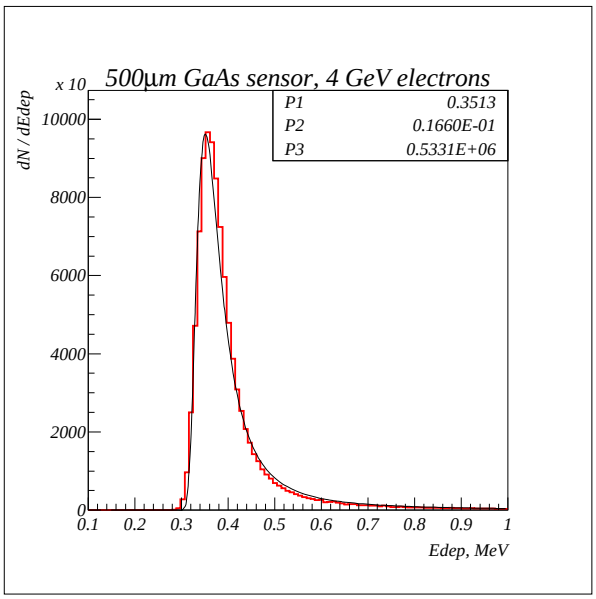

(c)

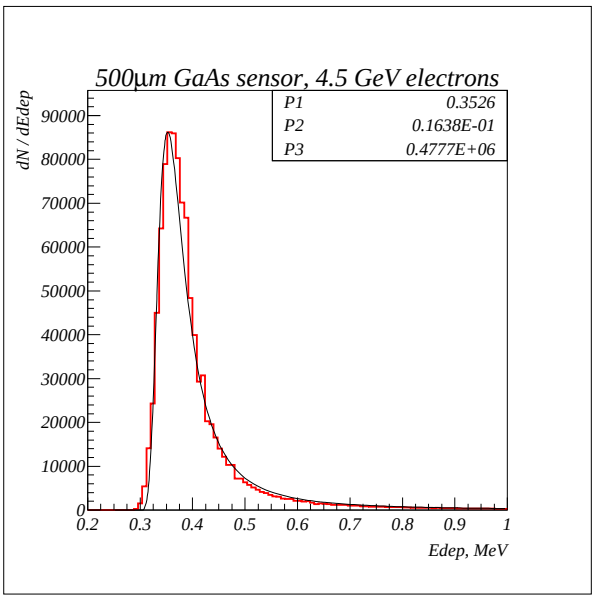

(d)

Figure 8.12: (a) Deposited energy in a 500 μm GaAs sensor by a ^{90}Sr source and triggered by two scintillators. (b) Deposited energy in 500 μm GaAs sensor glued on 500 μm PCB by 2 GeV electrons and triggered by tree scintillators. (c) Deposited energy in 500 μm GaAs sensor glued on 500 μm PCB by 4.0 GeV electrons and triggered by tree scintillators. (d) Deposited energy in 500 μm GaAs sensor glued on 500 μm PCB by 4.5 GeV electrons and triggered by tree scintillators.

Setup	Dep. En.	e-h pairs per μm
^{90}Sr	0.3512 MeV	163,4
2 GeV	0.3455 MeV	160,7
4 GeV	0.3513 MeV	163,4
4.5 GeV	0.3526 MeV	164,0

Table 8.1: The expected number of e-h pairs created by a relativistic particles passing through a 500 μm thick GaAs sensor.

Chapter 9

Data Analysis

In the following chapter the analysis of the test beam data is presented and the performance of the two assembled GaAs:Cr sensor planes is evaluated.

9.1 Definitions

All measurements at test beams were done with sampling ADCs. For each trigger an event length was set defining the time window for the ADC readout. The time window is divided in two sub-windows, as shown in figure 9.1(a). The first is used for the baseline and pedestal calculations and the second for the signal analysis. **The Baseline** is defined as the average of the ADC values in the first time window:

$$BL = \frac{\sum s_i}{N},$$

where i is the sample number, s_i is the content of the i-th ADC bin and N is the number of summed samples.

The Pedestal is defined as the average value of samples or the integral over several samples in a time window not containing signals

$$ped =< s_i >.$$

The Noise is the random variation of the samples not containing a signal. The standard deviation of this variation is the noise. It is calculated by the formula:

$$\sigma = \sqrt{\frac{1}{N}\sum_{i=1}^{N}(s_i - ped)^2}.$$

Common Mode Noise, CMN, is a synchronous variation of the baseline in several channels. The CMN is calculated for individual chips. For the samples values, s_i, the CMN, v_i^{CMN}, is defined as:

$$v_i^{CMN} = \frac{1}{N}\sum_{j=1}^{N}(s_i^j - ped^j),$$

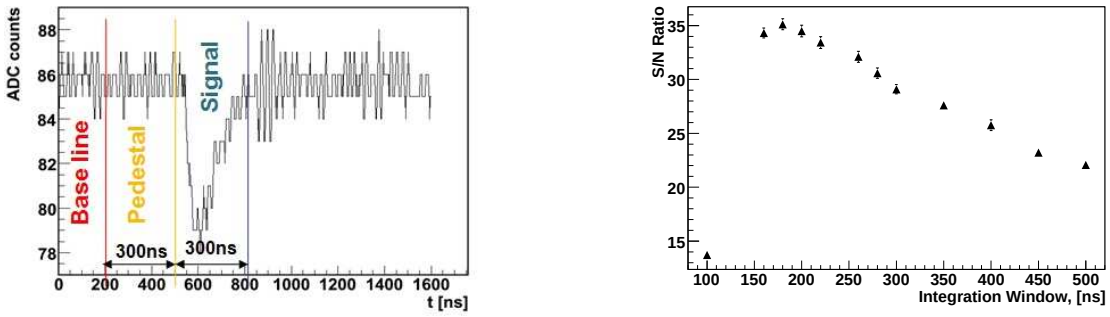

(a) (b)

Figure 9.1: (a) Signal example with pedestal, baseline and signal time windows. (b) The signal-to-noise ratio for different integration time windows for the signal.

where j is the channel number, running over all channels of the chip and ped^j is the pedestal value calculated for each channel independently.

The Common Mode Noise Subtraction is performed by calculating firstly the CMN and subtracting it from each sample i for a channel under investigation.

$$v_i^{CMNS} = s_i - v_i^{CMN}$$

The **Signal Amplitude** is the difference between the sample with the maximum value in the signal window and the baseline.

The **Signal Integral** is the integral over a signal in a certain time window.

The **Signal-to-Noise Ratio, S/N,** is the ratio between the most probable value of the signal amplitude or integral signal distributions and the noise,

$$S/N = \frac{MPV_{\mathrm{LG}}}{\sigma},$$

where MPV_{LG} is the most probable value of signal spectrum.

In the test beam for each trigger 8 or 32 channels were read out simultaneously in 2010 or 2011, respectively. This data is called an **event**. Data of a single channel is called **Sub-event**.

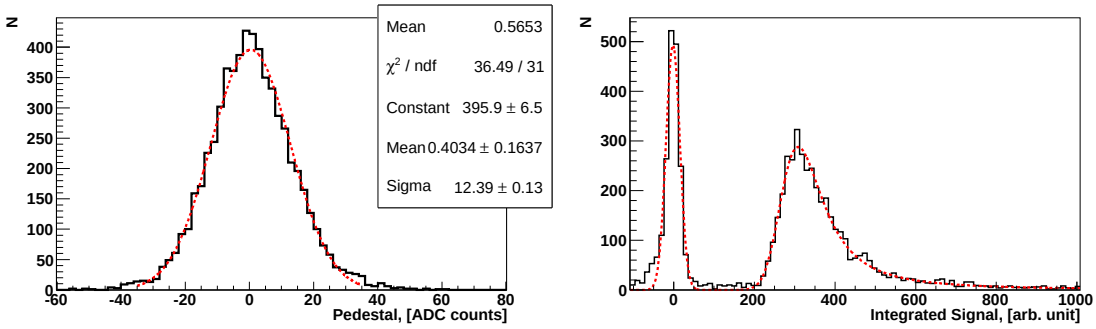

(a) (b)

Figure 9.2: Signal and noise spectra examples for test beam data taken in 2010.

9.2 Test Beam 2010

9.2.1 Data Analysis

An example of a signal in the external ADC is shown in figure 9.1(a). The trigger to read out of the ADC arrives 500 ns before the signal. The maximum amplitude of the signal is around 600 ns (300 samples). The full readout window was chosen to be 1600 ns.

The first 200 ns are used for the baseline calculation. The signal was calculated using the maximum amplitude or the integral over the signal time window. In figure 9.1(a) the integration window is chosen to be 300 ns. The length of the integration time windows is varied to obtain the maximum S/N. Figure 9.1(b) shows the signal to noise ratio as a function of the length of the time windows of the integration. The maximum of the S/N is at 180 ns.

An example of the pedestal distribution is shown in figure 9.2(a) and an example of the signal integral spectrum is shown in figure 9.2(b). The pedestal distributions were fitted with a Gaussian to obtain σ. The measured signal integral spectra are fitted with a convolution of a Landau distribution and a Gaussian to obtain MPV.

The stability of the signal integral and the noise over time were checked for 4 data sets for each channel. It it shown in figure 9.3(a) for the signal integral and for the noise in figure 9.3(b). Each group of 4 points corresponds to the measurement of one channel over 1 hour. The signals were found to be stable within few percent. Each point in figure 9.3(b) is the standard deviation of the distribution like in figure 9.2(a). The noise was found to be stable within 10 %. The final S/N is stable within 6 %.

9.2.2 Charge Collection Efficiency (CCE)

Charge Collection Efficiency, CCE, is the fraction of the released charge that is collected in the active volume of the detector when a charged particle crossed the detector. The related charge is obtained from the simulation of the setup as described in section 8.2. For the calculation of the CCE the integral signal is multiplied by the calibration factor as described in section 8.1.5. The CCE obtained is 42%, when the applied voltage is above 60 V. The CCE measurement is compatible with the measurement of GaAs:Cr sensors done in the laboratory using the ^{90}Sr source before irradiation as shown in section 1.4.

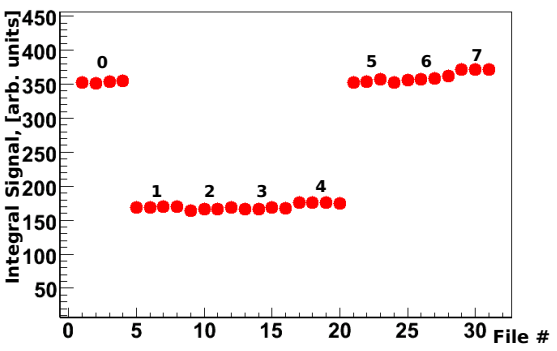

(a)

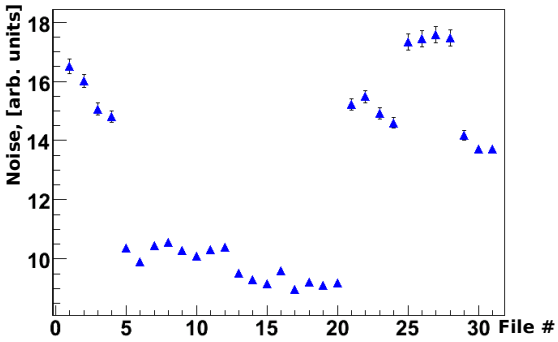

(b)

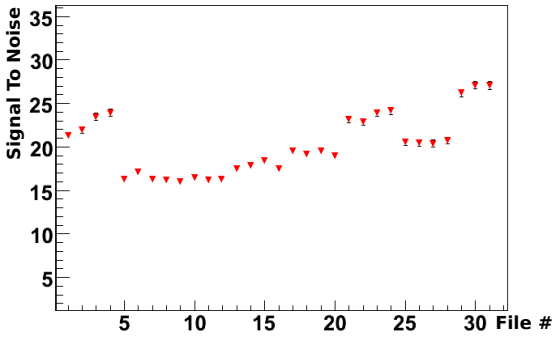

(c)

Figure 9.3: (a) Signal and (b) noise as a function of time for 8 channels, 4 set of measurements for each channel. (c) - S/N for 8 channels. The time between the first and the fourth measurement was 1 hour.

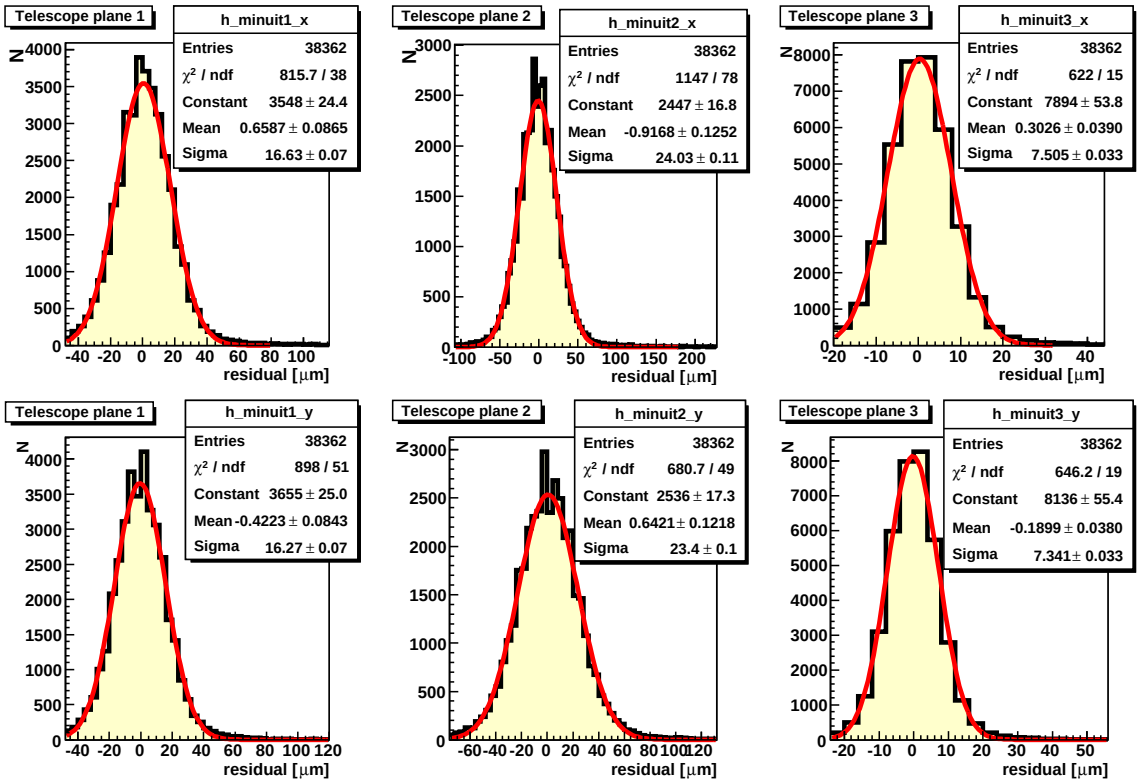

Figure 9.4: Residual distributions for all telescope planes after alignment.

9.2.3 Tracking with the Telescope

For the reconstruction of tracks in the telescope the program called "TelAna" was used [109]. Firstly, it calculates the hit position from the fired strips by the center of gravity method using the signals in the X and Y telescope planes. Assuming that horizontal and vertical telescope planes are independent, the track reconstruction can be done separately in X and Y directions. The tracks are obtained from linear interpolation between 3 points.

Then, the alignment was performed with the DUT installed between the telescope planes. The TelAna alignment was checked using the Millepede I program [110]. The difference between the coordinate measured and the predicted coordinates using the hits in other telescope planes is shown in figure 9.4 for all 6 telescope sensors. The mean values of the residual distributions deviate by less than 1 μm from zero. The position resolution was measured to be better than announced by ZEUS collaboration.

The position of the trajectory in the GaAs plane was reconstructed by linear interpolation using three telescope planes in X and Y independently. The hit positions predicted at the sensor as plotted in figure 9.5(a) have different colors. The different colors refer to events when the signal amplitude or integral is above a predefined threshold. The biggest pad was subdivided into smaller areas and signal amplitudes were distributed for each area separately. The most probable values of each area were shown to be stable within 2 %.

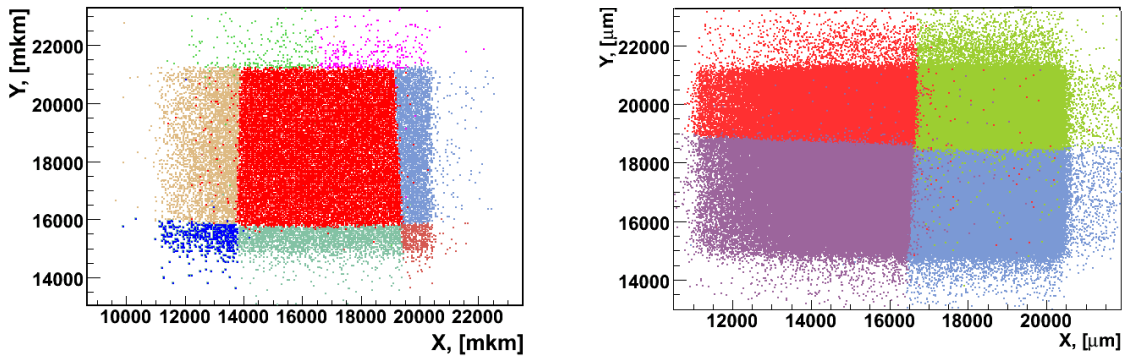

(a) (b)

Figure 9.5: (a) Pads structure of the GaAs sensor reconstructed from telescope data [111]. (b) The pads structure at the edge between 4 pads.

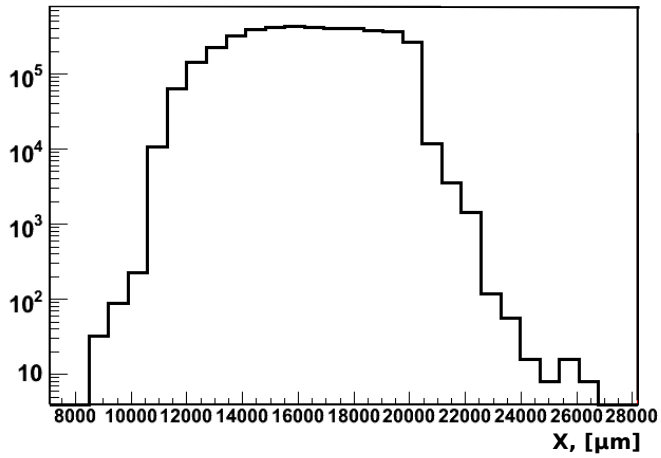

Figure 9.6: The beam profile in the X coordinate.

9.2.4 Beam Profile

The beam profile, a characteristic of the beam, was measured at the beginning of the test beam. Figure 9.6 shows the beam profile obtained from one of the telescope planes in X direction. The beam was not centered with respect to the telescope in X and Y directions. The size of the beam spot used was 7 mm in Y and 9 mm in X direction.

9.2.5 Edge Effects

The signal size was studied as a function of the hit position. The edge between pads as shown in figure 9.5(b) was subdivided in 50 μm stripes and signal spectra were done for each stripe. Each spectrum was fitted with the Landau distribution and the mean value as a function of the stripe position is shown in figure 9.7(a). Figure 9.7(b) shows the mean value of the summed signal of the two neighboring pads for each stripe. As one can see in the gap between two pads, the signal drops by 10%.

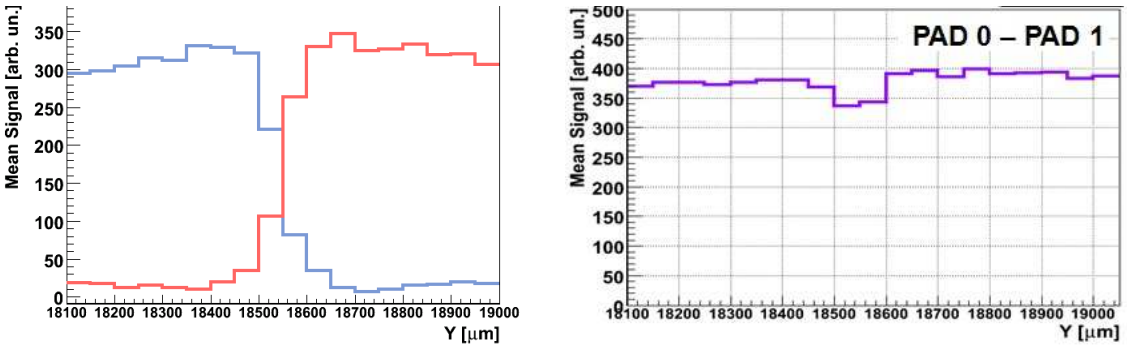

(a) (b)

Figure 9.7: (a) The signal integral mean value as a function of the hit position on the border between two pads. (b) The signal integral sum of two pads as a function of hit position on the border between two pads.

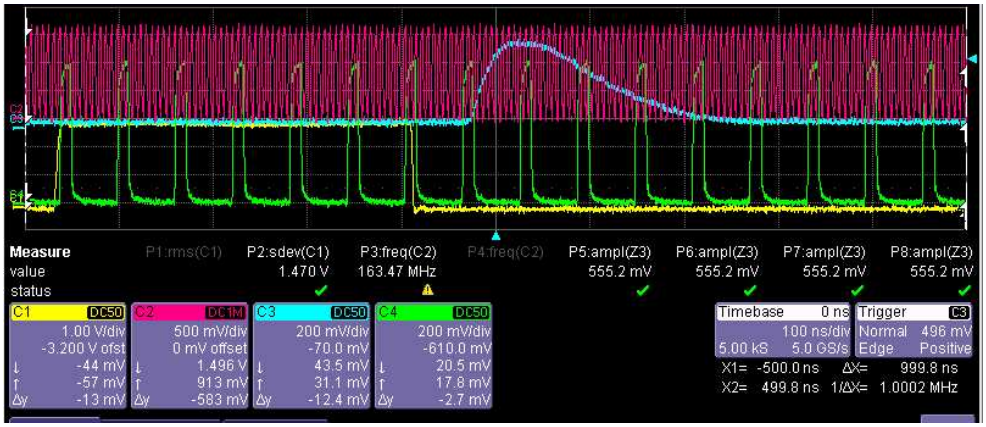

Figure 9.8: A screen-shot of the oscilloscope. In blue the output signal from the sensor plane, in green the sampling clock of the ADC ASIC, synchronized with the beam clock and yellow is the trigger signal from the scintillators.

9.3 Test Beam 2011

9.3.1 Synchronous and Asynchronous Readout

The ADC ASIC provides data digitized with using its internal clock of 50 ns. If it is not synchronized with the particle arrival time using the beam clock, then the digitization is performed with a random phase shift. In case of synchronization of the ADC clock with the beam clock, as it will be done at the ILC, the digitization occurs at a fixed time with respect to the signal arrival time. During the test beam the ADC ASICs were operated both in synchronized and non-synchronized modes. In the asynchronous mode the sensor signals are digitized with ADC clock independent from the beam clock. In the synchronized mode the first sampling appears at the time when the signal amplitude approaches the maximum. Figure 9.8 shows an example of synchronous read out. The blue line is the signal from the FE ASIC, the green line the 50 ns sampling of the ADC and the yellow line is a trigger from the scintillators.

9.3.2 Measured Signals and Analysis Technique

Signals from channels readout in addition with an external ADC are compared to the output of the ADC ASIC. The result is shown in figure 9.9. The shape of the digitized signals is, apart of the different sampling time, almost the same.

Amplitude and integral of signals were calculated with the same procedure like in the previous section. Examples of the distribution of the pedestals and a signal amplitude spectrum using the external ADC are shown in figure 9.10(a) and 9.10(b), respectively. The pedestal distribution is fitted with a Gaussian. The amplitude spectrum shows a sharp pedestal, a peak corresponding to the expectation for a MIP and a saturation peak due to limited dynamic range of the ADC. In figures 9.11(a), 9.11(b), 9.11(c) and 9.11(d) are shown the ADC ASIC amplitude spectra for "High High" and "High Low" amplification settings and for two different feed back technologies (channels 10 and 17 for MOS and 6 and 7 channels for R_f feed back). The beam is sent to the center of each irradiated pad and the triggered events are distributed over the beam spot size 7 by 9 mm. The events appearing between pedestal peak and MIP hit the sensor near the edges of the pad. The spectra are fitted with a Landau distribution convoluted with a Gaussian. The peak corresponding to the expectation of a relativistic particle is clearly visible for the "High High" and "High Low" read out mode. This will allow to study S/N and provides calibration of the sensors in the calorimeter in future.

9.3.3 Correlations

Figure 9.12(a) shows sample values in the baseline time window of ADC ASICs for two adjacent channels. The distribution shows a correlation between these values. To quantify the correlations between samples of different channels the following formula was used:

$$r_{xy} = \frac{\sum (x_i - \overline{x})(y_i - \overline{y})}{\sqrt{\sum (x_i - \overline{x})^2 \sum (y_i - \overline{y})^2}},$$

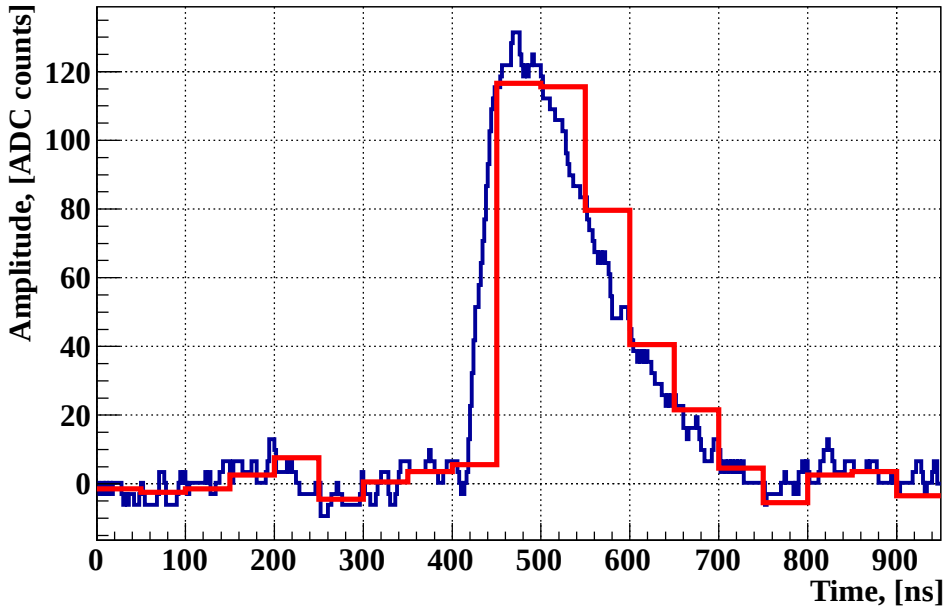

Figure 9.9: An example of the signal digitized by the external ADC (blue) and the ADC ASIC (red).

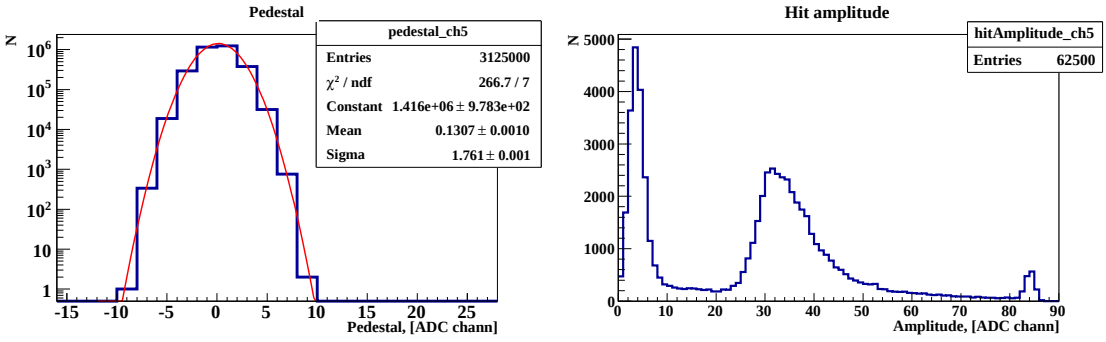

(a) (b)

Figure 9.10: (a) The pedestal distribution measured by an external ADC fitted by a Gaussian. (b) The signal amplitude spectrum using the external ADC.

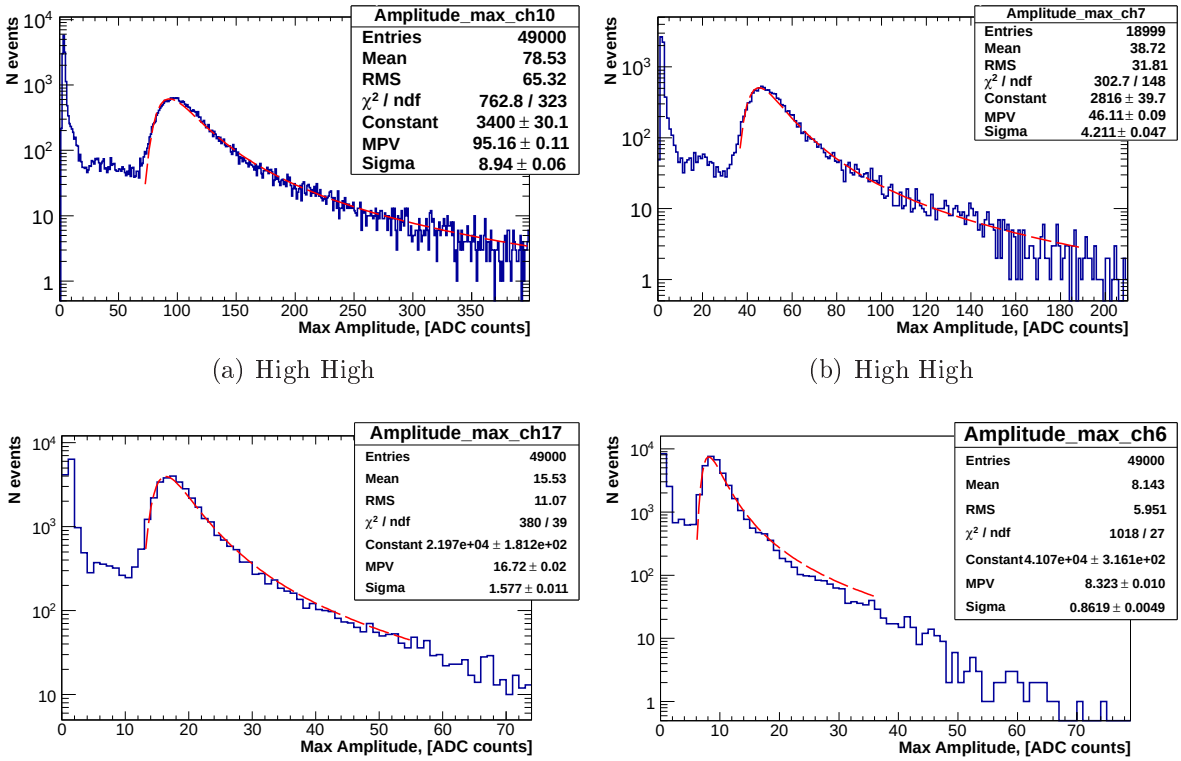

(a) High High (b) High High

(c) High Low (d) High Low

Figure 9.11: The amplitude spectra measured with ADC ASICs for "High High" and "High Low" amplification settings and for two different feed back technologies of the FE ASICs. In channels 10 and 17 MOS and 6 and 7 channels R_f feed back was used.

where x_i, y_i are the sample values from two compared channels at the same time and $\overline{x}$, $\overline{y}$ are their baseline values. Figure 9.12(b) shows the values of r_{xy} for x and y running over all 32 channels. Large correlation coefficients were found for groups of 8 channels belonging to four front-end and ADC ASICs. The large correlation coefficients point to common mode noise within the front-end ASIC chip. This conclusion is done on the basis of the signal analysis measured by a stand alone ADC. As the same correlations were observed.

Figure 9.13(a) shows the correlation between each channel and the averaged value of other 7 channel samples of each chip. This strong correlation shows a possibility for the calculation of the common mode noise as an average between several channels.

9.3.4 CMN Subtraction Procedure

To study how to subtract the common mode noise the following steps were done. The averaged ADC sample values of 7 channels were determined and the correlation coefficients with the 8^{th} channel under investigation were calculated. Figure 9.13(a) shows that there is a strong correlation between the sample values in the channel under investigation and the averaged value of the other seven channels sample values. The averaged values of seven out of eight channels sample values in the baseline time window are calculated going through all channels on a chip. These average values are subtracted from samples of the

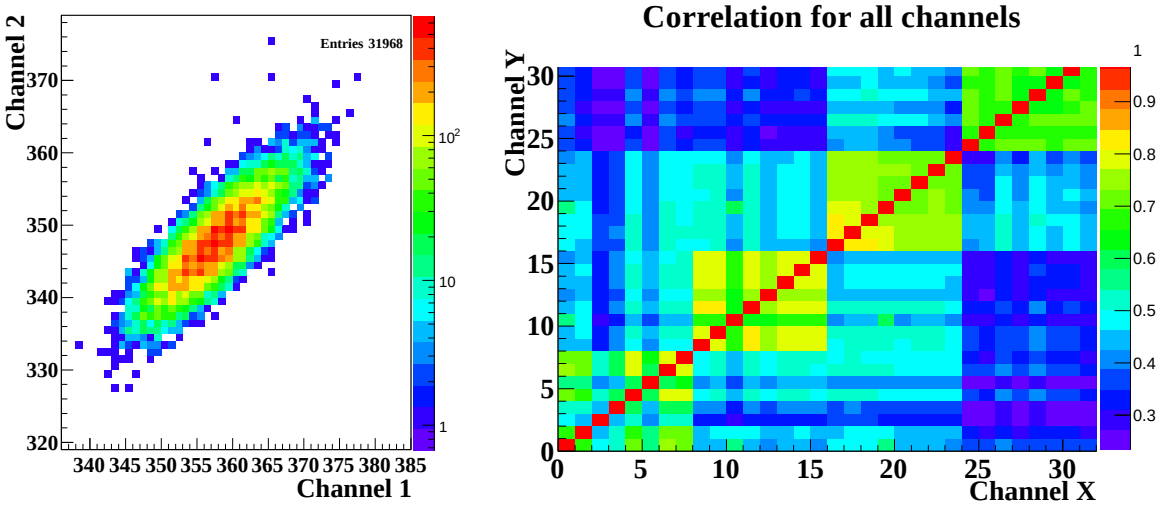

(a) (b)

Figure 9.12: (a) The scatter plot between channel 1 and 2 of ADC sample values in the baseline time window. (b) Correlation coefficients between the ADC sample values of 32 channels.

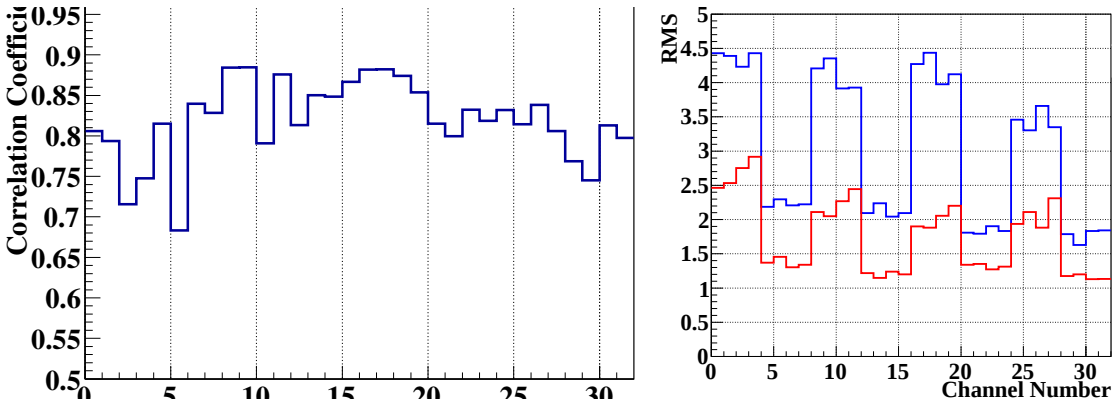

(a) (b)

Figure 9.13: (a) Correlation coefficients between the ADC sample values of one channel and the averaged sample values in the baseline time window of 7 other channels of each chip. (b) The comparison of the RMS of ADC sample value distributions. The blue line is obtained from the ADC sample values before the CMN subtraction, the red line is obtained after the subtraction of the mean value of the other 7 channels.

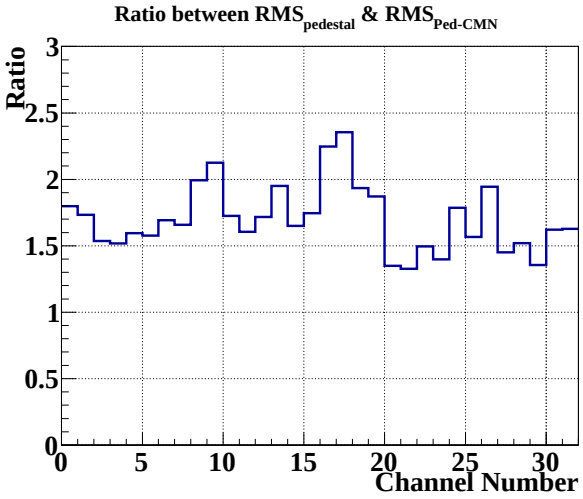

Figure 9.14: The ratio between one standard deviation of sample values distribution without and with common mode noise subtraction procedure.

channel under investigation. The new sample values are filled into a histogram and fitted with a Gaussian. The standard deviations are shown in figure 9.13(b) by the *red* line. For comparison, the *blue* line shows the standard deviation of the same samples before the subtraction. As can be seen, the noise in all channels is reduced by a factor of about two.

To account for common mode noise the following procedure is applied to the data:

- The baselines are determined for all channels. The baseline of each channel is subtracted from all samples of this channel.
- Identify the channel containing a signal above a certain threshold.
- From the remaining 7 channels in the same ASIC the averaged value for each sample is calculated.
- These values are subtracted from each sample of the channel with the signal.

Figure 9.14 shows the ratio between the standard deviations of sample value distributions without and with common mode noise subtraction. The noise was reduced in average by a factor of 1.8. The common mode noise subtraction was applied to all data analyses below.

9.3.5 S/N Measurements

As mentioned in section 6.7, there are several settings of the FE ASIC denoted as calibration and physics modes. Changing between modes was possible remotely and independently for shaper and preamplifier. The mode “Low Low” is supposed to be used for showers with high energy deposition in the calorimeter, the mode “High High” for the measurements of single relativistic particle for calibration and alignment. The modes “High Low” and “Low High” are implemented here for technical reasons.

Data with beam were taken for all 4 combinations of gains. For the two modes “High High” and “High Low” the MIP peak was visible and S/N calculations are presented in

table 9.1. The S/N results obtained using either signal amplitude or integral spectra are shown in figure 9.15(a). The amplitude method showed a higher S/N ratio than the integral method for all channels. With the amplitude method a S/N of more than 20 was obtained. The variation between channels is less than 16 %. Using the integral method the S/N is larger then 15 and the variation between channels is less than 15 %.

Gain Preamp. Gain Shap.	HH	HL	LH
MOS feedback ch 10	MPV = 93.7 ± 1.4	MPV = 16.68 ± 0.01	no MIP
	Ped = 4.13	Ped = 0.99	
	S/N = 22.7	S/N = 16.9	
MOS feedback ch 17	MPV = 94.7 ± 0.2	MPV = 16.72 ± 0.02	no MIP
	Ped = 4.4	Ped = 0.95	
	S/N = 21.5	S/N = 17.6	
R_f feedback ch 6	MPV = 46.2 ± 0.1	MPV = 8.32 ± 0.01	no MIP
	Ped = 2.25	Ped = 0.6	
	S/N = 20.53	S/N = 13.86	
R_f feedback ch 7	MPV = 46.1 ± 0.1	MPV = 8.31 ± 0.01	no MIP
	Ped = 2.25	Ped = 0.56	
	S/N = 20.49	S/N = 14.83	

Table 9.1: The S/N for the "High High" and "High Low" front-end electronics mode for two feed back technologies (MOS and R_f).

In both test beam measurements the MIP position is shown to be stable for all measured channels. The MOS feedback showed a twice higher gain than the R_f feedback and the S/N is similar for both of them. Figure 9.15(a) shows a slight increase of the S/N with increasing channel number. Then the noise of 32 pads was plotted as a function of the pad area in figuree 9.15(b). It is seen that the noise linearly depends on the pad size for both feed back technologies. Such behavior is expected, since the noise depends linearly on the detector capacitance and hence on the pad area [3].

9.3.6 Calibration

Separate calibrations were done for the read out with an external ADC and the ADC ASICs. The calibration constants are obtained by applying test pulses to the front-end ASICs via a capacitance of 0.5 pF for all odd or all even channels simultaneously. Then the charge induced is $Q = C\,\Delta\,V$, where $\Delta\,V$ is the voltage step of the test pulse. The test pulse with $\Delta\,V$ =1 V is attenuated by 6 to 60 dB. The attenuation, A_{dB}, relates to the value of the attenuated voltage step by:

$$A_{dB} = 20 * log(\frac{\Delta\,V_1}{\Delta\,V_0}),$$

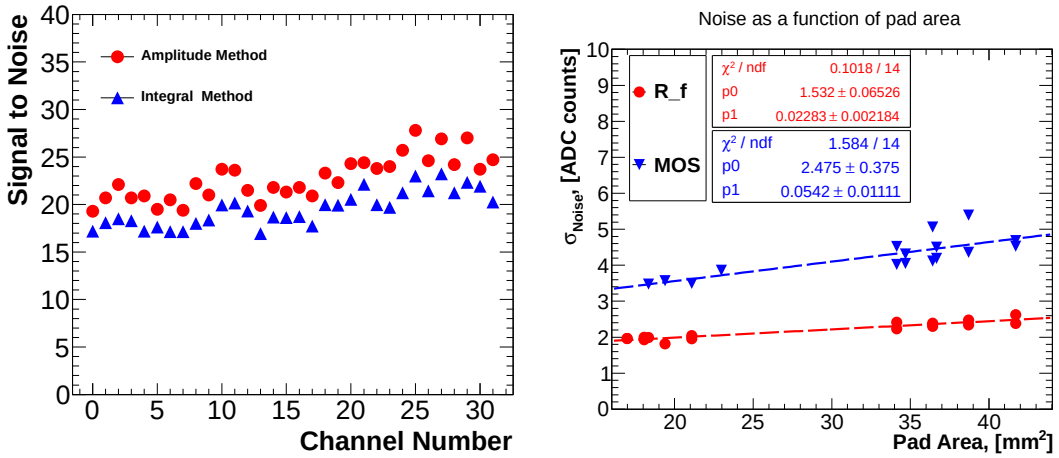

(a) (b)

Figure 9.15: (a) The S/N obtained for the amplitude method (red dot) and integral method (blue triangles). (b) The pedestal standard deviation as a function of the pad area for R_f and MOS feedback in the preamplifier.

where ΔV_1 is voltage step after and $\Delta\ V_0$ before attenuation. The injected charge, Q_{inject} is obtained as:

$$Q_{\text{inject}} = C\frac{\Delta\ V_0}{10^{\frac{dB}{20}}}\frac{1}{q},$$

where q - is electron charge, C is the coupling capacitance. Q_{inject} is in units of electrons. Plotting the measured signals as a function of the injected charge a linear function is obtained and the slope is the calibration factor. The resulting calibration factors for the "High High" mode are shown in figure 9.17(a) and for the "High Low" in figure 9.17(b). For a signal size measured in ADC counts, the primary signal charge is obtained as:

$$Q_{\text{Meas}} = k_{\text{Cal}} * ADC_{\text{counts}}.$$

9.3.7 Charge Collection Efficiency

Figure 9.16 shows the size of the MIP signal for the two feed back technologies used in the FE ASICs as a function of bias voltage. It slowly growth with increasing voltage and comes to the saturation at about 60 to 100 V. The value of the MIP signal is transformed into the CCE using the calibration factors shown in figure 9.17. The deposited charge is obtained from the simulations described in section 8.2 for a beam of 2 GeV electrons. The CCE at 100 V is then equal to 42.2%. It is in the agreement to previous test beam results and to the measurements done in the laboratory as shown in section 8.1.6 and other previous measurement results described in section 1.4.

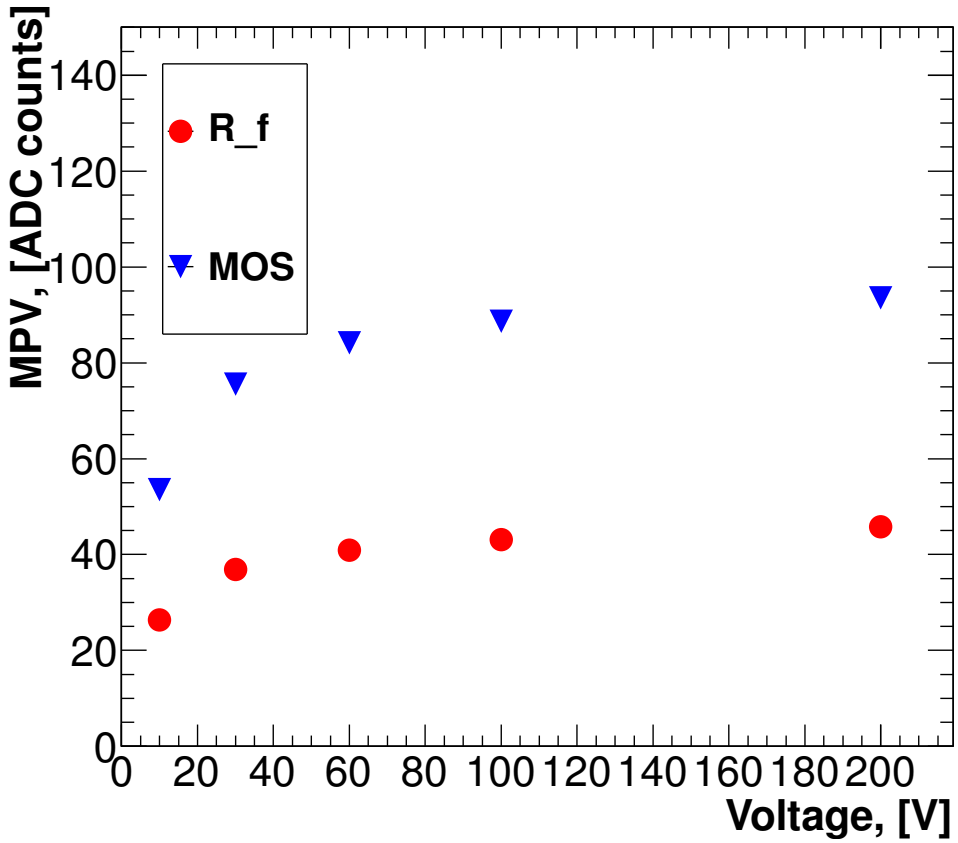

Figure 9.16: The signal size as a function of the applied bias voltage. FE ASICs with R_f feedback technology and MOS feedback technologies.

9.3.8 Deconvolution Method

The deconvolution method was developed in the 90-th of the last century. The idea is to use slow pulse shaping and then to apply a deconvolution algorithm to reconstruct the fast components of the input signal [112]. For the sampled output of a CR-RC shaper with the sharp response the signal amplitude, $v(t)$, as a function of time reads

$$v(t) = -\frac{t}{\tau} * e^{-t/\tau}.$$

A weighted sum is formed from three successive samples V_k, V_{k-1} and V_{k-2},

$$V_k = w_1 * V_k + w_2 * V_{k-1} + w_3 * V_{k-2},$$

with the weights

$$w_1 = \frac{1}{x} * e^{x-1},\ w_2 = -\frac{2}{x} * e^{-1},\ w_3 = \frac{1}{x} * e^{-(x+1)}.$$

The weights depend on the sampling interval, $\Delta\, t$, and the shaping time constant, τ,

$$x = \frac{\Delta\, t}{\tau}.$$

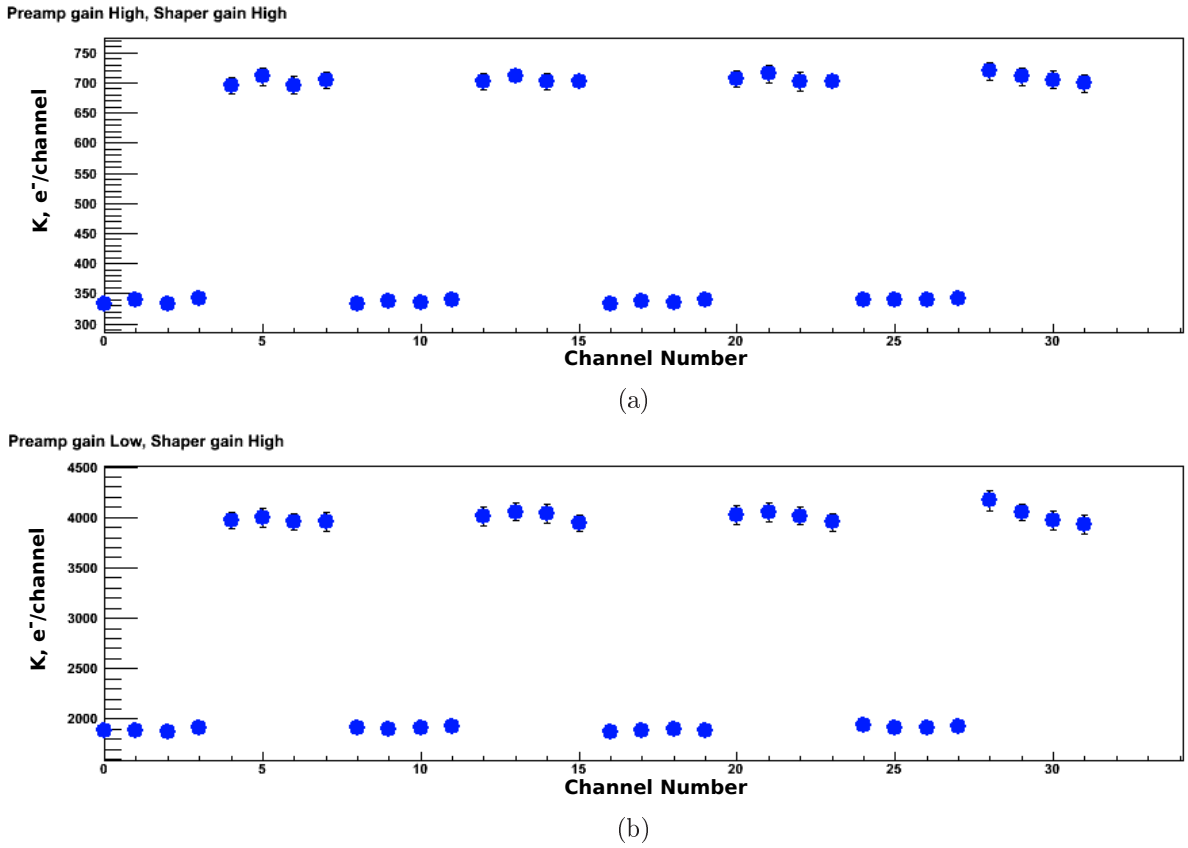

Figure 9.17: (a) The calibration factors for all channels in the "High High" mode, (b) and in the "High Low" mode.

Here, the time constant is $\tau = 60$ ns and the sampling interval of the ADC Δt=50 ns. For a finite rise time the result is a short pulse with the duration of the rise time [64]. By knowing the characteristics of the FE and ADC ASICs, one can deconvolve the initial detector signals. For illustration, figure 9.18 shows the signal formation from the sensor, the FE ASIC, the ADC and the deconvolution filter.

Figure 9.19 shows in the left plots the data measured by the ADC ASICs in four channels belonging to one FE ASIC. The common mode noise is visible in the left pictures by synchronous moving of the baseline of the 4 channels. In the right plots the dotted line shows the original signal from ADC ASIC in one channel, in blue the signal after the common mode noise subtraction and in red the signal after the deconvolution filter. The upper plot shows data taken in synchronous mode and the bottom plot data taken in asynchronous mode. In data taken asynchronous the first signal sample not always correspond to the maximum of the amplitude.

Figure 9.20(a) shows proportionality between the signal amplitude after the deconvolution filter for the synchronous data taking mode to the signal amplitude measured from the ADC ASICs. Very good proportionality was observed. Using the deconvolution filter with asynchronous readout and taking only the first value of the deconvoluted amplitude, no proportionality to the amplitude of the full ADC readout is found, as expected. However, taking the sum of the first two non-zero samples after the deconvolution filter, the proportionality is restored, as can be seen in figure 9.20(b). This is explained by the low

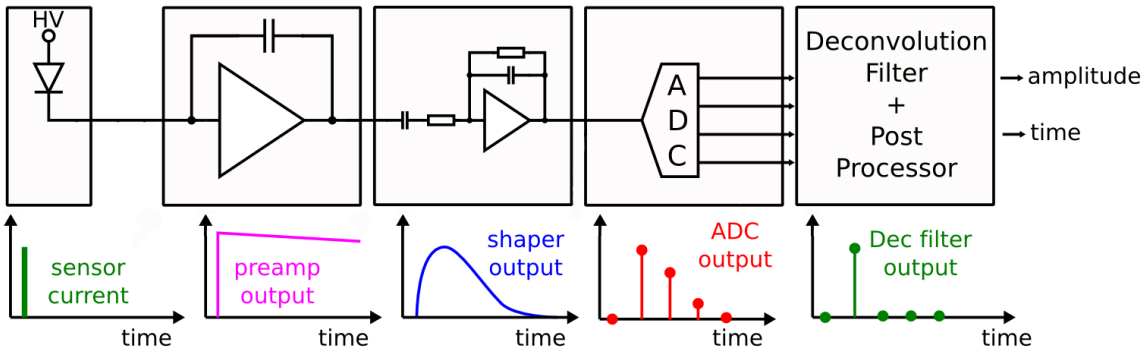

Figure 9.18: The schematics of the full read out chain signal processing.

sampling rate of the ADC ASIC for 300 ns signal length in contrary to high sampling rate of used CAEN ADC. In the asynchronous mode the ADC ASIC will not always measure amplitude correctly and sum of two samples is used to restore the signal amplitude. The final signal calculation for 32 channels after deconvolution filter is shown in figure 9.21. The deconvolution method showed S/N variation between channels less than 8 %.

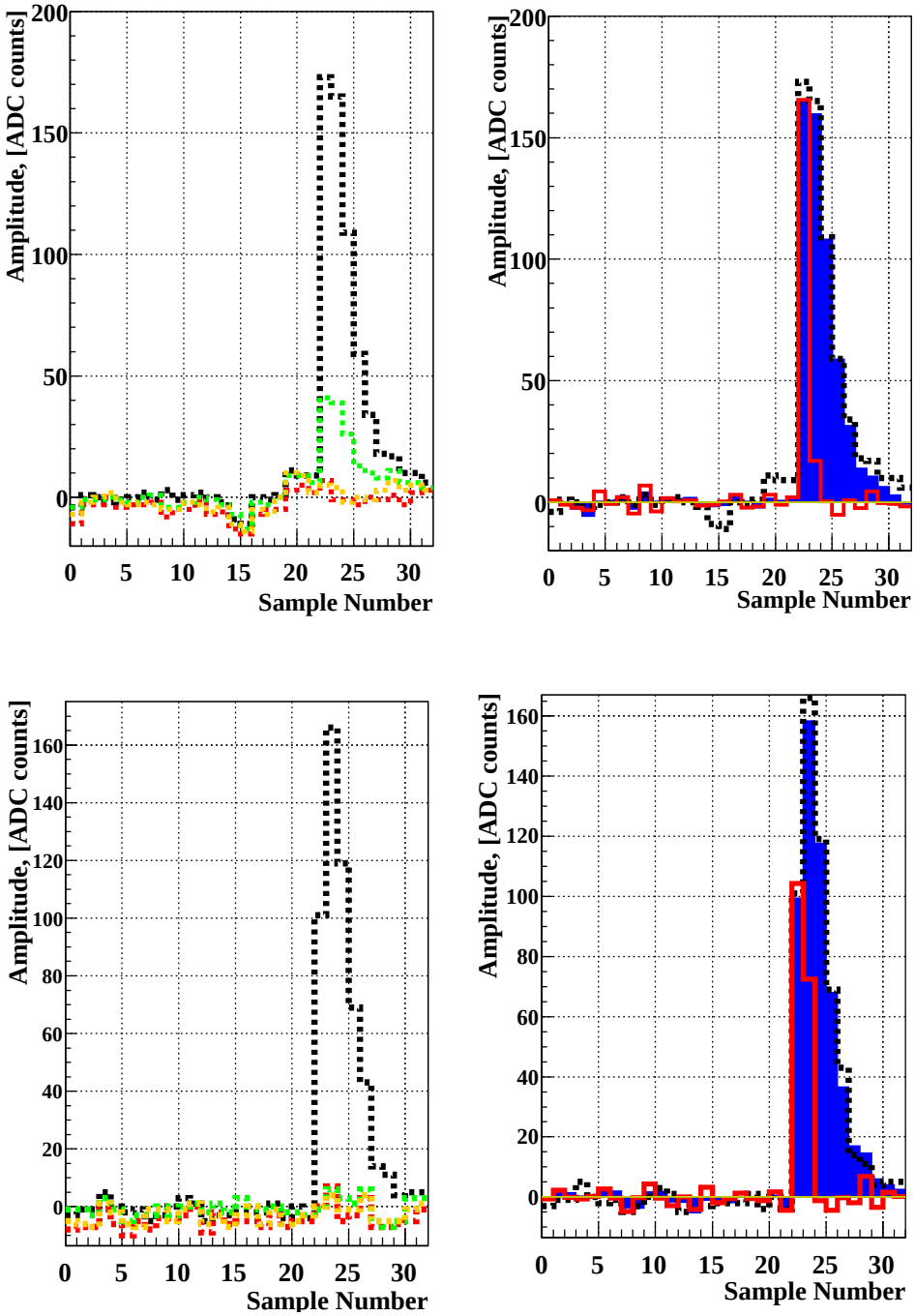

Figure 9.19: Left: The amplitude in four channels digitized by the ADC ASICs as a function of time. Right: The amplitude in the channel with a signal digitized by the ADC ASICs as a function of time (black dotted line), the amplitude values after the common mode noise subtraction (blue), the deconvoluted amplitude (red line). Upper plots correspond to synchronous read out mode and bottom plots to asynchronous mode.

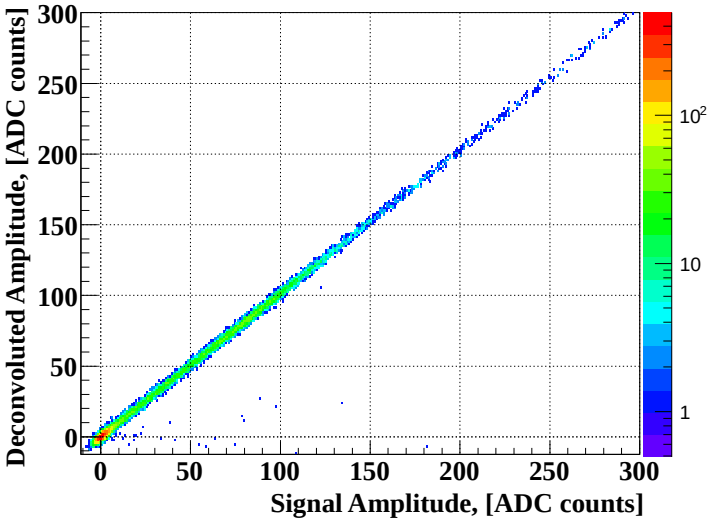

(a)

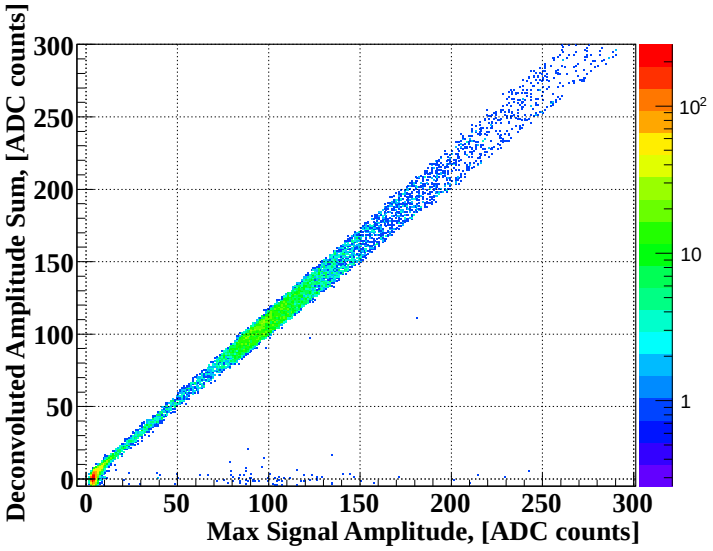

(b)

Figure 9.20: (a) The deconvoluted amplitude as a function of the signal amplitude for the synchronous read out mode. (b) The sum of two first non zero amplitudes after the deconvolution filter as a function of the signal amplitude.

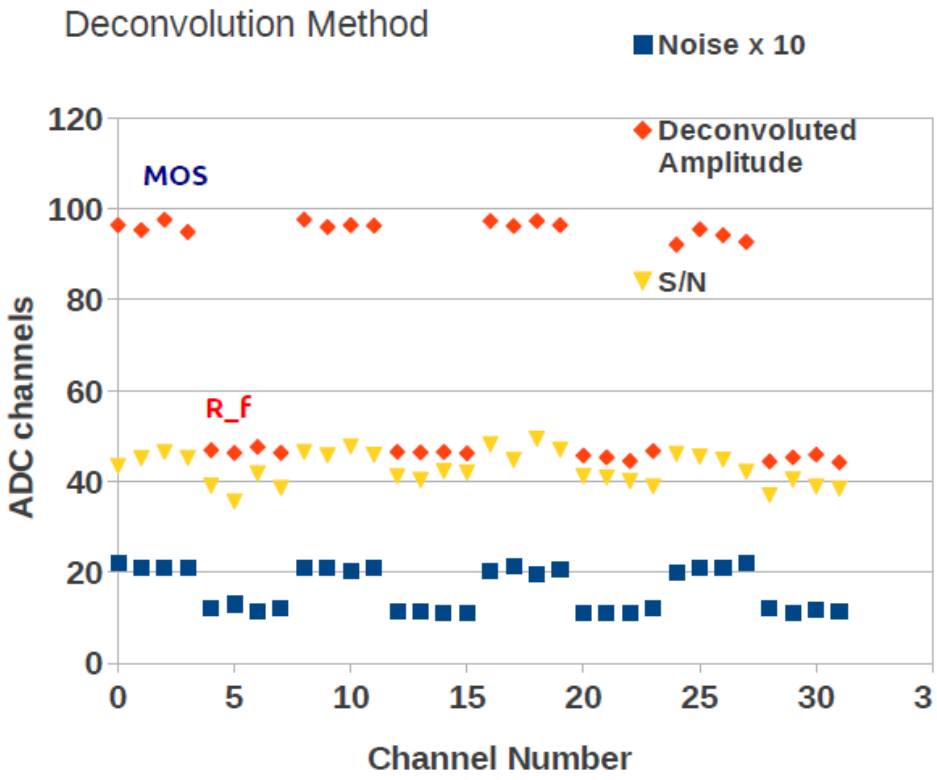

Figure 9.21: The signal amplitude from the 32 channels before deconvolution (orange rhombus). The signal to noise ratio of the signal amplitude after the deconvolution filter (yellow triangles). The noise multiplied by factor of 10 (blue squares).

9.4 Shower Development Studies

Several runs were taken with tungsten plates of different thickness installed in front of the GaAs sensor plane. The beam electrons generate an electromagnetic shower in the tungsten plates, and the performance of the readout of many particles crossing the sensor is investigated.

9.4.1 Transverse Shower Development

The transverse shower development is shown in figure 9.22 for 2 X_0, 4 X_0, 6 X_0 and 8 X_0 absorber depth. The amplitude maximum in each pad was used. A threshold of 5 ADC counts was applied.

Figure 9.23 (top) shows the sum of the depositions after 2, 4, 6, 8 and 10 X_0 and figure 9.23 (bottom) the normalized sum. The normalized plot shows that 90% of all showers deposits are within a radius of about 12 mm.

9.4.2 Longitudinal shower Development

Figure 9.24 shows the two dimensional shower profile in x-z plane using data taken with the "High High" readout mode. For 2, 4, 6, 8, 10, 12 and 14 X_0 radiation length in front of

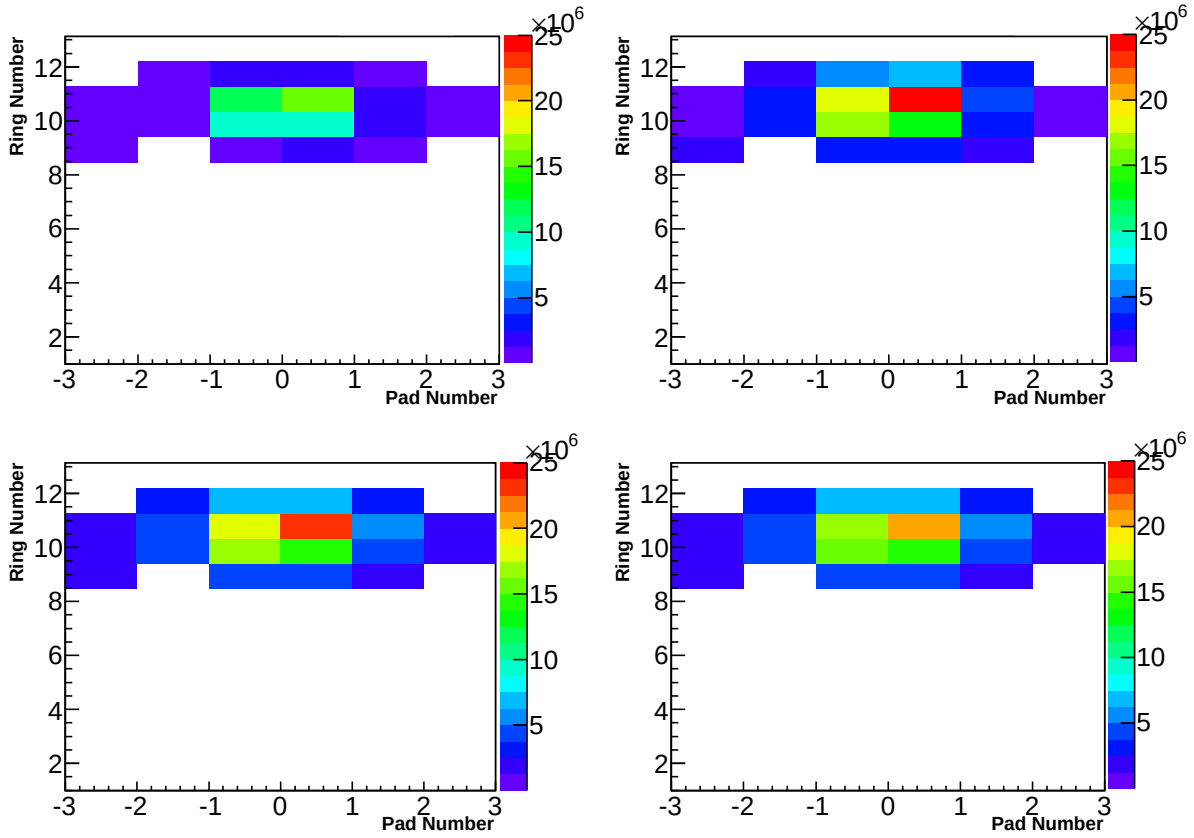

Figure 9.22: The transverse shower shape after 2 X_0 tungsten plates (top left), 4 X_0 (top right), 6 X_0 (bottom left) and 8 X_0 (bottom right).

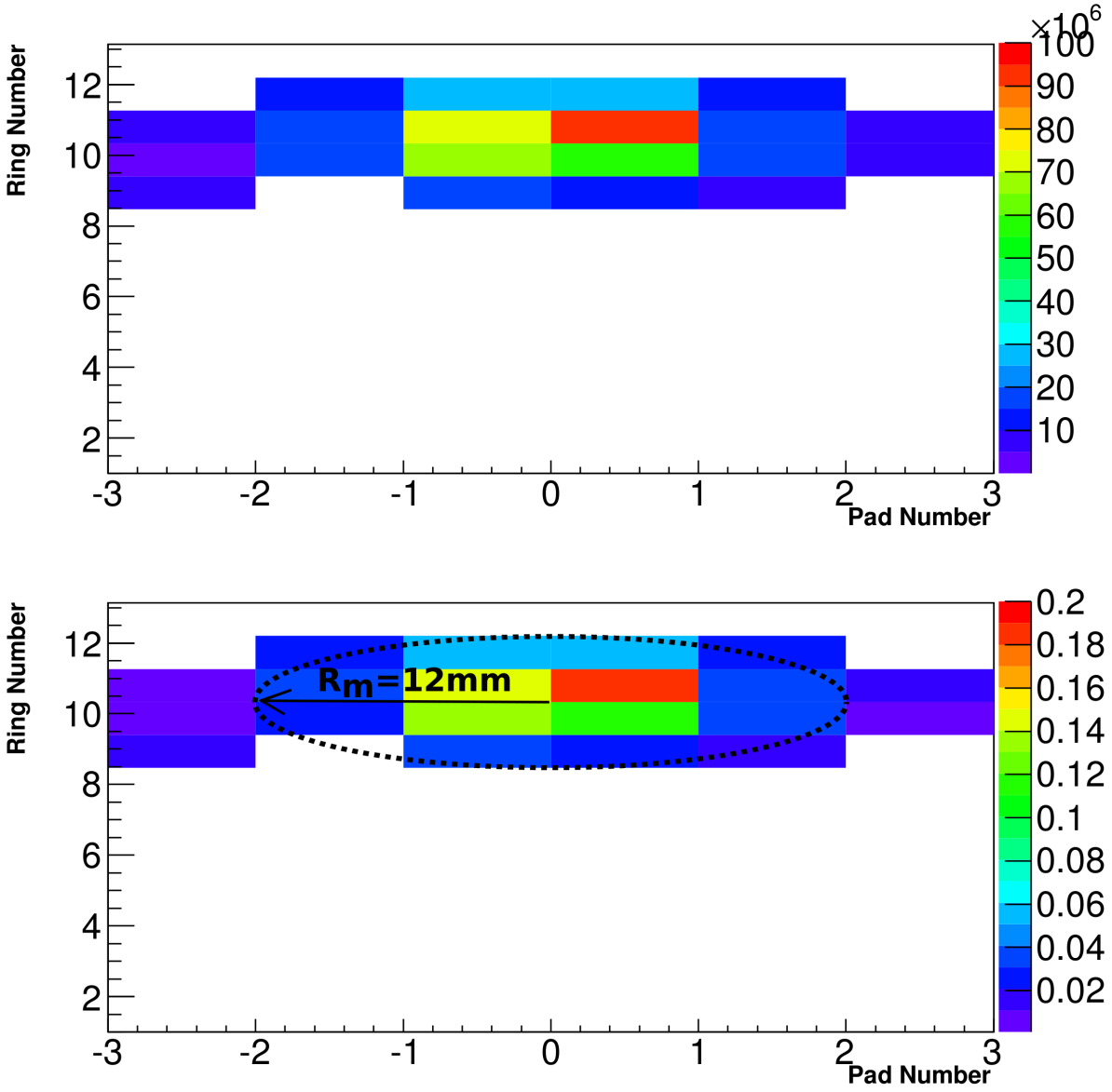

Figure 9.23: Top: The transverse shower shape as the sum of all depositions on the sensor pads after 2, 4, 6 and 8 X_0 radiation length of tungsten in front of the prototype. Bottom: The transverse shower shape normalized to the full signal in all pads and overlayed with a Moliere Radius ring of 12 mm.

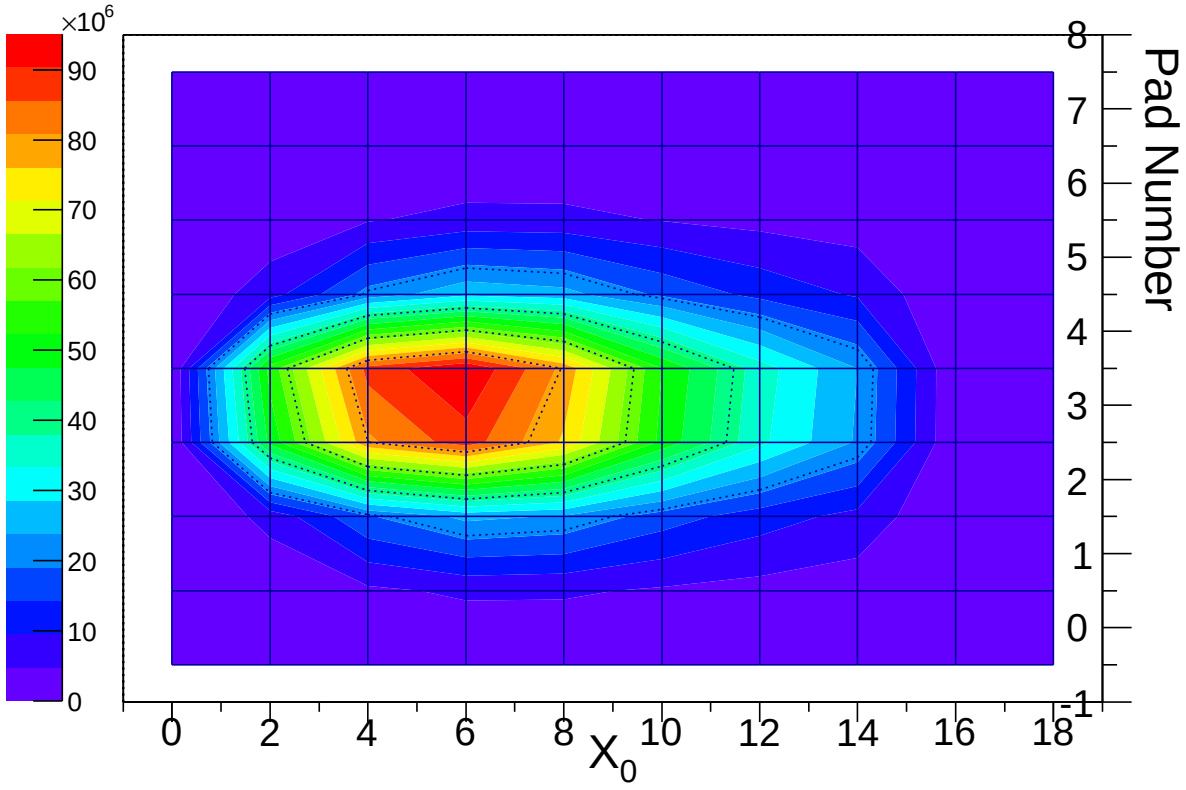

Figure 9.24: The two dimensional shower profile using data taken with the "High High" readout mode. X_0 is used for the depth measuring in Z axis.

the sensor, depositions from all pads are summed up and plotted in figure 9.25 in units of MIP particles. Similar plots for "High Low" and "Low High" readout mode are shown in appendix D. The spectra are fitted with a convolution of a Landau and a Gaussian. The bottom right plot of figure 9.25 shows the longitudinal shower profile as the most probable value of the fitted values (red triangles) and the mean value of the spectra (blue dots) as a function of the number of radiation length. The maximum of the shower development is around 6-th radiation length, as was shown in the simulation chapter.

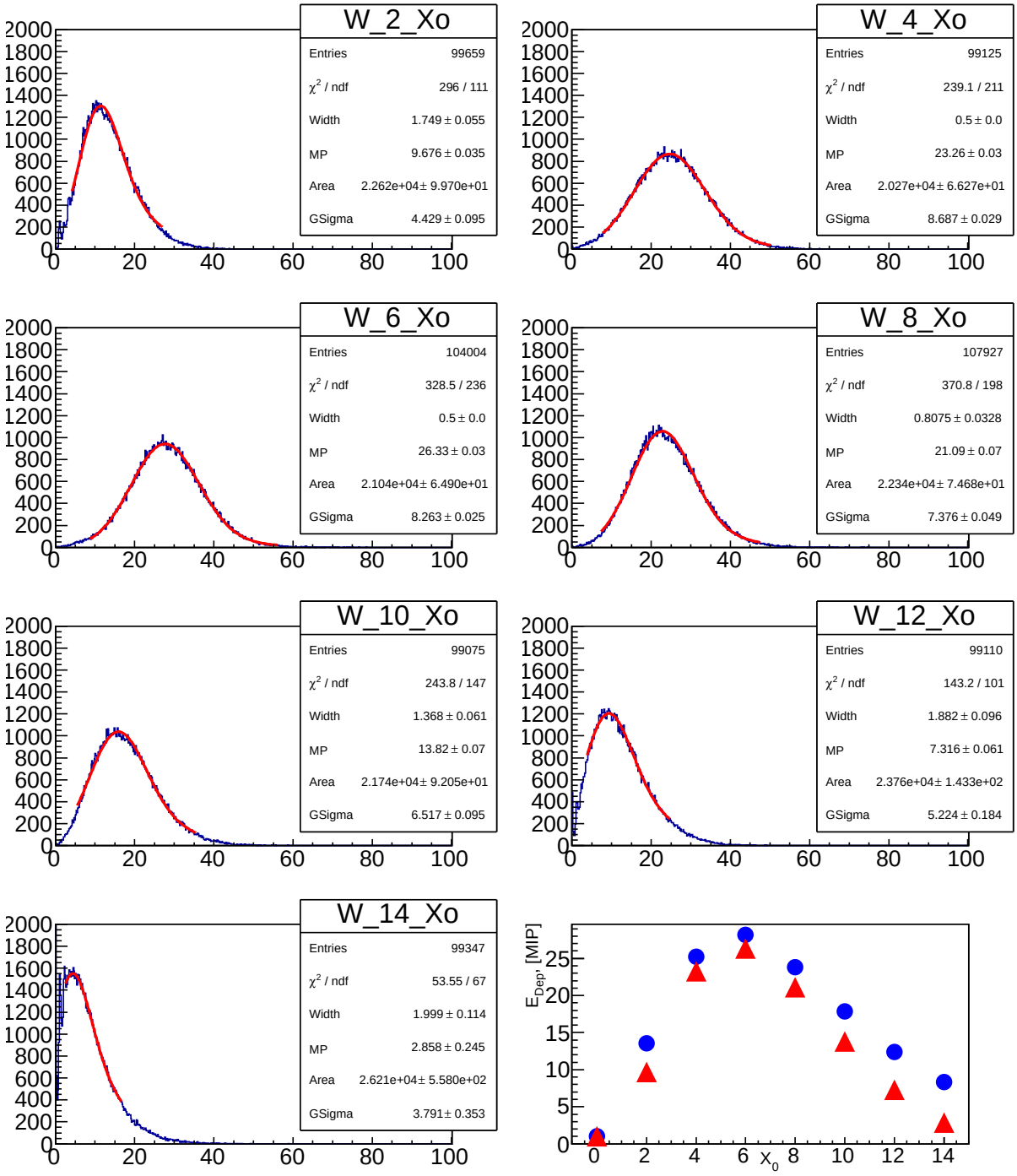

Figure 9.25: "High High" amplification mode resulting amplitude spectra for the different number of absorber layers in front of the GaAs:Cr sensor plane.

Summary and Conclusions

Two radiation hard sensor types and their applications are the main topics of this thesis. Diamond sensors are used in the beam condition monitor at LHC and GaAs sensors for a prototype sensor for a calorimeter at the ILC.

The BCM1F - the fast beam condition monitoring system - is the fully working and active in CMS since the first day of LHC operation. In this thesis the performance of BCM1F was studied during data taking. The BCM1F detector was proved to be sensitive to beam conditions and beam losses, resolve incoming and outgoing bunches and to monitor the luminosity.

BCM1F Data Analysis Results

1. Baseline Monitoring was performed permanently. Short scale temperature changes lead to a shifts in the baseline. Long scale movements are caused by the front-end degradation due to irradiation.

2. Radiation tolerance - the front-end and diamond degradation was monitored from the beginning of the BCM1F operation. The main degradation was observed for the optical driver. Diamond degradation was observed, but was hard to quantify.

3. Intrinsic time resolution of BCM1F was obtained to be 1.5 ns. Constant fraction discrimination demonstrated an improvement of the time resolution and should be implemented in the future upgrades.

4. BCM1F count rates were shown to be linear to the luminosity after applying correction function for the deadtime due to saturated signals and overshoots. In addition, the measurement of the luminosity bunch-by-bunch was demonstrated.

Beam Calorimeter for the ILC Detector

The second part of this thesis is devoted to the design of a detector at a future International Linear Collider. Important subsystems are the very forward calorimeters. Simulation to optimize the design of the BeamCal, a calorimeter adjacent to the beam-pipe, are presented. Prototypes of large area sensors with pad structure are investigated in the laboratory and a full system comprising a sensor, dedicated FE ASICs and ADC ASICs was tested in an electron beam.

Beam Calorimeter Simulation Studies

The BeamCal in the Very Forward Region of the ILC detector is important for new particle searches. It measures high energy electrons, positrons and photons down to very low polar angles. In addition, it serves for fast beam diagnostics and shields the inner part of the detector from back-scattered beamstrahlung pairs and synchrotron radiation.

The e^+e^- pairs originating from beamstrahlung - a new phenomenon at the ILC - cause large energy deposition in the BeamCal. The next generation of the beam parameters set, SB2009, was compared with the nominal beam parameters to estimate the expected dose deposited in the sensors. The new beam parameters with 500 GeV energy in the center mass system lead to similar doses than the nominal beam parameters set, but the energy deposition per bunch crossing is two times larger. This deposition forms a background for the detection of a single high energy electron or photon. Simulation were done to estimate the efficiency of single high energy electron showers reconstruction on top of the beamstrahlung pairs.

Two sensor segmentations were compared with respect to the electron reconstruction efficiencies for the nominal beam parameter set. Newly proposed segmentation showed increase of the shower reconstruction efficiency at low polar angles. The fake rate of the reconstruction algorithm was found to be less then 1.5% for showers above 50 GeV energies. The energy resolution of the showers without background was found to be

$$\frac{\sigma_E}{E} = \frac{(30 \pm 2)\%}{E}.$$

Sensor Characterisation

The leakage current was measured as a function of the applied voltage and the capacitances were measured for all pads. It was shown that the capacitances are in the range between 6 and 12 pF. The capacitance of the pad to the back plane is behaving similarly to a parallel plate capacitors.

The data analysis showed that all fabricated GaAs:Cr sensors have sufficient quality for the future BeamCal prototype. Only sensors with series numbers 84 showed problems with the guard ring. Operation without guard ring is possible and all 22 sensors can be used.

Test Beams Campaigns 2010-2011

Sensor plane prototypes for LumiCal and BeamCal were prepared and tested in the laboratory and in an electron beam. Three successful test beam campaigns were performed in 2010-2011 at the DESY II accelerator. The following results were obtained:

1. Calibration of each readout channel was done in the preparation to the test beam. The prototype signal output was shown to be linear to the injected test pulses.

2. There were three techniques discussed for the signal processing: amplitude, integral and deconvoluted amplitude methods. The deconvolution method was shown to be a good filter for the signal processing.

3. A common mode noise was observed in the second sensor plane prototype in groups of 8 channels and corresponded to the FE ASICs. The common mode noise subtraction algorithm was written and improved the signal to noise ratio by almost a factor two.

4. All instrumented channels with FE and ADC ASICs showed a signal to noise ratio around 20. The noise was found to be linearly dependent on the pad's capacitance.

5. The deposited charge was estimated from a GEANT simulation for all beam energies used. The obtained number of generated electron-hole pairs per μm is between 160 and 164, comparing these numbers with the measured charge, a charge collection efficiency of about 42% was estimated.

6. Edge investigations for the gaps between pads showed a loss of the signal of about 10%.

7. The shower development was studied with one sensor plane by installation of tungsten absorbers in front. The Moliere radius was estimated to be around 12 mm and the maximum of the longitudinal shower development after 6-th radiation length, what is in agreement with the simulation studies.

Conclusions

The BCM1F system was shown to be working with very good performance in the data taking period in 2010-2012. It is an invaluable tool to ensure low beam halo for data taking and perform a real-time luminosity measurement. The performed studies will be taken into account for the BCM1F upgrade during the LHC shut down 2013-2014.

The BeamCal simulation studies have shown that a sandwich calorimeter can detect single high energetic electrons, positrons or photons on top of large beamstrahlung background for two considered ILC beam parameters.

The GaAs:Cr sector sensor prototype were successfully tested in the laboratory and in the electron beam tests. A full chain of sensor, fanout, FE ASICs and ADC ASICs was validated and showed stability in baseline and between channels. Work on the future full calorimeter segment was started and is expected to be in 2013-2014.

Appendix A

BCM1F Signal Analysis

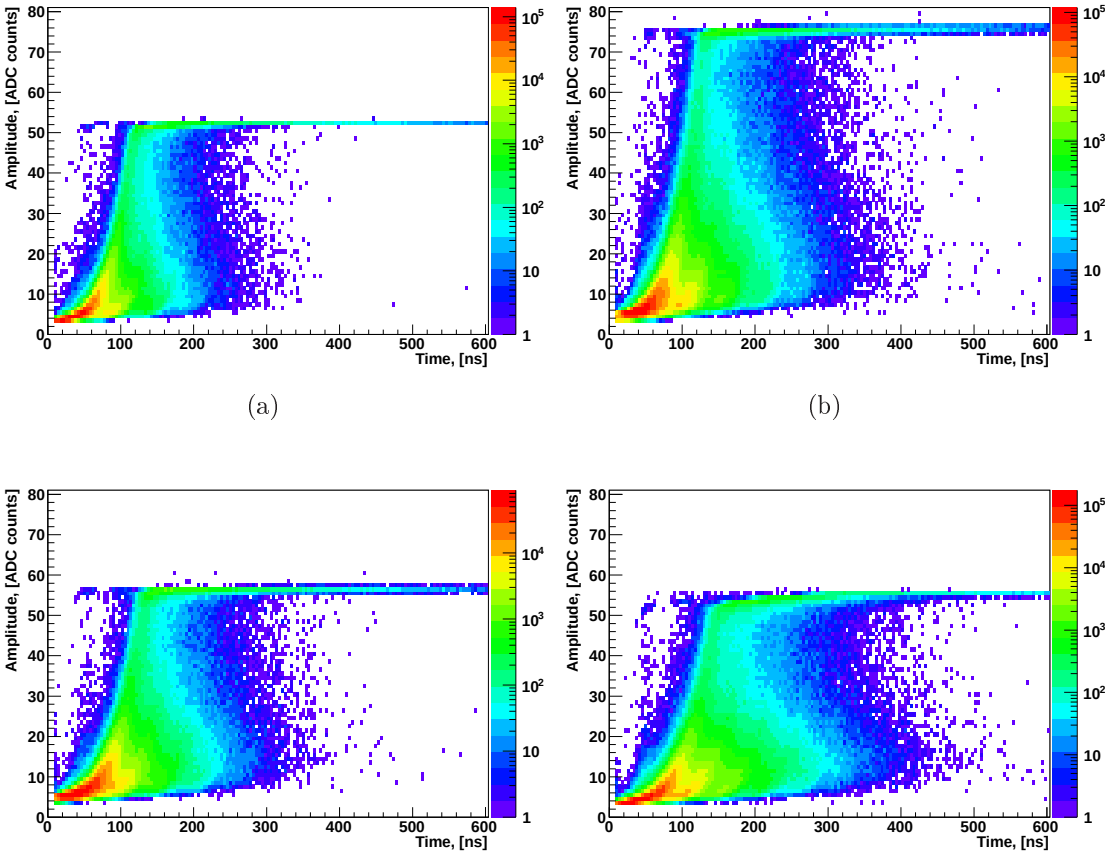

(a) (b)

(c) (d)

Figure A.1: Time over threshold vs Amplitude of signals for BCM1F. (a) to (d) channels from 1 to 4. Measured from Fill 2691 in 2012.

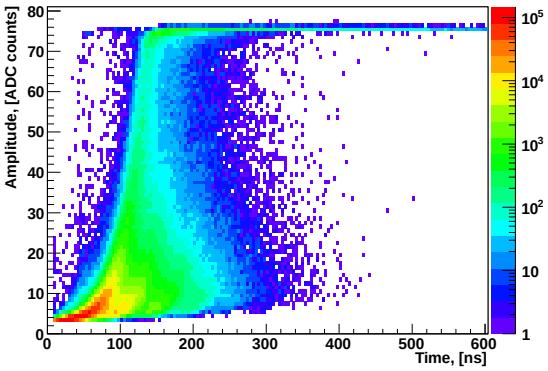

(a)

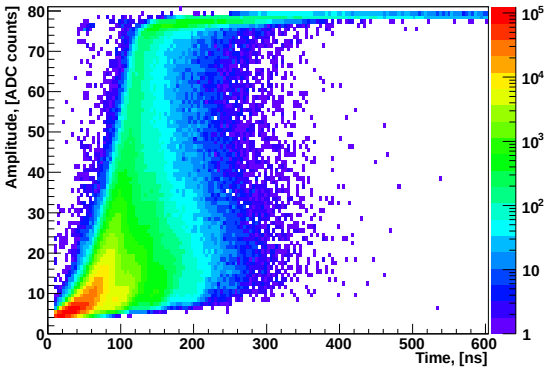

(b)

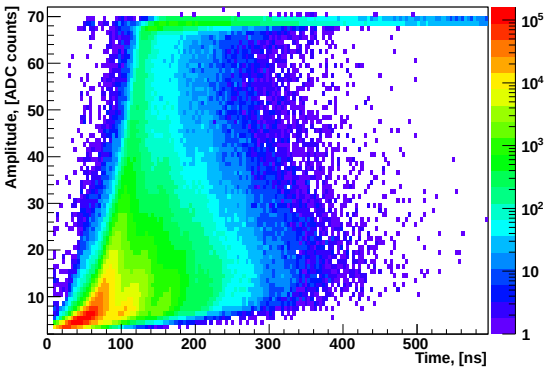

(c)

Figure A.2: Time over threshold vs Amplitude of signals for BCM1F. (a) to (c) are channels from 5 to 7. Measured from Fill 2691 in 2012.

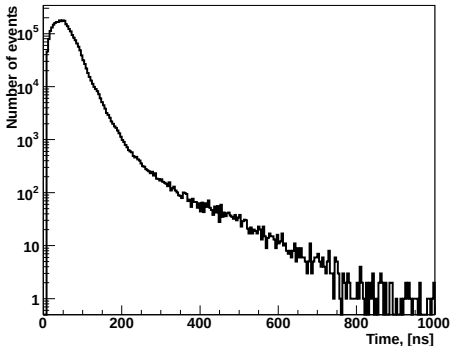

(a)

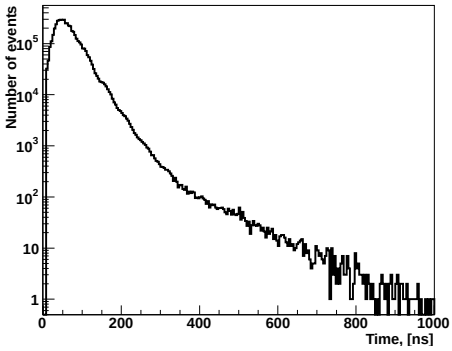

(b)

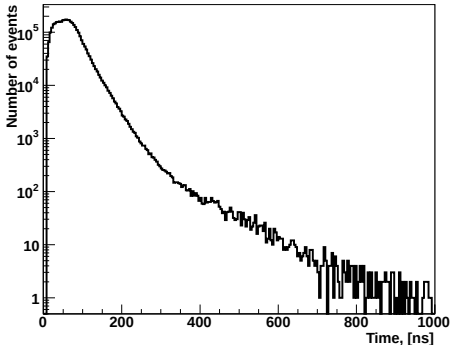

(c)

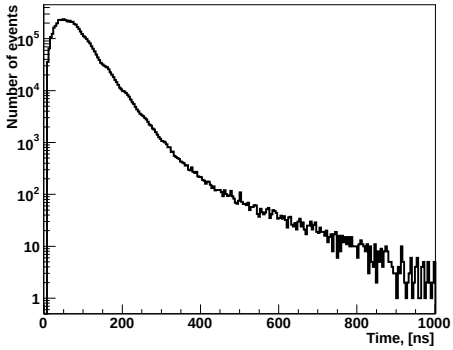

(d)

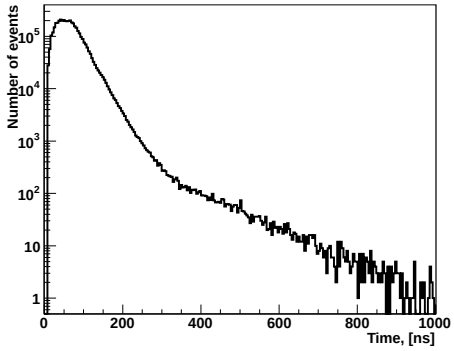

(e)

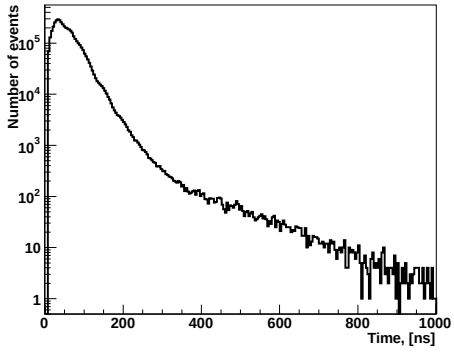

(f)

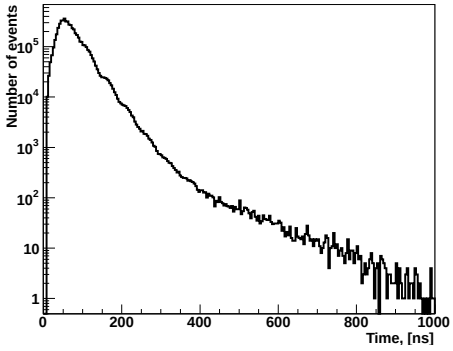

(g)

Figure A.3: Time over threshold of signals for BCM1F. (a) to (g) are channels from 1 to 7. Measured from Fill 2691 in 2012.

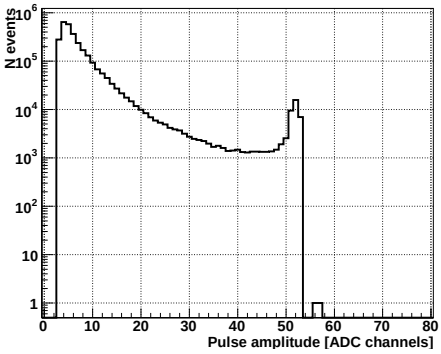

(a)

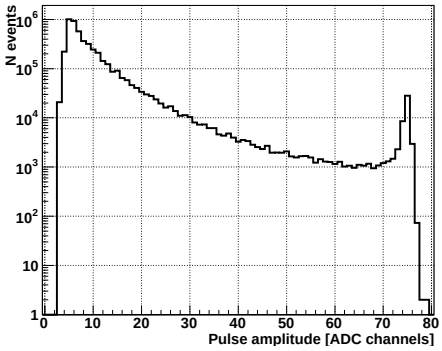

(b)

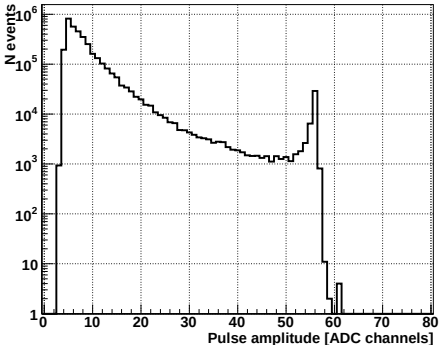

(c)

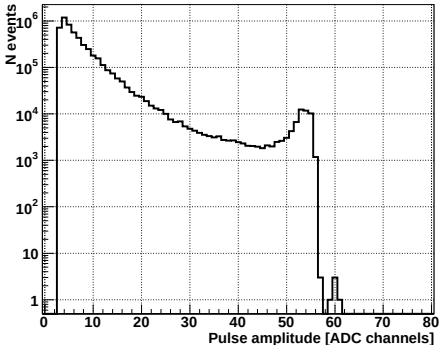

(d)

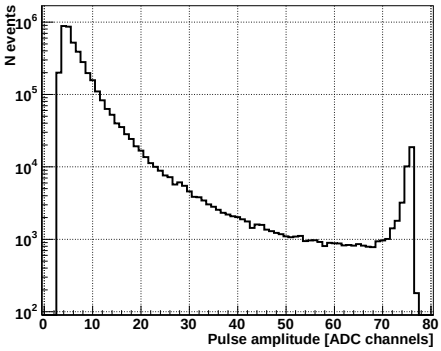

(e)

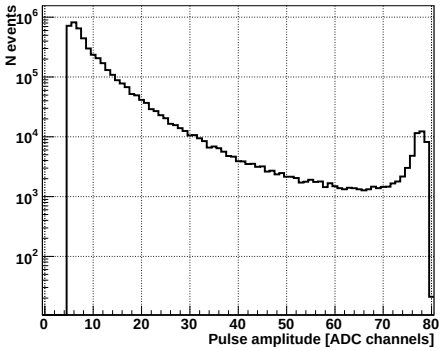

(f)

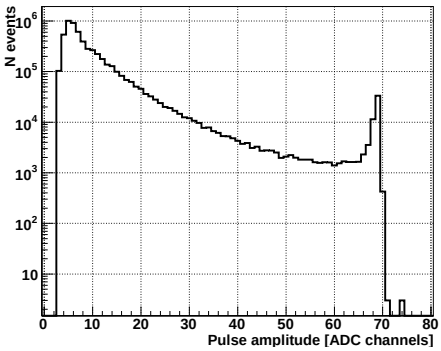

(g)

Figure A.4: Signal amplitude spectra for BCM1F. (a) to (g) are channels from 1 to 7. Measured from Fill 2691 in 2012.

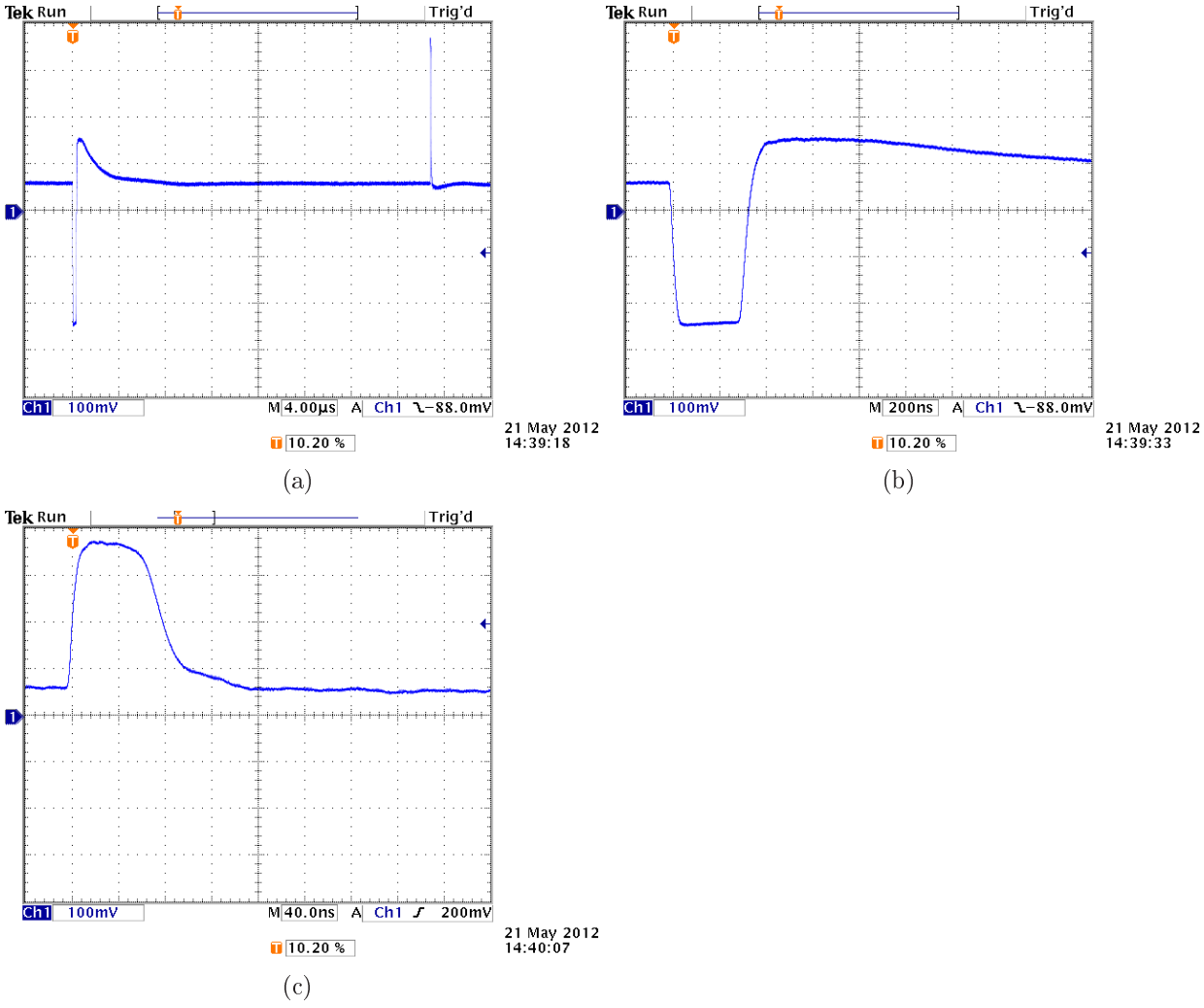

Figure A.5: Test pulses measurements in the Lab with high voltages, 2012. (a) The test pulse signal for one test pulse. (b) Zoom in for the first part of the test pulse with observed overshoot. (c) Zoom in for the second part of the signal with no overshoot observed.

Appendix B

Signal Shape Function

In the [64, 23] the signal shape function is described:

$$s(t) = -V_0 \frac{t}{\tau} e^{(-\frac{t}{\tau})}$$

Properties of signal shape function:
First derivative:

$$s'(t) = -V_0 \frac{1}{\tau} exp(-\frac{t}{\tau}) + V_0 \frac{t}{\tau^2} exp(\frac{t}{\tau})) = 0;$$

Equals to zero to find extreme values:

$$0 = \frac{V_0}{\tau} exp(-\frac{t}{\tau}))(\frac{t}{\tau} - 1);$$

1. $0 = exp(-\frac{t}{\tau})$; can not be fulfilled
2. $0 = \frac{t}{\tau} - 1$;

Maximum value of the amplitude is

$$A = s(t = \tau) = -V_0 exp(-1);$$

The integral -

$$S(t) = \int s(t)dt = -\frac{V_0}{\tau} \int t * exp^{(-\frac{t}{\tau})} dt$$

Integration was done using:

$$\int u(t) * v(t)dt = u(t) * v'(t)dt - \int u'(t) * v(t)dt;$$

With assumption:

$$u(t) = t$$

and

$$v'(t) = exp^{(-\frac{t}{\tau})}$$

$$S(t) = \int s(t)dt = -V_0 t(-\tau)exp^{(-\frac{t}{\tau})} - \int (-\tau)exp^{(-\frac{t}{\tau})}dt$$

The area, F, under the signal in the range from t=0 to t=a:

$$F(a) = \int s(t)dt = V_0 exp^{(-\frac{t}{\tau})}(t+\tau)$$

$$F(a) = V_0(exp^{(-\frac{a}{\tau})}(a+\tau) - \tau)$$

and the area in the limit $a \to \infty$:

$$F_{full} = F(a \to \infty) = V_0(\lim_{a\to\infty}\left[exp(-\frac{a}{\tau})(a+\tau) - \tau\right]) = -V_0\tau$$

To get 99% of the full area:

$$-0.99V_0\tau = V_0(exp^{(-\frac{a}{\tau})}(a+\tau) - \tau)$$

$$0.01\tau = exp^{(-\frac{a}{\tau})}(a+\tau)$$

$$ln\left(\frac{0.01\tau}{(a+\tau)}\right) = -\frac{a}{\tau}$$

Solution can be found numerically or graphically.

Appendix C

Leackage Current at 100 V

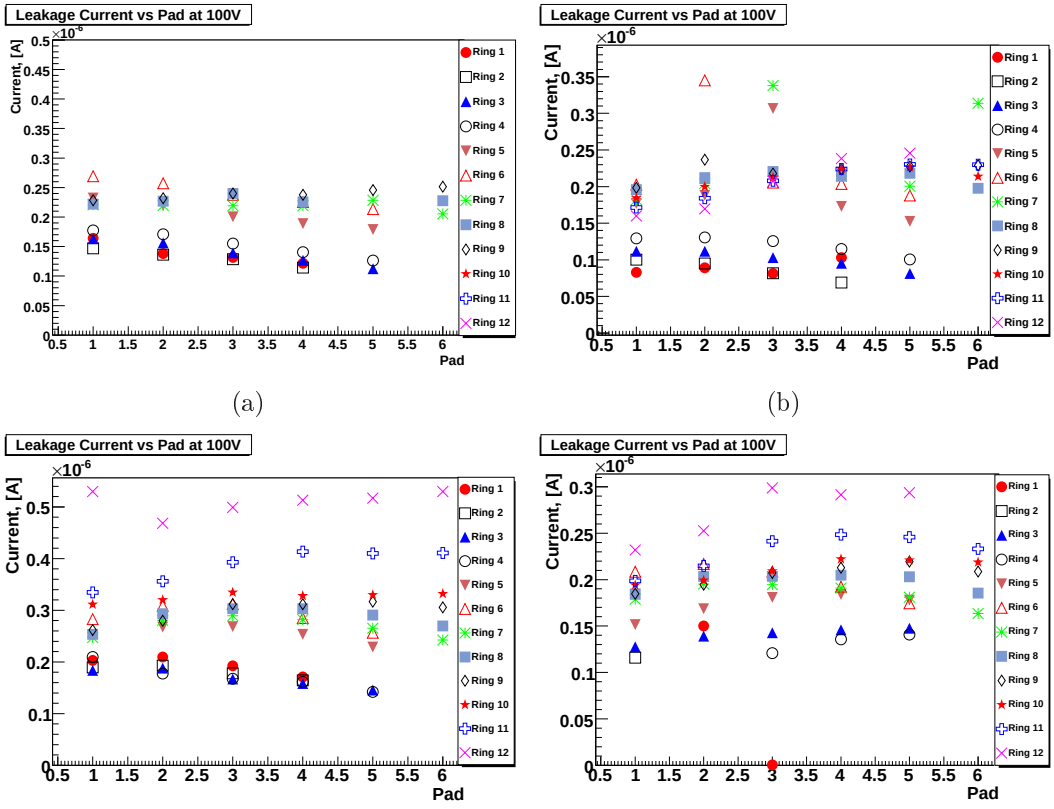

Figure C.1: The leakage current of all GaAs:Cr sensor pads of a type 2 sample at 100 V bias voltage as a function of the pad number from left to right. (a) No 84-19, (b) No 84-41, (c) No 84-7 and (c) No 84-13.

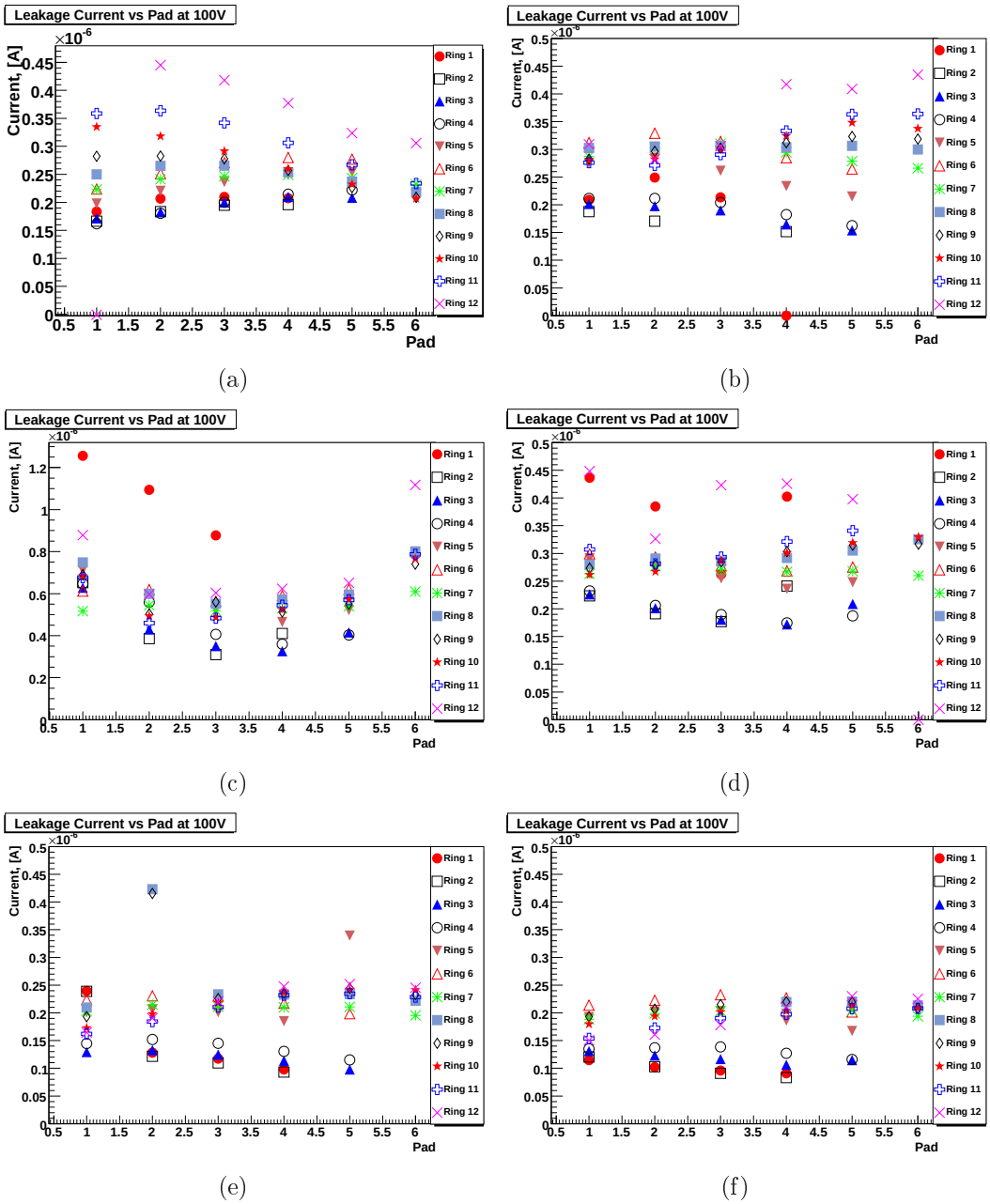

Figure C.2: The leakage current of all GaAs:Cr sensor pads of a type 2 sample at 100 V bias voltage as a function of the pad number from left to right. See the layout in figure 2.1(b). (a) No 221-25, (b) No 84-21, (c) No 84-26, (d) No 84-28 , (e) No 84-32 and (f) No 84-39.

Appendix D

Shower Development Measurements

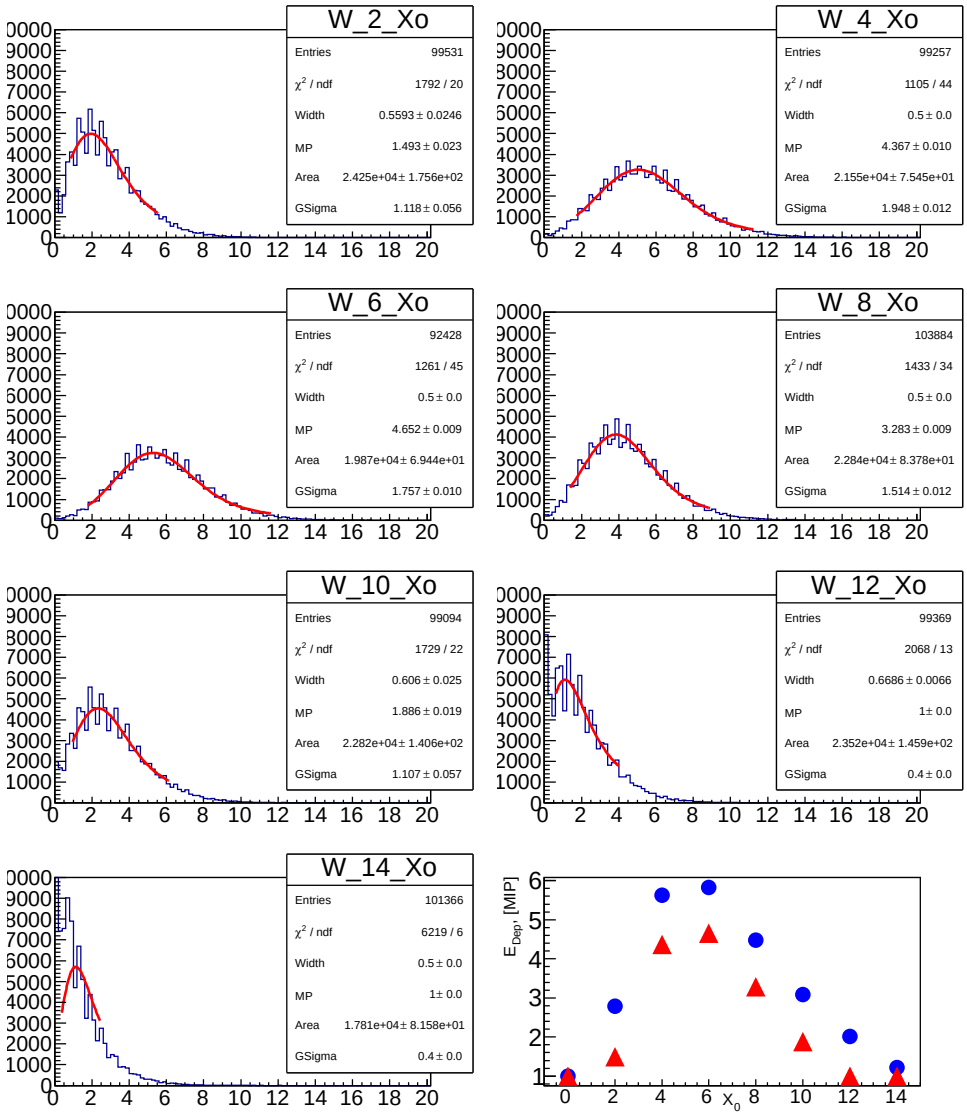

Figure D.1: "High Low" amplification mode amplitude spectra for different numbers of absorber layers in front of the GaAs:Cr sensor plane.

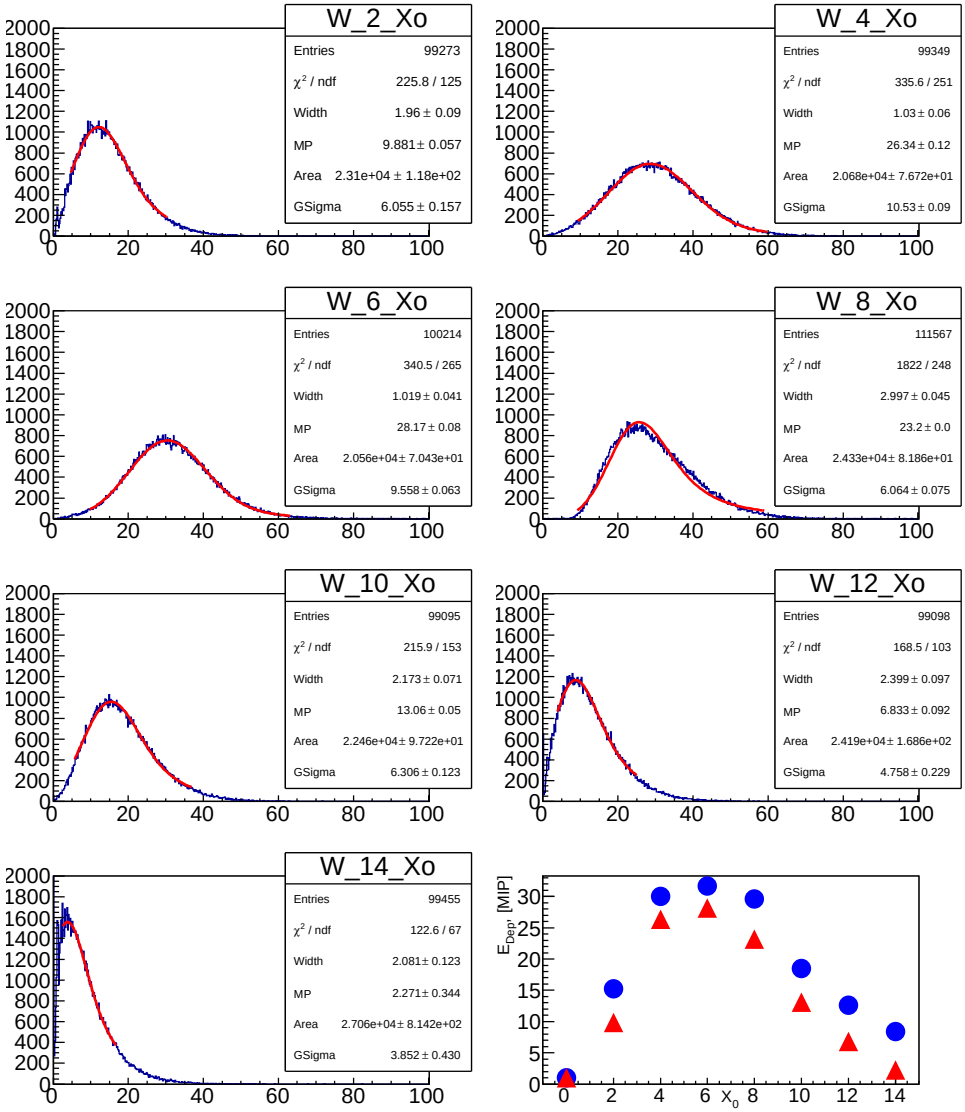

Figure D.2: "Low High" amplification mode amplitude spectra for different numbers of absorber layers in front of the GaAs:Cr sensor plane.

Bibliography

[1] W. Leo, *Techniques for Nuclear and Particle Physics Experiments*, Springer Verlag, 1987, ISBN 3-540-17386-2. 8

[2] N. Ashcroft and N. Mermin, *Solid State Physics*, Saunders College, Philadelphia, 1976. 9

[3] L. Gerhard, *Semiconductor Radiation Detectors: Device Physics*, Springer Verlag, 1999. 10, 123

[4] I. Tiginyanu, S. Langa, H. Foell, and V. Ursachi, *Porous III-V Semiconductors*, Online Book, http://www.porous-35.com/, 2009, http://www.porous-35.com/electrochemistry-semiconductors-5.html. 11

[5] Particle Data Group Collaboration, J. Beringer and et al., *Review of Particle Physics (RPP)*, Phys.Rev. **D86**(2012) 010001, DOI 10.1103/PhysRevD.86.010001. 10, 12, 81

[6] S. Ramo, *Currents induced by electron motion*, Proc.Ire. **27**(1939) 584, RX-1548, PIREA,27,584. 13

[7] A. Einstein, *Uber die von der molekularkinetischen Theorie der Warme geforderte Bewegung von in ruhenden Flussigkeiten suspendierten Teilchen*, Annalen der Physik **322**(1905) 549, DOI 10.1002/andp.19053220806, Provided by the SAO/NASA Astrophysics Data System, http://adsabs.harvard.edu/abs/1905AnP...322..549E. 14

[8] C. Canali, M. Martini, G. Ottaviani, and A. Alberigi Quaranta, *Measurements of the average energy per electron-hole pair generation in silicon between 5-320 k.*, Trans. Nucl. Science **19(4)**(1972) 9. 15

[9] C. Grah, *FCAL Sensor Properties Webpage* (2012), http://www.ifh.de/~chgrah/diamondproperties.html. 15

[10] C. Canali, E. Gatti, S. Kozlov, *et al.*, *Electrical properties and performances of natural diamond nuclear radiation detectors*, Nucl. Instrum. Meth. A **160(1)**(1979) 73. 15

[11] L. Reggiani, S. Bosi, and et al., *Hole drift velocity in the natural diamond*, Phys. Rev. B **23(6)**(1981) 3050. 15

[12] *NSM archive - physical properties of semiconductors* (2012), http://www.ioffe.rssi.ru/SVA/NSM/Semicond/index.html. 15

[13] G. Alix, H. Khaled, S. François, and A. Jocelyn, *CVD diamond films: from growth to applications*, Current Applied Physics **1**(2001) 479. 14

[14] E. Kuznetsova, *Design Studies and Sensor Tests for the Beam Calorimeter of the ILC Detector*, Ph.D. thesis, HU Berlin, 2007, DOI 10.3204/DESY-THESIS-2007-010. 15, 84, 89

[15] A. Salimi, M. Hyde, C. Banks, and R. Compton, *Boron doped diamond electrode modified with iridium oxide for amperometic detection of ultra trace amounts of arsenic(iii)*, Analyst **129**(2004)(1) 9. 15

[16] T. Behnke, *et al.*, *The Charge collection properties of CVD diamond*, Nucl.Instrum.Meth. **A414**(1998) 340, DOI 10.1016/S0168-9002(98)00696-2, DESY-98-027, hep-ex/9804006. 15

[17] M. Ohlerich, *Investigations of the physics potential and detector development for the ILC*, Ph.D. thesis, Brandenburgische Technische Universitat Cottbus, 2010, DOI 10.3204/DESY-THESIS-2010-008. 16, 17

[18] S. Schuwalow, *Personal Discussions*. 16

[19] G. Ayzenshtat, M. Bimatov, O. Tolbanov, and A. Vorobev, *Charge collection in X-ray pixel detectors based on semi-insulating GaAs doped with Cr*, Nucl.Instrum.Meth. **A494**(2002) 210, DOI 10.1016/S0168-9002(02)01467-5. 17

[20] P. Tomaszewski, *Jan Czochralski i jego metoda, Jan Czochralski and his method*, Oficyna Wydawnicza ATUT (2003), ISBN 83-89247-27-5. 18

[21] K. Afanaciev, *et al.*, *Investigation of the radiation hardness of GaAs sensors in an electron beam*, JINST **7**(2012) P11022, DOI 10.1088/1748-0221/7/11/P11022. 18, 19

[22] *Technical Proposal for the Upgrade of the CMS detector through 2020*, Technical Report CERN-LHCC-2011-006. LHCC-P-004, CERN, Geneva, Jun 2011. 18

[23] S. Kollowa, *Aufbau und Test einer Detektorebene mit Galliumarsenidsensor* Diploma thesis, Brandenburgische Technische Universitat Cottbus, DESY-THESIS-2012-020. 21, 106, 147

[24] *HP 4263A Precision LCR Meter Operation Manual*, Hewlett-Packard, Ltd (2013), http://cp.literature.agilent.com/litweb/pdf/04263-90001.pdf. 24

[25] G. Ayzenshtat, M. Lelekov, and et al., *Current transport in gallium arsenide detector compensated by chromium*, Solid State Physics **41**(2007), http://journals.ioffe.ru/ftp/2007/05/p631-634.pdf. 26, 28

[26] S. Sze, *Physics of Semiconductor Devices*, 1981, John Wiley and Sons, Inc. 26, 29

[27] G. Ayzenshtat, M. Lelekov, and O. Tolbanov, *Measurement of the barrier height on border of metal-semiinsulating gallium arsenide*, Solid State Physics **41-11**(2007), http://journals.ioffe.ru/ftp/2007/11/p1327-1328.pdf. 26, 27

[28] J. Bennett, *et al.*, *Design Concept for a 100-GeV e+ e- Storage Ring (LEP)* (1977), CERN-77-14, CERN-YELLOW-77-14. 33

[29] *ATLAS: Detector and physics performance technical design report. Volume 2* (1999), CERN-LHCC-99-15, ATLAS-TDR-15. 33

[30] *ATLAS: Detector and physics performance technical design report. Volume 1* (1999), CERN-LHCC-99-14, ATLAS-TDR-14. 33

[31] CMS Collaboration, G. Bayatian *et al.*, *CMS physics: Technical design report* (2006), CERN-LHCC-2006-001, CMS-TDR-008-1. 33, 35, 36, 37, 38

[32] CMS Collaboration, G. Bayatian *et al.*, *CMS technical design report, volume II: Physics performance*, J.Phys. **G34**(2007) 995, DOI 10.1088/0954-3899/34/6/S01. 33, 63

[33] *The CMS experiment at the LHC*, JINST **3**(2008). 33

[34] *LHCb VELO TDR: Vertex locator. Technical design report* (2001), CERN-LHCC-2001-011. 33

[35] ALICE Collaboration, K. Aamodt *et al.*, *The ALICE experiment at the CERN LHC*, JINST **3**(2008) S08002, DOI 10.1088/1748-0221/3/08/S08002. 33

[36] *LHC Maschine Outreach* (2012), http://lhc-machine-outreach.web.cern.ch/lhc-machine-outreach/. 34

[37] CMS Pixel Collaboration, A. Dominguez, *The CMS pixel detector*, Nucl.Instrum.Meth. **A581**(2007) 343, DOI 10.1016/j.nima.2007.07.156. 36

[38] CMS HCAL Collaboration, V. Hagopian, *The Compact Muon Solenoid (CMS) hadron calorimeter*, Nucl.Phys.Proc.Suppl. **78**(1999) 182, DOI 10.1016/S0920-5632(99)00543-5. 37

[39] SIPM Collaboration, B. Dolgoshein, *Silicon photomultipliers in particle physics: Possibilities and limitations* (2003) 442, INSPIRE-639461. 37

[40] T. Brantova, V. Kantserov, and F. Kayumov, *Possibilities of using silicon photomultipliers in the scintillation technique*, Instrum.Exp.Tech. **52**(2009) 519, DOI 10.1134/S0020441209040083, INETA,52,519. 37

[41] CMS Collaboration, B. Lutz, *Upgrade of the CMS Hadron Outer Calorimeter with SiPM sensors*, J.Phys.Conf.Ser. **404**(2012) 012018, DOI 10.1088/1742-6596/404/1/012018. 37

[42] S. Basegmez, *et al.*, *Performance studies for the prototype III of CASTOR forward calorimeter at the CMS experiment*, Indian J.Phys. **84**(2010) 1689, DOI 10.1007/s12648-010-0158-0, CERN-CMS-CR-2008-039, IJPYA,84,1689. 38

[43] X. Aslanoglou, *et al.*, *Performance studies of the final prototype for the CASTOR forward calorimeter at the CMS experiment* (2008), CERN-CMS-NOTE-2008-022 ETC. 38

[44] CMS Collaboration, O. Grachov *et al.*, *Performance of the combined zero degree calorimeter for CMS*, J.Phys.Conf.Ser. **160**(2009) 012059, nucl-ex, DOI 10.1088/1742-6596/160/1/012059, CMS-CR-2008-038, ARXIV:0807.0785. 38

[45] *The Large Hadron Collider: Conceptual design* (1995), CERN-AC-95-05-LHC, CM-P00047618. 39

[46] Dehning, B., *LHC machine protection*, Beam Instrumentation Workshop 2008, proceedings of the 13th Beam Instrumentation Workshop, Tahoe City, California, USA, 4-8 May 2008 59–67, INSPIRE-839724, http://accelconf.web.cern.ch/AccelConf/BIW2008/papers/movtio01.pdf. 39

[47] *BRM webpage*, Technical report, 2012, http://ts-dep-lea-int.web.cern.ch/ts-dep-lea-int/images/BRM/. 39

[48] BRM Group Collaboration, A. Dabrowski and et al., *The Performance of the Beam Conditions and Radiation Monitoring System of CMS*, IEEE (2011), http://ieeexplore.ieee.org/stamp/stamp.jsp?tp=&arnumber=6153979. 39

[49] R. Walsh, *Performance of the The CMS Fast Beam Conditions Monitoring*, proceedings of the 2010 IEEE Nuclear Science Symposium Conferenc (2010). 39

[50] A. Bell, *BRM webpage* (2012), http://ajbell.web.cern.ch/ajbell/Documents/Home/Dresden_Poster_Portrait.pdf. 39

[51] S. Müller, *The Beam Condition Monitor 2 and the Radiation Environment of the CMS Detector at the LHC*, Ph.D. thesis, Karlsruhe U., 2010, CERN-THESIS-2011-085, CMS-TS-2010-042. 40

[52] R. Eusebi, *et al.*, *A Diamond-Based Beam Condition Monitor for the CDF Experiment*, Technical report, 2013, http://www.hep.man.ac.uk/u/roger/abstracts/papers/760/CDF_diamond_proceedings.pdf. 41

[53] RD42 Collaboration, W. Trischuk, *Recent Advances in Diamond Detectors* (2008), physics.ins-det, arXiv 0810.3429. 41

[54] HERA-B Inner Tracker Collaboration, Y. Bagaturia *et al.*, *Studies of aging and HV break down problems during development and operation of MSGC and GEM detectors for the inner tracking system of HERA-B*, Nucl.Instrum.Meth. **A490**(2002) 223, hep-ex 0204011, DESY-02-056. 41

[55] A. J. Bell *et al.*, *Fast Beam Conditions Monitor BCM1F for the CMS Experiment* (2009), CMS-NOTE-2009-018, CERN-CMS-NOTE-2009-018. 41

[56] A. Bell, *et al.*, *Fast Beam Conditions Monitor BCM1F for the CMS Experiment*, Nucl.Instrum.Meth. **A614**(2010) 433, DOI 10.1016/j.nima.2009.12.056, physics.ins-det, DESY-09-178, 0911.2480. 41, 43, 58

[57] J. Kaplon and W. Dabrowski, *Fast CMOS binary front end for silicon strip detectors at LHC experiments*, IEEE Trans.Nucl.Sci. **52**(2005) 2713, DOI 10.1109/TNS.2005.862826. 43

[58] G. Cervelli, A. Marchioro, P. Moreira, and F. Vasey, *A radiation tolerant laser driver array for optical transmission in the LHC experiments* (2001) 155, INSPIRE-571079. 43

[59] J. Troska, *et al.*, *Optical readout and control systems for the CMS tracker*, IEEE Trans.Nucl.Sci. **50**(2003) 1067, DOI 10.1109/TNS.2003.815124. 43

[60] *Readout Histogramming Unit*, 2013, https://wiki-zeuthen.desy.de/CMS/RhU?action=AttachFile&do=view&target=RHU_concept_R2.pdf. 44

[61] *LHC Project Document No. LHC-OP-ES-0005* (2012), http://lhc-commissioning.web.cern.ch/lhc-commissioning/systems/data-exchange/doc/LHC-OP-ES-0005-10-00.pdf. 47

[62] BRM Group Collaboration, R. Walsh, *Performance of the CMS Fast Beam Conditions Monitor*, IEEE (2010) 1569, DOI 10.1109/NSSMIC.2010.5874040, http://ieeexplore.ieee.org/stamp/stamp.jsp?tp=&arnumber=5874040. 48

[63] *Personal Discussions with Ringo Schmidt* (2011-2012), Brandenburgische Technische Universitat Cottbus. 48, 50

[64] H. Spieler, *Semiconductor detector systems*, Ser.Semicond.Sci.Tech. **12**(2005) 1. 49, 126, 147

[65] R. S. Schmidt, *Fast Beam Monitoring and Top-Pair Analyses for CMS*, Ph.D. thesis, Brandenburgische Technische Universitat Cottbus, not published. 52

[66] *Cern Setup Calibration*, 2012, https://wiki-zeuthen.desy.de/CMS/CernSetupCalibration. 55

[67] *Personal Discussions with Elena Castro* (2011-2012), DESY Zeuthen. 57

[68] *Absolute Calibration of the Luminosity Measurement at CMS: Winter 2012 Update* (2012), CMS-PAS-SMP-12-008. 63

[69] *Public CMS Luminosity Information*, 2013, https://twiki.cern.ch/twiki/bin/view/CMSPublic/LumiPublicResults. 65

[70] CMS HCAL Collaboration, E. Gulmez, *The CMS-HF calorimeter readiness for data taking* (2009), DOI 10.1142/9789814307529 0058. 64

[71] *Measurement of CMS Luminosity* (2010), CMS-PAS-EWK-10-004, http://cds.cern.ch/record/1279145. 64

[72] *Absolute Calibration of Luminosity Measurement at CMS:Summer 2011 Update* (2011), CMS-PAS-EWK-11-001, http://cds.cern.ch/record/1376102/files/EWK-11-001-pas.pdf. 64

[73] *Absolute Calibration of the Luminosity Measurement at CMS: Winter 2012 Update* (2012), CMS-PAS-SMP-12-008 ETC, http://cds.cern.ch/record/1478132/files/DP2012_021.pdf. 66

[74] O. Napoly, *The Luminosity for beam distributions with error and wake field effects in linear colliders*, Part.Accel. **40**(1993) 181, CERN-SL-92-34-AP, CERN-CLIC-NOTE-17, PLACB,40,181. 67

[75] S. Van der Meer, *Calibration of the effective beam height in the ISR*, Technical Report CERN-ISR-PO-68-31. ISR-PO-68-31, CERN, Geneva, 1968. 67

[76] CMS Collaboration, O. Nathaniel, *Measurements of luminosity and normalised beam-induced background using the CMS Fast Beam Condition Monitor* (2012). 68

[77] *The CAEN Model V258B is a 16 Channel Programmable Discriminator*, 2013, http://hallaweb.jlab.org/compton/Documentation/Jlab/Neyret/v258bman.pdf. 68

[78] J. Brau, *et al.*, *International Linear Collider reference design report. 1: Executive summary. 2: Physics at the ILC. 3: Accelerator. 4: Detectors* (2007), ILC-REPORT-2007-001, CERN-2007-006, DESY-07-046, FERMILAB-TM-2382. 77

[79] T. Behnke, *et al.*, *The International Linear Collider Technical Design Report - Volume 1: Executive Summary* (2013), ILC-REPORT-2013-040, CERN-ATS-2013-037, DESY-13-062, FERMILAB-TM-2554, ARXIV:1306.6327. 78

[80] ILD Concept Group - Linear Collider Collaboration, T. Abe *et al.*, *The International Large Detector: Letter of Intent* (2010), FERMILAB-LOI-2010-03, FERMILAB-PUB-09-682-E, DESY-2009-87, hep-ex 1006.3396. 79, 82

[81] T. Behnke, *et al.*, *The International Linear Collider Technical Design Report - Volume 4: Detectors* (2013), arXiv, 1306.6329, ILC-REPORT-2013-040, CERN-ATS-2013-037, DESY-13-062. 80

[82] S. Schuwalow, *Calorimetry at the ILC detectors*, Nucl.Instrum.Meth. **A598**(2009) 258, DOI 10.1016/j.nima.2008.08.122. 82

[83] K. Mönig, *Physics needs for the forward region*, Technical Report 2011/197, 2004, V. Workshop: Instrumentation of the Forward Region of a Linear Collider Detector, http://www-zeuthen.desy.de/lcdet/Aug_04_WS/aug_04_ws.html. 82

[84] FCAL Collaboration, H. Abramowicz and et al., *Revised requirements on the readout of the luminosity calorimeter* (2008), http://www.eudet.org/e26/e28/e615/eudet_memo_2008_08.pdf. 84

[85] C. Grah and A. Sapronov, *Beam parameter determination using beamstrahlung photons and incoherent pairs*, JINST **3**(2008) P10004, DOI 10.1088/1748-0221/3/10/P10004. 84

[86] K. Ito, *et al.*, *Beam Size Measurement with Pair Monitor and BeamCal* (2009), physics.ins-det, 0901.4446. 84

[87] M. Idzik, S. Kulis, and S. Przyborowski, *Development of front-end electronics for the luminosity detector at ILC*, Nucl. Instr. and Meth. A **608**(2009). 85

[88] M. Idzik, K. Swientek, and S. Kulis, *Development of pipeline ADC for the Luminosity Detector at ILC*, JINST **5 P04006**(2010). 85

[89] Y. Cheng and C. Hu, *MOSFET Modeling and Bsim3 User's Guide*, Kluwer Academic Publishers, 1999, Chapter 2, ISBN 0-7923-8575-6. 85

[90] A. Abusleme, A. Dragone, G. Haller, and B. A. Wooley, *BeamCal Instrumentation IC: Design, implementation, and test results*, IEEE Trans.Nucl.Sci. **59**(2012) 589, DOI 10.1109/TNS.2012.2194308. 86

[91] A. Abusleme, A. Dragone, G. Haller, and B. Wooley, *BeamCal Instrumentation IC: Design, Implementation and Test Results*, IEEE Nuclear Science Symposium Conference Record (2011). 86

[92] W. Lohmann and et al., *Report for the ILC Detector R and D Panel Instrumentation of the Very Forward Region* (2007), http://www.desy.de/prc/docs_rd/prc_rd_02_01_update_05_07.pdf. 87

[93] *ILC Beam PLHC Project Document No. LHC-OP-ES-0005* (2009), SB2009 Proposal Document, ILC Global Design Effort, http://lcdev.kek.jp/SB2009/SB20091217B.pdf. 88

[94] B. Morse, *GamCal - A Beam-strahlung Gamma Detector for Beam Diagnostics*, eConf **C0705302**(2007), MDI01. 88

[95] D. Schulte, *Guinea Pig* (2012), http://www.slac.stanford.edu/accel/nlc/local/systems/beamdelivery/guinea_pig/ver_1999_07_08/program. 90

[96] A. Sapronov, *ILC Beam Diagnostics using BeamCal and GamCal*, eConf **C0705302**(2007) MDI02, LCWS-2007-MDI02. 91

[97] J. Allison, *et al.*, *Geant4 developments and applications*, IEEE Trans.Nucl.Sci. **53**(2006) 270, DOI:10.1109/TNS.2006.869826, SLAC-PUB-11870, IETNA. 91

[98] A. Seryi, T. Maruyama, and B. Parker, *IR Optimization, DID and anti-DID* (2006), SLAC-PUB-11662 ETC. 91

[99] R. De Masi and M. Winter, *Improved Estimate of the Occupancy by Beamstrahlung Electrons in the ILD Vertex Detector* (2009), physics.ins-det, ARXIV:0902.2707. 91

[100] O. Novgorodova, *Studies on the Electron Reconstruction Efficiency for the Beam Calorimeter of an ILC Detector* (2010), physics.ins-det, arXiv, 1006.3402. 93

[101] C. Grah, *et al.*, *Polycrystalline CVD diamonds for the beam calorimeter of the ILC*, IEEE Trans.Nucl.Sci. **56**(2009) 462, DOI 10.1109/TNS.2009.2013853. 93

[102] C. Fabjan and T. Ludlam, *Calorimetry in High Energy Physics*, Ann. Rev. Nucl. Part. Sci. **32**(1982) 335, CERN-EP-82-37. 95

[103] *Test Beams at DESY*, 2012, http://adweb.desy.de/~testbeam/. 99

[104] *Test Beam at DESY*, 2013, http://adweb.desy.de/home/testbeam/WWW/Description.html. 100

[105] *ZEUS MVD Telescope* (2013), http://www.desy.de/~gregor/short_intro.html. 100

[106] L. Bauerdick, *et al.*, *Beam test of silicon strip sensors for the ZEUS micro vertex detector*, Nucl.Instrum.Meth. **A501**(2003) 340, DOI:10.1016/S0168-9002(03)00619-3. 100

[107] S. Kulis, *Development of prototype luminosity detector modules for future experiments on linear colliders*, Ph.D. thesis, Faculty of Physics and Applied Computer Science - AGH, 2012, CERN-THESIS-2012-358, https://cds.cern.ch/record/1613815/files/CERN-THESIS-2012-358.pdf. 102

[108] M. Idzik, S. Kulis, and D. Przyborowski, *Development of front-end electronics for the luminosity detector at ILC* (2009), Nucl. Instrum. Meth. A. 104

[109] *The TELAna package* (2013), http://www.desy.de/~gregor/TELAna/. 115

[110] *Millepede: Linear Least Squares Fits with a Large Number of Parameters* (2013), http://www.desy.de/~blobel/wwwmille.html. 115

[111] O. Novgorodova, *et al.*, *Forward calorimeters for the future electron-positron linear collider detectors*, PoS **QFTHEP2010**(2010) 030. 116

[112] S. Gadomski, *et al.*, *The Deconvolution method of fast pulse shaping at hadron colliders*, Nucl.Instrum.Meth. **A320**(1992) 217, DOI 10.1016/0168-9002(92)90779-4. 125

Acknowledgments

I would like to express my gratitude to Professor Dr. Wolfgang Lohmann for being an excellent professor and providing all what is necessary for this thesis to be finished. Thank you for your constant encouragement, support, motivation and ideas made this work successful. Thank you!

I am deeply appreciate my committee members Professor Dr. Hermann Kolanoski and Professor Dr. Juergen Reif for their time and effort in reviewing this work.

I thank DESY for the possibility to work and BTU Cottbus to study for my thesis. I would like to thank Marie-Curie Framework and MC-PAD for funding the projects I was involved for 3 years and DESY for the last year of my PhD.

My sincere thanks go to Dr. S. Schuwalow for helping me with advices, tips, discussions and being an outstanding advisor during this work.

I would like to acknowledge FCAL and CMS collaborations together with BRM group, especially Dr. A. E. Dabrowski, for team work and all possible help and hints. Especially I would like to thank DESY CMS group for so warm and easy atmosphere at work and chance to learn, grow and supervise.

I would like to thank from my hurt my friends T. Brantova, R. Schmidt and M. Stanescu-Bellu for providing help and for Ringo for reviewing my thesis.

I am deeply and forever indebted to my parents for their love, support and encouragement throughout my entire life. I'm thankful to my mother for surviving me being always away. I am also very grateful to my only sister Anna for support and humor in any situation. Especially I'm indebted for help, believe and support to my boyfriend, B. Lutz.

In the end I would like to devote this thesis to the memory of my father, Vladimir Novgorodov, who could not see this thesis ready, but would be happy to see it...